NATIONAL TECHNICAL UNIVERSITY OF ATHENS
SCHOOL OF APPLIED MATHEMATICAL AND PHYSICAL SCIENCES
DEPARTMENT OF PHYSICS

Study of the fission cross-section of ^{230}Th at the CERN n_TOF facility

Ph.D. Thesis

Veatriki Michalopoulou

Athens, October 2021

Acknowledgements

With this PhD thesis coming to an end, I would like to take the opportunity to express my gratitude to many people for their help and guidance along the way. It goes without saying that this thesis could not have been completed without their support.

First of all I would like to thank my supervisor Roza Vlastou-Zanni and Michael Kokkoris. They gave me an academic home, in which I had the opportunity to evolve my experimental skills without being afraid of making mistakes, to express my thoughts and ideas, as they were always there open to listen and discuss and help me in all the difficulties I encountered. Their trust and appreciation, from the beginning of my diploma thesis, was invaluable and I am really grateful for their support along the way.

I would also like to thank Nikolas Patronis, for his help from the beginning (the experiments at n_TOF) to the end of this work (reading this PhD thesis). I really appreciate the time I spend with him at CERN, the fruitful discussions and his perceptive comments at various points in this PhD thesis.

Special thanks to Daniela Macina, my CERN supervisor. During my time at CERN, Daniela was there to help, organize and understand the needs of this PhD thesis, always with a smile on her face. It was a great pleasure working with her.

Athanasios Stamatopoulos, was there from the beginning of my PhD, to guide me in my first steps in the time-of-flight world. I would really like to thank him for the long hours he spent in the preparation of the n_TOF experiments, for introducing me to the analysis procedure and techniques and for his support during this PhD thesis.

Andrea Tsinganis, even though most of the time we were at different places, was always an email away, to discuss various steps of the analysis. I would like to thank him for his interest in my work, his guidance and the support in organizing the n_TOF experiments.

I am thankful to Maria Diakaki, for always being open to discuss the progress of this work along the way. It was great working with her at n_TOF, NTUA, through emails, virtual meetings and over the phone.

Special thanks to Laurent Tassan-Got, who was there to help with the experimental details, solve physics questions and help in any way possible.

I am really grateful to Nicola Colonna, for following the analysis procedure through the n_TOF meeting, making comments, questions and observations, which were great help for the progress of this work.

Special thanks to Peter Schillebeeckx, for his help, support and constant communication regarding the ^{230}Th targets. I would like to thank Peter, Jan Heyse, Goedele Sibbens and their team for the target preparation and for managing to complete the characterization during the COVID-19 pandemic, so the cross-section results can be presented in this thesis. Thank you!

I would also like to thank all the members of the nuclear physics group of NTUA. Especially, my office mates Antigoni Kalamara and Sotiris Chasapoglou for the nice moments in our office, which made the working place a better place.

Thanks to many people from CERN, Oliver Aberle and Dennis Boon who were there to help us find solutions on various technical problems, Massimo Barbagallo, my office mate in the Mediterranean office, Mario Mastromarco, Federica Mingrone, Michael Bacak, Sebastian Urlass, Sam Bennett, Adhitya Shekhar, Alice Manna and many others for the help and support in the n_TOF control room and the coffee breaks! Special Thanks to Zinovia Eleme, with whom we took our first steps of the PhD together. I would really like to thank Enrico Chiaveri, who was there to support our work and believe in us. The long working hours during the conduction of the experiments at n_TOF would not have been the same without all these people.

Last, I would like to thank my family and loved ones for their love and support along the way. It is not always easy to express how much I appreciate you, but I think you know.

Abstract

Accurate data on neutron induced reactions on actinides is of considerable importance for the design of advanced nuclear systems and alternative fuel cycles. Specifically, ^{230}Th is present in the thorium cycle produced from the decay of ^{234}U. Thus, knowledge of the ^{230}Th(n,f) reaction cross-section is strongly required. However, few experimental datasets exist in literature with large deviations among them, covering the energy range between 0.2 to 25 MeV. In addition, the study of fission cross-sections is of great interest in the research of the fission process related to the structure of the fission barriers. In the case of the thorium isotopes, narrow resonances and fine structures appear in the threshold region of the fission cross-section, known as the thorium anomaly. Specifically, previous measurements on the fission cross-section of ^{230}Th revealed a main resonance at E_n=715 keV and additional fine structures, but with high discrepancies among the measured cross-section values.

The scope of this work is to provide cross-section data for the ^{230}Th(n,f) reaction, covering a wide energy range from the fission threshold up to 400 MeV. For this reason the experiment was performed in both experimental areas EAR-1 and EAR-2 of the CERN n_TOF facility. Seven high purity targets of the natural, unstable but very rare isotope ^{230}Th, were produced at JRC-Geel in Belgium. The experimental setup was based on Micromegas detectors, while the ^{235}U(n,f) cross-section was used as reference. A detailed description of the experimental setup, the analysis procedure, starting from the raw data to the final cross-section results, including the Monte-Carlo simulations performed and the theoretical study of the ^{230}Th(n,f) reaction with the EMPIRE code are presented.

Abstract (in Greek)

Τα δεδομένα ενεργών διατομών για τις ακτινίδες παίζουν σημαντικό ρόλο στη μελέτη και το σχεδιασμό προηγμένων πυρηνικών συστημάτων παραγωγής ενέργειας και εναλλακτικών πυρηνικών κύκλων καυσίμων. Συγκεκριμένα, το ^{230}Th συναντάται στον κύκλο του θορίου, όπου παράγεται από την αποδιέγερση του ^{234}U. Για το λόγο αυτό απαιτείται η γνώση της ενεργού διατομή της αντίδρασης σχάσης ^{230}Th(n,f). Μέχρι σήμερα, λίγα πειραματικά δεδομένα για την αντίδραση αυτή συναντώνται στη βιβλιογραφία, τα οποία καλύπτουν το ενεργειακό εύρος από 0.2 έως 25 MeV και παρουσιάζουν μεγάλες αποκλίσεις μεταξύ τους. Επίσης, η μελέτη των ενεργών διατομών αντιδράσεων σχάσης αποτελεί ένα μέσο για τη μελέτη της διαδικασίας της σχάσης και της δομής του δυναμικού της σχάσης. Όσο αναφορά τα ισότοπα του θορίου, παρουσιάζονται λεπτοί συντονισμοί στην περιοχή του κατωφλίου της σχάσης. Συγκεκριμένα, προηγούμενες μετρήσεις στην ενεργό διατομή σχάσης του ^{230}Th έχουν αναδείξει ένα βασικό συντονισμό με ενέργεια E_n=715 keV με επιπλέον δομές, αλλά μεγάλες αποκλίσεις μεταξύ των υπάρχοντων πειραματικών ενεργών διατομών.

Στόχος της παρούσας διδακτορικής διατριβής είναι η παροχή πειραματικών δεδομένων για την αντίδραση σχάσης του ^{230}Th, καλύπτοντας το ενεργειακό εύρος από το κατώφλι της σχάσης μέχρι τα 400 MeV. Για το σκοπό αυτό πραγματοποιήθηκαν μετρήσεις στις πειραματικές περιοχές EAR-1 και EAR-2 της εγκατάστασης n_TOF στο CERN, με τη χρήση επτά στόχων υψηλής καθαρότητας του φυσικού και πολύ σπάνιου ισοτόπου ^{230}Th, οι οποίοι κατασκευάστηκαν στο JRC-Geel στο Βέλγιο. Η πειραματική διάταξη βασίστηκε στους ανιχνευτές αερίου Micromegas, ενώ η αντίδραση ^{235}U(n,f) χρησιμοποιήθηκε σαν αντίδραση αναφοράς. Η αναλυτική περιγραφή της πειραματικής διάταξης, της διαδικασίας της ανάλυσης των δεδομένων και των προσομοιώσεων Monte-Carlo που πραγματοποιήθηκαν ώστε να υπολογιστεί η ενεργός διατομή της αντίδρασης ^{230}Th(n,f), καθώς και η θεωρητική μελέτη της αντίδρασης που υλοποιήθηκε με τον κώδικα EMPIRE, παρουσιάζονται στην παρούσα διδακτορική διατριβή.

Contents

Extended abstract (in Greek)

Εισαγωγή

Ο ακριβής προσδιορισμός των ενεργών διατομών αντιδράσεων νετρονίων στις ακτινίδες αποτελεί ένα σημαντικό κομμάτι στη διαδικασία του σχεδιασμού πυρηνικών συστημάτων παραγωγής ενέργειας, καθώς και στη μελέτη εναλλακτικών πυρηνικών κύκλων καυσίμων. Συγκεκριμένα, το ^{230}Th παράγεται στον κύκλο του θορίου από την α-αποδιέγερση του ^{234}U. Επομένως, απαιτείται η γνώση της ενεργού διατομής της αντίδρασης ^{230}Th(n,f) με μεγάλη ακρίβεια. Μέχρι την παρούσα στιγμή λίγες πειραματικές μετρήσεις έχουν πραγματοποιηθεί για την αντίδραση αυτή, με μεγάλες αποκλίσεις μεταξύ τους, ενώ καλύπτουν το ενεργειακό εύρος από τα 0.2 μέχρι τα 25 MeV. Επιπλέον, η μελέτη των ενεργών διατομών σχάσης παρουσιάζει μεγάλο ενδιαφέρον στη μελέτη της διαδικασίας της σχάσης και των παραμέτρων του πυρήνα. Προηγούμενες μετρήσεις ενεργών διατομών στα ισότοπα του Th παρουσιάζουν στενούς συντονισμούς και λεπτές δομές στην περιοχή του κατωφλίου της σχάσης. Συγκεκριμένα, η ενεργός διατομή σχάσης του ^{230}Th εμφανίζει έναν κεντρικό συντονισμό σε ενέργεια E_n=715 keV και επιπλέον λεπτές δομές, αλλά με μεγάλες διαφορές μεταξύ των υπαρχόντων πειραματικών μετρήσεων.

Στόχος της παρούσας διδακτορικής διατριβής ήταν η μέτρηση της ενεργού διατομής της αντίδρασης ^{230}Th(n,f), καλύπτοντας ένα ευρύ ενεργειακό εύρος από το κατώφλι της σχάσης μέχρι τα 400 MeV. Σε αυτό το πλαίσιο πραγματοποιήθηκε η μέτρηση της αντίδρασης αυτής στην εγκατάσταση παραγωγής νετρονίων n_TOF, το οποίο βρίσκεται στο CERN. Για τις μετρήσεις χρησιμοποιήθηκαν επτά στόχοι υψηλής καθαρότητας του ασταθούς και σπάνιου ισοτόπου ^{230}Th, οι οποίοι κατασκευάστηκαν στο JRC-Geel στο Βέλγιο. Για την ανίχνευση των θραυσμάτων σχάσης χρησιμοποιήθηκαν οι ανιχνευτές Micromegas και η ενεργός διατομή υπολογίστηκε σχετικά με την αντίδραση αναφοράς ^{235}U(n,f).

Ο κύκλος του θορίου

Οι ενεργειακές ανάγκες των σύγχρονων κοινωνιών, σε συνδυασμό με τους περιορισμένους πόρους των ορυκτών καυσίμων, καθιστούν αναγκαία την αναζήτηση εναλλακτικών μέσων παραγωγής ενέργειας. Η πυρηνική ενέργεια είναι η μόνη εναλλακτική πηγή ενέργειας που μπορεί να εξυπηρετήσει τις ανάγκες των σύγχρονων κοινωνιών, χωρίς να συμβάλει στο φαινόμενο του θερμοκηπίου [1].

Διάφορες εναλλακτικές λύσεις έχουν προταθεί για την αντικατάσταση των συμβατικών αντιδραστήρων, όπως είναι οι πυρηνικοί αντιδραστήρες τέταρτης γενιάς [2], καθώς και αντιδραστήρες που λειτουργούν σε συνδυασμό με έναν επιταχυντή (ADS), με στόχο να γίνει η παραγωγή ενέργειας μέσω πυρηνικών συστημάτων πιο ασφαλής, οικονομική και βιώσιμη. Επίσης, αναγκαία είναι και η μελέτη εναλλακτικών πυρηνικών κύκλων καυσίμων, διότι

τα αποθέματα ουρανίου φαίνεται ότι δεν είναι αρκετά για τη συνεχή παραγωγή ενέργειας με πυρηνικά μέσα. Ο κύκλος του θορίου, είναι μία εναλλακτική πρόταση στον συμβατικό κύκλο ουρανίου-πλουτωνίου. Στον κύκλο αυτό, το ^{232}Th μετατρέπεται στο σχάσιμο ^{233}U μετά από την απορρόφηση ενός νετρονίου, που ακολουθείται από δύο αποδιεγέρσεις β^-.

Για την μελέτη και ανάπτυξη συστημάτων παραγωγής ενέργειας που βασίζονται στον κύκλο του θορίου, απαιτούνται πειραματικά δεδομένα ενεργών διατομών για τα ισότοπα που βρίσκονται στον κύκλο, ειδικά για τις αντιδράσεις (n, γ), (n, xn) και (n, f). Συγκεκριμένα το ^{230}Th με χρόνο ημιζωής 7.54×10^4 χρόνια παράγεται από την α-αποδιέγερση του ^{234}U και έχει περίπου διπλάσια ενεργό διατομή από το ^{232}Th στις υψηλές ενέργειες, το οποίο έχει σαν αποτέλεσμα μια μικρή αύξηση στην παραγωγή ενέργειας, αφού συμβάλει στον παραγόμενο αριθμό νετρονίων.

Η μελέτη των ενεργών διατομών αντιδράσεων σχάσης παίζουν επιπλέον ένα σημαντικό ρόλο στη μελέτη της ίδιας της διαδικασίας της σχάσης. Συγκεκριμένα, στα ισότοπα του θορίου λεπτές δομές εμφανίζονται στην ενεργό διατομή σχάσης σε ενέργειες κοντινές με το κατώφλι τις σχάσης, οι οποίες δεν έχουν εξηγηθεί ακόμα στα πλαίσιο της θεωρίας του διπλού δυναμικού σχάσης.

Προηγούμενες μετρήσεις για την αντίδραση ^{230}**Th**(**n**,**f**)

Λίγες πειραματικές μετρήσεις για την ενεργό διατομή σχάσης του ^{230}Th υπάρχουν στη βιβλιογραφία [3], οι οποίες παρουσιάζονται στα σχήματα 1α′ (για όλο το ενεργειακό εύρος) και 1β′ (για την περιοχή του συντονισμού) και καλύπτουν το ενεργειακό εύρος από το κατώφλι της σχάσης μέχρι τα 25 MeV, με διαφορές μεταξύ τους και μεγάλες τιμές αβεβαιότητας.

Στόχος της παρούσας διδακτορικής διατριβής είναι η παροχή πειραματικών δεδομένων για την αντίδραση σχάσης του ^{230}Th καλύπτοντας ένα ευρύ εύρος ενεργειών. Για το σκοπό αυτό πραγματοποιήθηκαν μετρήσεις στις πειραματικές περιοχές EAR-1 και EAR-2 της εγκατάστασης n_TOF στο CERN.

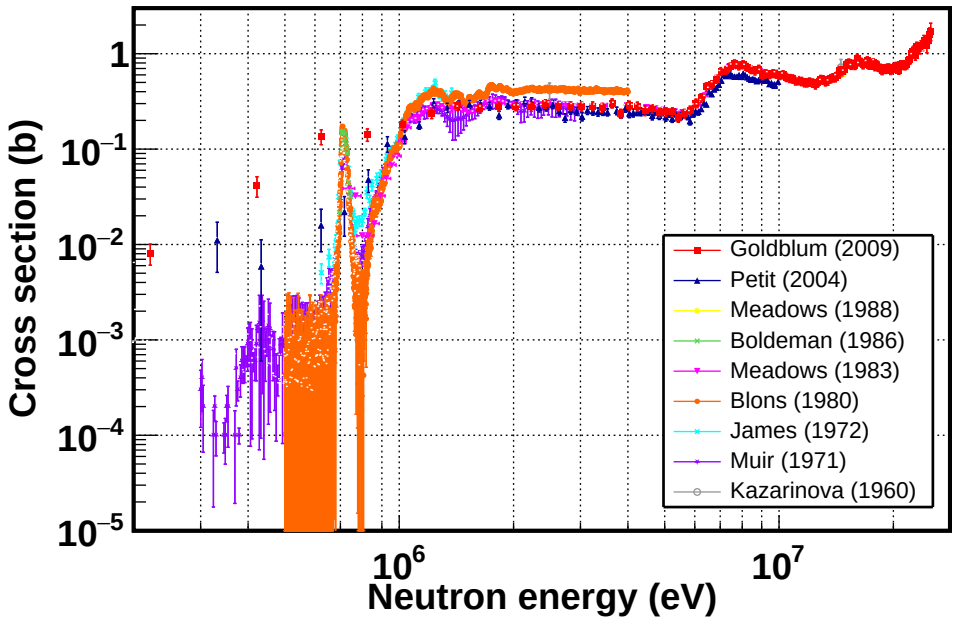

(α′) Όλα τα πειραματικά δεδομένα

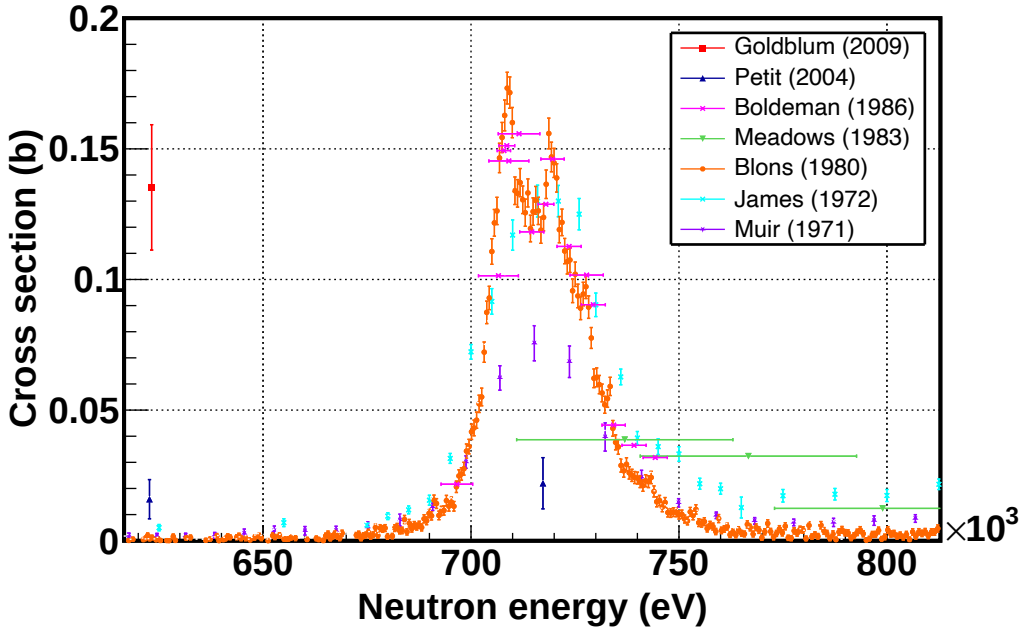

(β′) Πειραματικά δεδομένα στην περιοχή του συντονισμού

Σχήμα 1: Πειραματικά δεδομένα για την ενεργό διατομή σχάσης του ^{230}Th που υπάρχουν στη βιβλιογραφία.

Πειραματική διάταξη

Η εγκατάσταση n_TOF βρίσκεται στο CERN και βασίζεται σε μία ιδέα του Rubbia *et al.* [4, 5, 6]. Η λευκή δέσμη νετρονίων παράγεται από αντιδράσεις κατακερματισμού παλμικής δέσμης πρωτονίων που προσκρούει σε έναν στόχο μολύβδου. Αποτελείται από δύο πειραματικές περιοχές: την EAR-1 που βρίσκεται σε οριζόντια απόσταση 185 m από το στόχο μολύβδου και την EAR-2 που βρίσκεται σε κάθετη απόσταση 19 m από τον στόχο μολύβδου, όπως φαίνεται στο σχήμα 2.

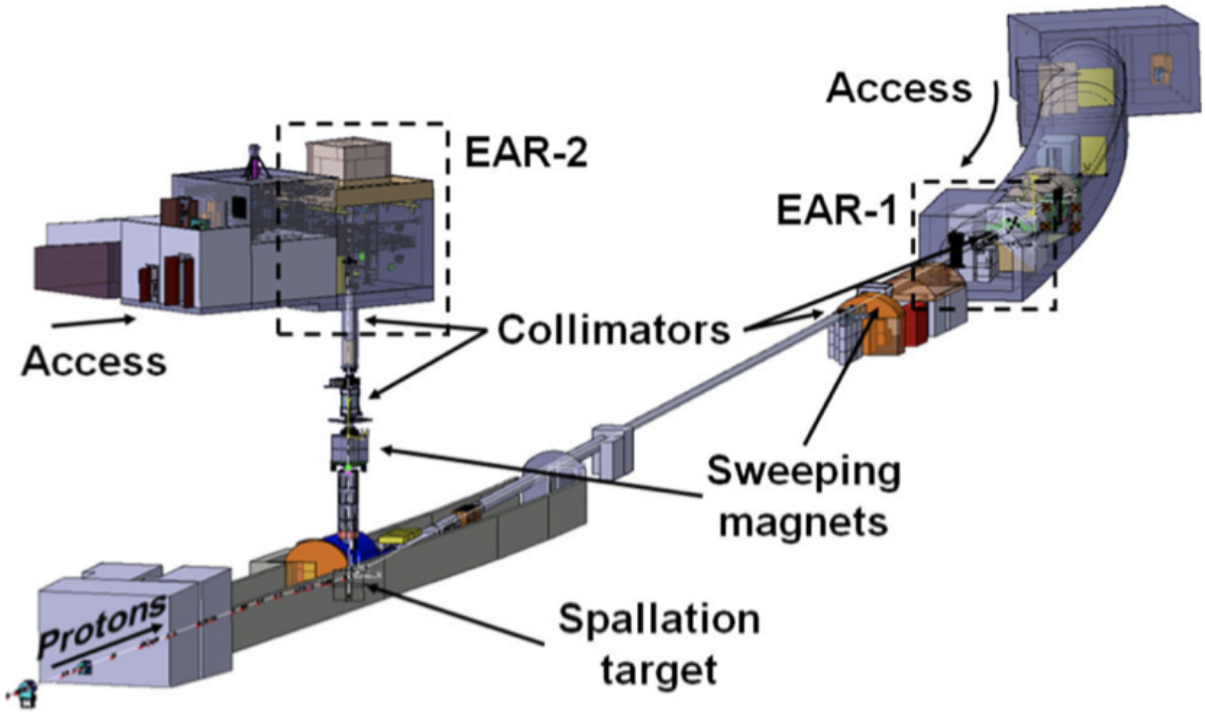

Σχήμα 2: Σχηματική αναπαράσταση της εγκατάστασης n_TOF στο CERN [7].

Η δέσμη νετρονίων της εγκατάστασης n_TOF καλύπτει το ενεργειακό εύρος από τη θερμική περιοχή μέχρι ∼1 GeV [8, 9]. Η διαφορετική απόσταση των δύο περιοχών από το στόχο μολύβδου έχει σαν αποτέλεσμα διαφορετικά χαρακτηριστικά στη ροή μεταξύ των δύο πειραματικών περιοχών, όπως φαίνεται στο σχήμα 3. Συγκεκριμένα η EAR-1 είναι καταλληλότερη για μετρήσεις που απαιτούν υψηλότερη ενέργεια νετρονίων ή για μετρήσεις που απαιτούν καλύτερη ενεργειακή διακριτική ικανότητα των νετρονίων. Από την άλλη η EAR-2, λόγω της υψηλότερης ροής νετρονίων, επιλέγεται σε περιπτώσεις όπου ο μετρούμενος στόχος έχει μεγάλη ενεργότητα, μικρή μάζα, μικρή ενεργό διατομή ή και κάποιον συνδυασμό των παραπάνω.

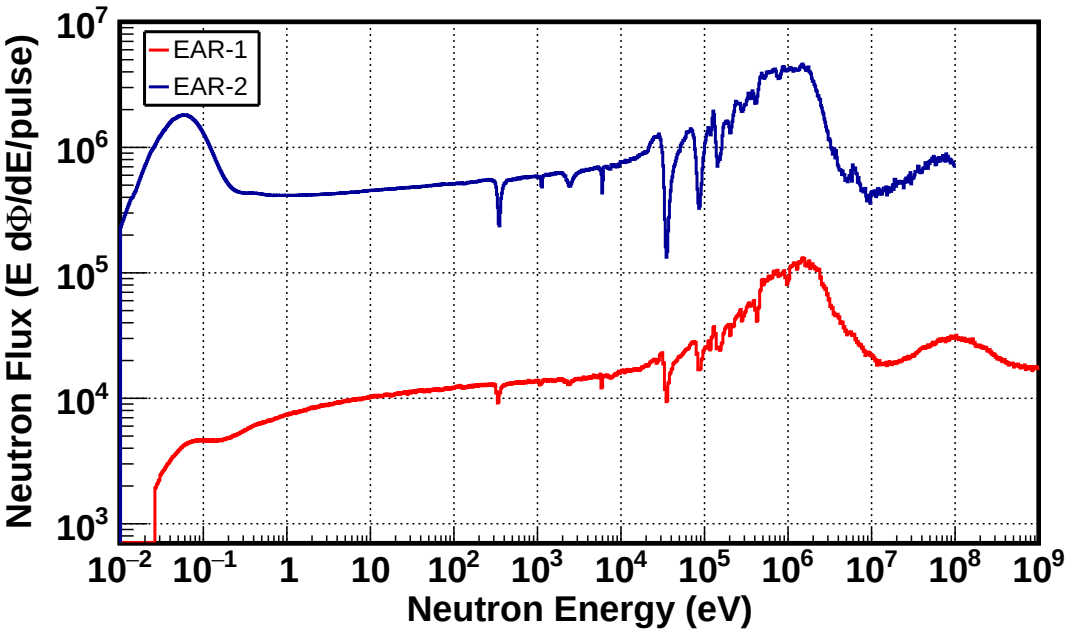

Σχήμα 3: Σύγκριση της νετρονικής ροής της πειραματικής περιοχής EAR-1 (κόκκινη γραμμή) [8] και EAR-2 (μπλε γραμμή) [9].

Από το χρόνο πτήσης στην ενέργεια του νετρονίου

Η μετατροπή της χρονικής διαφοράς από τη στιγμή της δημιουργίας του νετρονίου στην ενέργειά του σύμφωνα με την κλασική προσέγγιση είναι:

$$E_n = \frac{1}{2} m_n v^2 = \frac{1}{2} m_n \left(\frac{L}{t}\right)^2 \tag{1}$$

όπου $m_n = 939.6\ \mathrm{MeV}/c^2$ η μάζα του νετρονίου, $v = L/t$ η ταχύτητα του νετρονίου, L είναι η διαδρομή που διανύει το νετρόνιο και t ο χρόνος πτήσης του νετρονίου. Για ενέργειες μεγαλύτερες από μερικά keV χρησιμοποιείται η σχετικιστική εξίσωση:

$$E_n = m_n c^2(\gamma - 1) = m_n c^2 \left(\frac{1}{\sqrt{1 - \left(\frac{L}{tc}\right)^2}} - 1\right) \tag{2}$$

όπου $c = 299.8\ \mathrm{m}/\mu\mathrm{s}$ είναι η ταχύτητα του φωτός γ είναι ο παράγοντας Λόρεντζ.

Στόχοι ακτινίδων

Επτά στόχοι υψηλής καθαρότητας του ισοτόπου ^{230}Th χρησιμοποιήθηκαν για τις μετρήσεις συνολικής μάζας 27.14 mg. Οι στόχοι κατασκευάστηκαν στο JRC-Geel και ήταν εναποτεθειμένοι σε βάση αλουμινίου πάχους 0.025 mm. Τα χαρακτηριστικά των στόχων παρουσιάζονται στον πίνακα 1. Στους στόχους υπήρχαν προσμίξεις από ισότοπα του Pu με αναλογία Pu/Th 0.0004942. Οι περιεκτικότητες των διάφορων ισοτόπων του Pu παρουσιάζονται στον πίνακα 2. Παρότι η ποσότητα των ισοτόπων του Pu στους στόχους ήταν μικρή, λόγω της μεγάλης ενεργού διατομής μερικών από αυτά είναι αρκετή ώστε τα γεγονότα που προέρχονται από το Pu να κυριαρχούν για ενέργειες μικρότερες του κατωφλίου της σχάσης του ^{230}Th.

Πίνακας 1: Χαρακτηριστικά των στόχων ^{230}Th.

Αριθμός στόχου	Ταυτότητα στόχου	Μάζα (mg)	Επιφανειακή πυκνότητα (μg/cm^2)	Ενεργότητα (MBq)
^{230}Th #3	TP2017-06-19	4.61	92	3.52
^{230}Th #4	TP2017-06-21	4.19	83	3.20
^{230}Th #5	TP2017-06-24	2.31	46	1.76
^{230}Th #6	TP2017-06-22	2.46	49	1.88
^{230}Th #7	TP2017-06-25	4.14	82	3.16
^{230}Th #8	TP2017-06-20	4.89	97	3.73
^{230}Th #9	TP2017-06-18	4.53	90	3.46

Πίνακας 2: Αναλογίες των προσμίξεων Pu στους στόχους ^{230}Th. Η αναλογία Pu/Th είναι 0.0004942.

Ισότοπο	Περιεκτικότητα (%)
^{238}Pu	0.2681
^{239}Pu	22.40
^{240}Pu	20.23
^{241}Pu*	7.76
^{242}Pu	49.15
^{244}Pu	0.199

* Ενδεικτική τιμή.

Σαν στόχοι αναφοράς χρησιμοποιήθηκαν ένας στόχος ^{235}U με επιφανειακή πυκνότητα 72 μg/cm^2 (ενεργότητας 587.5 Bq) και ένας στόχος ^{238}U με επιφανειακή πυκνότητα 287 μg/cm^2 (ενεργότητας 179.5 Bq).

Ανιχνευτές **Micromegas**

Για τις μετρήσεις χρησιμοποιήθηκαν οι ανιχνευτές Micro-Bulk Micromegas (Micro-Mesh Gaseous Structure) [10, 11, 12, 13, 14]. Οι ανιχνευτές Micromegas [15, 16, 17] είναι ανιχνευτές αερίου που χωρίζονται σε δύο περιοχές από το ηλεκτρόδιο της καθόδου (micromesh): την περιοχή ολίσθησης μεταξύ του ηλεκτροδίου ολίσθησης (drift electrode) και της καθόδου και την περιοχή ενίσχυσης μεταξύ της καθόδου και της ανόδου. Η άνοδος γειώνεται μέσω μίας αντίστασης 50 Ω, ενώ η τάση στα ηλεκτρόδια της ολίσθησης και της καθόδου επιλέγεται αναλόγως με την ενέργεια και τον τύπο του προς ανίχνευση σωματιδίου ή ακτινοβολίας.

Όταν μία ιονίζουσα ακτινοβολία εισέρχεται στην περιοχή της ολίσθησης, δημιουργεί ζεύγη ηλεκτρονίων-οπών. Λόγω του ηλεκτρικού πεδίου τα ηλεκτρόνια κατευθύνονται προς την κάθοδο και οδηγούνται μέσω των οπών του ηλεκτροδίου της καθόδου στην περιοχή της ενίσχυσης. Εκεί, πραγματοποιείται ο πολλαπλασιασμός τους μέσω του φαινομένου της χιονοστιβάδας. Το σήμα δημιουργείται από την κίνηση των φορτισμένων φορέων φορτίου, ενώ στην παρούσα εργασία συλλέχτηκε από το ηλεκτρόδιο της καθόδου. Μια σχηματική αναπαράσταση της κίνησης των ηλεκτρονίων, όταν ένα θραύσμα σχάσης εισέρχεται στον ανιχνευτή παρουσιάζεται στο σχήμα 4.

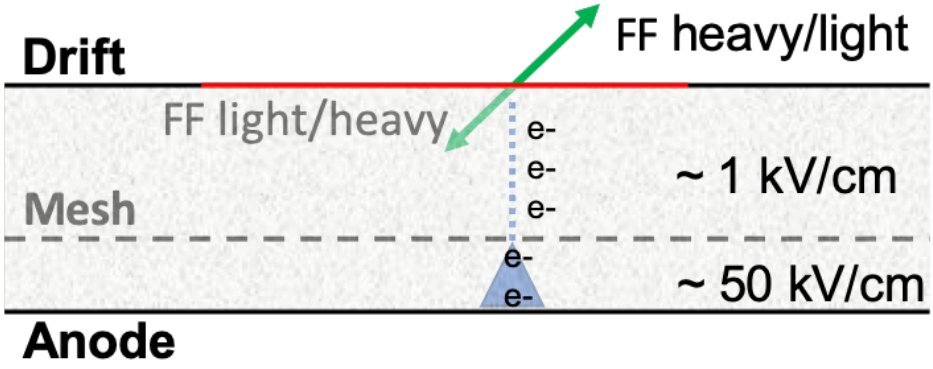

Σχήμα 4: Σχηματική αναπαράσταση της κίνησης των ηλεκτρονίων, όταν ένα θραύσμα σχάσης εισέρχεται στον ανιχνευτή Micromegas.

Για τη μέτρηση της ενεργού διατομής σχάσης του ^{230}Th οι ανιχνευτές Micromegas τοποθετήθηκαν μαζί με τους στόχους ακτινίδων σε ένα θάλαμο σχάσης αλουμινίου (σχήμα 5), ο οποίος γέμισε με ένα μείγμα αερίου Ar:CF_4:isoC_4H_{10} (88:10:2) το οποίο κρατήθηκε σε θερμοκρασία δωματίου και ατμοσφαιρική πίεση για όλη τη διάρκεια των πειραματικών μετρήσεων. Η ίδια πειραματική διάταξη χρησιμοποιήθηκε για τις μετρήσεις στις πειραματικές περιοχές EAR-1 και EAR-2.

Ηλεκτρονικά και σύστημα καταγραφής δεδομένων

Για τις μετρήσεις στις πειραματικές περιοχές EAR-1 και EAR-2 χρησιμοποιήθηκαν προενισχυτές που κατασκευάστηκαν στο INFN-Bari. Κάθε προενισχυτής τοποθετήθηκε μόνος του σε ένα χοντρό αλουμινένιο κουτί, ώστε να αποφευχθεί η επικοινωνία μεταξύ των διαφορετικών προενισχυτών και μέσω της θωράκισης να μειωθεί ο θόρυβος. Οι προενισχυτές

χρησιμοποιήθηκαν για την τροφοδοσία του ηλεκτροδίου της καθόδου αλλά και για την συλλογή του σήματος από το ίδιο ηλεκτρόδιο.

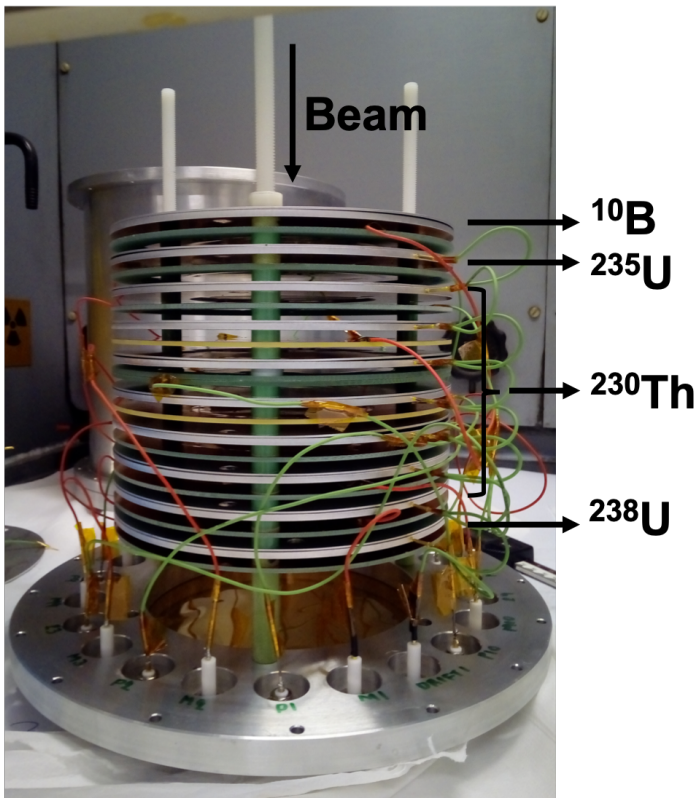

Σχήμα 5: Η πειραματική διάταξη που χρησιμοποιήθηκε για τις μετρήσεις στις πειραματικές περιοχές EAR-1 και EAR-2.

Ανάλυση δεδομένων

Τα σήματα από κάθε ανιχνευτή αποθηκεύονται στο σύστημα αποθήκευσης δεδομένων του CERN CASTOR (CERN Advanced STORage manager), ώστε να γίνει η περαιτέρω επεξεργασία τους.

Πρώτο βήμα στη διαδικασία της ανάλυσης των δεδομένων είναι η επεξεργασία του γ-flash. Το γ-flash είναι η πρώτη μεγάλη κορυφή που εμφανίζεται στα πειραματικά χρονικά φάσματα. Η επεξεργασία του παλμού αυτού αποτελεί ένα πολύ σημαντικό κομμάτι της ανάλυσης, διότι ο υπολογισμός του χρόνου πτήσης του νετρονίου (και επομένως και της ενέργειάς του) πραγματοποιείται σχετικά με την κορυφή του γ-flash. Επίσης, μετά την κορυφή του γ-flash εμφανίζονται κάποιες ταλαντώσεις ή κορυφές στο υπόβαθρο. Η περιγραφή των επιπτώσεων του γ-flash στο υπόβαθρο είναι μια βασική προϋπόθεση ώστε να γίνει σωστή αναγνώριση των παλμών θραυσμάτων σχάσης και ο προσδιορισμός του χρόνου στον οποίο αντιστοιχούν, ειδικά στις υψηλότερες ενέργειες όπου οι επιπτώσεις στο υπόβαθρο μετά το γ-flash είναι πιο έντονες.

Ο χειρισμός του γ-flash περιγράφεται στο [18] και περιλαμβάνει τον υπολογισμό του μέσου σχήματος της κορυφής (και του υποβάθρου μετά) από πολλούς παλμούς γ-flash, όπως παρουσιάζεται στο σχήμα 6α΄ για την πειραματική περιοχή EAR-1 και στο σχήμα 6β΄ για την πειραματική περιοχή EAR-2.

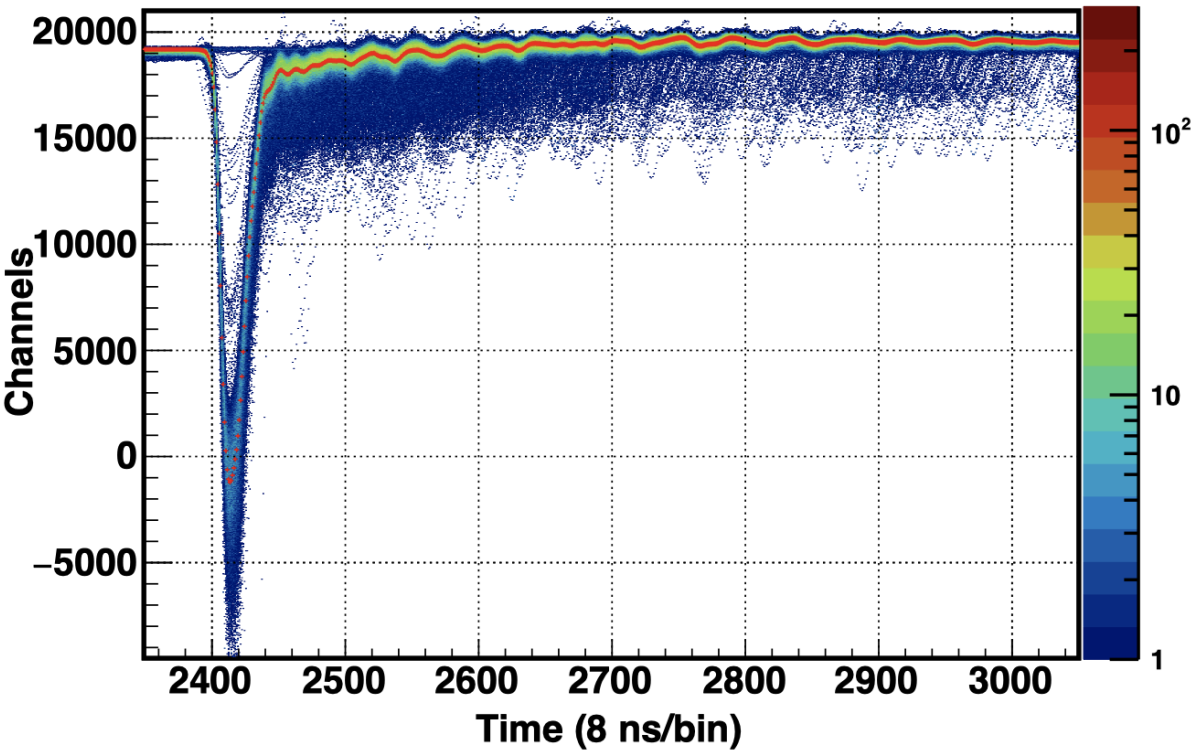

(α′) EAR-1

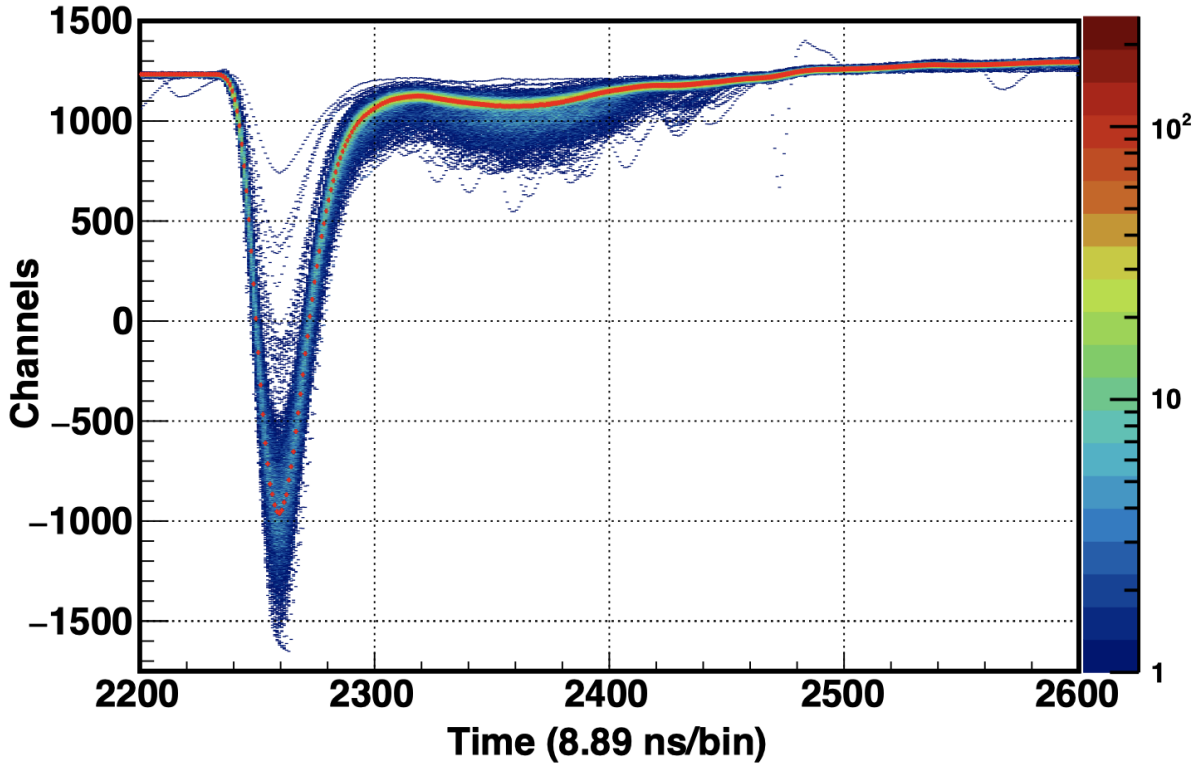

(β′) EAR-1

Σχήμα 6: Πολλοί παλμοί γ-flash από τις μετρήσεις στην (α) EAR-1 και (β) EAR-2 από τους οποίους υπολογίζεται το μέσο σχήμα του γ-flash (κόκκινη γραμμή).

Η διαδικασία της αναγνώρισης των παλμών ξεκινάει από τον υπολογισμό της παραγώγου, όπως φαίνεται στο δεύτερο πλαίσιο του σχήματος 7. Αν συγκεκριμένες συνθήκες καλύπτονται από την παράγωγο και τον ίδιο τον παλμό (ύψος, ολοκλήρωμα κτλ.) τότε ο παλμός χαρακτηρίζεται σαν πραγματικό γεγονός. Στη συνέχεια ακολουθεί ο υπολογισμός του υποβάθρου, που προσεγγίζεται σαν μία σταθερή γραμμή κοντά στον παλμό, ενώ κοντά στο γ-flash από το μέσο σχήμα του. Ο καθαρός παλμός υπολογίζεται μετά την αφαίρεση του υποβάθρου (τρίτο πλαίσιο του σχήματος 7). Για την ανακατασκευή των παλμών χρησιμοποιείται η μέθοδος της προσαρμογής του σχήματος των παλμών με σχήματα παλμών που ορίζονται από το χρήστη.

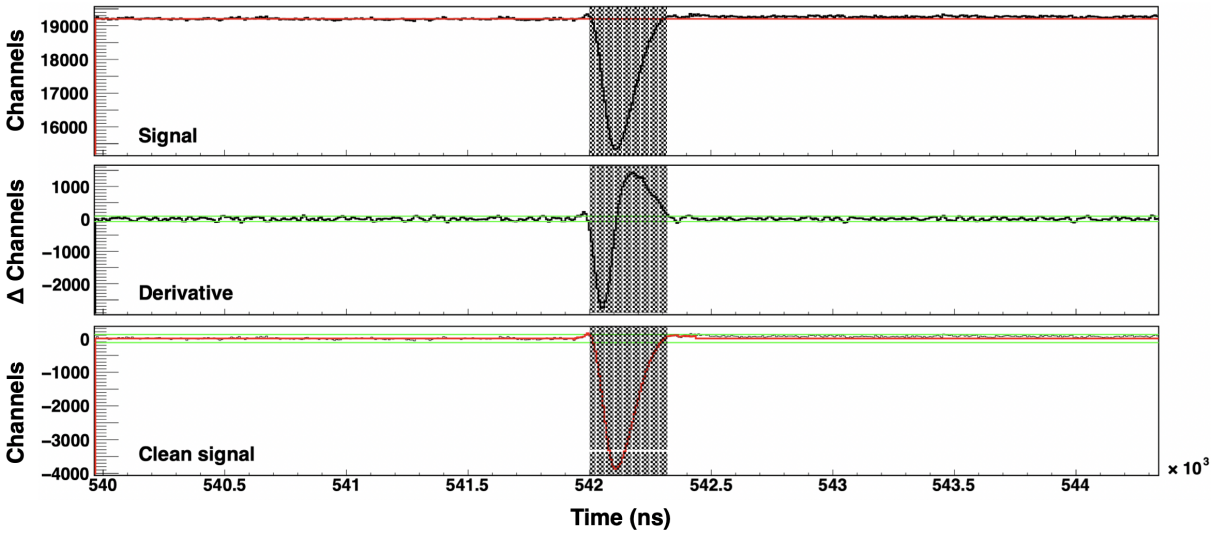

Σχήμα 7: Η ρουτίνα της ανάλυσης των παλμών υπολογίζει την παράγωγο του σήματος (δεύτερο πλαίσιο), ώστε να επιτευχθεί η αναγνώριση του καθαρού σήματος (τρίτο πλαίσιο).

Έλεγχος ποιότητας δεδομένων

Η διαδικασία της αναγνώρισης των παλμών ακολουθείται από ελέγχους της ποιότητας των δεδομένων και επιλογή από τα δεδομένα αυτά. Για το λόγο αυτό γίνεται ο έλεγχος διάφορων παραμέτρων των παλμών που έχουν αναγνωριστεί από την ρουτίνα ώστε να γίνει η επιβεβαίωση ότι οι παλμοί που καταγράφονται αντιστοιχούν σε θραύσματα σχάσης.

Πρώτος έλεγχος που πραγματοποιείται στο στάδιο αυτό είναι το κατά πόσον η ενίσχυση των ανιχνευτών του πειράματος παρέμεινε σταθερή για όλη τη διάρκεια των πειραμάτων. Για το λόγο αυτό συλλέγονται φάσματα χωρίς την παρουσία δέσμης νετρονίων και συγκρίνονται τα φάσματα αυτά στην αρχή και στο τέλος της μέτρησης. Όπως φαίνεται στο σχήμα 8 η ενίσχυση των ανιχνευτών είναι σταθερή για όλη της διάρκεια της μέτρησης.

Επόμενο βήμα στη διαδικασία ελέγχου της ανάλυσης είναι ο χρόνος άφιξης της κορυφής του γ-flash, ώστε να γίνει ξεκάθαρο ότι γίνεται σωστή αναγνώριση της κορυφής του γ-flash και δεν αναγνωρίζονται λανθασμένα παλμοί που έρχονται πριν την δέσμη πρωτονίων που δημιουργεί τα νετρόνια σαν την κορυφή αυτή. Αυτό εξακριβώνεται από τις κατανομές του χρόνου άφιξης του γ-flash, όπως παρουσιάζονται στο σχήμα 9.

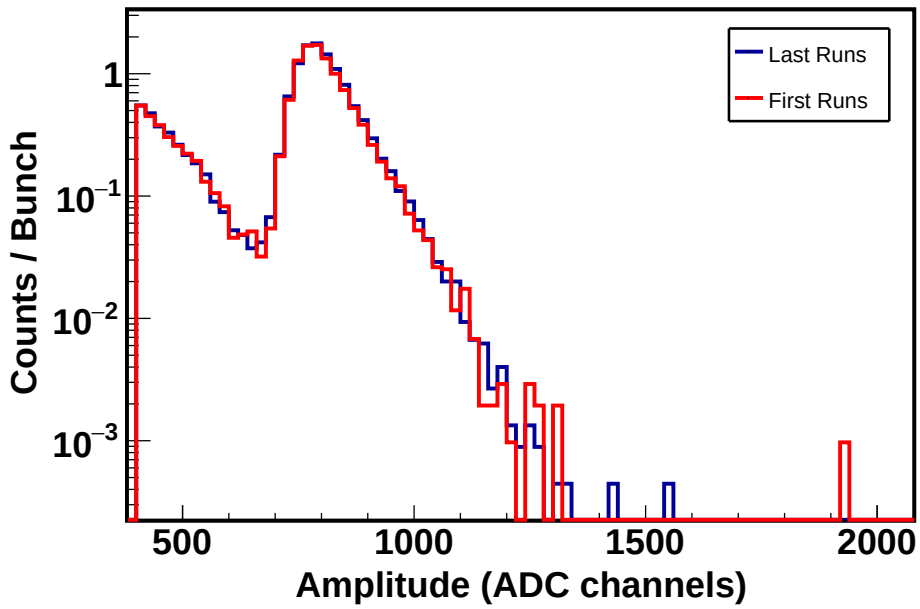

Σχήμα 8: Φάσματα χωρίς δέσμη από την αρχή (κόκκινη γραμμή) και το τέλος (μπλε γραμμή) της μέτρησης στην EAR-1 για έναν από τους στόχους του ^{230}Th, από τα οποία επιβεβαιώνεται η σταθερότητα των ανιχνευτών για όλη τη διάρκεια της μέτρησης.

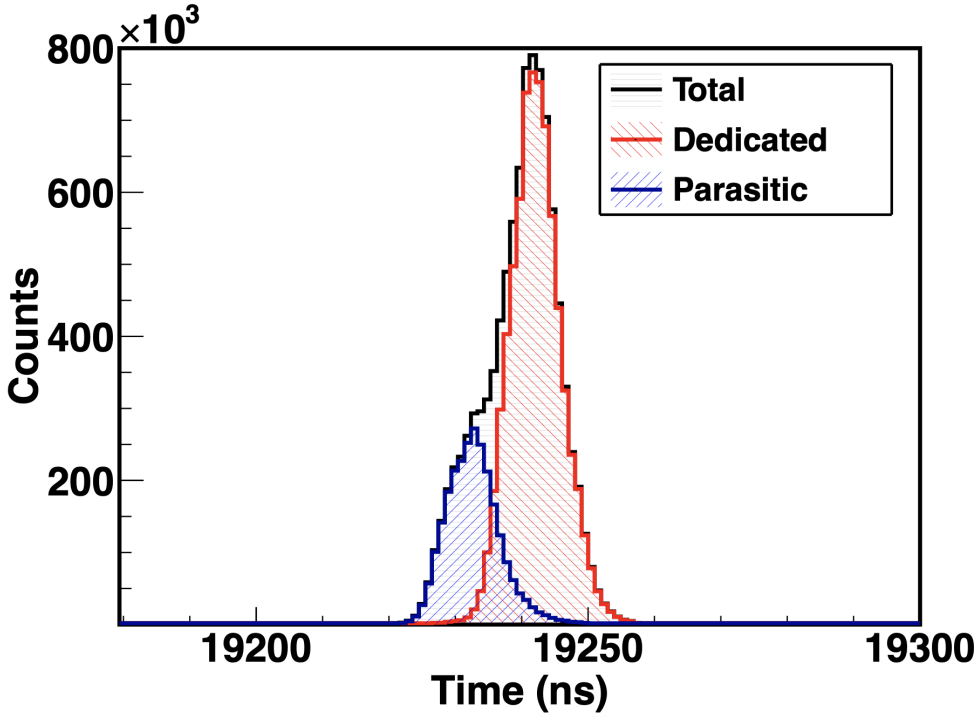

Σχήμα 9: Κατανομές για το χρόνο άφισης του γ-flash.

Σε κάποιες περιπτώσεις θόρυβος μπορεί να αναγνωριστεί σαν παλμός, ο οποίος απορρίπτεται σε πρώτο στάδιο κατά τη διαδικασία της αναγνώρισης των παλμών από τη ρουτίνα και σε δεύτερο στάδιο στη μετέπειτα ανάλυση των σημάτων μέσω του κώδικα ROOT [19].

Δύο ήταν οι πηγές του θορύβου στην παρούσα εργασία. Η πρώτη πηγή ήταν σήματα μεγάλου ύψους τα οποία καταγράφονταν ταυτόχρονα σε όλους τους ανιχνευτές, όπως παρουσιάζεται στο σχήμα 10. Η δεύτερη πηγή ήταν η αναγνώριση θορύβου σαν παλμούς, λόγω των αυξημένων υπολειμμάτων από την αφαίρεση του υποβάθρου μετά την κορυφή του γ-flash, όπως παρουσιάζεται στο σχήμα 11, όπου το ύψος των παλμών σχεδιάζεται σα συνάρτηση της ενέργειας του νετρονίου. Στις υψηλότερες ενέργειες παρατηρείται αύξηση του θορύβου που καταγράφεται.

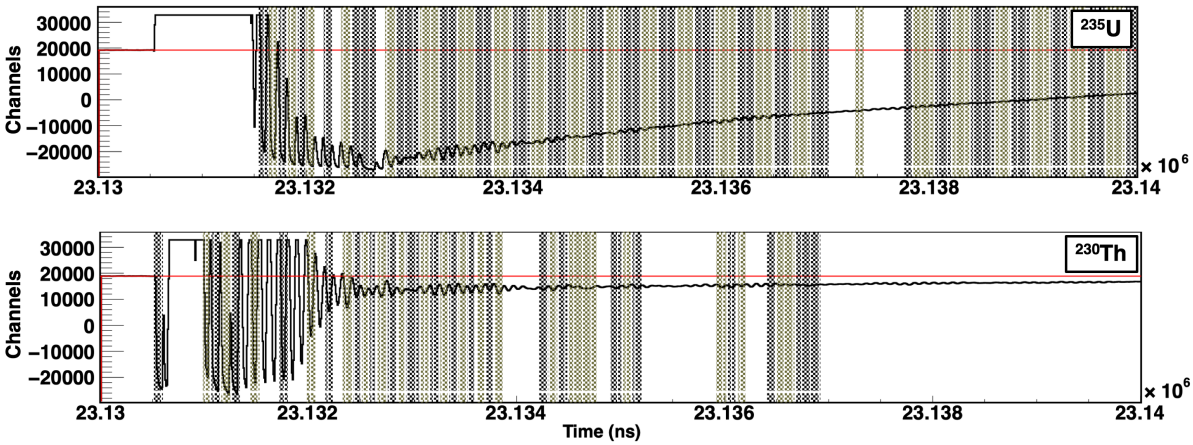

Σχήμα 10: Θόρυβος που έχει καταγραφεί ταυτόχρονα σε δύο από τους ανιχνευτές.

Προκειμένου να γίνει η διόρθωση για την αύξηση του θορύβου στις μεγαλύτερες ενέργειες επιλέγεται μεγαλύτερο κατώφλι για την απόρριψη παλμών μεγαλύτερου ύψους. Πρώτα γίνεται έλεγχος ότι τα φάσματα των γεγονότων δεν αλλοιώνονται με την αύξηση της ενέργειας, διατηρώντας το σχήμα τους από το υψηλό κατώφλι που εφαρμόζεται στην ανάλυση και μετά, όπως παρουσιάζεται στο σχήμα 12 για το στόχο του ^{235}U (σχήμα 12α′) για το στόχο του ^{230}Th #3 (σχήμα 12β′) και για το στόχο του ^{238}U (σχήμα 12γ′).

Επιπλέον, γίνεται ο έλεγχος ότι το μεγαλύτερο κατώφλι για το ύψος του παλμού δεν αλλοιώνει την αναγνώριση των σημάτων, μέσω της σύγκρισης των πειραματικών γεγονότων για ένα χαμηλό και ένα υψηλό κατώφλι στην ανάλυση κανονικοποιημένα μεταξύ τους, όπως παρουσιάζονται στο σχήμα 13 για το στόχο του ^{235}U (σχήμα 13α′) για το στόχο του ^{230}Th #3 (σχήμα 13β′) και για το στόχο του ^{238}U (σχήμα 13γ′).

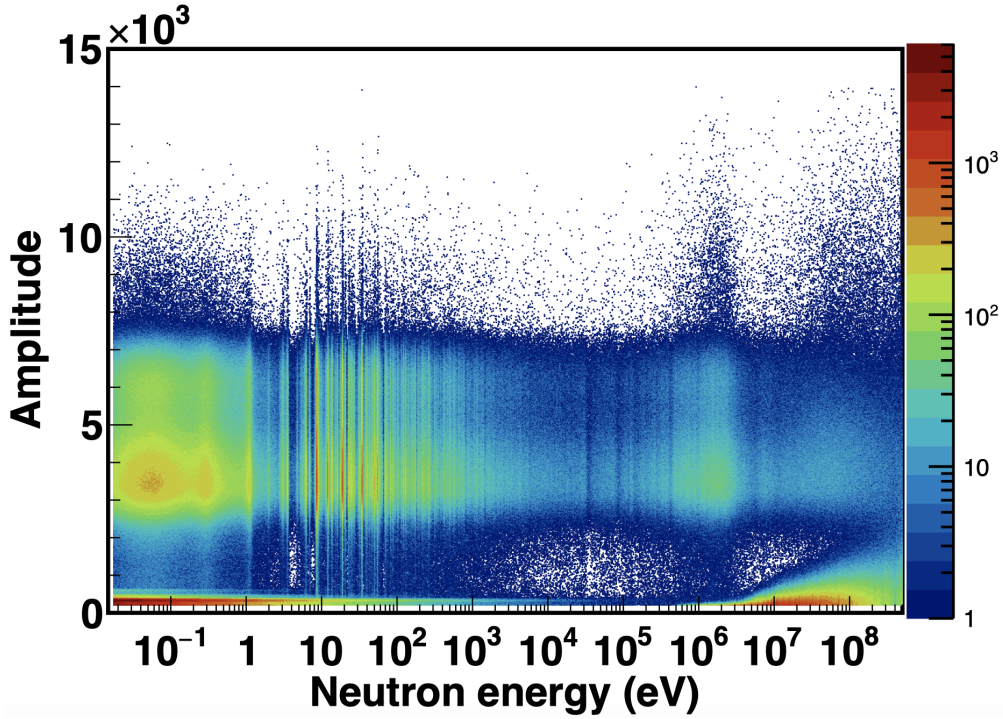

(α′) Όλο το ενεργειακό εύρος

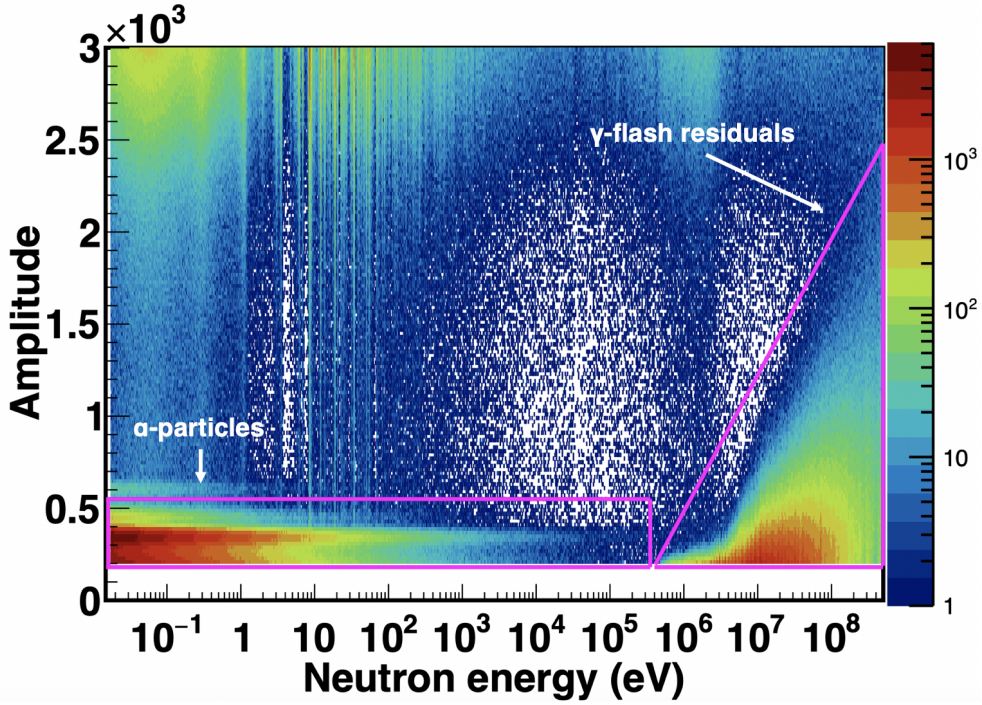

(β′) Μεγέθυνση στον y άξονα

Σχήμα 11: Κατανομή του ύψους των παλμών συναρτήσει της ενέργειας του νετρονίου για το στόχο του ^{235}U της EAR-1 σε (α) όλο το ενεργειακό εύρος και (β) για τους παλμούς χαμηλότερου ύψους. Τα σωματίδια-α από τη φυσική ραδιενέργεια των στόχων φαίνονται στις χαμηλότερες ενέργειες, καθώς και τα υπολείμματα από το γ-flash που αυξάνονται με την αύξηση της ενέργειας.

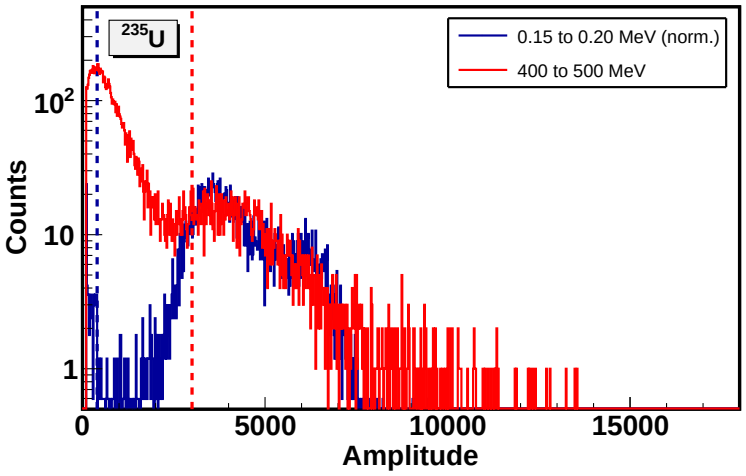

(α′) Φάσμα για το στόχο του ^{235}U της EAR-1.

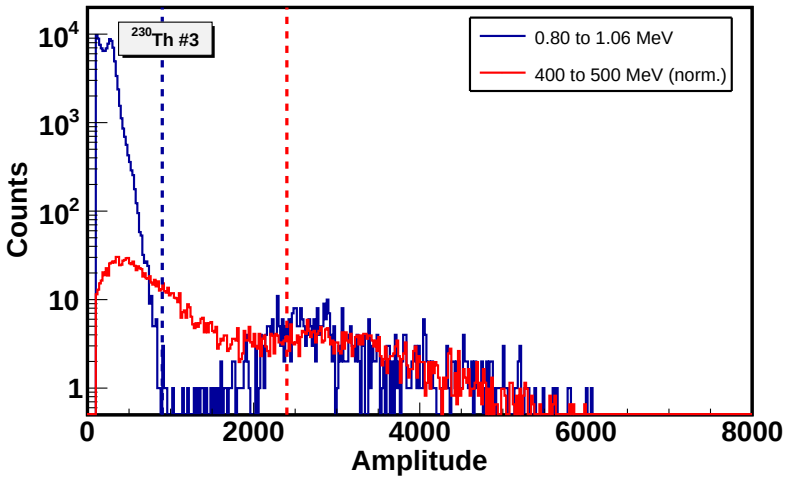

(β′) Φάσμα για το στόχο του ^{230}Th της EAR-1.

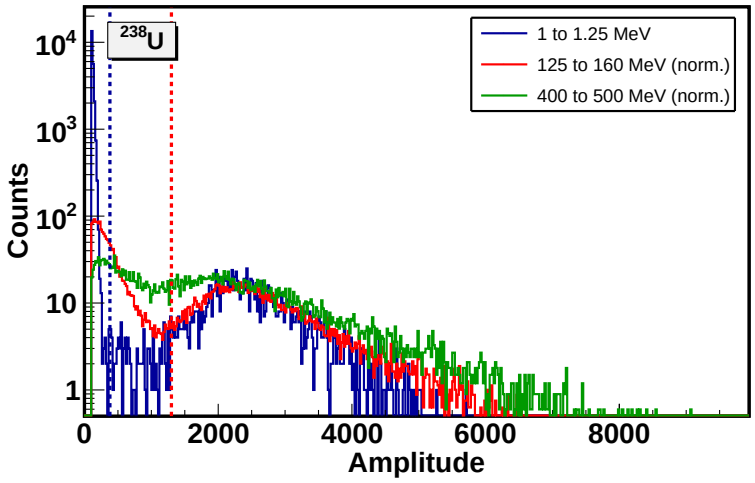

(γ′) Φάσμα για το στόχο του ^{238}U της EAR-1.

Σχήμα 12: Φάσματα που αντιστοιχούν σε διαφορετικές ενέργειες νετρονίων για τους στόχους (α) ^{235}U, (β) ^{230}Th #3 και (γ) ^{238}U. Η διακεκομμένη μπλε γραμμή αντιστοιχεί στο χαμηλό κατώφλι για το ύψος των παλμών που χρησιμοποιείται στην ανάλυση και στόχο έχει την απόρριψη των σωματιδίων-α. Η διακεκομμένη μπλε γραμμή αντιπροσωπεύει το μεγάλο κατώφλι που χρησιμοποιείται για την απόρριψη του θορύβου στις υψηλότερες ενέργειες. Για το στόχο του ^{238}U το πράσινο φάσμα αντιπροσωπεύει υψηλότερες ενέργειες νετρονίων, στις οποίες παρατηρείται αλλοίωση του σχήματος σε σχέση με τις μικρότερες ενέργειες, οπότε και η ανάλυση δε μπορεί να θεωρηθεί αξιόπιστη εκεί.

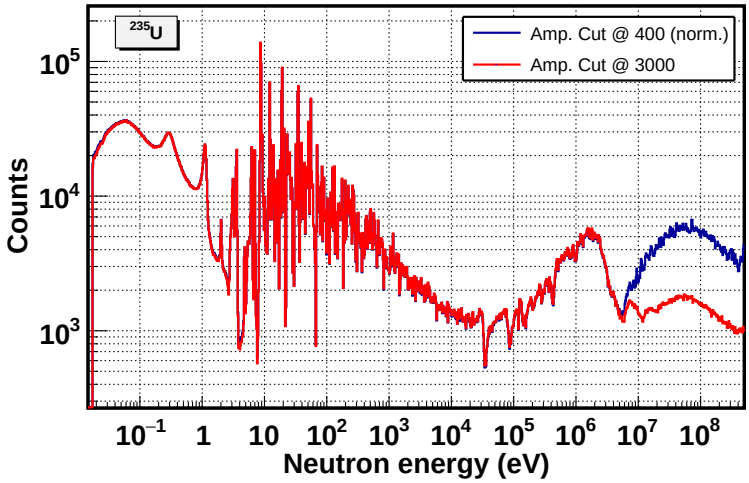

(α′) Φάσμα των καταμετρημένων γεγονότων για το στόχο του ^{235}U της EAR-1.

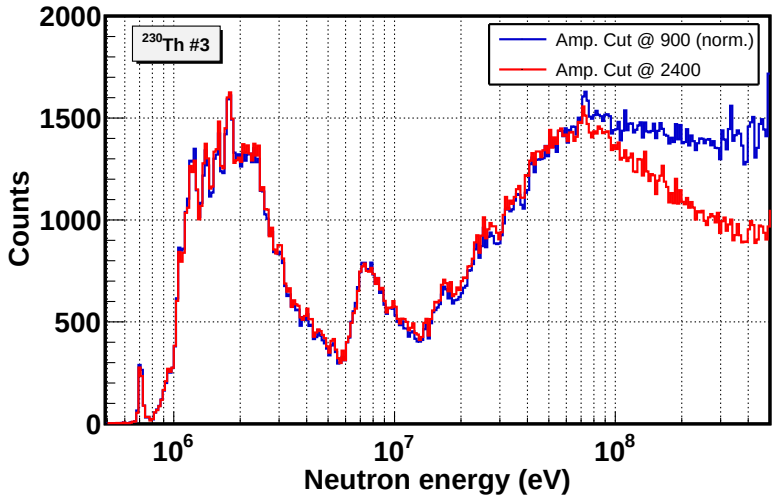

(β′) Φάσμα των καταμετρημένων γεγονότων για το στόχο του ^{230}Th της EAR-1.

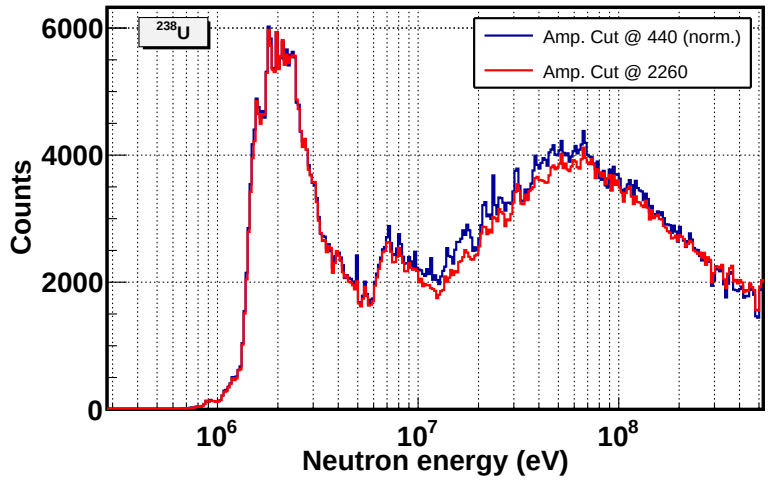

(γ′) Φάσμα των καταμετρημένων γεγονότων για το στόχο του ^{238}U της EAR-1.

Σχήμα 13: Φάσματα των καταμετρημένων γεγονότων με διαφορετικό κατώφλι για την απόρριψη παλμών που δεν αντιστοιχούν σε θραύσματα σχάσης, ένα χαμηλό κατώφλι (μπλε γραμμή) και ένα υψηλότερο (κόκκινη γραμμή) για τους στόχους του (α) ^{235}U, (β) ^{230}Th και (γ) ^{238}U της EAR-1. Τα φάσματα είναι κανονικοποιημένα στις χαμηλές ενέργειες.

Στο n_TOF υπάρχουν δύο είδη παλμών νετρονίων: οι παλμοί υψηλής έντασης (dedicated pulses) και οι παλμοί χαμηλής έντασης (parasitic pulses). Ένας σημαντικός έλεγχος της συνέπειας της ανάλυσης των δεδομένων (χειρισμός του γ-flash, αναγνώριση παλμών, διόρθωση του νεκρού χρόνου κτλ.) προκύπτει από τη σύγκριση των παλμών υψηλής και χαμηλής έντασης, όταν αυτοί είναι κανονικοποιημένοι στον αριθμό των πρωτονίων. Η σύγκριση αυτή για την μέτρηση στην EAR-1 παρουσιάζεται στο σχήμα 14 για το στόχο του ^{235}U (σχήμα 14α΄) για το στόχο του ^{230}Th #3 (σχήμα 14β΄) και για το στόχο του ^{238}U (σχήμα 14γ΄), ενώ αντίστοιχα για την EAR-2 στο σχήμα 15 για το στόχο του ^{235}U (σχήμα 15α΄) για το στόχο του ^{230}Th #3 (σχήμα 15β΄) και για το στόχο του ^{238}U (σχήμα 15γ΄). Όσο αναφορά την EAR-1 παρατηρείται πολύ καλή συμφωνία μεταξύ των δύο ειδών παλμών για τους στόχους του ^{235}U και του ^{230}Th, ενώ οι διαφορές στο στόχο του ^{238}U αποδίδονται σε συσσώρευση παλμών. Οι διαφορές που παρατηρούνται μεταξύ των δύο ειδών παλμών σε όλους τους στόχους της EAR-2, αποδίδονται και πάλι σε συσσώρευση των παλμών λόγω των πολύ υψηλών συχνοτήτων άφιξης των παλμών, κάτι που ήταν αναμενόμενο αφού η μάζα των στόχων είχε επιλεχθεί για τη μέτρηση της EAR-1.

Ο τελευταίος έλεγχος που πραγματοποιείται στην ανάλυση των δεδομένων είναι η σύγκριση μεταξύ των στόχων του ^{230}Th, κανονικοποιημένοι στο ενεργειακό εύρος 1 - 5 MeV, όπως παρουσιάζεται στο σχήμα 16. Όπως φαίνεται στο σχήμα, πολύ καλή συμφωνία παρατηρείται μεταξύ των επτά στόχων του ^{230}Th, χωρίς κάποια συστηματική απόκλιση μεταξύ τους. Οι μεγαλύτερες διαφορές στο υψηλότερο ενεργειακό εύρος αναδεικνύουν την πολυπλοκότητα της ανάλυσης για τις ενέργειες αυτές.

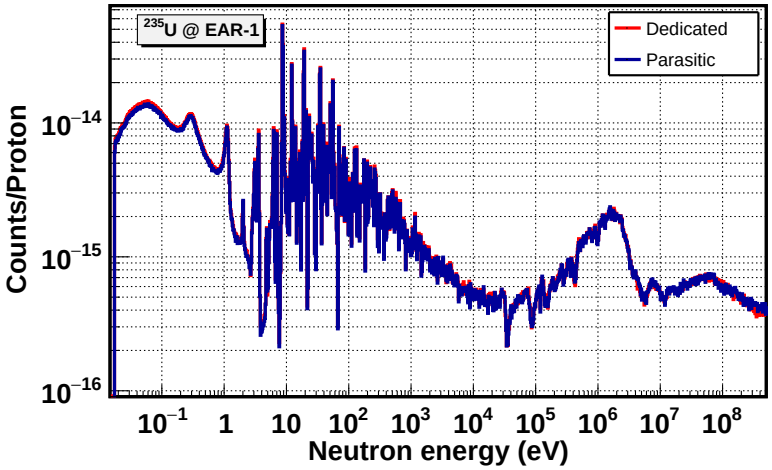

(α′) ^{235}U της EAR-1

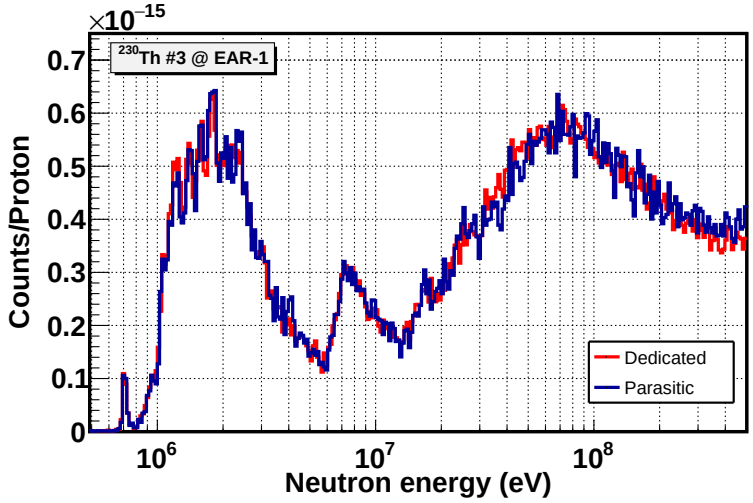

(β′) ^{230}Th #3 της EAR-1

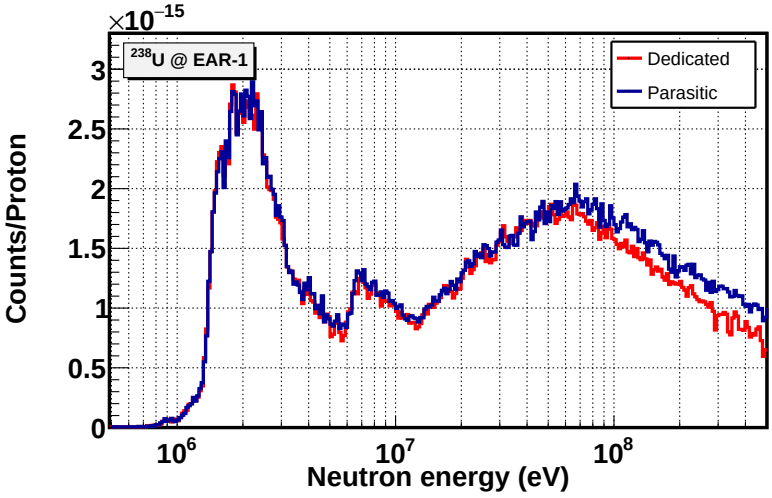

(γ′) ^{235}U της EAR-1

Σχήμα 14: Σύγκριση του αριθμού των γεγονότων κανονικοποιημένα στον αριθμό των πρωτονίων για τους παλμούς υψηλής έντασης (dedicated) με την κόκκινη γραμμή και για τους παλμούς χαμηλής έντασης (parasitic) με την μπλε γραμμή για την μέτρηση στην EAR-1.

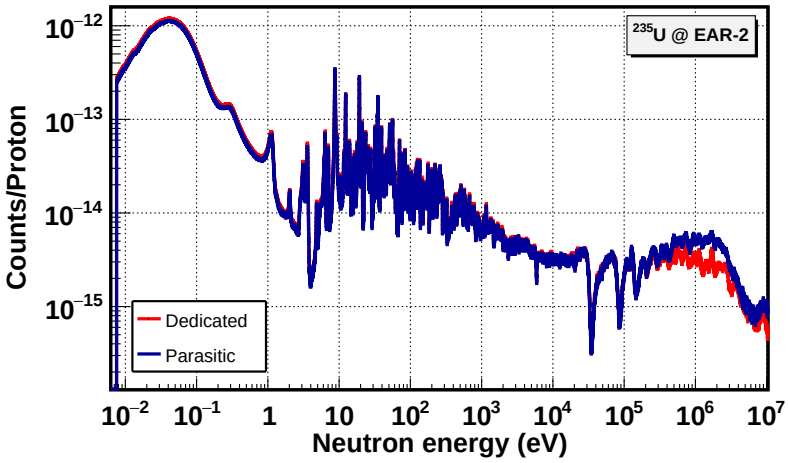

(α′) ^{235}U της EAR-2

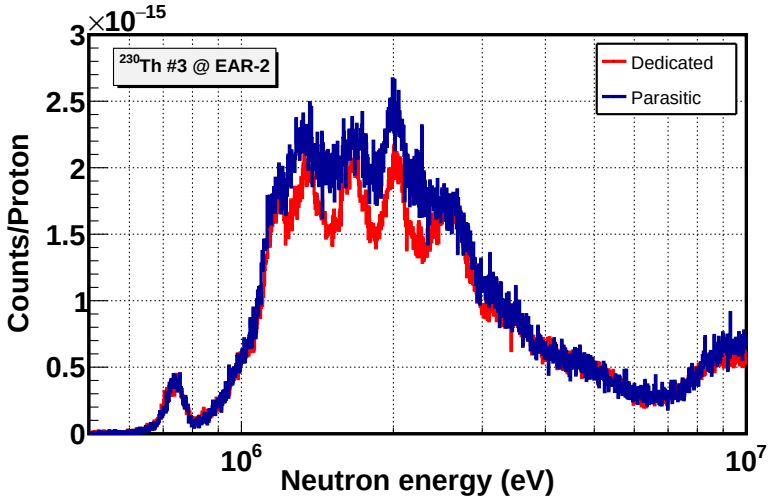

(β′) ^{230}Th #3 της EAR-2

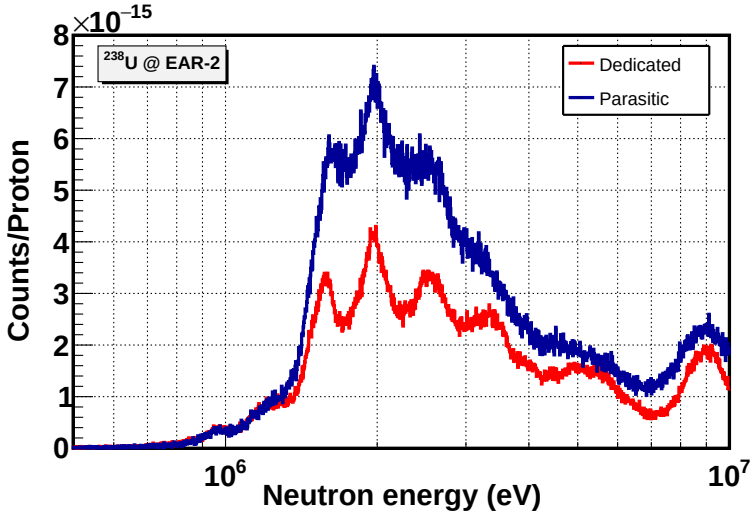

(γ′) ^{238}U της EAR-2

Σχήμα 15: Σύγκριση του αριθμού των γεγονότων κανονικοποιημένα στον αριθμό των πρωτονίων για τους παλμούς υψηλής έντασης (dedicated) με την κόκκινη γραμμή και για τους παλμούς χαμηλής έντασης (parasitic) με την μπλε γραμμή για την μέτρηση στην EAR-2.

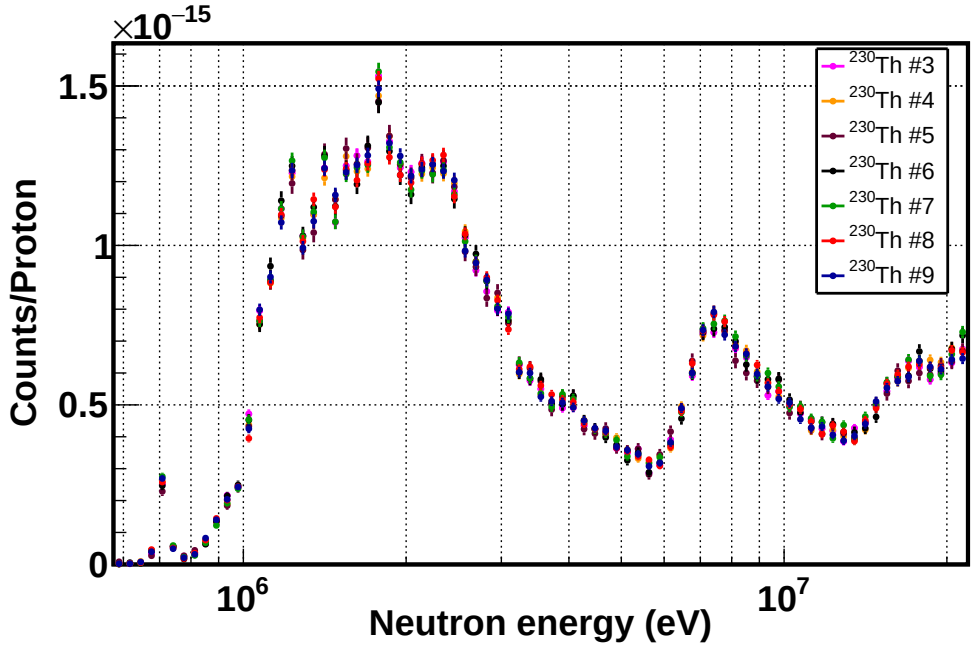

(α′) Χαμηλές ενέργειες σε 50 bpd

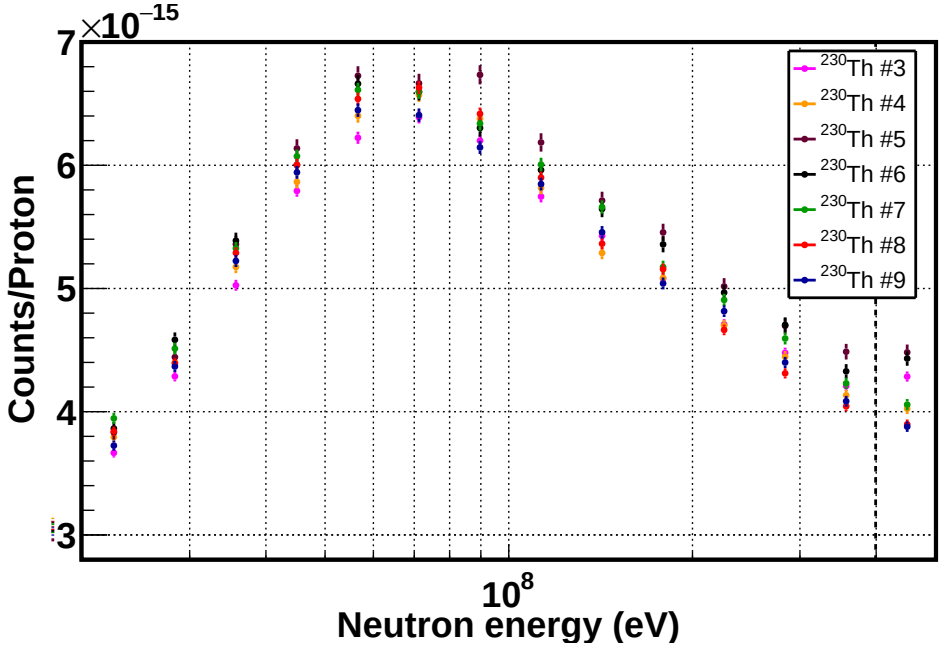

(β′) Υψηλές ενέργειες σε 10 bpd

Σχήμα 16: Σύγκριση των καταγεγραμμένων γεγονότων για τους στόχους του ^{230}Th κανονικοποιημένα στον αριθμό των πρωτονίων για την μέτρηση στην EAR-1, όπου (α) οι χαμηλότερες ενέργειες σε 50 bpd και (β) οι υψηλότερες ενέργειες σε 10 bpd. Τα γεγονότα είναι κανονικοποιημένα μεταξύ τους στο ενεργειακό εύρος 1 με 5 MeV.

Διορθώσεις

Στην ενότητα αυτή παρουσιάζονται οι διορθώσεις πάνω στα γεγονότα της σχάσης λόγω της συσσώρευσης παλμών, λόγω του κατωφλίου στο ύψος των παλμών και των προσμίξεων των στόχων. Επίσης παρουσιάζεται ο τρόπος με τον οποίο γίνεται η μετατροπή από το χρόνο πτήσης σε ενέργεια νετρονίου.

Για τη διόρθωση της συσσώρευσης παλμών ακολουθήθηκε η μέθοδος του περιγράφεται στο [20] (nonparalyzable model, σχήμα 17). Πρώτο βήμα για την εφαρμογή της μεθόδου είναι η απόρριψη των παλμών που βρίσκονται χρονικά πιο κοντά από το χρόνο που έχει επιλεχθεί ως νεκρός χρόνος του συστήματος (FWHM του παλμού) και έχουν αναγνωριστεί ως παλμοί σχάσης, ώστε ο ανιχνευτής να ακολουθεί το μοντέλο όπως περιγράφεται στο [20].

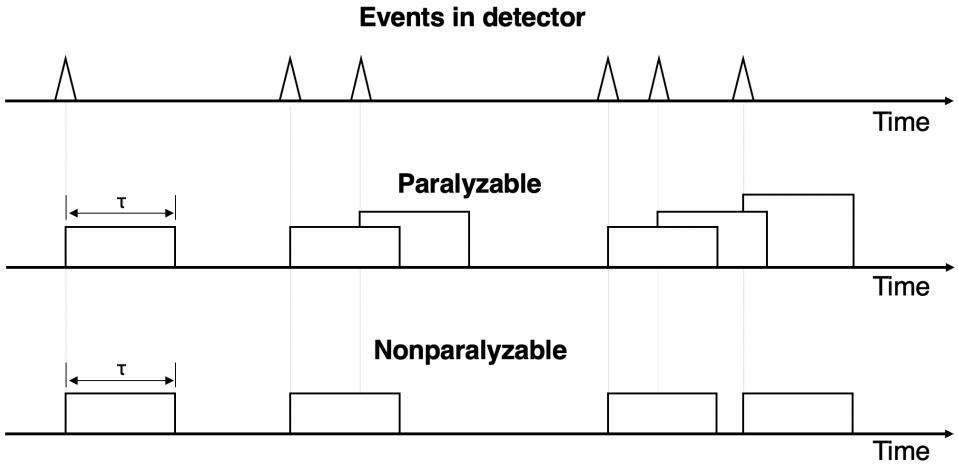

Σχήμα 17: Γραφική αναπαράσταση της συμπεριφοράς του ανιχνευτή σε δύο περιπτώσεις: στην περίπτωση που ένας παλμός φτάσει στον ανιχνευτή όταν αυτός ήδη είναι απασχολημένος με την επεξεργασία του προηγούμενου παλμού ο νεκρός χρόνος του συστήματος επεκτείνεται κατά χρόνο τ (paralyzable model) και στην περίπτωση που ο δεύτερος παλμός χάνεται και δεν έχει καμία επίδραση στη συμπεριφορά του ανιχνευτή (nonparalyzable model).

Στη συνέχεια ο πραγματικός ρυθμός καταγραφής των γεγονότων υπολογίζεται σύμφωνα με την παρακάτω εξίσωση

$$n = \frac{m}{1 - m\tau} \tag{3}$$

όπου m είναι ο καταγεγραμμένος ρυθμός των γεγονότων και τ ο νεκρός χρόνος που έχει θεωρηθεί για το σύστημα.

Τα βήματα που ακολουθούνται για τη διόρθωση παρουσιάζονται στο σχήμα 18 για τους παλμούς πρωτονίων υψηλής έντασης στον στόχο ^{238}U της EAR-1.

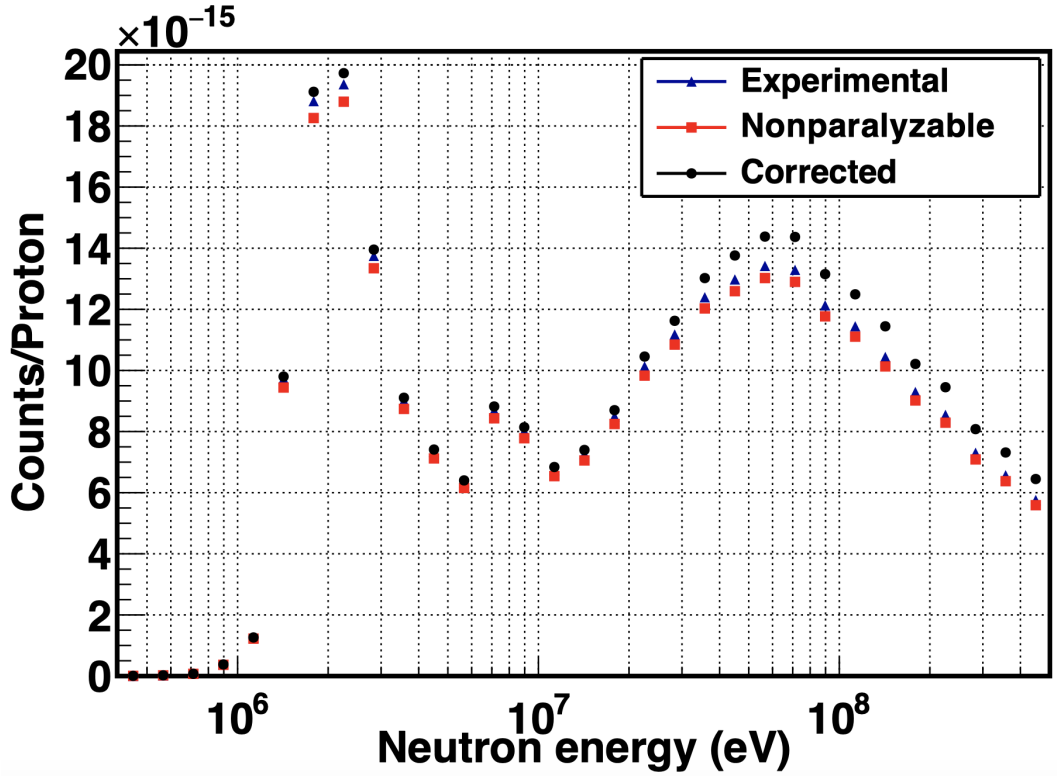

Σχήμα 18: Διαδικασία που ακολουθείται για τη διόρθωση των χαμένων γεγονότων λόγω της συσσώρευσης παλμών στο στόχο ^{238}U της EAR-1. Τα μπλε τρίγωνα αντιστοιχούν στα πειραματικά σημεία, τα κόκκινα τετράγωνα στα διορθωμένα σημεία ώστε το σύστημα να ακολουθεί το μοντέλο της μη παράλυσης (nonparalyzable model) και οι μαύροι κύκλοι είναι τα διορθωμένα για το νεκρό χρόνο σημεία.

Διάφορα ισότοπα του Pu υπήρχαν στους στόχους του ^{230}Th. Η συνεισφορά των ισοτόπων αυτών για ενέργειες μεγαλύτερες του κατωφλίου της σχάσης του ^{230}Th είναι αμελητέα, όπως φαίνεται στο σχήμα 19. Όμως, αυτό δεν ισχύει για τις χαμηλότερες ενέργειες όπως φαίνεται στο σχήμα 20, όπου παρουσιάζονται τα αναμενόμενα γεγονότα από όλα τα ισότοπα του Pu στους στόχους, τα οποία έχουν υπολογιστεί λαμβάνοντας υπόψιν τη μάζα και την ενεργό διατομή του καθενός συνδυασμένα με την αξιολογημένη ροή της EAR-2 και έχει γίνει η κανονικοποίηση τους στα πειραματικά γεγονότα. Όπως φαίνεται από το σχήμα δεν υπάρχουν γεγονότα που μπορούν να αποδοθούν στη σχάση του ^{230}Th.

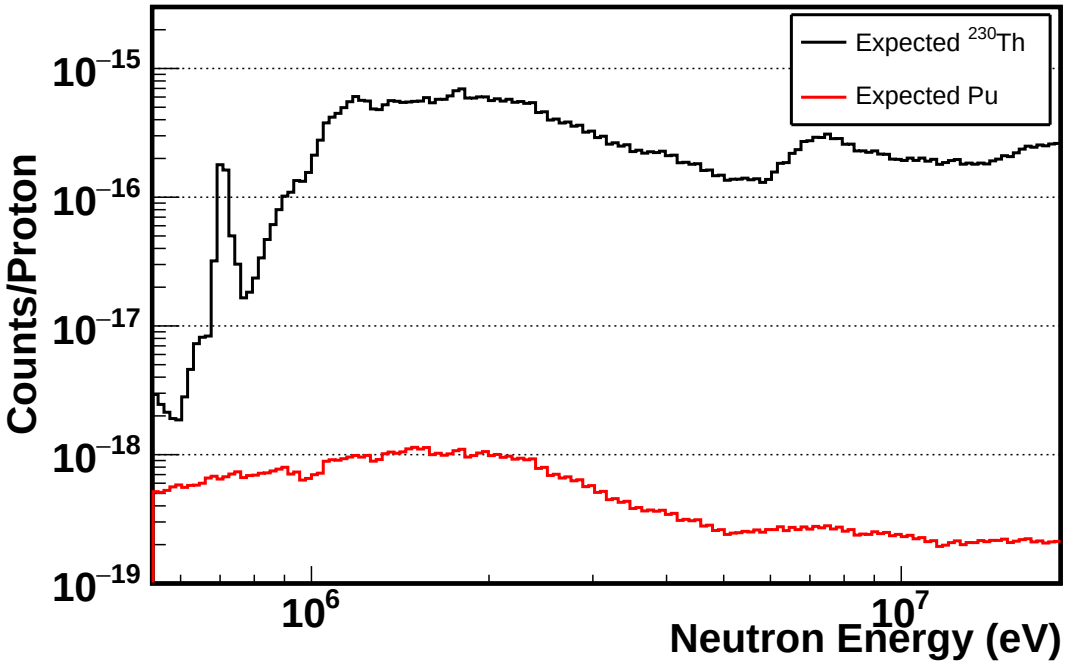

Σχήμα 19: Αναμενόμενα γεγονότα κανονικοποιημένα στον αριθμό των πρωτονίων για το ^{230}Th (μαύρη γραμμή) και για όλα τα ισότοπα του Pu που περιέχονται στο στόχο του ^{230}Th (κόκκινη γραμμή) για την EAR-1.

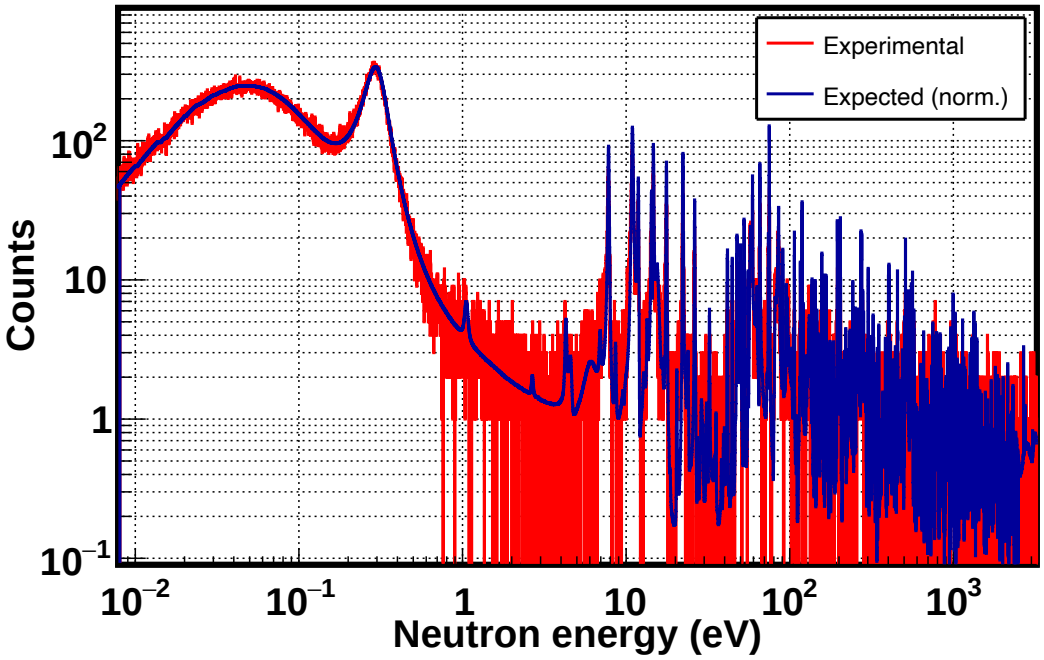

Σχήμα 20: Σύγκριση μεταξύ των πειραματικών γεγονότων (κόκκινη γραμμή) και των αναμενόμενων γεγονότων (κόκκινη γραμμή) για την EAR-2, λαμβάνοντας υπόψιν μόνο τα ισότοπα του Pu που περιέχονται στους στόχους. Τα αναμενόμενα γεγονότα είναι κανονικοποιημένα στα πειραματικά στην ενεργειακή περιοχή μεταξύ 4 eV και 3 keV.

Για τη μετατροπή του χρόνου πτήσης του νετρονίου σε ενέργεια χρησιμοποιήθηκε ένα σταθερό μήκος για τη μέτρηση της EAR-1 (πίνακας 3), διότι παρατηρήθηκε ότι η διαφορά στην ενέργεια είτε ληφθεί υπόψιν η απόσταση που διανύει το νετρόνιο μέσα στο στόχο (από τις προσομοιώσεις) είτε όχι ήταν για όλες τις ενέργειες μικρότερη του 0.7% (σχήμα 21). Η ακρίβεια στη μετατροπή του χρόνου πτήσης σε ενέργεια παρουσιάζεται και στα σχήματα 22 και 23, όπου φαίνεται η πολύ καλή αναπαραγωγή των συντονισμών του ^{235}U και του ^{230}Th υπολογισμένοι χρησιμοποιώντας σα στόχους αναφοράς το ^{10}B και το ^{235}U αντίστοιχα.

Πίνακας 3: Μήκος διαδρομής που χρησιμοποιήθηκε για την μετατροπή του χρόνου πτήσης του νετρονίου σε ενέργεια για τους στόχους της EAR-1.

Στόχος	Απόσταση (m)
^{235}U	183.40
^{230}Th #3	183.42
^{230}Th #4	183.43
^{230}Th #5	183.45
^{230}Th #6	183.46
^{230}Th #7	183.48
^{230}Th #8	183.50
^{230}Th #9	183.51
^{238}U	183.53

Για τη μετατροπή του χρόνου πτήσης του νετρονίου σε ενέργεια για τη μέτρηση της EAR-2 χρησιμοποιήθηκαν δύο σταθερά μήκη πτήσης: ένα για τις χαμηλές ενέργειες και ένα για την περιοχή του συντονισμού. Όπως φαίνεται στα σχήματα 24 και 25 οι ενέργειες των συντονισμών του ^{235}U αναπαράγονται πολύ καλά με το μήκος πτήσης για τις χαμηλές ενέργειες, καθώς και η ενέργεια του συντονισμού του ^{230}Th με το μήκος πτήσης για το συντονισμό. Οι αποστάσεις που χρησιμοποιήθηκαν για τη μετατροπή παρουσιάζονται στον πίνακα 4.

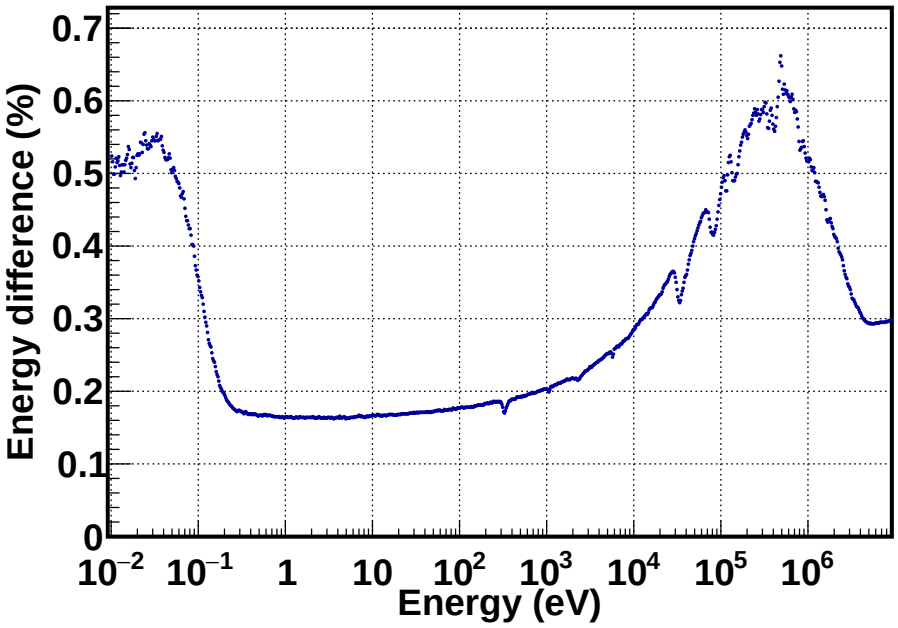

Σχήμα 21: Επί τοις εκατό διαφορά στον υπολογισμό της ενέργειας του νετρονίου της EAR-1, όταν η μετατροπή από το χρόνο πτήσης γίνεται με ένα σταθερό μήκος και λαμβάνοντας υπόψιν το επιπλέον μέσο μήκος που το νετρόνιο διανύει μέσα στο στόχο για κάθε ενέργεια.

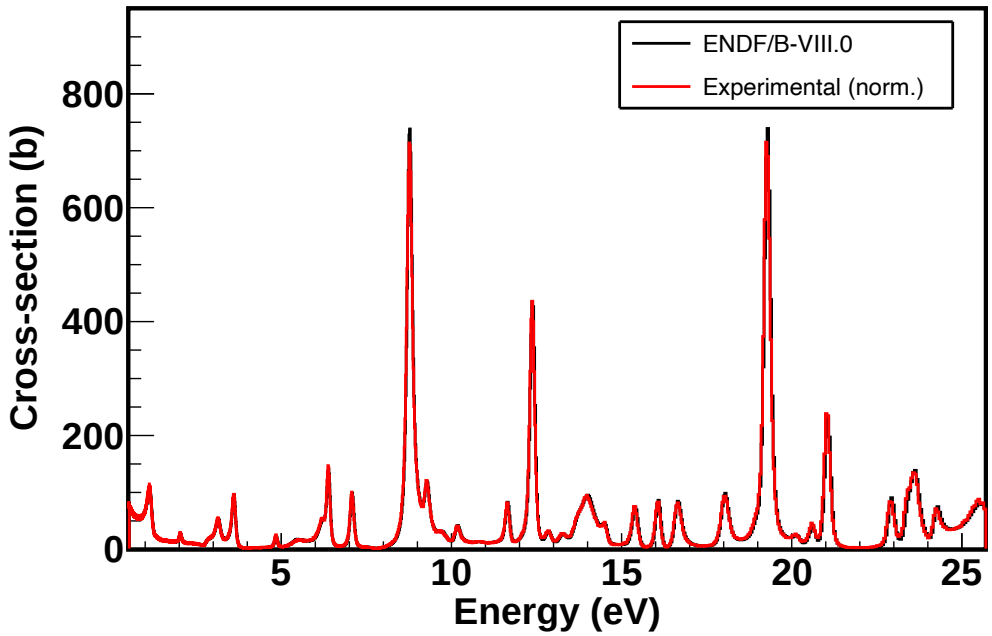

Σχήμα 22: Ενεργός διατομή της αντίδρασης ^{235}U(n,f) υπολογισμένη χρησιμοποιώντας την αντίδραση αναφοράς ^{10}B(n,a) (κόκκινη γραμμή) για τη μέτρηση της EAR-1, κανονικοποιημένη στην ENDF/B-VIII.0 (μαύρη γραμμή) στο ενεργειακό εύρος 0.5 με 26 eV.

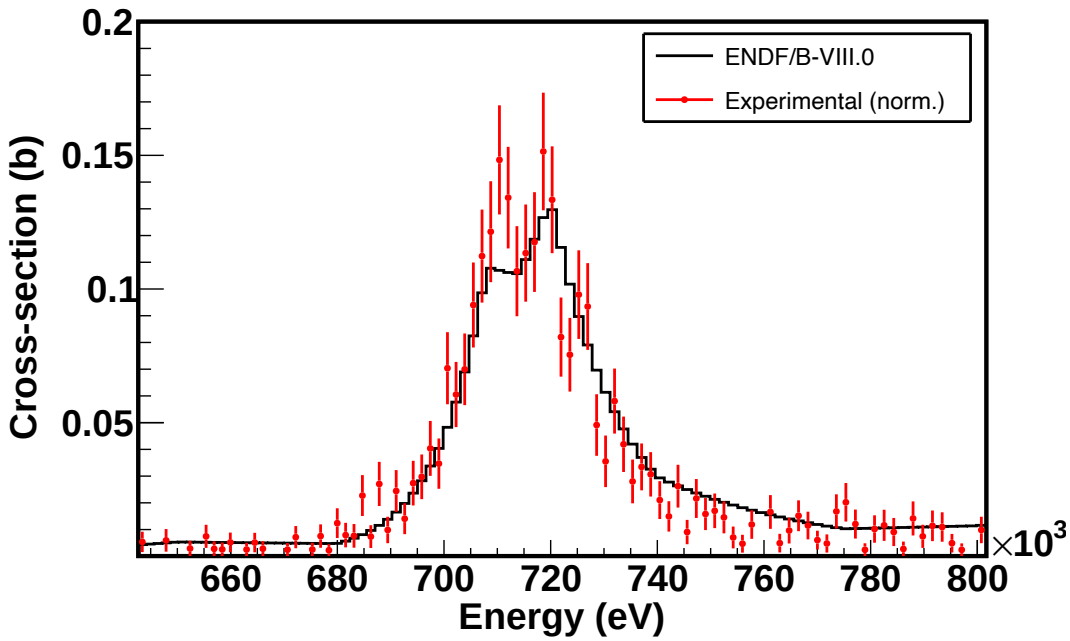

Σχήμα 23: Ενεργός διατομή της αντίδρασης ^{230}Th(n,f) υπολογισμένη χρησιμοποιώντας την αντίδραση αναφοράς ^{235}U(n,f) (κόκκινα σημεία) για τη μέτρηση της EAR-1, κανονικοποιημένη στην ENDF/B-VIII.0 (μαύρη γραμμή) στο ολοκλήρωμα του συντονισμού.

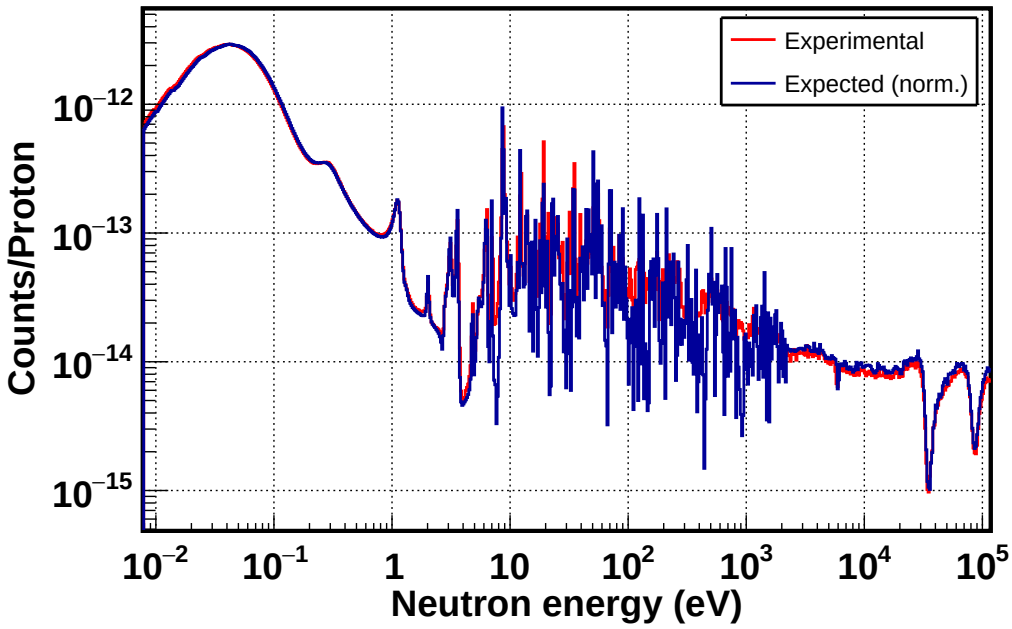

Σχήμα 24: Σύγκριση μεταξύ των πειραματικών (κόκκινη γραμμή) και των αναμενόμενων (μπλε γραμμή) γεγονότων κανονικοποιημένων στα πρωτόνια για το στόχο ^{235}U της EAR-2. Τα αναμενόμενα γεγονότα είναι κανονικοποιημένα στα πειραματικά.

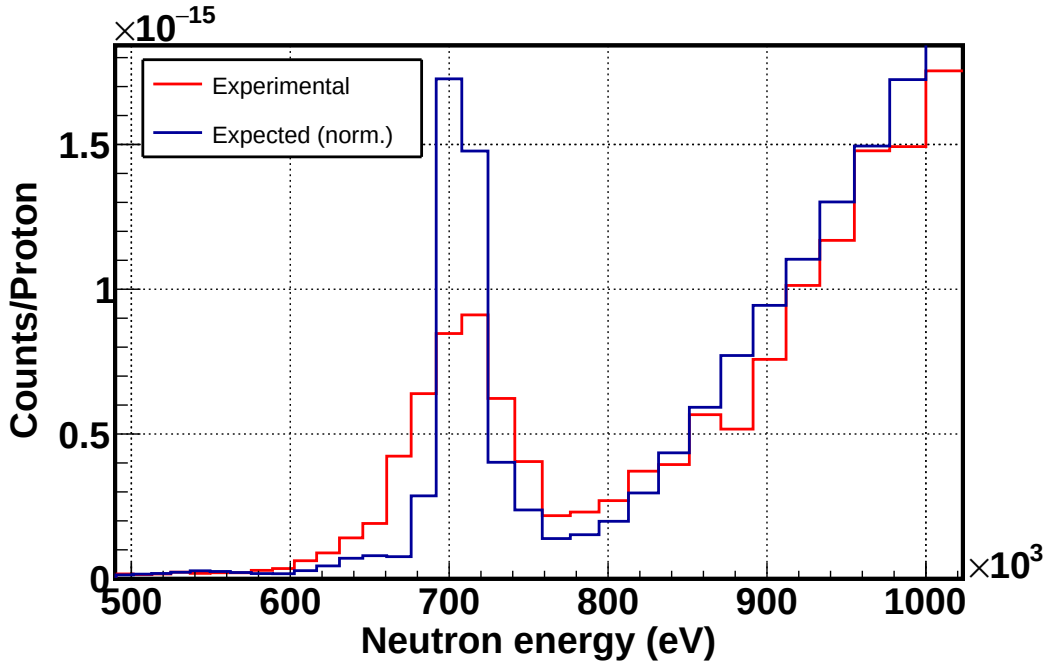

Σχήμα 25: Σύγκριση μεταξύ των πειραματικών (κόκκινη γραμμή) και των αναμενόμενων (μπλε γραμμή) γεγονότων κανονικοποιημένων στα πρωτόνια για το στόχο ^{230}Th #3 της EAR-2. Τα αναμενόμενα γεγονότα είναι κανονικοποιημένα στα πειραματικά.

Πίνακας 4: Αποστάσεις που χρησιμοποιούνται για τη μετατροπή του χρόνου πτήσης του νετρονίου σε ενέργεια για τη μέτρηση της EAR-2.

Στόχος	Απόσταση χαμηλά (m)	Απόσταση συντονισμός (m)
^{235}U	19.20	18.78
^{230}Th #3	19.22	18.80
^{230}Th #4	19.23	18.81
^{230}Th #5	19.25	18.83
^{230}Th #6	19.26	18.84
^{230}Th #7	19.28	18.86
^{230}Th #8	19.30	18.88
^{230}Th #9	19.31	18.89
^{238}U	19.33	18.91

Προσομοιώσεις **Monte Carlo**

Προσομοιώσεις Monte Carlo για την ενεργειακή εναπόθεση των θραυσμάτων σχάσης στο αέριο των ανιχνευτών Micromegas πραγματοποιήθηκαν με τον κώδικα FLUKA [21, 22] χρησιμοποιώντας τον κώδικα GEF [23] για τις πληροφορίες των μαζών και των ενεργειών των θραυσμάτων σχάσης (σχήμα 26). Τα συνημίτονα κατεύθυνσης των θραυσμάτων σχάσης ορίστηκαν με τις παρακάτω σχέσεις, ώστε να εκπέμπονται ισοτροπικά από τους στόχους των ακτινίδων.

$$\begin{aligned} \cos x &= \sqrt{1-\cos^2 z} \times (-1 + 2 \cdot \mathrm{Rand}) \\ \cos y &= \sqrt{1-\cos^2 z} \times (-1 + 2 \cdot \mathrm{Rand}) \\ \cos z &= -1 + 2 \cdot \mathrm{Rand} \end{aligned} \tag{4}$$

όπου Rand είναι ένας τυχαίος αριθμός μεταξύ 0 και 1.

Ο υπολογισμός από τις προσομοιώσεις με τον κώδικα FLUKA χρησιμοποιείται για τον υπολογισμό των γεγονότων των θραυσμάτων σχάσης που παραλείπονται από την ανάλυση λόγω του κατωφλίου στο ύψος των παλμών για την απόρριψη των σωματιδίων-α από τη φυσική ενεργότητα των στόχων και του θορύβου στα φάσματα. Οπότε γίνεται η συνέλιξη των φασμάτων της προσομοίωσης με μία ασύμμετρη γκαουσιανή συνάρτηση, αφού πρώτα γίνει η βαθμονόμηση τους. Η σύγκριση μεταξύ των προσομοιωμένων και των πειραματικών φασμάτων παρουσιάζεται στο σχήμα 27, όπου παρατηρείται η καλή συμφωνία μεταξύ των δύο.

Προσομοιώσεις Monte Carlo πραγματοποιήθηκαν με τον κώδικα MCNP5 [24] για τον υπολογισμό της μεταβολής της ροής μεταξύ των στόχων ακτινίδων. Η γεωμετρία που χρησιμοποιήθηκε για τις προσομοιώσεις περιλαμβάνει το θάλαμο σχάσης, το αέριο, τους στόχους των ακτινίδων και τους ανιχνευτές Micromegas, ενώ για τη ροή νετρονίων χρησιμοποιήθηκε η αξιολογημένη ροή που παρουσιάζεται στο σχήμα 3.

Τα αποτελέσματα από τις προσομοιώσεις Monte Carlo με τον κώδικα MCNP5 και συγκεκριμένα ο λόγος της ροής του στόχου που χρησιμοποιήθηκε ως στόχος αναφοράς σε κάθε πειραματική περιοχή προς τον στόχο του ^{230}Th που ήταν τοποθετημένος πιο κοντά στη δέσμη των νετρονίων και πιο μακριά από αυτήν, παρουσιάζεται στο σχήμα 28. Όπως φαίνεται από το σχήμα η διαφορά είναι μικρότερη του 1% για όλες τις ενέργειες νετρονίων και για τις δύο πειραματικές περιοχές.

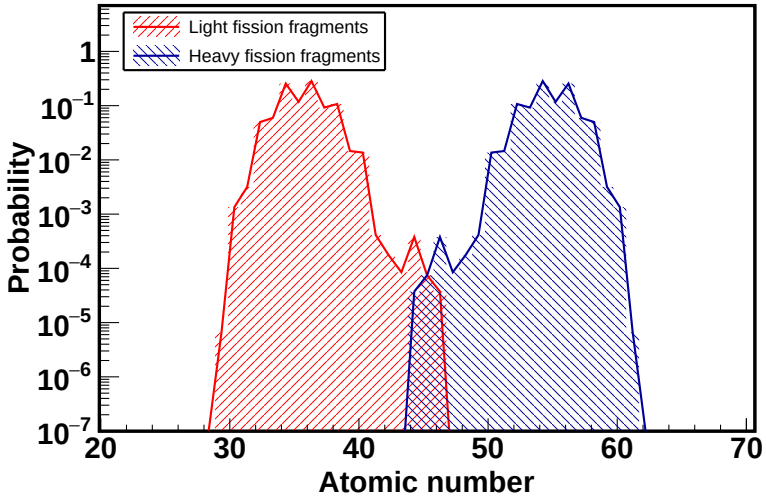

(α′) Κατανομές ατομικής μάζας

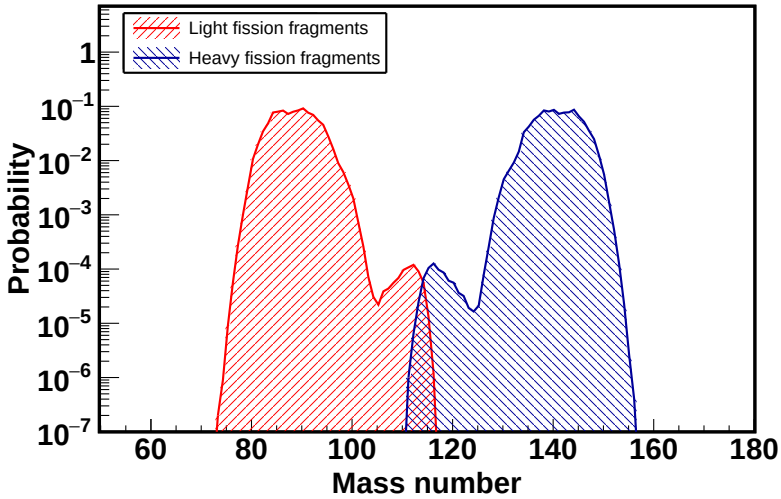

(β′) Κατανομές μαζικού αριθμού

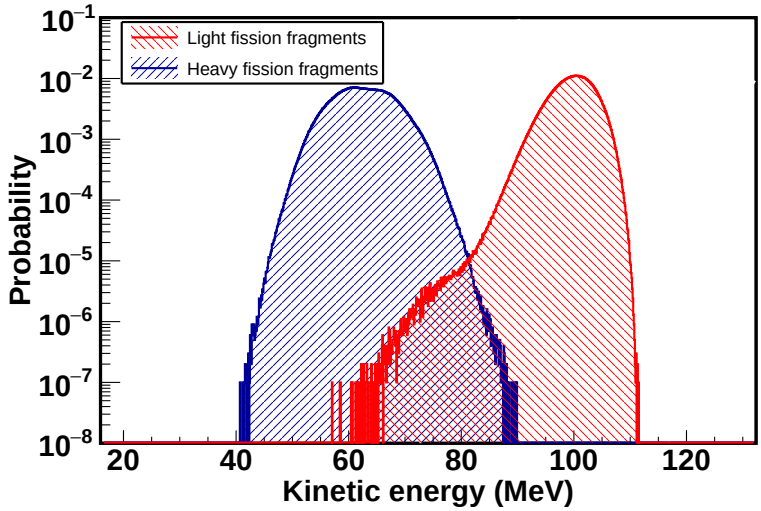

(γ′) Κατανομές κινητικής ενέργειας

Σχήμα 26: Κατανομές της (α) ατομικής μάζας, (β) μαζικού αριθμού και (γ) κινητικής ενέργειας των ελαφρών (κόκκινη γραμμή) και βαριών (μπλε γραμμή) θραυσμάτων σχάσης για ενέργειες νετρονίου 1 MeV, όπως προκύπτουν από τον κώδικα GEF.

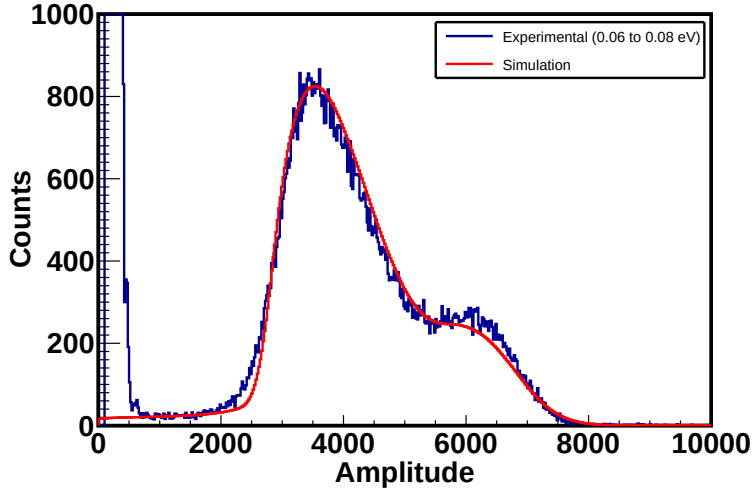

(α′) ^{235}U

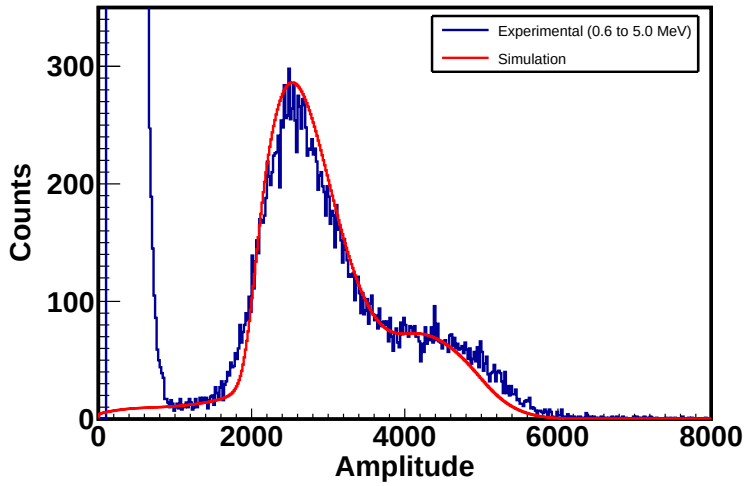

(β′) ^{230}Th #3

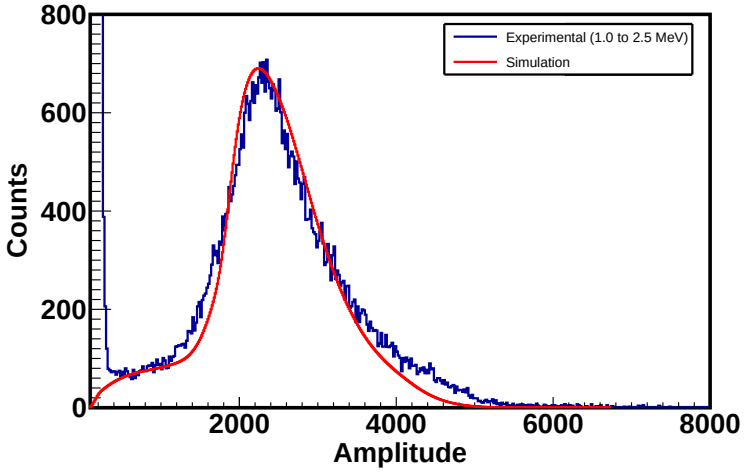

(γ′) ^{238}U

Σχήμα 27: Σύγκριση μεταξύ των πειραματικών (μπλε γραμμή) και προσομοιωμένων (κόκκινη γραμμή) κατανομών, μετά τη βαθμονόμηση και συνέλιξη τους με ασύμμετρη γκαουσινή συνάρτηση, για τους στόχους (α) ^{235}U, (β) ^{230}Th #3 και (γ) ^{238}U για τη μέτρηση της EAR-1.

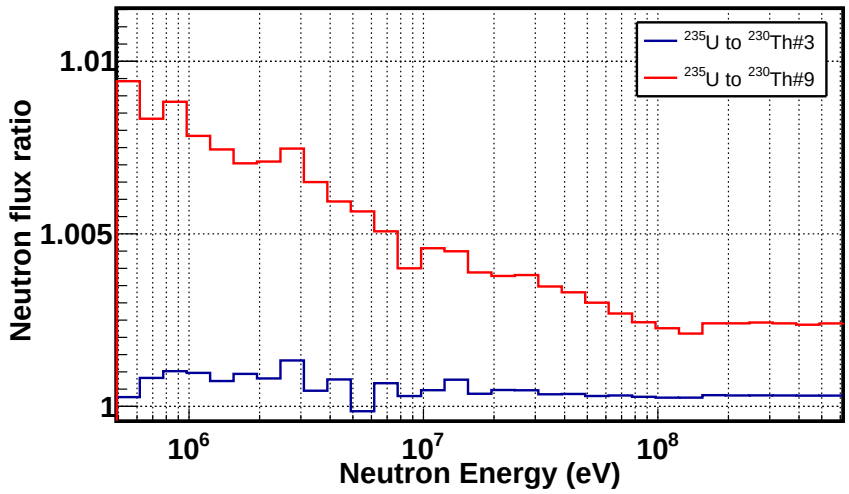

(α′) EAR-1

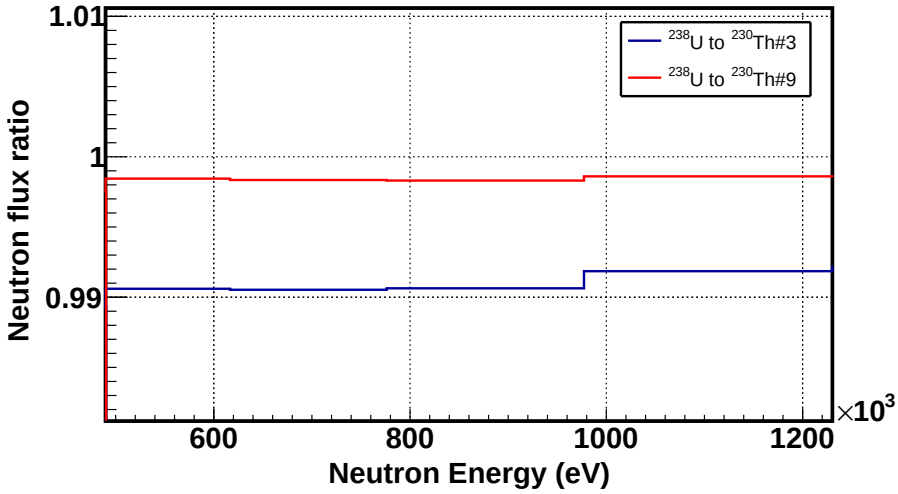

(β′) EAR-2

Σχήμα 28: Λόγος της προσομοιωμένης ροής με τον κώδικα MCNP5 του στόχου αναφοράς που χρησιμοποιήθηκε σε κάθε πειραματική περιοχή προς τον στόχο του ^{230}Th που ήταν τοποθετημένος πιο κοντά στη διεύθυνση των νετρονίων (μπλε γραμμή) και πιο μακριά (κόκκινη γραμμή).

Αποτελέσματα

Η ενεργός διατομή για κάθε ενέργεια υπολογίζεται ως προς το στόχο αναφοράς σύμφωνα με την εξίσωση:

$$\sigma(E) = \frac{N(E)}{N^{ref}(E)} \cdot \frac{f_{abs}}{f_{abs}^{ref}} \cdot \frac{f_{amp}(E)}{f_{amp}^{ref}(E)} \cdot \frac{f_{dt}(E)}{f_{dt}^{ref}(E)} \cdot \frac{f_{cont}(E)}{f_{cont}^{ref}(E)} \cdot f_{flux}(E) \cdot \frac{n}{n^{ref}} \cdot \sigma^{ref}(E) \quad (5)$$

όπου N είναι τα καταγεγραμμένα γεγονότα, f_{abs} είναι ο διορθωτικός παράγοντας για τα θραύσματα σχάσης που δεν επιτυγχάνουν να εισέλθουν στον ανιχνευτή, f_{amp} είναι η διόρθωση για τα χαμένα θραύσματα σχάσης λόγω του κατωφλίου που χρησιμοποιείται

στην ανάλυση, f_{dt} είναι ο διορθωτικός παράγοντας για το νεκρό χρόνο, f_{cont} είναι ο διορθωτικός παράγοντας για τη συμβολή των προσμείξεων, f_{flux} είναι ο διορθωτικός παράγοντας για τη διαφορετική ροή μεταξύ του στόχου και του στόχου αναφοράς, n είναι η επιφανειακή πυκνότητα των στόχων (σε άτομα/barn) και σ^{ref} είναι η ενεργός διατομή του στόχου αναφοράς, ενώ ο εκθέτης $'ref'$ αφορά το στόχο αναφοράς.

Για την επαλήθευση της διαδικασίας της ανάλυσης, πραγματοποιείται ο υπολογισμός της ενεργού διατομής σχάσης του ^{238}U μέχρι τα 160 MeV, χρησιμοποιώντας σα στόχο αναφοράς το ^{235}U. Για τον υπολογισμό χρησιμοποιήθηκε η ενεργός διατομή της αντίδρασης ^{235}U(n,f) από τις βιβλιοθήκες ENDF/B-VIII.0 [25] (από 0.15 μέχρι 30 MeV) και IAEA 2017 Neutron Data Standards library [26] (για ενέργειες από 30 μέχρι 200 MeV). Για ενέργειες μεγαλύτερες των 200 MeV η ενεργός διατομή της αντίδρασης βρίσκεται στη βιβλιοθήκη IAEA Report [27]. Η ενεργός διατομή της αντίδρασης ^{238}U(n,f), όπως υπολογίστηκε στην παρούσα εργασία, παρουσιάζεται στο σχήμα 29. Η διαφορά της ενεργού διατομής από τις τιμές αναφοράς είναι μικρότερη από 5% για όλες τις ενέργειες νετρονίων.

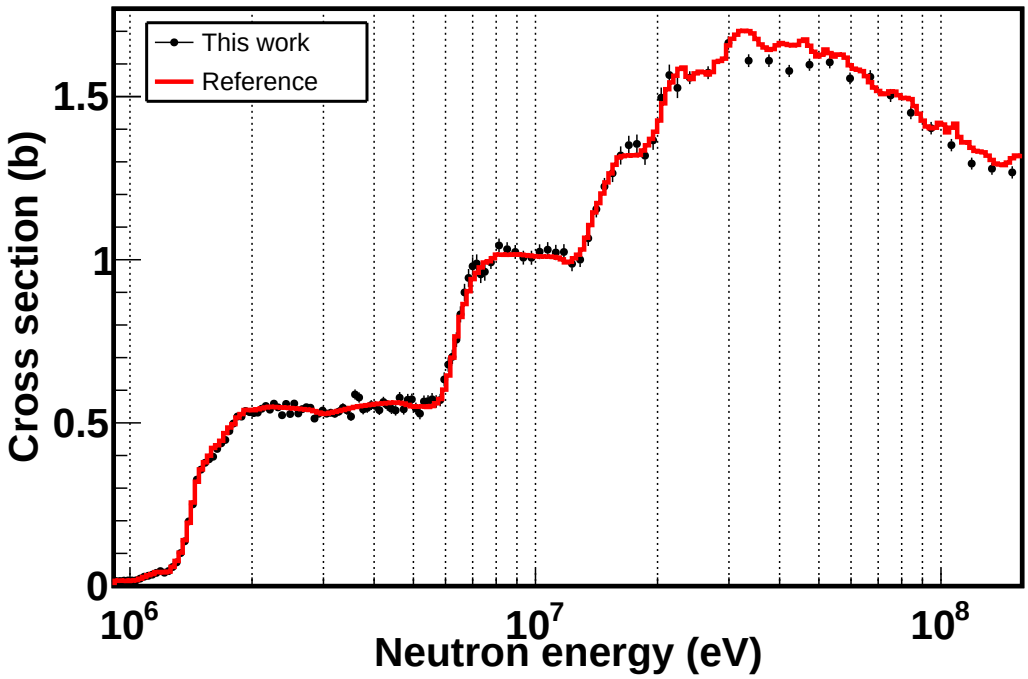

Σχήμα 29: Ενεργός διατομή της αντίδρασης ^{238}U(n,f) (μαύροι κύκλοι) υπολογισμένη από τη μέτρηση της EAR-1, χρησιμοποιώντας σαν αντίδραση αναφοράς την ^{235}U(n,f). Η κόκκινη γραμμή αντιστοιχεί στην αξιολογημένη ενεργό διατομή της αντίδρασης ^{238}U(n,f). Μόνο οι στατιστικές αβεβαιότητες απεικονίζονται στο σχήμα.

Η ενεργός διατομή της αντίδρασης ^{230}Th(n,f) και από τους επτά στόχους ^{230}Th παρουσιάζεται στο σχήμα 30, υπολογισμένη κάνοντας χρήση της αντίδρασης αναφοράς ^{235}U(n,f). Όπως φαίνεται από το σχήμα η συμφωνία μεταξύ των στόχων είναι πολύ καλή. Τα τελικά αποτελέσματα, υπολογισμένα από τη μέση τιμή των επτά στόχων ^{230}Th, παρουσιάζονται στο σχήμα 31, μαζί με τις προηγούμενες μετρήσεις.

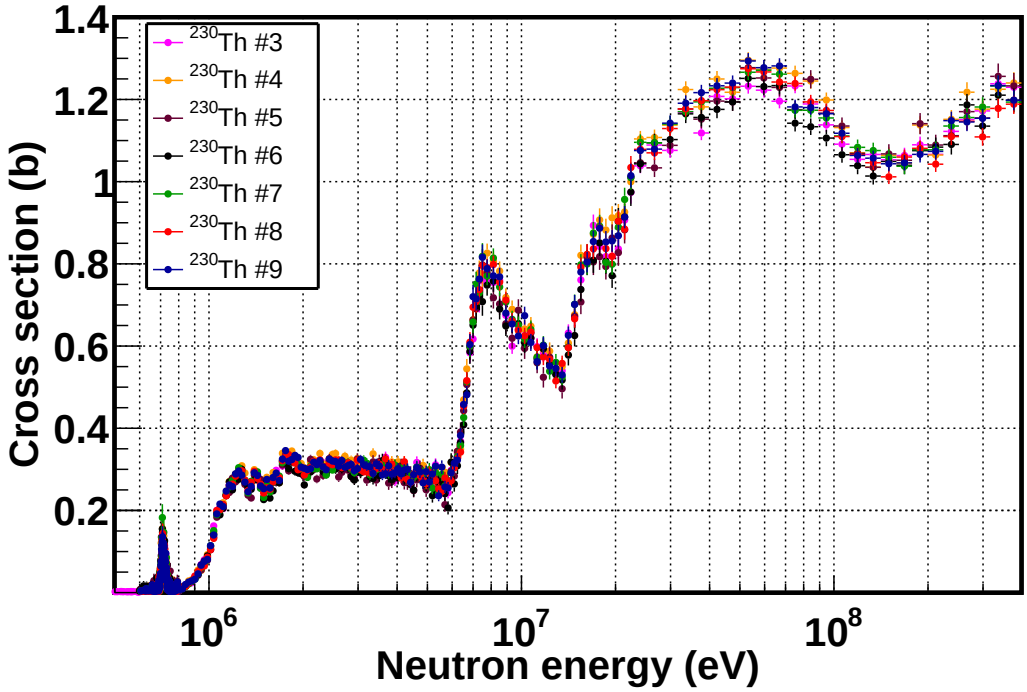

Σχήμα 30: Ενεργός διατομή της αντίδρασης ^{230}Th(n,f) υπολογισμένη από τη μέτρηση της EAR-1, χρησιμοποιώντας σαν αντίδραση αναφοράς την ^{235}U(n,f), για τους επτά στόχους του ^{230}Th. Μόνο οι στατιστικές αβεβαιότητες απεικονίζονται στο σχήμα.

Όπως φαίνεται από το σχήμα 31β′, στην περιοχή του συντονισμού τα αποτελέσματα από την παρούσα εργασία φαίνεται ότι έχουν χαμηλότερες τιμές ενεργού διατομής από τα δεδομένα των και Boldeman και Walsh [28], Blons *et al.* [29], James *et al.* [30] και μεγαλύτερες τιμές από τα δεδομένα των Muir και Veeser [31]. Ωστόσο τείνουν να επιβεβαιώσουν τις δομές που παρουσιάζονται στα δεδομένα των Blons *et al.*. Αξίζει να σημειωθεί εδώ ότι τα δεδομένα των Blons *et al.* και James *et al.* είναι κανονικοποιημένα στην τιμή 0.37 b στα 1.4 MeV. Όσο αναφορά τις υψηλότερες ενέργειες (σχήμα 31α′), τα δεδομένα βρίσκονται σε πολύ καλή συμφωνία μέσα στις αβεβαιότητες τους με τα δεδομένα των Meadows [32, 33], Muir και Veeser, το σημείο των Kazarirova *et al.* [34] στα 14.6 MeV και με τα δεδομένα των Goldblum *et al.* [35] για ενέργειες μεγαλύτερες από 1.2 και μικρότερες των 17 MeV. Όπως και στις χαμηλότερες ενέργειες, τα δεδομένα από την παρούσα εργασία είναι συστηματικά χαμηλότερα από αυτά των Blons *et al.* και James *et al.*, αλλά και από το σημείο στα 2.5 MeV των Kazarirova ετ αλ.. Επίσης, τα δεδομένα των Petit *et al.* [36] φαίνεται να συμφωνούν εντός αβεβαιοτήτων σε κάποιες ενέργειες με τα δεδομένα της παρούσας εργασίας, αλλά σε γενικές γραμμές παρουσιάζουν χαμηλότερες τιμές για την ενεργό διατομή. Για ενέργειες μεγαλύτερες των 25 MeV δεν υπάρχουν άλλα πειραματικά δεδομένα στη βιβλιογραφία.

Η στατιστική αβεβαιότητα για ενέργειες μεγαλύτερες των 0.8 MeV για την ενεργό διατομή της αντίδρασης ^{230}Th(n,f) παρουσιάζεται στο σχήμα 32. Η στατιστική αβεβαιότητα είναι μικρότερη του 4.5% για ενέργειες μεγαλύτερες των 0.8 MeV, ενώ στην κορυφή του συντονισμού είναι μικρότερη του ∼7%, αλλά αυξάνεται στις άκρες της κορυφής λόγω της χαμηλής στατιστικής.

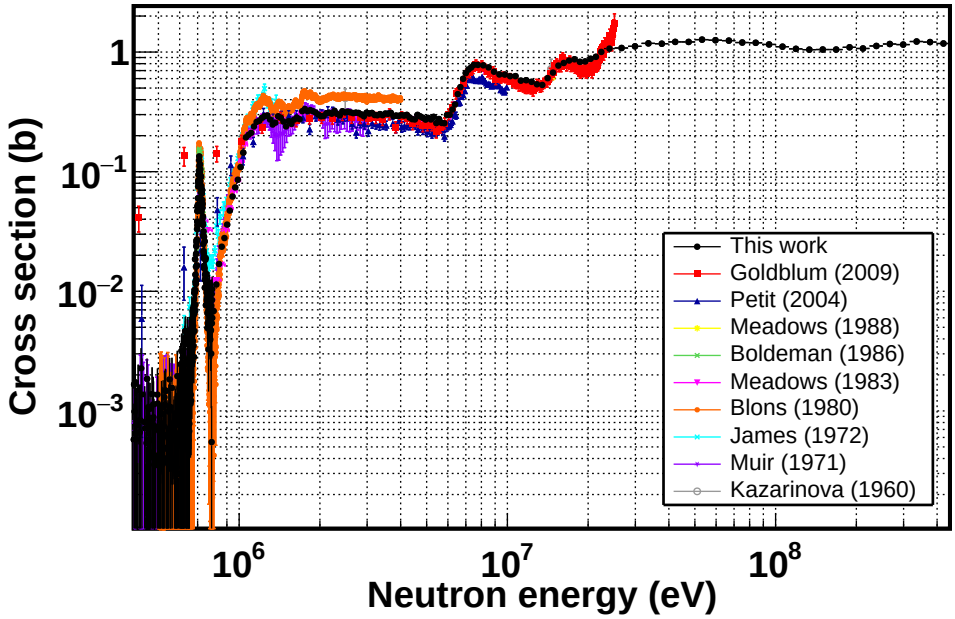

(α′) Όλα τα πειραματικά δεδομένα

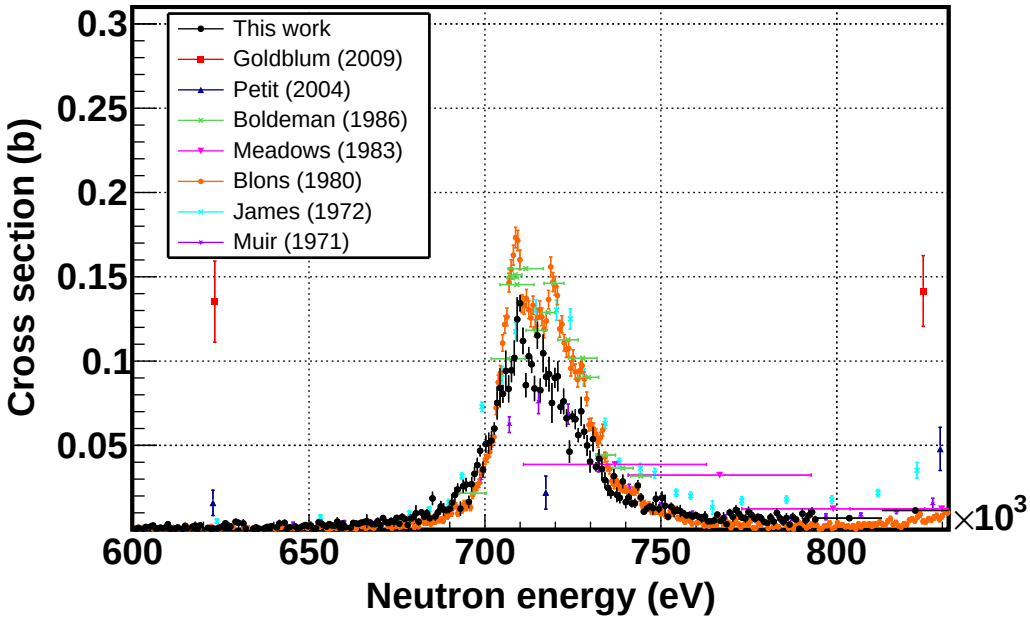

(β′) Πειραματικά δεδομένα στην περιοχή του συντονισμού

Σχήμα 31: Ενεργός διατομή της αντίδρασης ^{230}Th(n,f) (μαύροι κύκλοι) υπολογισμένη από τη μέτρηση της EAR-1, χρησιμοποιώντας σαν αντίδραση αναφοράς την ^{235}U(n,f), μαζί με τα διαθέσιμα πειραματικά δεδομένα που υπάρχουν στη βιβλιογραφία [3] για (α) όλες τις ενέργειες και (β) την περιοχή του συντονισμού. Μόνο οι στατιστικές αβεβαιότητες απεικονίζονται στο σχήμα.

Οι συστηματικές αβεβαιότητες της μέτρησης παρουσιάζονται στον πίνακα 5 και περιλαμβάνουν την αβεβαιότητα στη μέτρηση της μάζας, την αβεβαιότητα για τη διόρθωση των θραυσμάτων σχάσης που χάνονται κάτω από το κατώφλι στο ύψος του παλμού που χρησιμοποιείται στην ανάλυση, την αβεβαιότητα στην ενεργό διατομή της αντίδρασης αναφοράς ^{235}U(n,f) και τις αβεβαιότητες στις διορθώσεις για το νεκρό χρόνο και τη μεταβολή της

ροής των νετρονίων από το στόχο αναφοράς στους στόχους του ^{230}Th.

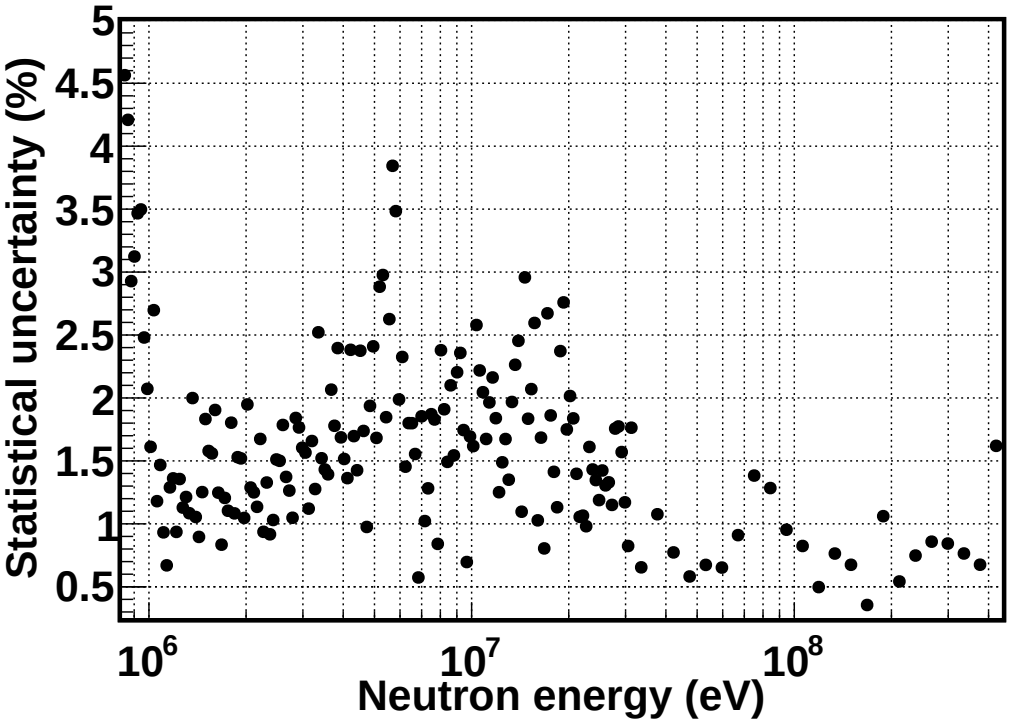

Σχήμα 32: Στατιστικές αβεβαιότητες στη μέτρηση της ενεργού διατομής της αντίδρασης ^{230}Th(n,f) για ενέργειες μεγαλύτερες των 0.8 MeV.

Πίνακας 5: Συστηματικές αβεβαιότητες στη μέτρηση της ενεργού διατομής της αντίδρασης ^{230}Th(n,f).

Συμβολή	Αβεβαιότητα
Μάζα στόχου	1%
Διόρθωση κατωφλίου	$< 2.2\%$
Ενεργός διατομή ^{235}U(n,f)	1.3 - 5%
Νεκρός χρόνος	$< 1\%$
Ροή νετρονίων	$< 1\%$

Θεωρητική μελέτη

Η θεωρητική μελέτη της ενεργού διατομής της αντίδρασης ^{230}Th(n,f) πραγματοποιήθηκε με τον κώδικα EMPIRE [37] στα πλαίσια του στατιστικού προτύπου Hauser-Feshbach, με στόχο την αναπαραγωγή των πειραματικών σημείων.

Σύμφωνα με τη θεωρία του Bohr η πιθανότητα της δημιουργίας του σύνθετου πυρήνα είναι ανεξάρτητη από την πιθανότητα αποδιέγερσής του. Στα πλαίσια του μοντέλου Hauser-Feshbach η ενεργός διατομή της αντίδρασης (α, b) δίνεται από τη σχέση:

$$\sigma_{\alpha,b}(E) = \sum_{J\pi} \sigma_a(E, J\pi) P_b(E, J\pi) \tag{6}$$

όπου $\sigma_a(E, J\pi)$ είναι η ενεργός διατομή για τη δημιουργία του πυρήνα σε μία κατάσταση με σπιν και ομοτιμία $J\pi$ και $P_b(E, J\pi)$ η πιθανότητα αποδιέγερσης του σύνθετου πυρήνα στο κανάλι b. Η ενεργός διατομή της σχάσης στα πλαίσια του μοντέλου Hauser-Feshbach περιγράφεται σαν ένα πιθανό κανάλι αποδιέγερσης του σύνθετου πυρήνα.

Για τον θεωρητικό υπολογισμό της ενεργού διατομής σχάσης με τον κώδικα EMPIRE (έκδοση 3.2.3 Malta) έγινε χρήση του διπλού δυναμικού της σχάσης. Για τον υπολογισμό τα κανάλια αποδιέγερσης με φορτισμένα σωματίδια δεν λήφθηκαν υπόψιν, ενώ πέρα από τη σχάση τα κανάλια (n,el), (n,inl), (n,γ) και (n,xn) λήφθηκαν υπόψιν για τον υπολογισμό. Οι παράμετροι για το οπτικό δυναμικό λήφθηκαν από τη βιβλιοθήκη RIPL-3 [38] με αριθμό καταλόγου 2408 [39]. Το μοντέλο PCROSS [40, 41] (με παράμετρο 1.5) χρησιμοποιήθηκε για την περιγραφή του μηχανισμού της προϊσορροπίας. Για τη μοντελοποίηση των ακτίνων-γ χρησιμοποιήθηκε η μοντελοποιημένη λορεντζιανή MLO1 [42]. Τέλος, για την πυκνότητα ενεργειακών καταστάσεων χρησιμοποιήθηκε το μοντέλο EGSM [43]. Όσον αφορά στο δυναμικό της σχάσης των διάφορων ισοτόπων, χρησιμοποιήθηκαν οι διαθέσιμες τιμές της βιβλιοθήκης RIPL-3, ενώ για τα ισότοπα με μαζικό αριθμό μικρότερο του 230, για τα οποία δεν υπάρχουν διαθέσιμες τιμές στη βιβλιοθήκη, οι τιμές για τα δυναμικά της σχάσης προσαρμόστηκαν ώστε να αναπαραχθούν με τον καλύτερο δυνατό τρόπο τα πειραματικά δεδομένα της παρούσας εργασίας.

Ο υπολογισμός με τις παραπάνω παραμέτρους, όπως πραγματοποιήθηκε με τον κώδικα EMPIRE, μέχρι τα 200 MeV παρουσιάζεται στο σχήμα 33 μαζί με τα πειραματικά δεδομένα από την παρούσα εργασία. Όπως φαίνεται από το σχήμα ο θεωρητικός αυτός υπολογισμός δεν αναπαράγει με ικανοποιητικό τρόπο την πειραματική ενεργό διατομή, αφού αποτυγχάνει να περιγράψει το κατώφλι της σχάσης και το πλατό, ενώ υποτιμάει την πειραματική ενεργό διατομή μέχρι τα 75 MeV. Για μεγαλύτερες ενέργειες ο θεωρητικός υπολογισμός είναι υπερεκτιμημένος σε σχέση με τις πειραματικές τιμές.

Προκειμένου να βελτιωθεί η συμφωνία μεταξύ των θεωρητικών υπολογισμών με τον κώδικα EMPIRE και των πειραματικών δεδομένων, πραγματοποιήθηκαν αλλαγές στο βάθος και στο πλάτος των πηγαδιών δυναμικού της σχάσης διάφορων ισοτόπων του Th και της ασυμπτωτικής παραμέτρου της πυκνότητας ενεργειακών καταστάσεων. Συγκεκριμένα, οι τιμές των πηγαδιών της σχάσης που χρησιμοποιήθηκαν για τον υπολογισμό παρουσιάζονται στον πίνακα 6, ενώ η ασυμπτωτική παράμετρος της πυκνότητας των ενεργειακών καταστάσεων του ισοτόπου ^{230}Th αυξήθηκε κατά 25%, ενώ του ισοτόπου ^{229}Th μειώθηκε κατά 17%. Ο θεωρητικός υπολογισμός με τις τροποποιημένες παραμέτρους παρουσιάζεται στο σχήμα 34, όπου φαίνεται ότι έχει γίνει σημαντική βελτίωση στη συμφωνία μεταξύ του θεωρητικού υπολογισμού και των πειραματικών δεδομένων.

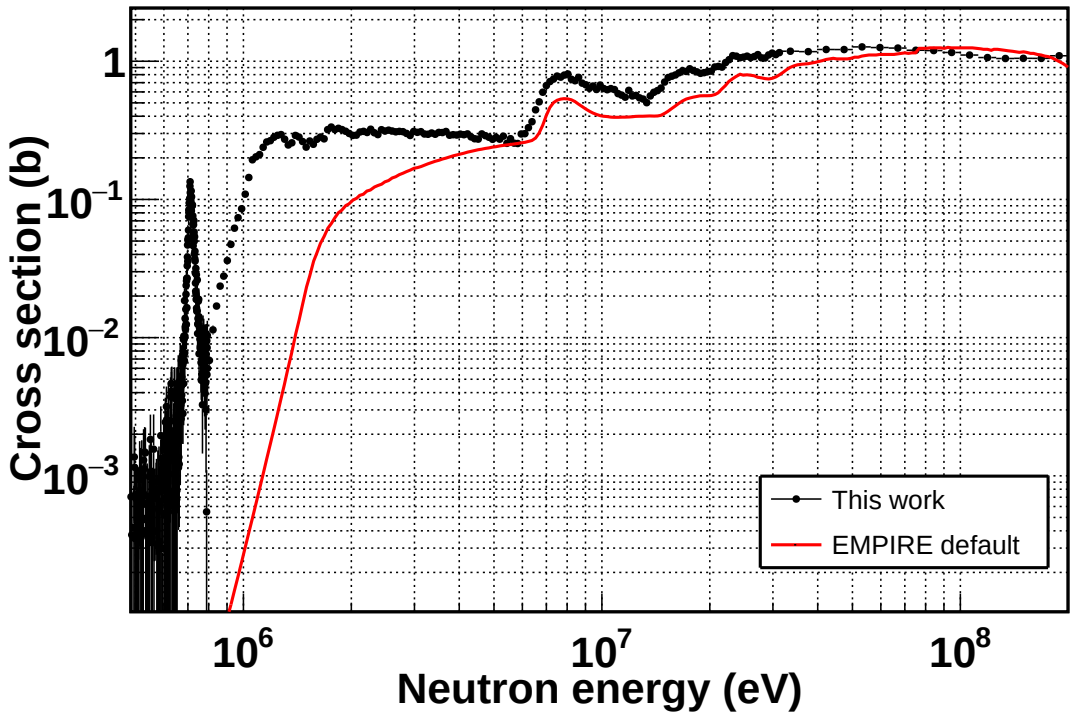

Σχήμα 33: Θεωρητικός υπολογισμός με τον κώδικα EMPIRE για ενέργειες από το κατώφλι της σχάσης μέχρι τα 200 MeV (κόκκινη γραμμή) μαζί με τα πειραματικά σημεία (μαύροι κύκλοι), για την ενεργό διατομή της αντίδρασης ^{230}Th(n,f).

Πίνακας 6: Ύψοι και πλάτη των δυναμικών της σχάσης για τα ισότοπα του Th που χρησιμοποιήθηκαν στον τροποποιημένο θεωρητικό υπολογισμό με τον κώδικα EMPIRE. Με έντονους χαρακτήρες είναι οι τιμές που έχουν τροποποιηθεί από τις προεπιλεγμένες, ενώ με πλάγια γράμματα είναι οι τιμές που δεν υπήρχαν στη βιβλιοθήκη RIPL-3 και επιλέχθηκαν για τους υπολογισμούς.

Ισότοπο	Πρώτο πηγάδι		Δεύτερο πηγάδι	
	V_A	$\hbar\omega_A$	V_B	$\hbar\omega_B$
^{223}Th	*6.00*	*0.90*	*6.70*	*0.60*
^{224}Th	*6.60*	*0.90*	*7.30*	*0.60*
^{225}Th	*6.60*	*0.90*	*7.30*	*0.60*
^{226}Th	*6.60*	*0.90*	*7.30*	*0.60*
^{227}Th	*6.60*	*0.90*	*7.30*	*0.60*
^{228}Th	*6.10*	*0.90*	*6.80*	*0.60*
^{229}Th	*6.10*	*0.90*	*6.30*	*0.60*
^{230}Th	6.10	0.90	**6.37**	0.60
^{231}Th	**5.80**	0.70	**6.15**	**0.36**

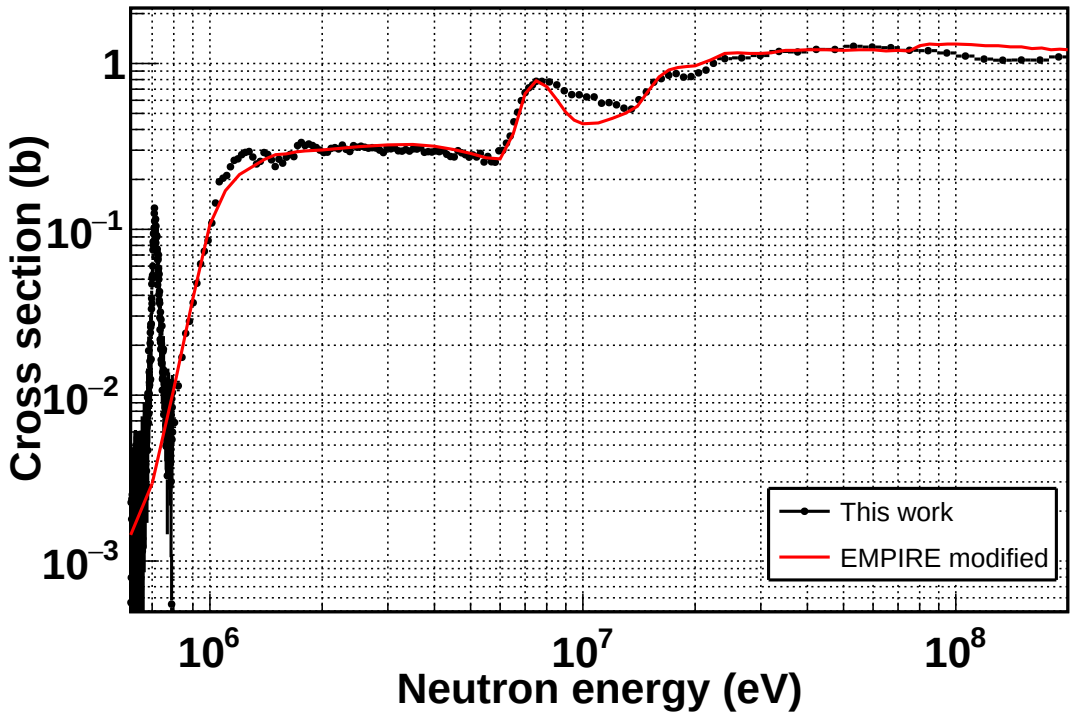

Σχήμα 34: Θεωρητικός υπολογισμός με τον κώδικα EMPIRE με τις τροποποιημένες παραμέτρους για ενέργειες από το κατώφλι της σχάσης μέχρι τα 200 MeV (κόκκινη γραμμή) μαζί με τα πειραματικά σημεία (μαύροι κύκλοι), για την ενεργό διατομή της αντίδρασης ^{230}Th(n,f).

Συμπεράσματα και προοπτικές

Στην παρούσα διδακτορική διατριβή πραγματοποιήθηκε η μέτρηση της ενεργού διατομής της αντίδρασης σχάσης του ^{230}Th στην εγκατάσταση παραγωγής νετρονίων n_TOF στο CERN, για ενέργειες νετρονίων από το κατώφλι της σχάσης μέχρι τα 400 MeV. Τα αποτελέσματα είχαν μικρές αβεβαιότητες, καλή ενεργειακή διακριτική ικανότητα και επιπλέον είναι τα πρώτα δεδομένα στη βιβλιογραφία για ενέργειες μεγαλύτερες των 25 MeV. Επιπλέον πραγματοποιήθηκε η θεωρητική μελέτη της αντίδρασης στα πλαίσια της θεωρίας Hauser-Feshbach, κάνοντας χρήση του κώδικα EMPIRE.

Μέσω της θεωρητικής μελέτης αναδείχθηκε η ανάγκη για επιπλέον πειραματικά δεδομένα, όπως δεδομένα γωνιακών κατανομών για τη σχάση και δεδομένα ενεργών διατομών για τις ανταγωνιστικές αντιδράσεις, προκειμένου να επιτευχθεί ο περιορισμός των θεωρητικών μοντέλων. Επιπλέον, συγκεκριμένα για το ^{230}Th μετρήσεις μεγάλης ακρίβειας στο συντονισμό που εμφανίζεται στο κατώφλι της σχάσης και μετρήσεις με καθαρότερους στόχους σε ενέργειες μικρότερες του κατωφλίου της σχάσης παρουσιάζουν ενδιαφέρον για τον ακριβή προσδιορισμό της ενεργού διατομής στις περιοχές αυτές. Τέλος, θεωρητικοί υπολογισμοί χρησιμοποιώντας το τριπλό δυναμικό της σχάσης παρουσιάζουν ενδιαφέρον στη θεωρητική μελέτη της αντίδρασης.

Introduction

Thorium fuel cycle

The continuously growing energy demand, in combination with the limits in fossil fuel resources highlight the need for studying alternative sources of power. Nuclear energy can be considered as the only source powerful enough to satisfy the needs of modern civilization, while at the same time it does not contribute to the greenhouse effect [1]. Conventional reactors are based on fission reaction of ^{235}U to release $\sim$200 MeV per fission as kinetic energy of heavy fragments, accompanied with radiation and 2-3 neutrons per fission [44]. Each secondary neutron can produce fission events, releasing additional neutrons, a process called chain reaction. In order to sustain a chain reaction, the neutron reproduction factor k_∞, defined as the average number of fission neutrons produced for each thermal neutron absorbed in the fuel, must be greater than 1. The neutrons emitted by fission are fast neutrons, for which the neutron cross-section is small. In order to take advantage of the high cross-section in the thermal region (about 580 b), the neutrons are moderated. For a steady release of energy the neutron reproduction factor must be exactly 1, the so-called critical condition. If the neutron reproduction factor is lower than 1, the reactor is in a subcritical condition, while if the neutron reproduction factor is greater than 1, the reactor is in a supercritical condition. However, only 0.7% of natural uranium is ^{235}U, of which only a small fraction is burned, rendering uranium resources a non-renewable energy source. In addition, the waste from the conventional reactors is highly radioactive (fission fragments, minor actinides) and needs to be stored in deep geological sites to prevent the release of the radiotoxic material in the environment.

Various solutions have been proposed to replace conventional reactors, such as the Generation IV reactors [2], in order to make the production of energy through nuclear reactions safer, sustainable, economic and proliferation resistant. Another solution considered are Accelerator-Driven Systems (ADS), which are reactors working together with an accelerator for the production of neutrons (via the spallation of charged particle impinging on a heavy target). ADS systems are safer, since the reactor is in a sub-critical condition and the neutrons needed to maintain the chain reactions are provided by the accelerator.

In addition, alternative fuel cycles are investigated, since the estimated uranium sources may not be enough for the continuous production of energy via nuclear power. The thorium fuel cycle, as it is shown in figure 1, can be implemented in the reactors as an alternative to the conventional uranium-plutonium fuel cycle, or in ADS. In the thorium cycle the fertile nucleus ^{232}Th transforms into the fissile nucleus ^{233}U by neutron capture followed by two β^- decays. The thorium fuel cycle

has several advantages compared to the uranium-plutonium fuel cycle, related to nuclear safety, radioactive waste management and nonproliferation.

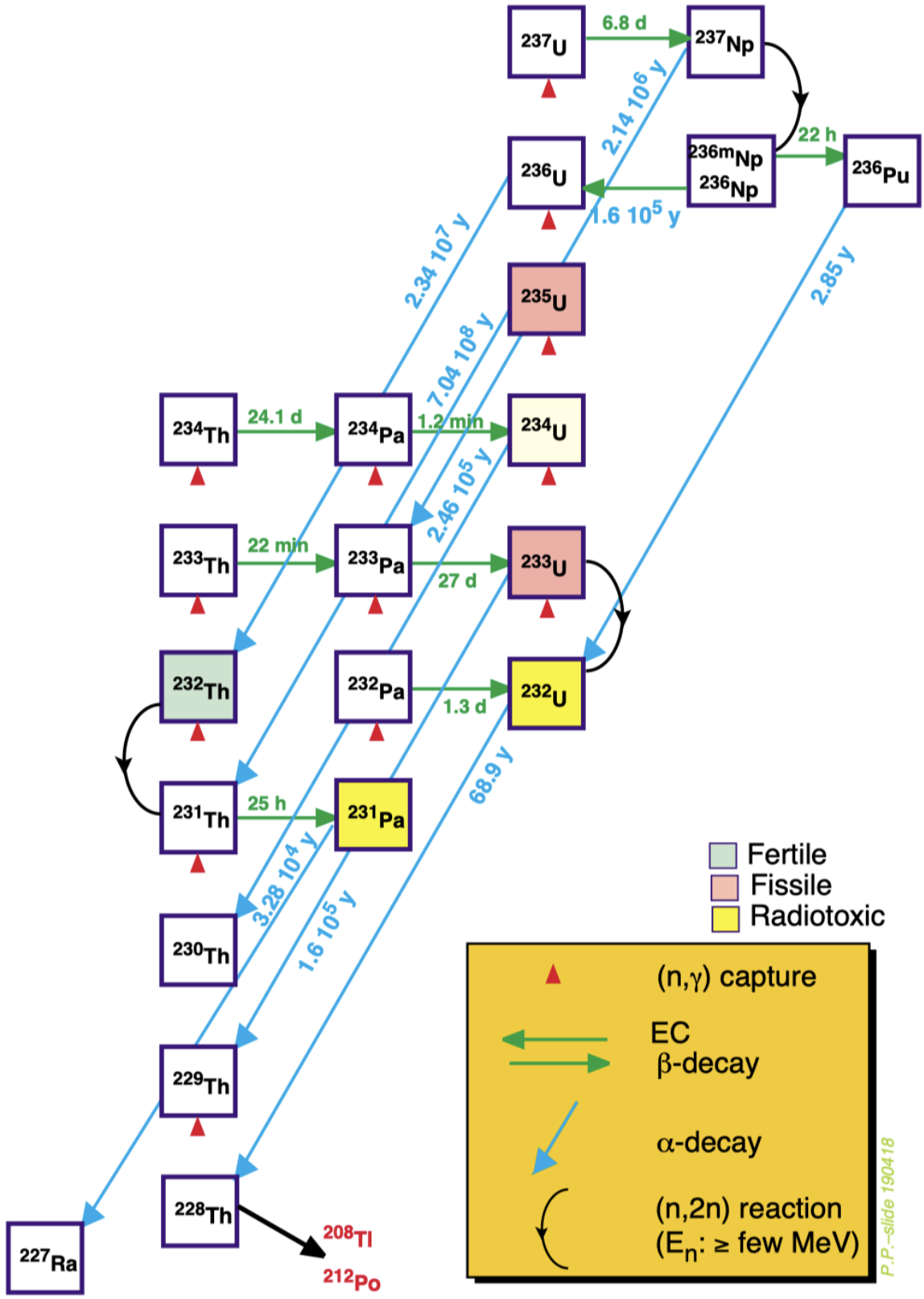

Figure 1: A schematic representation of the thorium cycle [45].

Thorium is a naturally occurring material, containing only the ^{232}Th isotope that can be used as a resource for breeding ^{233}U, while it is 3 to 4 times more abundant than uranium. The absorption cross-section of ^{232}Th at the thermal region is almost 3 times higher than ^{238}U, hence a higher conversion to the fertile material in thermal reactors can be achieved. In the thermal neutron region ^{233}U is the best fissile isotope, having a higher neutron yield per neutron absorbed than both ^{235}U and ^{239}Pu. In addition, thorium oxide is chemically more stable, has higher radiation resistance and does not oxidize unlike uranium oxide. However, one of the main drawbacks of the thorium fuel cycle is the production of a significant amount of ^{232}U, with a half-live of 73.6 years. The ^{232}U chain includes strong γ emitting isotopes, such as ^{212}Bi and ^{208}Tl, with very short half-lives, resulting in significant buildup of radiation dose while storing the spent thorium-based fuel [45, 46, 47].

For the research and development of systems based on the thorium cycle experimental nuclear data are needed, especially for the (n,γ), (n,xn) and (n,f) reactions, for the isotopes relevant to the thorium cycle. Regarding ^{230}Th ($T_{1/2}$=7.54$\times$10^4 y), is produced by the α decay of ^{234}U and has about twice the fission cross-section of ^{232}Th in the fast energy region, which results in a slight increase in the power production, as well as in impeding the ^{233}U from contributing to the neutron balance.

The study of the fission cross-section plays additionally an important role in the study of the fission process and the fission barrier. Specifically, for the thorium nuclei, fine structures appear in the fission cross-section, known as the 'thorium anomaly', which cannot be described by the double-humped fission barrier approach. This indicates that the second barrier is dominant for the thorium nuclei and a shallow third well appears, in order to describe these fine structures [48].

^{230}Th fission cross-section data

Regarding the ^{230}Th(n,f) reaction, few available cross-section data exist in literature, covering the energy range from the fission threshold up to 25 MeV, with many discrepancies among them. The existing experimental data available in the EXFOR database [3] are presented in figure 2.

The most recent measurements are those of Goldblum *et al.* [35] and of Petit *et al.* [36], both based on an indirect determination of the ^{230}Th(n,f) reaction via the surrogate ^{232}Th(^{3}He,α) reaction. A significant deviation is observed between the surrogate data and the other experimental data below 1 MeV, which suggests that the decay probabilities are not independent from the total angular momentum and parity of the populated states (breakdown of the Weisskopf-Ewing approximation) [35]. Deviations are observed also between the two surrogate measurements for energies higher than 7 MeV, with the data of Goldblum *et al.* being in agreement with the rest of the measurements in this energy range.

The quasi-monoenergetic neutron source in the measurements of Meadows [32, 33], Boldeman and Walsh [28], James *et al.* [30] and Kazarinova *et al.* [34] was produced via charged particle reactions. More specifically the ^{7}Li(p,n) reaction was used for the production of neutrons in the lower energy region for the measurements of Boldeman and Walsh and James *et al.*. However the data of James *et al.*

are normalized to the value of 0.37 b at 1.4 MeV after private communication with J.E. Evans and G.A. Jones [30]. The ^{2}H(d,n) reaction was used for the production of neutrons in the measurement of Meadows from 0.7 to 9.4 MeV, relative to ^{235}U. For the higher energy region, at 14.74 MeV, the neutrons were produced via the ^{3}H(d,n) reaction, with the measurement of Meadows performed relative to ^{235}U for the estimation of the neutron fluence, while the measurement of Kazarinova being an absolute measurement with the neutron fluence estimated from the alpha particles produced from the ^{3}H(d,n) reaction.

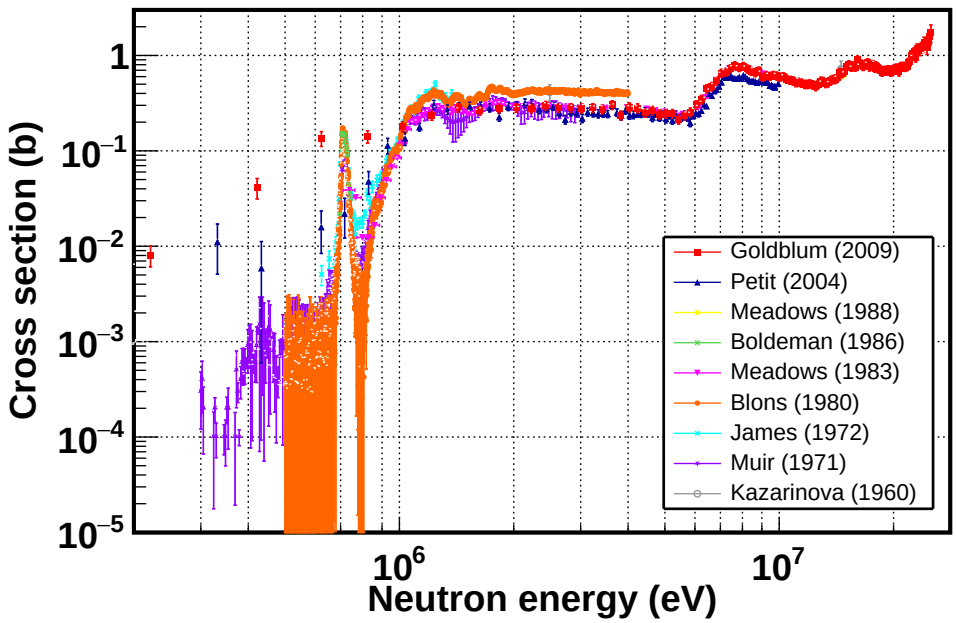

(a) All experimental data

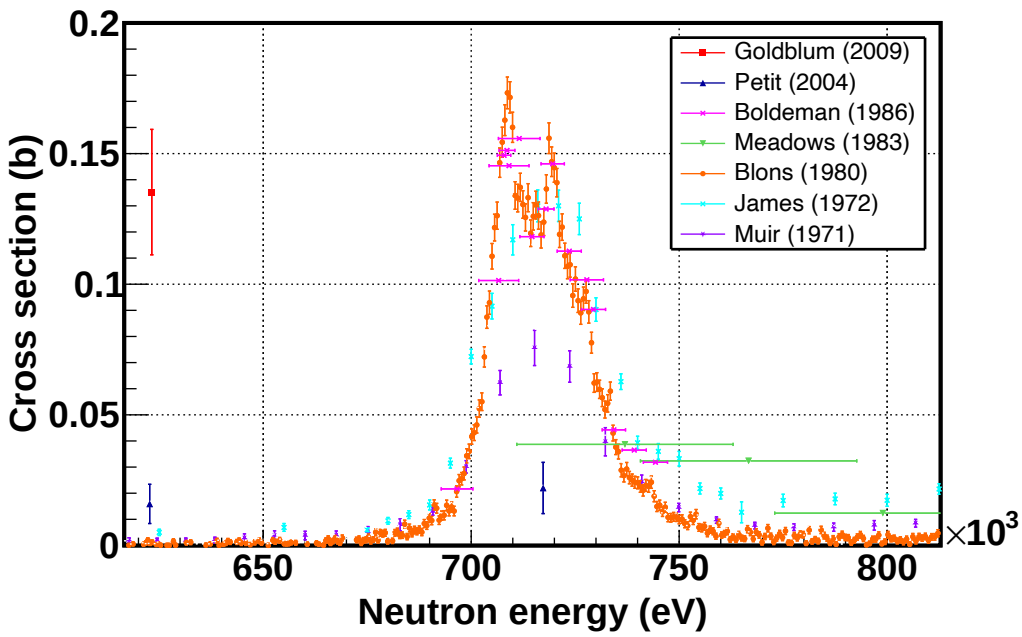

(b) Experimental data in the resonance

Figure 2: Experimental fission cross-section data for ^{230}Th available in literature.

The measurement of Blons *et al.* [29] was performed with the time-of-flight technique at the Geel Linear accelerator GELINA in the 51 m flight path. The energy resolution in the resonance achieved in this measurement was 1.7 keV for a neutron energy of 720 keV, being the best compared to the rest of the experimental data in literature. The measurement was performed relative to ^{237}Np to extract the cross-section shape, however, for the determination of the cross-section value, the data were normalized to 0.37 b at 1.4 MeV (same value with which the data of James *et al.* were normalized).

Finally, the pulsed neutron source in the data of Muir and Veeser [31] originated from an underground nuclear explosion. The cross-section values are the average data from each detection angle.

The uncertainties of the datasets in literature are presented in figure 3, while uncertainty values greater that 100% are omitted from the figure. As seen in the figure, most datasets have uncertainty values much greater than 5% (dashed line in the figure) with the exception of a few points by Muir and Vesser, Blons *et al.* and James *et al.* before the resonance, Blons *et al.* for energies higher than 0.9 MeV, Petit *et al.* for energies higher that 7 MeV and Meadows at 14.74 MeV. Regarding the data of Boldeman and Walsh and Meadows in the lower energy region, no uncertainties for the cross-section exist. The high uncertainty values are a result of the low cross-section of ^{230}Th combined with the fact that ^{230}Th is a rare isotope, making the target preparation a challenging procedure.

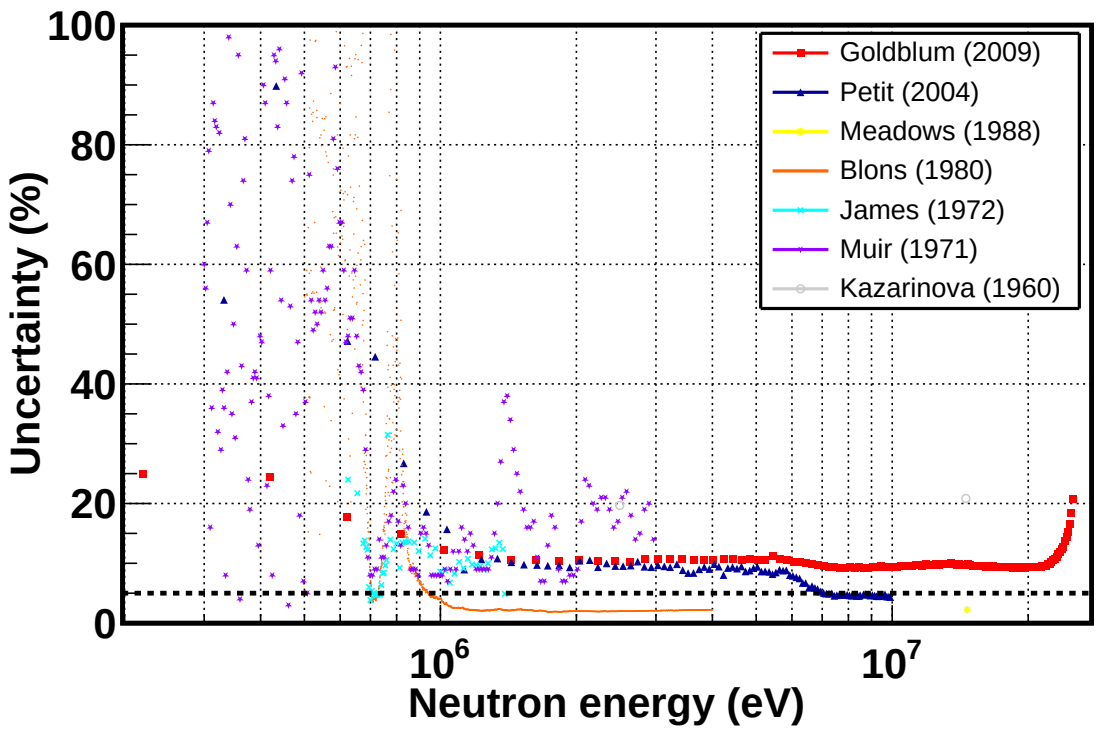

Figure 3: Uncertainties of the fission cross-section data for ^{230}Th available in literature. The dashed line shows the uncertainty value equal to 5%.

The latest evaluated cross-sections for the ^{230}Th(n,f) reaction from ENDF/B-VIII.0 [25], which adopts the JENDL-4.0 library [49], JEFF-3.3 [50] and TENDL-2019 [51]

are presented in figure 4. As seen in the figure, large deviations are observed between the evaluations in the whole energy region. For energies higher than 20 MeV only the TENDL-2019 evaluation exists in literature.

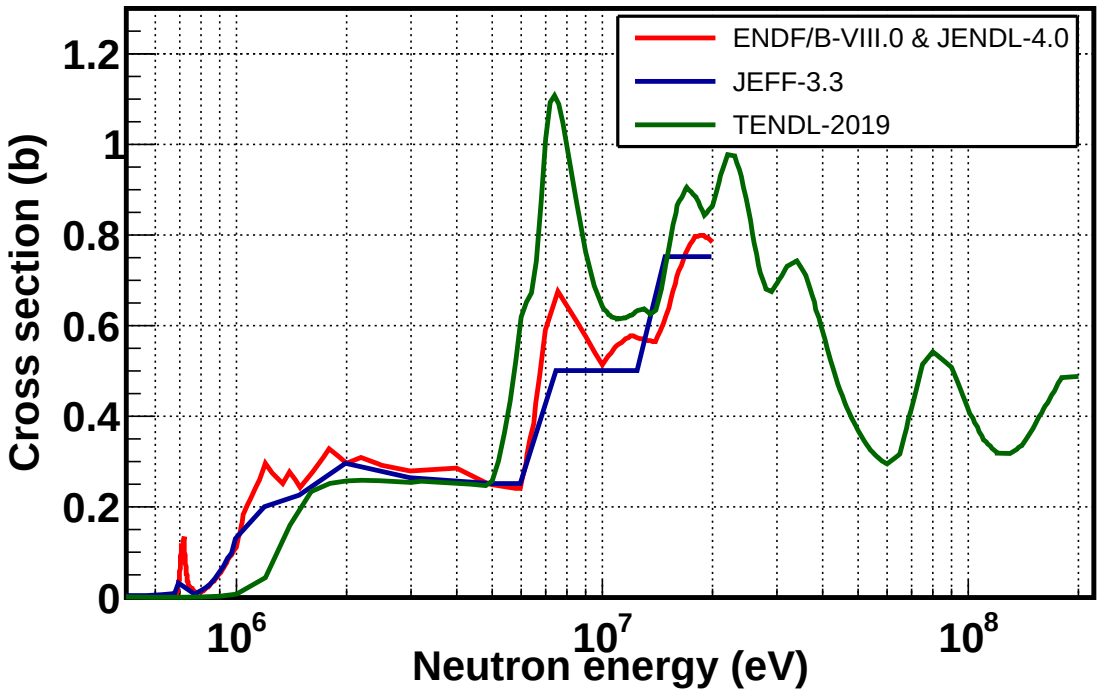

Figure 4: Evaluated cross-section data for the ^{230}Th(n,f) reaction from ENDF/B-VIII.0 which adopts the JENDL-4.0 library (red), JEFF-3.3 (blue) and TENDL-2019 (green).

The aim of this work

The aim of the present work was to obtain more accurate data for the fission cross-section of ^{230}Th over a wide energy range. The EAR-1 measurement aims at the measurement of the cross-section from the fission threshold up to 400 MeV, extending this way the energy range of the current measurements, with an accuracy better than 5% after the resonance. With the same ^{230}Th targets, the scope of the EAR-2 measurement was to investigate the cross-section below the fission threshold, provided that it is high enough to be measured by this configuration.

In addition, the data from the present work will help in solving the discrepancies of the previous datasets. Firstly, the data from this work will provide an insight on the disagreement between Blons *et al.* James *et al.* and Kazarinova with the rest of the datasets after the resonance. In addition, in the higher energy region they will help resolve the differences observed between the data of Goldblum *et al.* and Petit *et al.* above 6 MeV. Also, the data of Goldblum *et al.* can be validated with respect to the absolute cross-section value and shape, being the only data available for energies higher than 10 MeV. As a result, the data from the present work can assist in the improvement and proper tuning of the evaluations.

Chapter 1

Experimental setup

The experiments for the fission cross-section measurements of ^{230}Th were carried out at both experimental areas (EAR-1 and EAR-2) of the CERN (European Organization for Nuclear Research) n_TOF (neutron Time-Of-Flight) facility, in order to take advantage of the different beam characteristics of the two areas.

This chapter contains a brief description of the n_TOF facility, as well as of the time-of-flight technique utilized for the determination of the neutron energies from their time-of-flight. Furthermore, the fission detection setup consisting of the actinide samples, the Micromegas detectors, the electronics and the Data Acquisition System (DAQ) is described.

1.1 The n_TOF facility

The n_TOF facility at CERN is located in Switzerland and is based on an idea by Rubbia et al. [4, 5, 6]. In its present state it includes two experimental areas, the horizontal experimental area (EAR-1) with a neutron flight path of 185 m, commissioned in 2001 and the vertical experimental area (EAR-2) with a neutron flight path of 19 m, commissioned in 2014. A schematic representation of the n_TOF facility is shown in figure 1.1. Additional detailed information for the CERN n_TOF facility can be found in [7].

The neutron beam of the CERN n_TOF facility is produced via spallation reactions of 20 GeV/c proton pulses impinging on a thick lead target. Two types of pulses are provided by the CERN Proton Synchrotron (PS), the dedicated ones corresponding to the nominal intensity of the proton bunch and the parasitic corresponding to a low intensity. Each pulse, consists of 7-8 $\times$ 10^{12} protons for the dedicated and of $\sim$3 $\times$ 10^{12} protons for the parasitic pulses, respectively. The bunches have a width of 7 ns and maximum repetition rate of 0.8 Hz.

The spallation target is a lead cylinder, surrounded by 1 cm of water for cooling, with a diameter of 60 cm and a length of 40 cm. In the horizontal direction a second layer of 4 cm borated water (1.28% H_3BO_3 enriched with ^{10}B) has been added for moderation purposes. The very large neutron capture cross-section of ^{10}B contributes to the suppression of the thermal part of the neutron beam. At the same time, the probability of neutron capture in the ^{1}H of water is reduced, suppressing

this way the 2.2 MeV γ-rays emitted due to the capture, which contribute in the delayed photon background of the neutron beam.

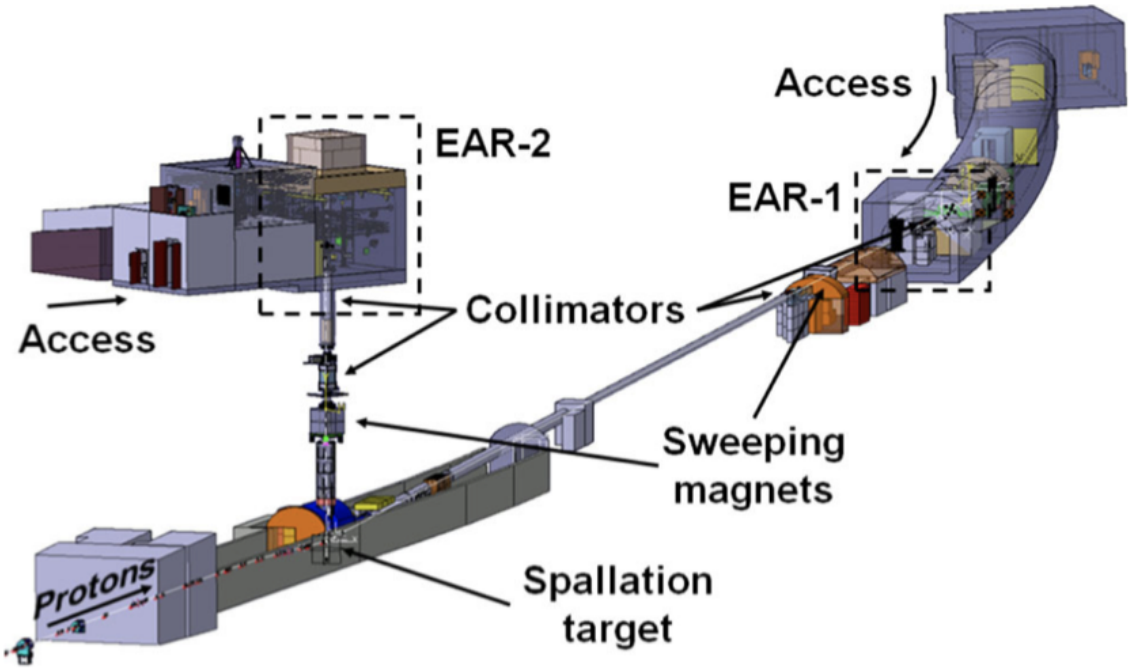

Figure 1.1: Schematic representation of the CERN n_TOF facility [7]. The proton beam, incident on the spallation target, produces the white-spectrum neutron beam. The neutrons travel in vacuum the 185 m horizontal and 19 m vertical flight paths simultaneously, in order to reach the experimental areas EAR-1 and EAR-2, respectively. (Drawing not to scale.)

The wide energy range of the n_TOF neutron flux (from the thermal region up to $\sim$1 GeV) [8, 9], alongside with the high resolution of experimental EAR-1 and the high instantaneous flux of the experimental EAR-2, are the main advantages of the facility. The differences in the beam characteristics make it possible to fulfill different measurement requirements. Specifically, EAR-1 is suitable for measurements requiring high resolution or higher neutron energies. On the other hand, EAR-2 is suited for lower neutron energy measurements (up to $\sim$100 MeV, varying with the detection system) for high activity, low mass and low cross-section samples.

In figure 1.2 the instantaneous intensity, which for simplicity from now on is referred as neutron beam flux, of EAR-1 and EAR-2 are compared, measured with the capture collimators for both areas. Due to the additional layer of the borated water, the thermal peak is suppressed in the neutron flux of EAR-1, resulting in a $\sim$400 times lower flux in the region. At higher energies, the ratio of the flux between the two areas decreases reaching $\sim$20 above 1 MeV.

During the CERN Long Shutdown 2, a new spallation target has being constructed, scheduled to be commissioned in 2021, having as main upgrades a higher neutron flux and a better resolution for the EAR-2 neutron beam [7], while no significant changes are expected for the neutron beam in EAR-1.

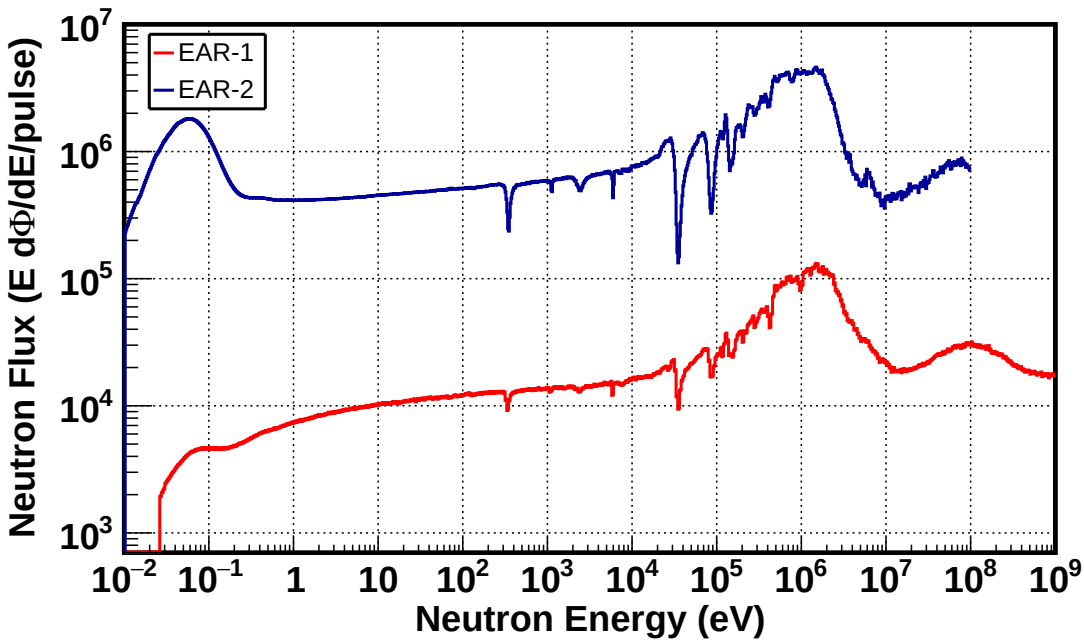

Figure 1.2: Comparison of the measured instantaneous flux integrated over the collimator surface in experimental EAR-1 (red line) [8] and EAR-2 (blue line) [9], measured with the capture collimators of 1.8 and 3.0 cm diameter for EAR-1 and EAR-2, respectively.

1.1.1 The first experimental area (EAR-1)

The first experimental area EAR-1 is located at a horizontal distance of 185 m from the spallation target. The neutrons, along with other inevitably produced background particles, the so-called "γ-flash" (γ-rays and ultra-relativistic particles), travel inside the stainless steel vacuum tubes to EAR-1. To prevent charged particles from reaching the experimental area, a sweeping magnet is placed between the two collimators [52, 53]. The first collimator, with an outer diameter of 50 cm and an inner diameter of 11 cm, is located at $\sim$137 m from the spallation target. The diameter of the second collimator, located $\sim$ 178 m from the spallation target, is chosen according to the requirements of the experiment performed, to be either 1.8 cm (capture collimator) or 8 cm (fission collimator). After crossing the experimental area the neutron beam travels an additional 12 m to the beam dump, made of polyethylene and cadmium. The schematic representation of the EAR-1 beam-line is shown in figure 1.3 [54]. Additional information of the experimental area EAR-1 and its performance can be found in [7, 8, 54].

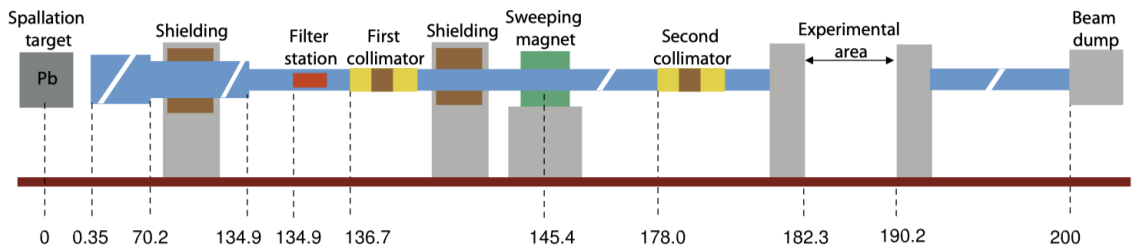

Figure 1.3: Schematic representation of the n_TOF EAR-1 beam-line [54]. The distances are given in meters. (Drawing not to scale.)

1.1.2 The second experimental area (EAR-2)

The second experimental area EAR-2 [55] is located ∼19 m vertically from the spallation target (located underground), with the experimental area being on the surface. The neutron beam travels in vacuum through the first collimator and a permanent magnet to sweep charged particles away from the neutron beam charged particles. The second collimator, located just below the surface of the experimental area, has two options regarding the inner diameter, either 3.0 cm (capture collimator) or 6.7 cm (fission collimator). The beam dump is located on the roof of the EAR-2 experimental area. A layout of the EAR-2 beam-line, depicting various components is shown in figure 1.4 [56]. Additional details for experimental EAR-2 can be found in [7, 56, 9].

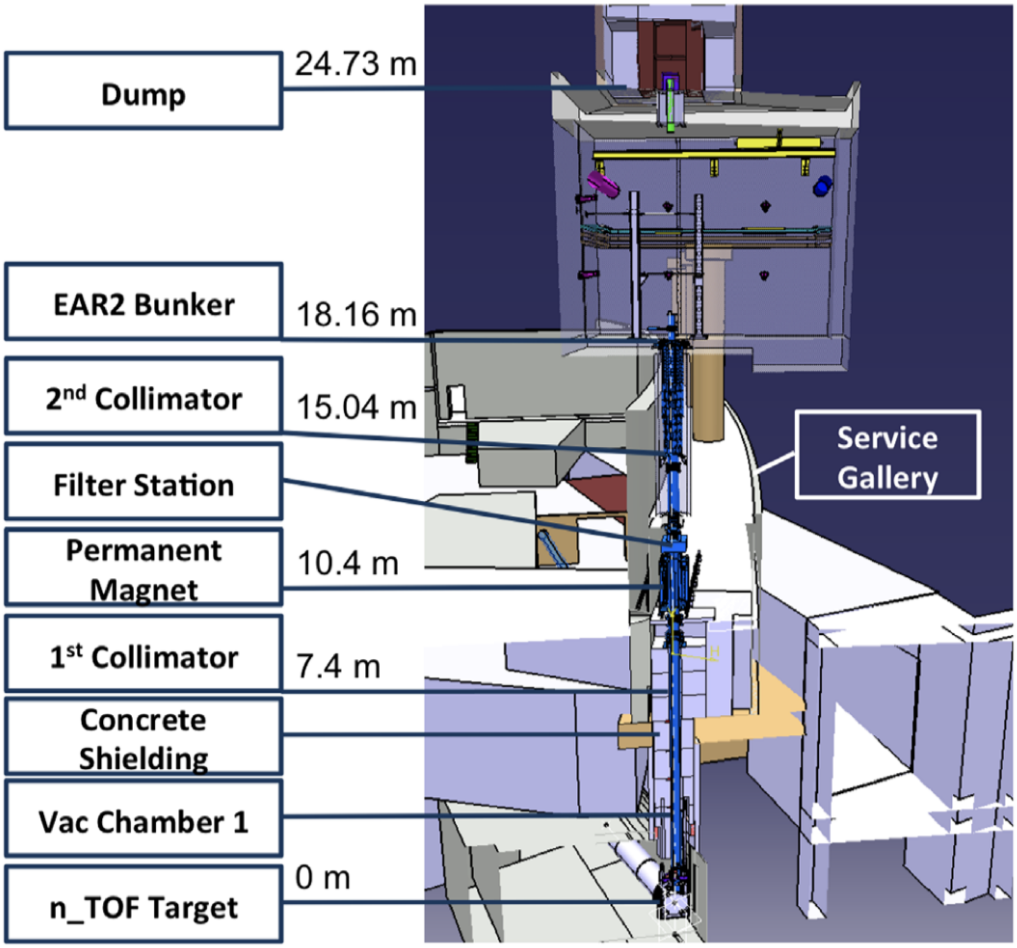

Figure 1.4: Schematic representation of the n_TOF EAR-2 beam-line [56].

The closer distance of EAR-2 to the spallation target in combination with the bigger diameter of the capture collimator, results in a higher neutron instantaneous flux than in EAR-1. This feature provides the opportunity for difficult and challenging measurements. For instance, low mass samples, highly radioactive, or reactions with low cross-sections can be measured in EAR-2, in a shorter time and with a better signal-to-background ratio than in EAR-1. On the other hand, it is important to note that due to the closer distance of EAR-2 to the spallation target the neutron

energy resolution is inevitably worse than the one of EAR-1. In addition, the maximum neutron energy that is possible to reach in EAR-2 (100 MeV) is lower than that of EAR-1 (1 GeV), since high energy neutrons are preferentially emitted along the direction of the proton beam. As a result, each experimental area serves different measurement purposes. Depending on each specific measurement, the combination of the experimental area and collimator (capture/fission) is chosen according to the experiment requirements. In some cases, as in this work, it was decided to measure at both experimental areas. The EAR-1 measurement aimed at higher reachable energies in combination with the good resolution of the area. Thus, it was possible to reach up to ~400 MeV in neutron energies and to measure the resonance of the ^{230}Th(n,f) reaction at 0.7 MeV with a better resolution than in EAR-2. Moreover, by measuring with the same setup at EAR-2, the higher achievable energies at EAR-2 could not be reached for successful cross-section measurements, due to the dead time of the system, since the masses of the targets were optimized for the EAR-1 measurement. In essence, the experimental campaign in EAR-2 was focused on the measurement of the expected low (and never measured before) fission cross-section of ^{230}Th below the fission threshold.

1.1.3 The time-of-flight technique

For the determination of the neutron energy, the time-of-flight technique is employed. In general, this is achieved by measuring the time difference between the production of the neutron and the interaction, which creates a signal in the detector. In classical terms the time-energy relation is given by the equation:

$$E_n = \frac{1}{2} m_n v^2 = \frac{1}{2} m_n \left(\frac{L}{t}\right)^2 \tag{1.1}$$

where m_n = 939.6 MeV/c^2 is the neutron mass, $v = L/t$ is the neutron speed, L is the neutron flight path and t is the time-of-flight of the neutron. The classical approach is used for neutron energies below a few keV. For higher neutron energies the general relativistic approach is adopted, given by the equation:

$$E_n = m_n c^2 (\gamma - 1) = m_n c^2 \left(\frac{1}{\sqrt{1 - \left(\frac{L}{tc}\right)^2}} - 1 \right) \tag{1.2}$$

where c = 299.8 m/μs is the speed of light and γ is the Lorentzian factor.

The relative resolution of the time-of-flight facility, at first approximation, is given by the equation:

$$\frac{\Delta E_n}{E_n} = 2 \times \sqrt{\left(\frac{\Delta t}{t}\right)^2 + \left(\frac{\Delta L}{L}\right)^2} \tag{1.3}$$

At n_TOF the time-of-flight of the neutron is estimated relative to the γ-flash. The interaction of the protons with the spallation target results in the production of γ-rays and other relativistic particles, which reach the experimental areas at (almost) the speed of light. These γ-rays and high energy particles cause the first signal in the detector, the so-called γ-flash. The γ-flash arrives in the measuring station at a time:

$$t_\gamma = t_0 + t_{light} = t_0 + \frac{L}{c} \tag{1.4}$$

where t_0 is the unknown time the neutron was created from the spallation process and t_{light} is the time required for the γ-flash signal to reach the detector after the protons impinged on the spallation target. The time-of-flight of the neutron causing a signal in the detector is estimated as follows:

$$t = t_{signal} - t_0 = t_{signal} - t_\gamma + \frac{L}{c} \tag{1.5}$$

where t_{signal} is the time the signal is recorded in the detector.

However, the conversion from time-of-flight to energy is not straightforward. Neutrons of the same energy arrive with a distribution of time-of-flights to the experimental area, as a result of the different flight paths they travel inside the spallation target and the moderator. So, for the correct estimation of the neutron energy, another term λ has to be added to the geometrical distance L_{geom} (from the surface of the spallation target to the position of the measuring station). This term depends on the neutron energy and is estimated via Monte Carlo simulations, taking into account the proton pulse width. Neutrons and photons created from the spallation process are estimated with Monte Carlo simulations, performed with the FLUKA code [21]. The transport code, developed within the n_TOF collaboration simulates the optical transport of these neutrons and photons from the target to the experimental areas, taking into account the specific characteristics of each experiment. The distribution of the flight paths with respect to the neutron energy, namely the resolution function of the neutron beam in each experimental area, is shown in figure 1.5a and figure 1.5b for EAR-1 and EAR-2 respectively, as it is estimated via the transport code.

The mean value of the moderation length for each energy region $\lambda(E_n)$ is estimated from the resolution function, as shown in figure 1.6 for EAR-1 1.6a and EAR-2 1.6b. For energies higher than 10 keV, the neutron energy is calculated from an iterative procedure, as described in [57]. The first step is the calculation of the approximate neutron energy from equation 1.1 for the classical or from equation 1.2 for the relativistic approach respectively, using the measured time-of-flight and the geometrical flight path L_{geom}. The next step is the calculation of the neutron energy using the effective flight path $L = L_{geom} + \lambda(E_{n-1})$. The same procedure continues by correcting the flight path with next energy's mean value for the moderation length $\lambda(E_n)$. The accurate neutron energy is estimated when two consecutive calculations of the neutron energy converge.

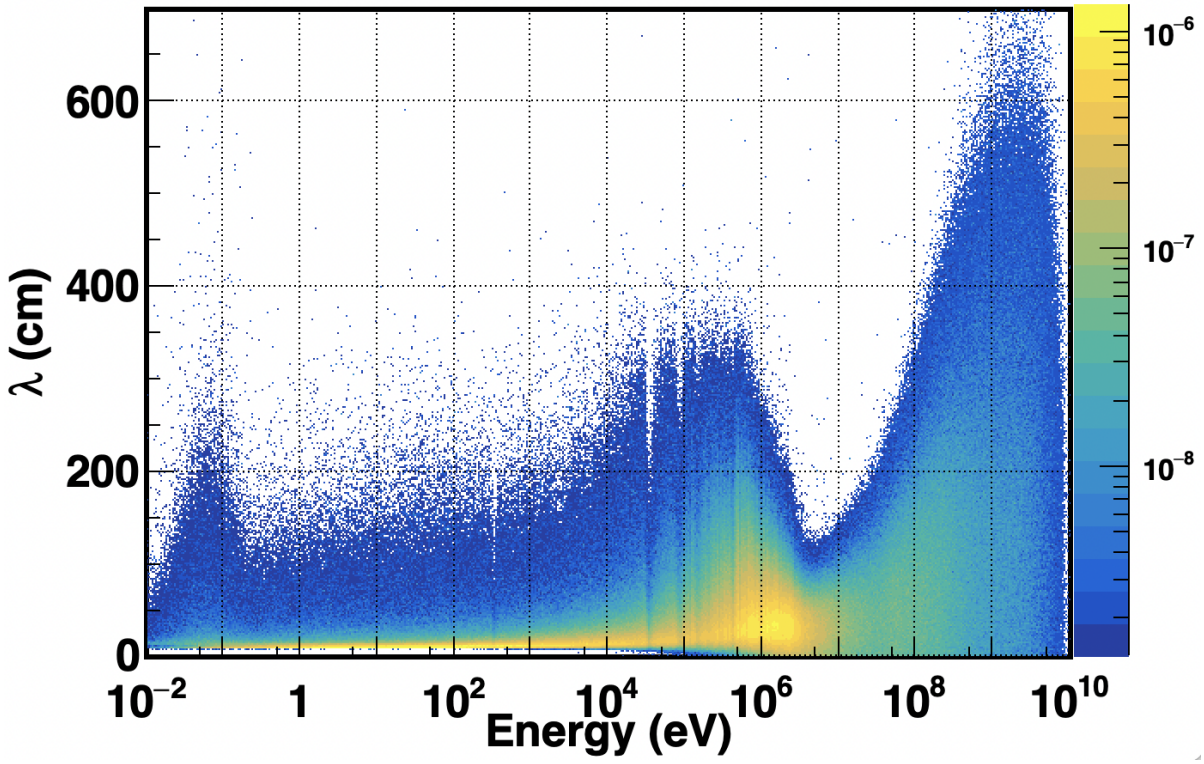

(a) EAR-1

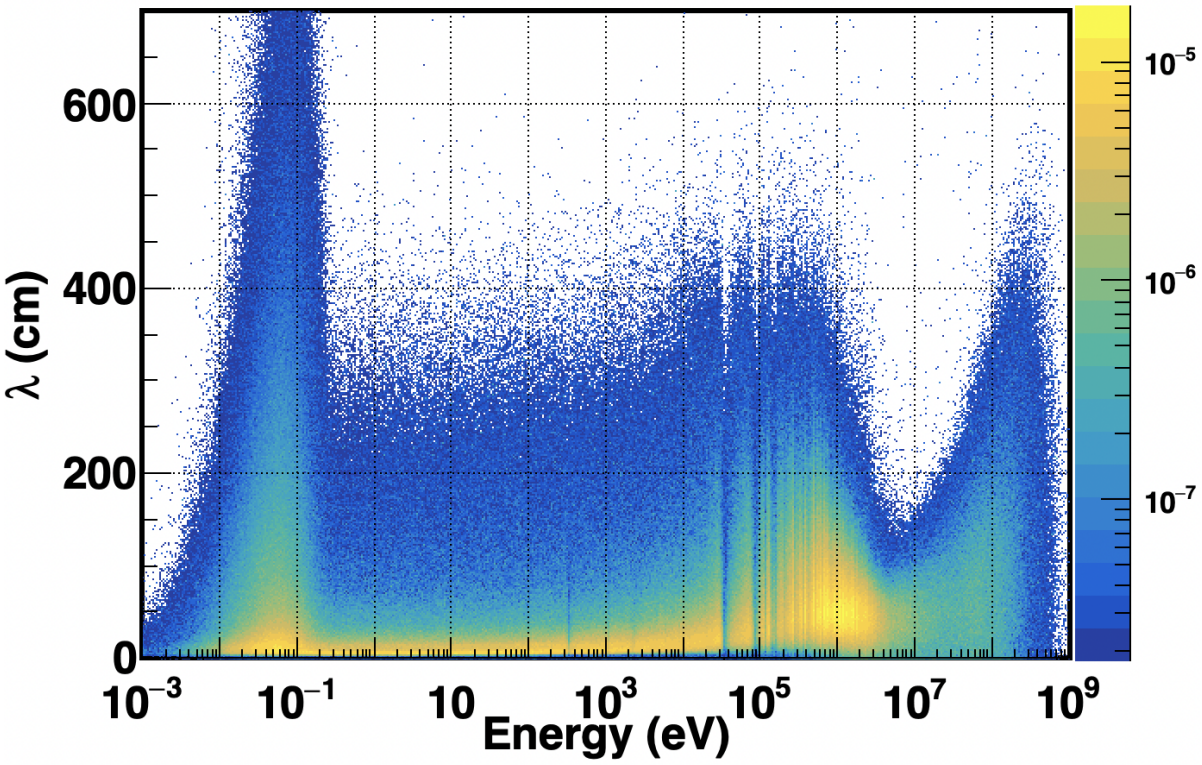

(b) EAR-2

Figure 1.5: Distribution of the moderation length λ as a function of the neutron energy for EAR-1 (a) and EAR-2 (b), estimated with the transport code.

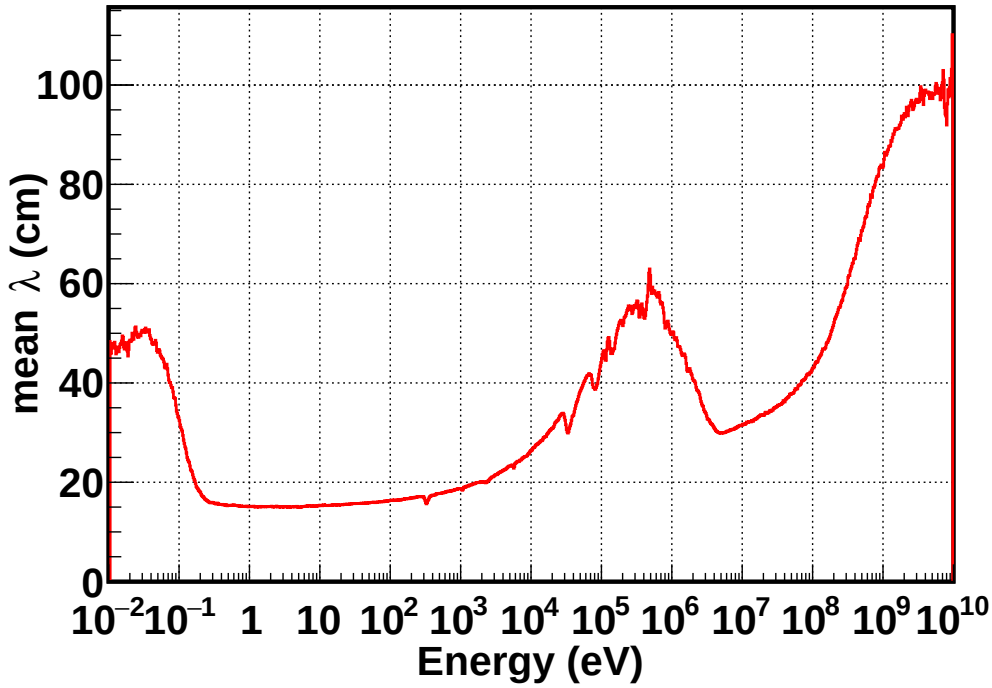

(a) EAR-1

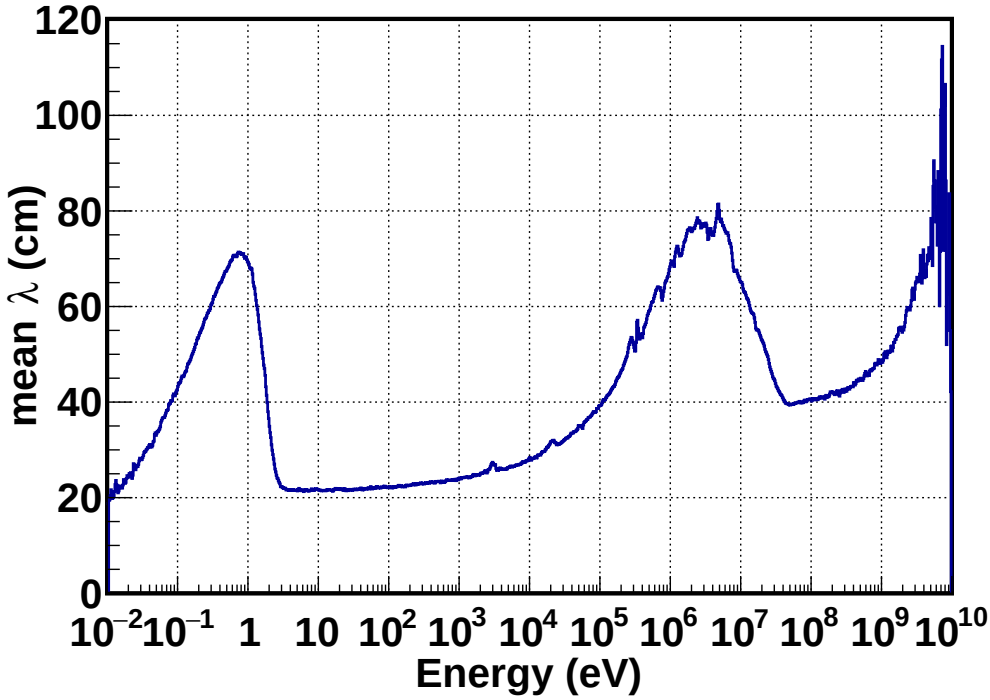

(b) EAR-2

Figure 1.6: The mean value of the moderation length λ as a function of the neutron energy for EAR-1 (a) and EAR-2 (b).

1.2 The fission measurements setup

1.2.1 The actinide samples

Seven high-purity ^{230}Th samples, provided from JRC-Geel, were used for the measurements with a total mass of 27.14 mg. The samples, of 8 cm diameter, were prepared by the molecular plating technique, deposited on a 0.025 mm thick aluminum backing. The target characteristics are presented in table 1.1. Various plutonium contaminants were present in the samples with the ratio of Pu/Th being equal to 0.0004942. The mass factions of the plutonium contaminants are presented in table 1.2. Regarding the mass fraction of ^{241}Pu, it is only an indicative value, due to the interference between ^{241}Pu and ^{241}Am. While the plutonium contaminants in the ^{230}Th samples are only a small faction of the sample mass, some of them are fissile with high cross-section values at lower energies, dominating over the small ^{230}Th cross-section below the fission threshold.

Table 1.1: Main characteristics of the ^{230}Th samples.

Target id	Reference number	Mass (mg)	Areal density (μg/cm^2)	Activity (MBq)
^{230}Th #3	TP2017-06-19	4.61	92	3.52
^{230}Th #4	TP2017-06-21	4.19	83	3.20
^{230}Th #5	TP2017-06-24	2.31	46	1.76
^{230}Th #6	TP2017-06-22	2.46	49	1.88
^{230}Th #7	TP2017-06-25	4.14	82	3.16
^{230}Th #8	TP2017-06-20	4.89	97	3.73
^{230}Th #9	TP2017-06-18	4.53	90	3.46

Table 1.2: Mass fraction of the plutonium contaminants present in the ^{230}Th samples. The Pu/Th ratio is 0.0004942.

Isotope	Mass fraction (%)
^{238}Pu	0.2681
^{239}Pu	22.40
^{240}Pu	20.23
^{241}Pu*	7.76
^{242}Pu	49.15
^{244}Pu	0.199

* Indicative value.

The characterization of the ^{230}Th samples was performed at JRC-Geel, by means of α-spectroscopy on the full area of 8 cm diameter of the targets. The systematic uncertainty on the measurements was estimated to be in the order of 1%. Additional γ-ray spectroscopy measurements were carried out, implementing a HPGe detector in open geometry. The 67.67 keV γ-ray, with an intensity of 0.377% of the parent ^{230}Th was used for the estimation of the quantity of ^{230}Th in the samples, with an uncertainty on the γ-ray intensity of 4.5%, taken from the Lund database [58]. The absolute efficiency of the measurement setup was estimated with the use of the 185.712 keV γ-ray (57.2% intensity) of a ^{235}U target with 8 cm diameter sample deposit (same as the ^{230}Th samples) and known activity (from α-spectroscopy measurements). The agreement between the α and γ-ray spectroscopy measurements was found to be less than 0.6% for all targets, with the exception of the ^{230}Th targets #4 and #6, where the differences were in the order of 4%. The reason behind this difference is not yet clear and it is still being investigated. The mass of the targets used for the estimation of the cross-section was taken from the α-spectroscopy measurements, due to the high uncertainty in the γ-ray used for the characterization of the samples in the γ-ray spectroscopy measurements.

The inhomogeneity of the samples was estimated by comparing the mass of a part of the samples (from the center with a diameter of 6 cm) with the one of the whole sample (8 cm). The diameters selected for the measurements were chosen from the availability of the on-site collimators. The mass difference was found to have different values depending on the sample, varying from 0.6 to 20%, while for all samples less mass was found in the outer parts of the targets.

Two high purity reference samples were used for the measurements, also prepared with the molecular plating technique and characterized by means of α-spectroscopy at JRC-Geel. The reference sample geometrical characteristics were the same as those of the ^{230}Th samples (8 cm diameter and 0.025 mm aluminum backing). The ^{235}U sample, with reference number TP2017-009-14 and an areal density of 72 μg/cm^2 (activity 587.5 Bq) was placed upstream of the ^{230}Th samples with respect to the neutron beam, while the ^{238}U sample, with reference number TP2017-008-03 and an areal density of 287 μg/cm^2 (activity 179.5 Bq), was placed after the stack of the ^{230}Th targets, being this way the last target hit by the neutron beam.

1.2.2 The Micromegas detector

The measurements of this work were carried out using a set-up based on Micro-Bulk Micromegas (Micro-Mesh Gaseous Structure) detectors [10, 11, 12, 13, 14]. The Micromegas detector [15, 16, 17] is a gas detector divided into two parts: the drift region between the drift electrode and the micromesh (cathode electrode) and the amplification region between the micromesh and the anode electrode. The drift electrode is the actinide target itself, while the micromesh is a thin 5 μm Cu plate, 9.5 cm in diameter, with holes of $\sim$35 μm in diameter at a distance of $\sim$50 μm from each other, as seen in figure 1.7. While the distance between the micromesh and the anode is fixed ($\sim$50 μm), the distance between the drift and the micromesh can vary (from a few hundred μm to some cm) and it is chosen specifically for each application.

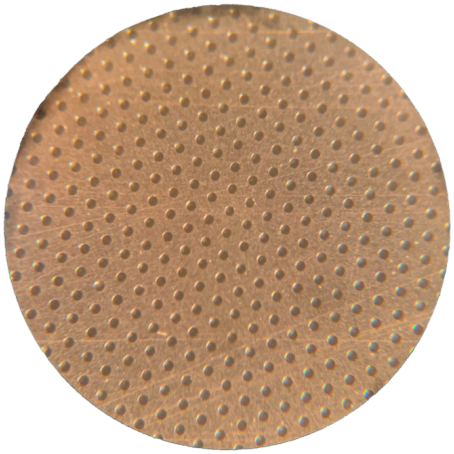

Figure 1.7: Photo of the micromesh, taken with an optical microscope, where the holes can be seen.

The anode electrode is grounded through a 50 Ω resistance. The voltage on the drift and mesh electrode is chosen depending on the application. On the drift electrode usually a voltage of a few hundred volts is applied, leading to a weak field of about 1 kV/cm. On the mesh electrode a smaller voltage is applied (lower than ∼400 V), leading to a strong electric field of about ∼50 kV/cm.

When an ionizing particle enters the drift region it creates electron-ion pairs. The weak electric field in the region causes the electrons to drift towards the micromesh. The electric field is chosen to be low enough to guide the electrons to the amplification region through the micromesh holes and high enough to avoid recombination of the electron-hole pairs [59]. Upon entering the amplification region the electrons are multiplied, through avalanches. The gain of the amplification region is selected through the voltage applied in the micromesh, depending on the gain required for each application, but it should be low enough to avoid sparks in the amplification region. The signal of the detector is created from the induction of the moving charges and in the present work is collected from the micromesh electrode. A schematic representation of the movements of the electrons, when a fission fragment enters the Micromegas detector is shown in figure 1.8.

The low mass of the detector and the materials used, based on the microbulk design [11], makes it almost transparent to neutrons, an ideal characteristic which allows the placement of the detector in the beam. In addition, the high efficiency (∼1) and angular acceptance of the detector (∼2π) constitute very important advantages for fission measurements. When a fission occurs two fission fragments are created, moving to opposite directions due to the kinematics of the reaction. Thus, one of the fission fragments enters the drift region and it is detected.

For the ^{230}Th(n,f) experiments the Micromegas detectors were placed in an aluminum alloy chamber, each detector coupled with a sample. The drift region was defined by spacers to be 6 mm. The chamber was filled with a gas mixture of Ar:CF_4:isoC_4H_{10} (88:10:2) kept at atmospheric pressure and room temperature. The Micromegas and samples stack mounted in the chamber is shown in figure 1.9. The ^{230}Th samples were placed in between the reference samples ^{10}B, ^{235}U and ^{238}U, as

seen in figure 1.9 The same setup was used for the measurements at both experimental areas, EAR-1 and EAR-2.

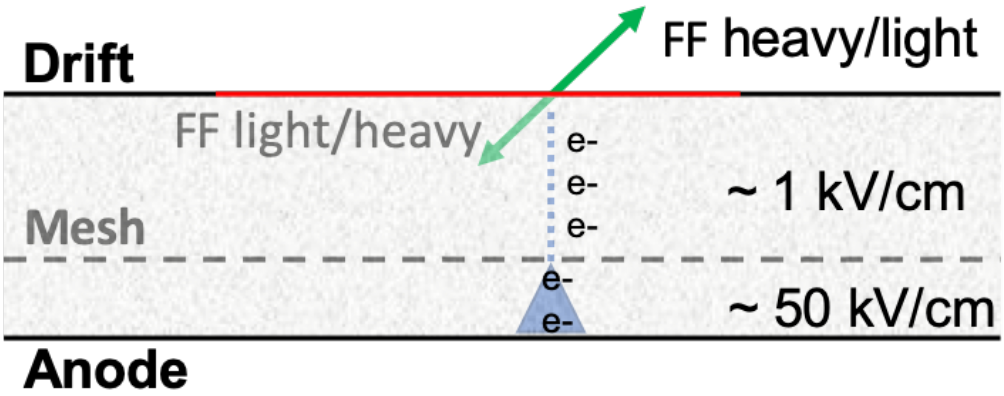

Figure 1.8: A schematic representation of the electron's movements inside the Micromegas detector.

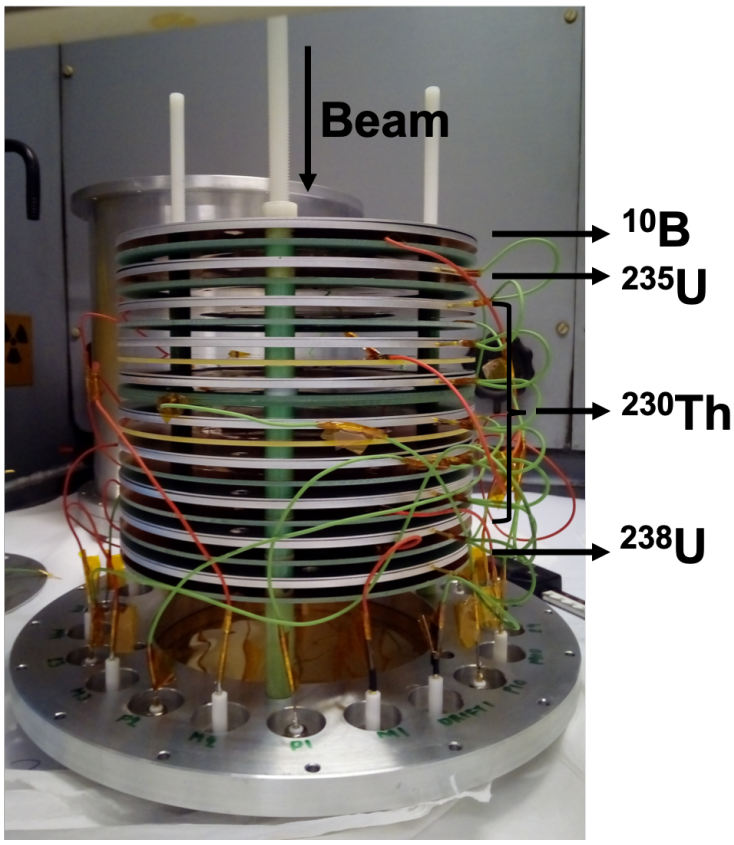

Figure 1.9: The experimental setup for the EAR-1 and EAR-2 measurements. The Micromegas detectors and the samples, with respect to the neutron beam direction, are shown in the picture.

The FWHM of the pulses, achieved with the above-mentioned setup, was ∼200 ns. The time response of the setup is of great importance, since it defines the maximum counting rate at which consecutive pulses can be resolved. In addition, for

time-of-flight measurements, the FWHM is closely related to the energy resolution of the setup, especially in the high energy region where the smaller time-of-flights are considered. The pulses with the same width correspond to a different energy resolution of the setup in the low and high energy region, because at lower time-of-flights (which means higher neutron energies) the same pulse width is equal to larger energy intervals.

1.2.3 Electronics and data acquisition

New improved current-sensitive preamplifier modules, constructed at INFN-Bari, were used for the measurements in both experimental areas, EAR-1 and EAR-2. The preamplifiers contained the same circuit used for previous fission measurements at n_TOF, namely ^{242}Pu(n,f) at EAR-1 (Phase-II) [60], ^{240}Pu(n,f) [61] and ^{237}Np(n,f) at EAR-2 (Phase-III) [18], but instead of forming 16-channel and 4-channel units, new preamplifiers were built, each one in its unique thick aluminum box. Thus, the shielding of the preamplifiers was improved and, at the same time, the cross-talk between the preamplifiers of the same module existing in the past was avoided. As a result, a significant improvement was observed regarding the noise in the measurements, especially in the high energy region, just after the γ-flash. Hence, for the EAR-1 measurement, in combination with improvements in the grounding of the experimental area from Phase-II to Phase-III, it was possible to reach 400 MeV, while the ^{242}Pu(n,f) experiment performed during the 2011-2012 campaign managed to reach only up to 20 MeV.

The preamplifiers are used both for voltage supply in the mesh electrodes and for the readout of the signals. The schematic representation of the circuit used in the preamplifiers is shown in figure 1.10. The gain of the preamplifiers was chosen according to the requirements of each target through the resistor R20 (marked with the red box in the figure) to be 2.2 kΩ for the actinide targets and 4.7 kΩ for the ^{10}B sample. For the drift electrode, the voltage was supplied directly to the electrodes through high-voltage filters. The setup, including the chamber and the electronics, is shown in figures 1.11a and 1.11b, for EAR-1 and EAR-2 respectively.

The signals collected from the preamplifiers are fed to a fast analog-to-digital converter [62]. This way the waveform is recorded in digital form in order to be analyzed offline. The analog-to-digital converters used at n_TOF are Signal Processing Devices (SPDevices), which are capable of sampling rates up to 1.8 GSamples/s. In the case of ^{230}Th(n,f) measurement at EAR-1 the sampling rate used was 125 MSamples/s, while at the EAR-2 measurement it was 112.5 MSamples/s and the full scale was chosen to be 5 V for both measurements.

In order to reduce the amount of data to be stored, only the first $\sim$60 μs after the γ-flash for both EAR-1 and EAR-2 experiments were recorded as is, corresponding to $\sim$0.05 MeV and $\sim$0.0005 MeV for EAR-1 and EAR-2, respectively. After that time the use of a zero-suppression technique was employed, in order to record the signal only if it was greater than an amplitude threshold chosen, unique for each detector. The selected data were stored at the CERN Advanced STORage manager (CASTOR) [63] for further offline analysis.

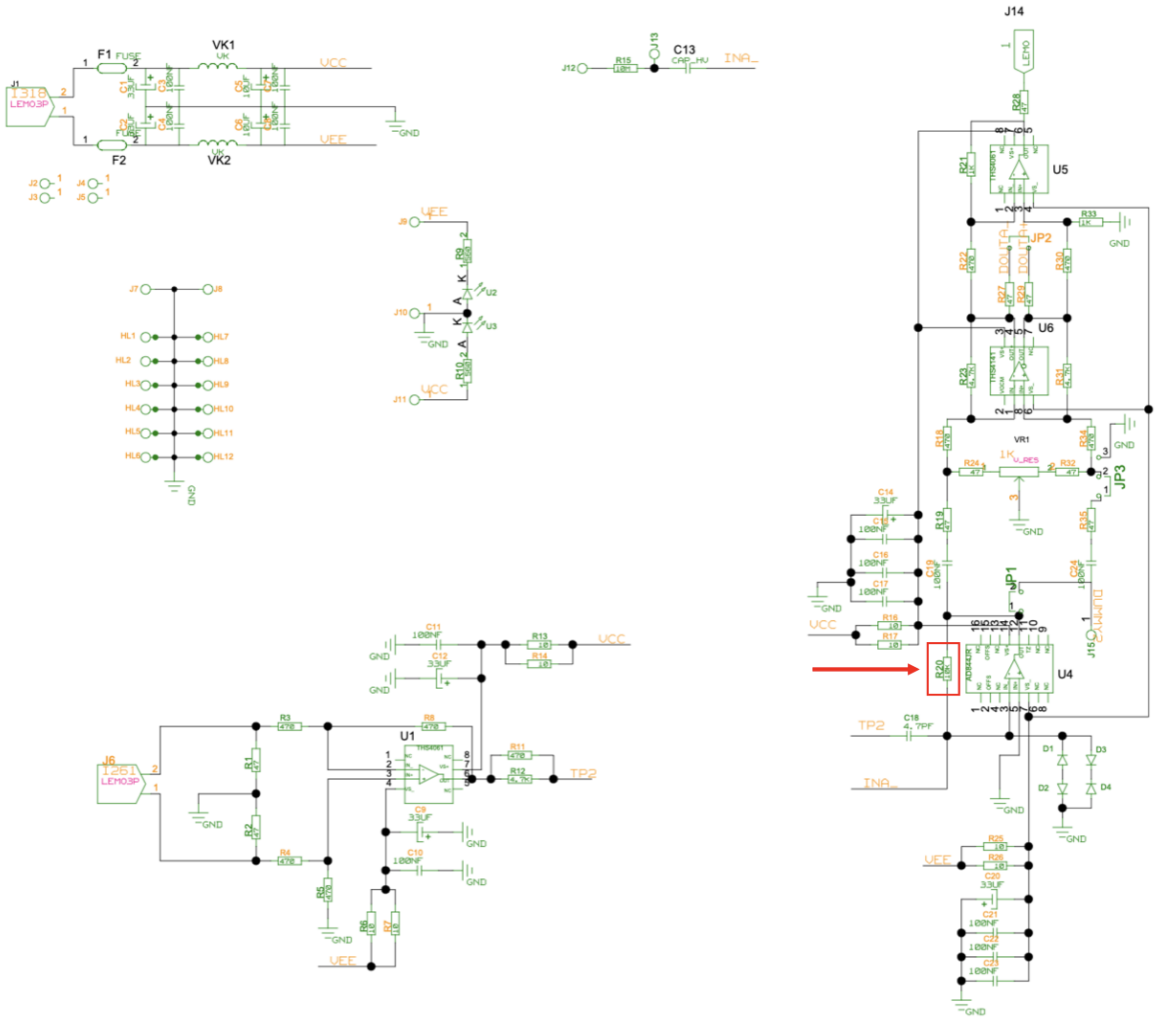

Figure 1.10: A schematic representation of the preamplifiers constructed at INFN-Bari, used for the measurements. The red box indicates the resistor R20, which can be replaced in order to adjust the gain of the preamplifiers.

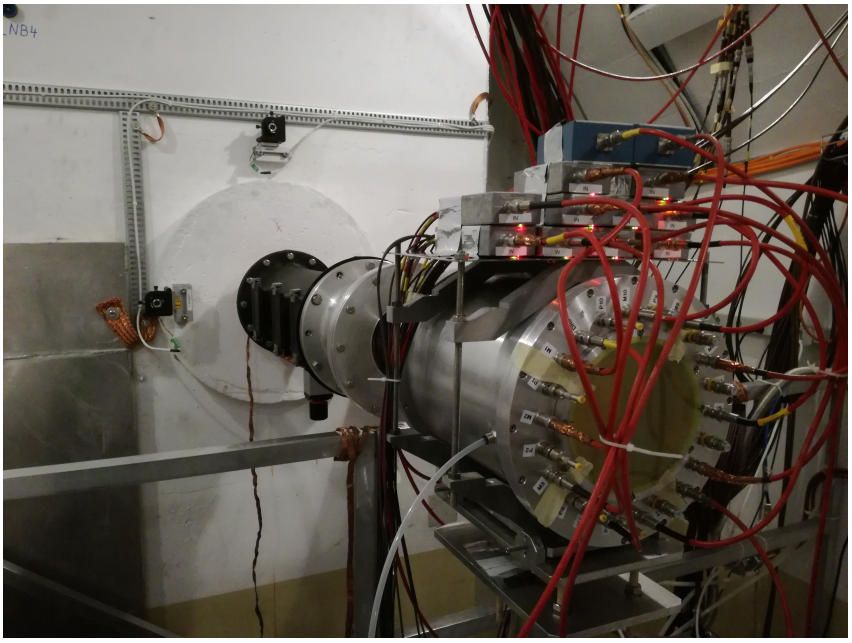

(a) EAR-1

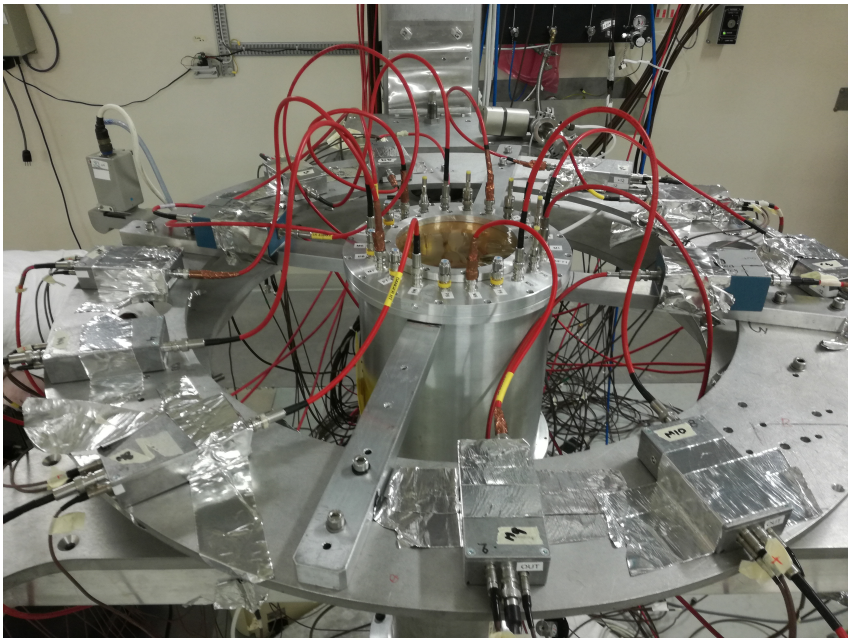

(b) EAR-2

Figure 1.11: A photograph of the experimental setup at (a) EAR-1 and (b) EAR-2, showing the fission chamber and the electronics. At EAR-1 the electronics were placed on top of the fission chamber, while at EAR-2 the electronics were placed around the fission chamber.

Chapter 2

Data analysis

The signals, recorded from each detector, are stored in the CERN Advanced STORage manager (CASTOR) for further offline analysis. The raw data are processed with a pulse shape analysis (PSA) routine developed at n_TOF [64]. Additional quality checks are applied in order to reject noise, bad runs etc. The cross-section is calculated after applying the proper, necessary corrections to the signals (amplitude cut, dead time etc.).

2.1 Raw data analysis

2.1.1 γ-flash

The data are stored and viewed in the so-called "movies", each one containing the recorded waveforms for the whole neutron bunch (100 ms for EAR1 and 16 ms for EAR2). The first frame of a specific detector, contains the γ-flash and the following $\sim$60 μ, as mentioned in Section 1.2.3. The next frames, contain one or more signals at various time-of-flights after the γ-flash. The scope of the data analysis procedure is to select the signals that correspond to fission events, rejecting this way alpha particles, noise, γ-flash residuals etc., attributing to each signal its time-of-flight and its proper corresponding amplitude.

The first step in the analysis procedure is the treatment of the γ-flash. The time-of-flight of each signal on a specific detector is estimated relative to the γ-flash, as mentioned in Section 1.1.3. In addition, fission fragment signals occur inside the peak of the γ-flash, as well as right after it, where the tail of the γ-flash is still present. The treatment of the γ-flash aims to mitigate its effects, making it possible to reach higher energies in the analysis.

The treatment of the γ-flash, as explained in detail in [18], is based on the calculation of an average value for the γ-flash and the baseline from a stack of different bunches. A threshold is applied on the z-axis of the γ-flash stack to estimate its average shape, as shown in figures 2.1a and 2.1b for two of the Micromegas detectors from the EAR-1 and EAR-2 measurement, respectively. The average shape is then provided in the PSA routine, and is subtracted from the signal, scaled to the amplitude of the γ-flash of each event.

The estimation of the effectiveness of the method is achieved by subtracting the average γ-flash shape from each individual movie. The stack from the subtracted movies is shown in figure 2.2. As seen in the figure the fluctuation is around zero at higher time-of-flights, corresponding to lower energies. Closer to the γ-flash, the fluctuation around zero is greater and inside the γ-flash pulse the baseline is overestimated. This is an indication that the recognition of the pulses is worse at higher energies.

The average γ-flash is estimated differently for the dedicated and the parasitic pulses and it is confirmed that the γ-flash shapes are identical, when scaled to the amplitude of the γ-flash pulse, as seen in figures 2.3a and 2.3b for the EAR-1 and EAR-2 measurements respectively. As seen from the figures, the characteristics of the γ-flash between the two experimental areas are different. Firstly, the absolute amplitude of the EAR-2 γ-flash is significantly higher than in EAR-1, as it was observed during the experimental campaigns. It is important to note that the mesh voltages of the Micromegas detectors in the EAR-2 measurement had to be reduced, by $\sim$20 V at each detector from the EAR-1 to the EAR-2 measurement, in order to avoid the saturation of the γ-flash peak, while the electronics and the whole sample and detector set-up used in both areas were exactly the same. As a result, the amplitude of the signals was also reduced in the EAR-2 measurement. In addition, the width of the γ-flash pulse is lower in the EAR-1 measurement. The FWHM of the γ-flash in the EAR-1 measurement is $\sim$170 ns, while in the EAR-2 measurement is $\sim$220 ns. Finally, a different shape of the baseline is observed after the γ-flash between the two experimental areas. In the EAR-1 measurement an oscillatory baseline is observed, while in the EAR-2 one, due to theγ-flash, a smaller peak is present at lower energies.

The differences between the γ-flash pulses between the two areas are a result of the nature of the γ-flash itself. Although the name indicates that the pulse is a result of energy deposition of γ-rays in the detectors, this is not the whole truth. In addition to the photon signals, the γ-flash peak contains signals, as mentioned in Section 1.1.3, from relativistic particles, all produced by the spallation process, as well as signals from interactions of high energy neutrons and photons with the samples, the materials of the beam line, the collimator and the detector itself. As a result, different detector types show a different sensitivity to the γ-flash. For example, a γ-ray sensitive detector, when placed in a high γ-ray environment (HPGe, C6D6, etc.), is expected to have a worse response to the γ-flash compared to a detector which is not sensitive to γ-rays (Micromegas, PPAC [65, 54]). In addition, different responses are observed between different detector types, when placed at the two experimental areas. This can be nicely seen when comparing the Micromegas detectors (used in this work) with the PPAC detectors (used at both areas of n_TOF). It is interesting to note that while the Micromegas γ-flash response is much worse in EAR-2 this is not the case for the PPACs. While having an excellent response to the γ-flash at both areas (due to the minimal material of the detector in beam and the low gas pressure used) at EAR-1 a small γ-flash peak is observed in comparison to EAR-2 where no pulse is observed as a response to the γ-flash. This indicates that the cause of the γ-flash peak can have different sources (neutrons, γ-rays, charged particles etc.).

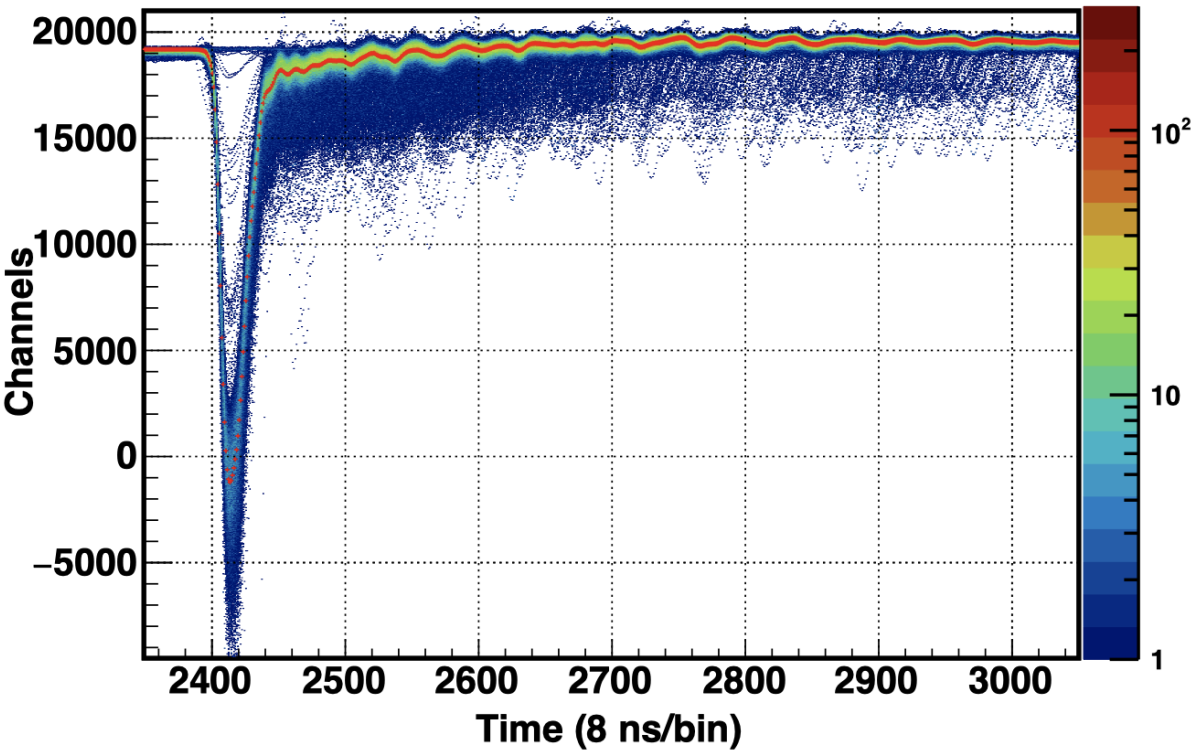

(a) EAR-1

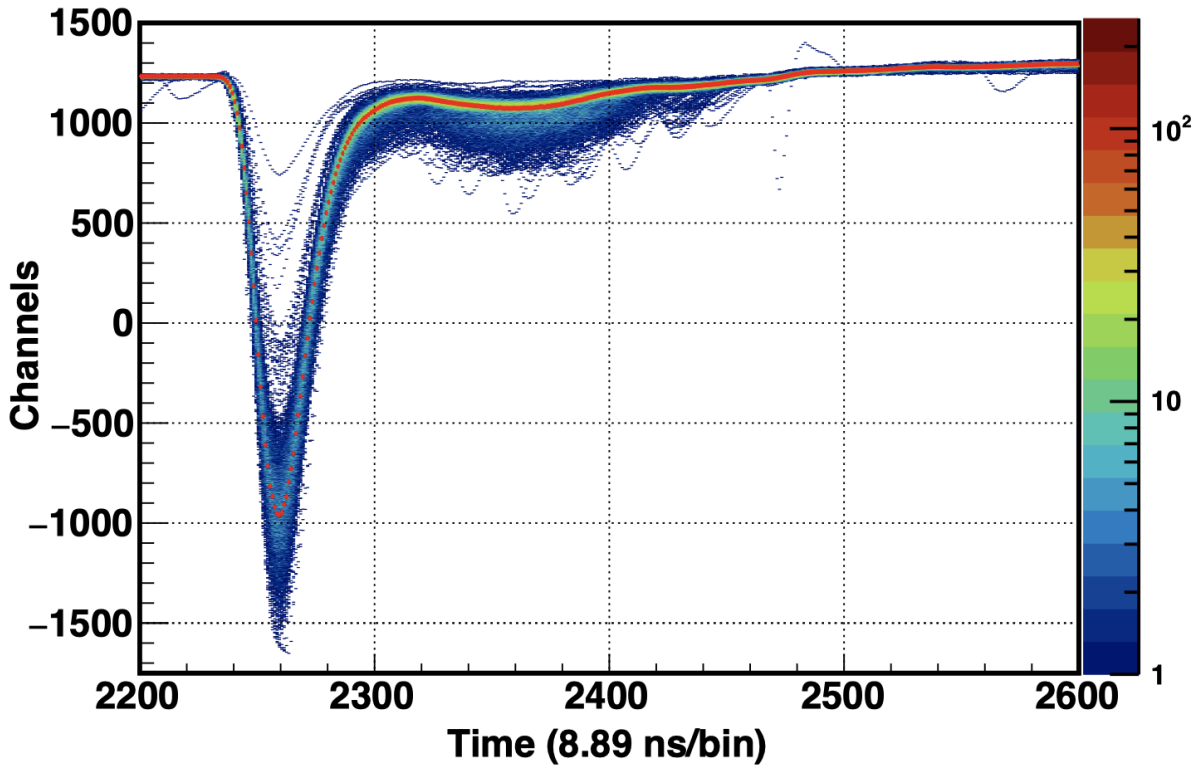

(b) EAR-2

Figure 2.1: γ-flash stacks from the (a) EAR-1 and (b) EAR-2 measurements and the average γ-flash shape (red line) estimated from the stacks.

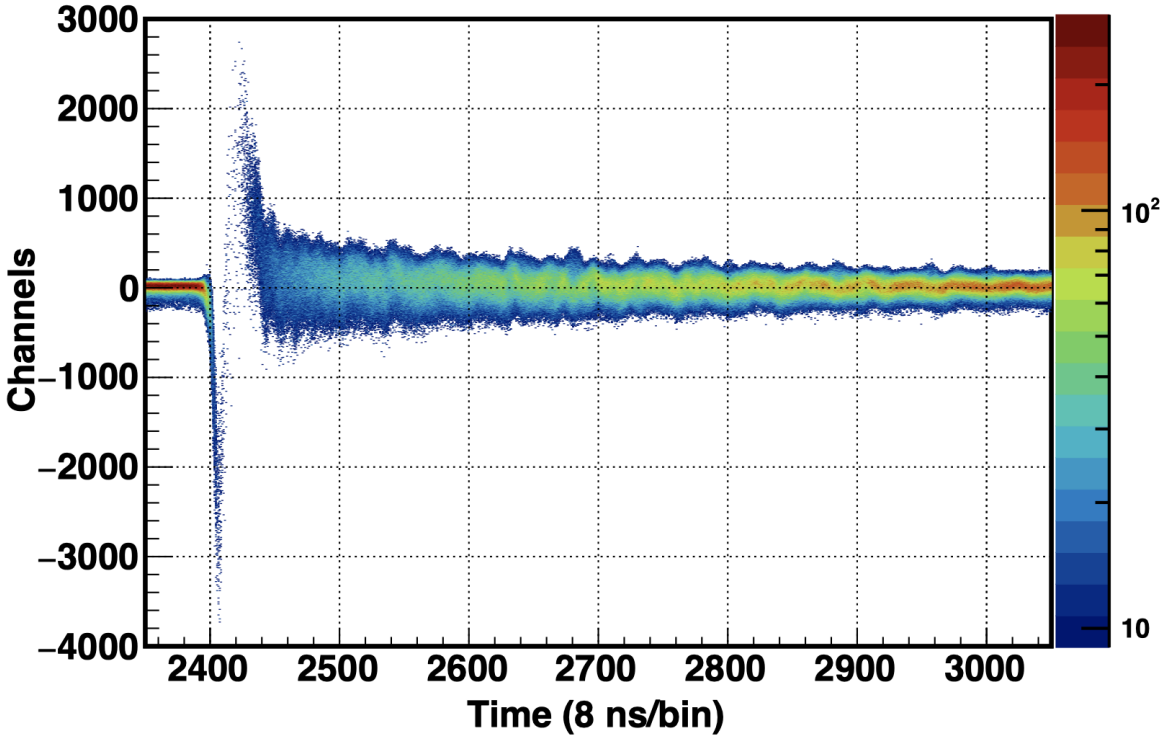

Figure 2.2: γ-flash residuals from the EAR-1 measurement.

Regarding this work, the cause of the γ-flash pulse can be better understood when comparing the EAR-1 and EAR-2 detector responses. Firstly, as mentioned above, the response is much worse in the EAR-2 measurement, resulting from the greater energy deposition in the detector, due to the higher neutron flux. The particle shower, however, created by the proton beam impinging on the lead target is strongly forward peaked. This is a first indication that the source of the γ-flash between the two areas could be different. While in EAR-1 the γ-flash could be caused by high energy photons arriving in the experimental area, in EAR-2 the source of the γ-flash could be the neutrons themselves, which are characterized by a much higher flux than in EAR-1 [7] and more specifically, signals from the neutron elastic and inelastic scattering could be the main component of the γ-flash in EAR2. This can be better understood by two additional features of the EAR-2 γ-flash, the wider FWHM and the second smaller peak observed after the γ-flash, as seen in figures 2.3a and 2.3b. If the high energy photons travelling at the speed of light (which are much less in EAR-2) were the source of the γ-flash at both areas, there is no reason to expect wider γ-flash in EAR-2. In addition, the delayed after-pulse, caused by elastic and inelastic scattering of neutrons in the detector gas and surrounding materials at lower energies, is an indication of the energy deposition in the detector through the scattering mechanism. During the last campaign of Phase-III of n_TOF the nature and effects of the γ-flash at various detectors (STEFF [66], Frisch-grid ionization chamber [67]), have been studied with the results indicating the importance of the neutron flux in the creation of the so-called γ-flash pulse and the effects in the detector response.

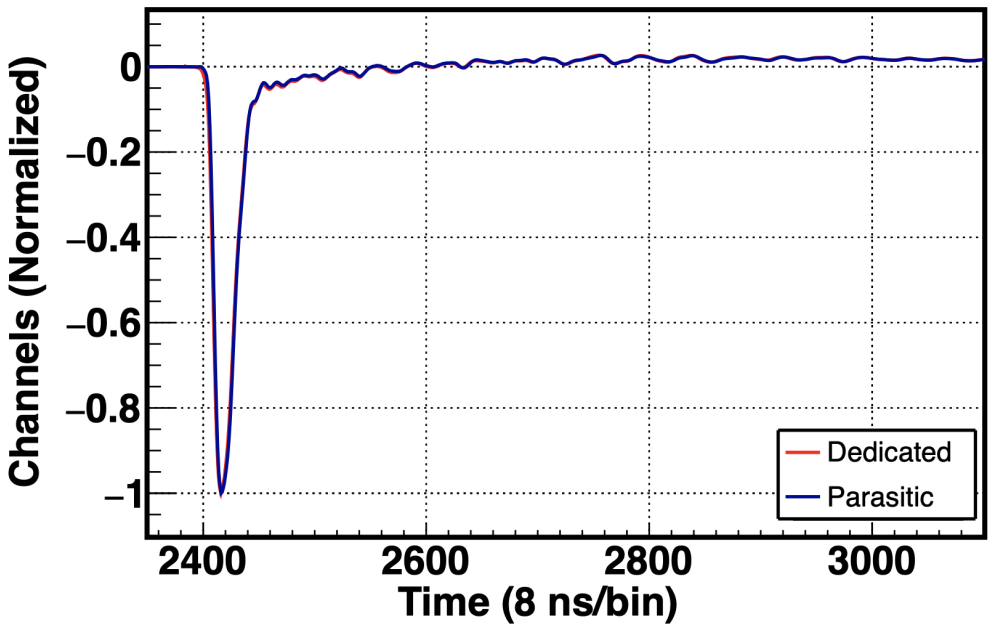

(a) EAR-1

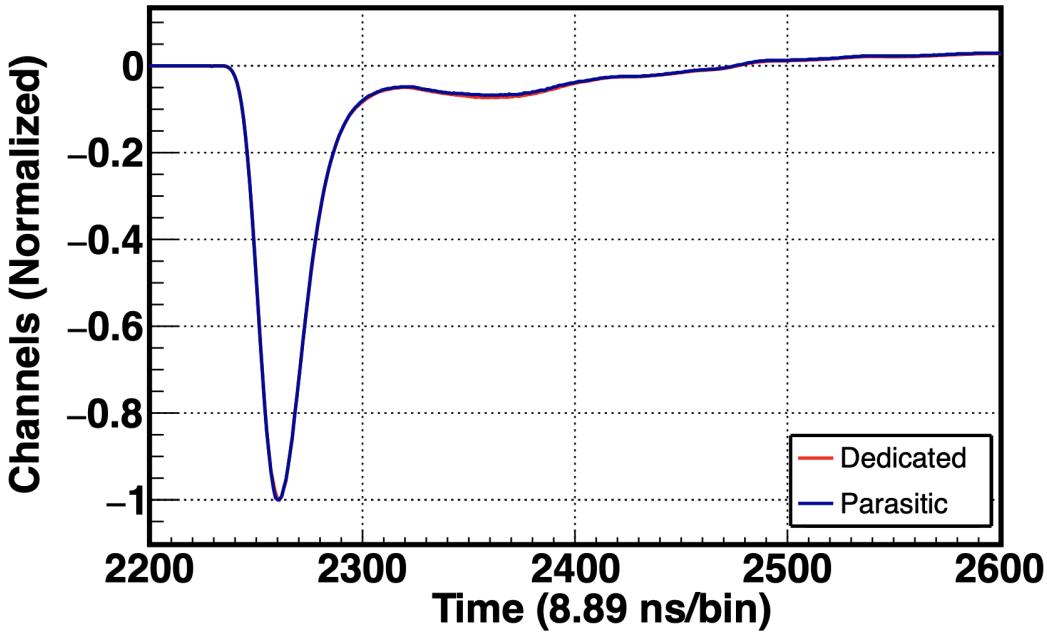

(b) EAR-2

Figure 2.3: Comparison of the average γ-flash shape from the dedicated (red line) and the parasitic (blue line) pulses of the (a) EAR-1 and (b) EAR-2 measurement, respectively.

2.1.2 Pulse Shape Analysis

The first step towards the recognition of the pulses is the calculation of the derivative, as shown in the middle panel of figure 2.4. The derivative is calculated by integrating the signal at both sides of a selected point, taking as points for the integration a step size (which is defined by the user). Pulses are recognized in the signal when their derivative crosses certain thresholds, namely 3.5 $\times$ the root mean square

(RMS) of the noise, which is represented by the green lines of the middle panel of figure 2.4. When a pulse is located a set of conditions are applied to the pulse, in order to be considered a real event. The boundaries of the eliminating conditions are selected by the user and include the limits of the pulse width, the limits of the pulse amplitude and the limits of the area-to-amplitude ratio, and they are applied to the pulses at various points during the analysis procedure.

The pulse recognition is followed by the baseline calculation, which is performed in two regions. Close to the γ-flash, a region is specified by the user in which different options for an adaptive baseline are available. Outside this region, a constant baseline is calculated as the average of all signal points, excluding the pulses previously recognized, as shown by the red line of the top panel in figure 2.4. In this work, the baseline close to the γ-flash was calculated from the average γ-flash shape, as mentioned in Section 2.1.1. The clean signal is calculated after subtracting the baseline, as shown in the bottom plot of figure 2.4.

Different methods are available in the PSA routine for the estimation of the amplitude of each identified pulse, namely by searching the highest point, by parabolic fitting and by fitting a shape provided to the routine by the user. In the cases where pulse shape fitting is possible, which means that the pulses of the detector have a fairly constant shape, this is considered as the most suitable of the three methods for pulse reconstruction. In addition, it is possible to provide different pulse shape types and the PSA routine selects the most suitable pulse shape for each case.

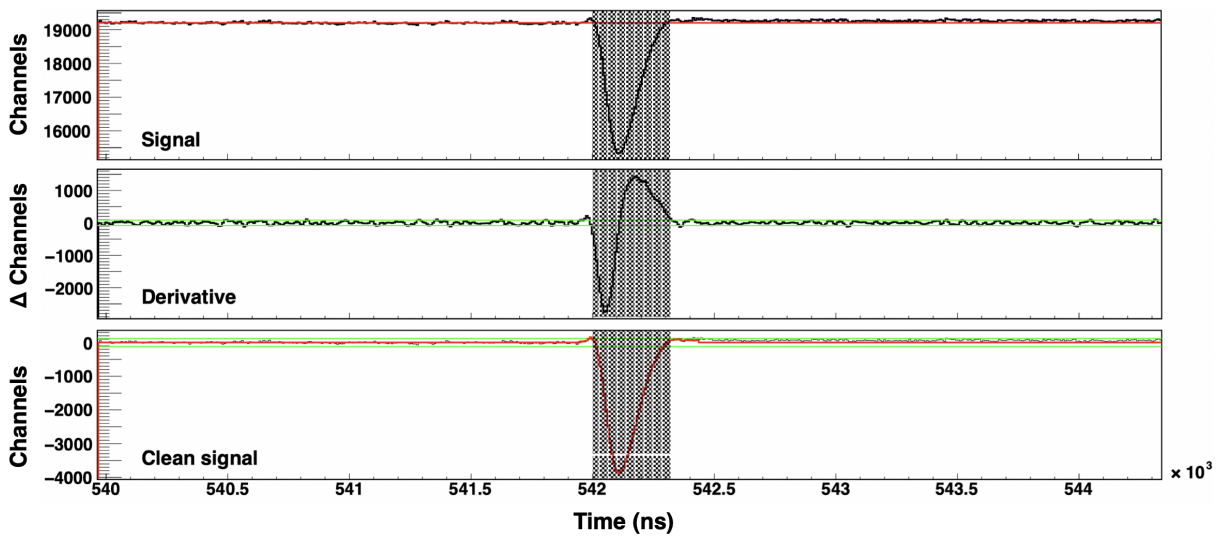

Figure 2.4: The PSA routine calculates the derivative (middle panel) of the signal (top panel) to recognize the clean signal (bottom panel).

2.1.3 Angular distributions

In the case of the Micromegas detectors, the feature of choosing between different pulse shapes can prove to be extremely useful. This is a result of the way the fission fragment signals are created. When a fission event occurs, two fission fragments are produced, travelling to opposite directions due to the kinematics of the reaction. Due to the geometry of the Micromegas detector, one of the two fission fragments

enters the detector gas and is detected. However, the angle in which the fission fragment enters the drift region results in slightly different pulse shapes, as seen in figure 2.5. When a fission fragment enters at 0° with respect to the neutron beam, the secondary electrons created move towards the mesh and enter the amplification region at different times, because of the different distance each electron has to travel to reach the mesh. This difference in arrival times at the mesh, leads to higher risetimes in comparison to a fission fragment entering the Micromegas detector with an angle of 90° with respect to the neutron beam. In this case the fission fragment creates electrons in its path parallel to the drift electrode. The electrons begin their path towards the mesh almost simultaneously, arriving at the mesh electrode approximately at the same time. As a result, the creation of the signal in the amplification region lasts for a shorter time, leading to smaller risetimes.

Another interesting aspect of the pulse shapes, as seen in figure 2.5, is a small bump of positive polarity observed prior to the pulse itself for higher amplitude pulses. The origin of the pulse can be attributed to the movement of the electrons in the drift region, which create through induction a signal in the mesh electrode. It is observed at higher amplitude pulses, which are coupled with smaller risetimes. The reason for this is the path and the direction of the fission fragments travelling inside the gas of the detector. A fission fragment will not deposit its entire energy inside the detector, but a portion of its energy depending on its path across the gas. When a fission fragment enters the detector at 0°, a path of 6 mm is available for the fission fragment to travel inside the detector and deposit the corresponding energy. This path can be higher in the direction of 90°, where in the extreme case (when a fission fragment is created in one side of the target and moves towards the detector) is approximately 8.75 cm (in this experiment). The higher energy deposited in this direction in combination with the faster signal makes it possible to see the induction from the movement of the electrons in the drift region, which is otherwise lost in the background.

Taking into account the different pulse shapes, which represent the various emission angles of the fission fragments in the detector gas, a qualitative estimation of the angular distribution of the fission fragments can be made. This can be achieved by providing different pulse shapes to the PSA routine. The routine selects the most suitable pulse shape for each case. In order to get an estimation for the angular distribution of each target the ratio of the extreme cases, the pulses with the low risetimes versus the pulses with the high risetimes corresponding to angles around 90° and 0° degrees respectively, is plotted with respect to the neutron energies. However, it is important to note that this is not an absolute measurement of the angular distribution, but only an indication of the trend with respect to the neutron energy.

The methodology is validated via the comparison of the angular distributions estimated in the present work for the ^{235}U(n,f) reaction with previous measurements. As seen in figure 2.6a the angular distributions estimated in the present work are in general consistent in the shape with the previous measurements, as seen in figure 2.6b. More specifically, the ratio from the present work is in good agreement with the shape of previous measurements up to approximately 20 MeV. At higher energies the ratio of the present work is found to be a bit higher than the previous

measurements. The worst reproduction of the higher energy region could be explained in the difficulties occurring in the analysis of the data in the region. The closer in time to the γ-flash a pulse is recorded the worse the recognition of the pulse is, due to the worse reproduction of the baseline at higher energies. So, it is expected to have worse recognition of the pulse shapes in the region. However, it is important to note that the qualitative estimation of the angular distributions is quite good with the method described, since it manages to give a good indication for the angular distribution shape. This information, although not an absolute measurement, can be extremely useful for the planning of new experiments to measure the angular distribution of fission fragments, which have not been measured before.

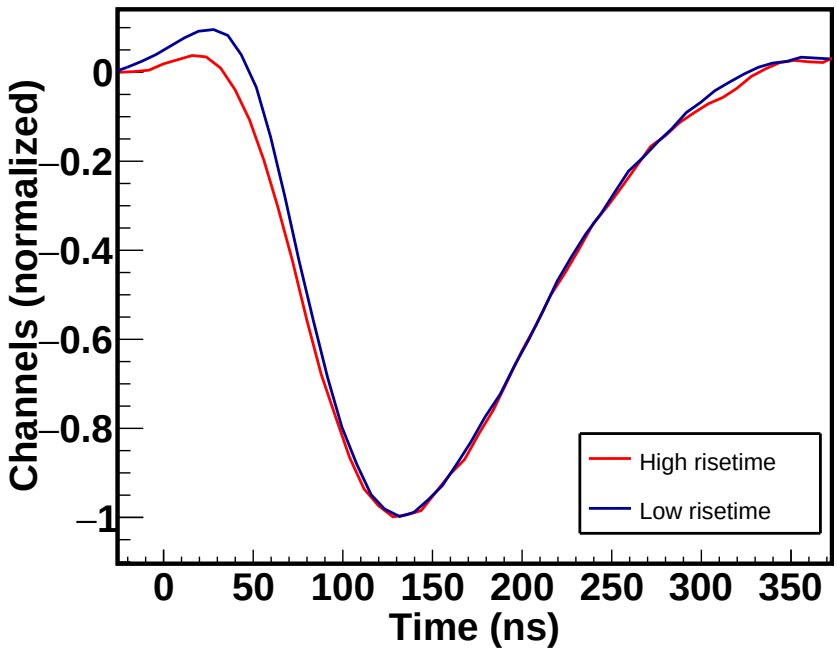

Figure 2.5: Different pulse shapes of the same Micromegas detector.

Concerning the ^{230}Th(n,f), the angular distribution results are presented in the two subplots of figure 2.7. In the top plot the results in the vicinity of the resonance are shown, while in the bottom plot the angular distribution of higher energies is presented. As seen in figure 2.7a, a structure appears in the region of the ^{230}Th resonance at $\sim$700 keV. In addition, a structure is present in the region of the second chance fission of ^{230}Th, as seen in figure 2.7b. As a result, the angular distribution of the ^{230}Th(n,f) reaction seems to present interesting components in this qualitative approach. A measurement dedicated to the study of the angular distribution of the ^{230}Th(n,f) reaction could be important, in order to reveal the structures in the angular distribution.

It is important to note that a similar behavior is observed in all ^{230}Th targets, when normalized to each other. This can be seen in figure 2.8, where all targets are in very good agreement with each other up to $\sim$60 MeV. At higher energies ^{230}Th #7 appears to have larger values, while the other targets appear to show the same trend. The difference of the ^{230}Th #7 is not clear, but it could be attributed to potentially worse resolution of this detector. However, it is important to note that the general trend of

the angular distribution shape is still reproduced by ^{230}Th #7 having an increase in the second chance fission peak.

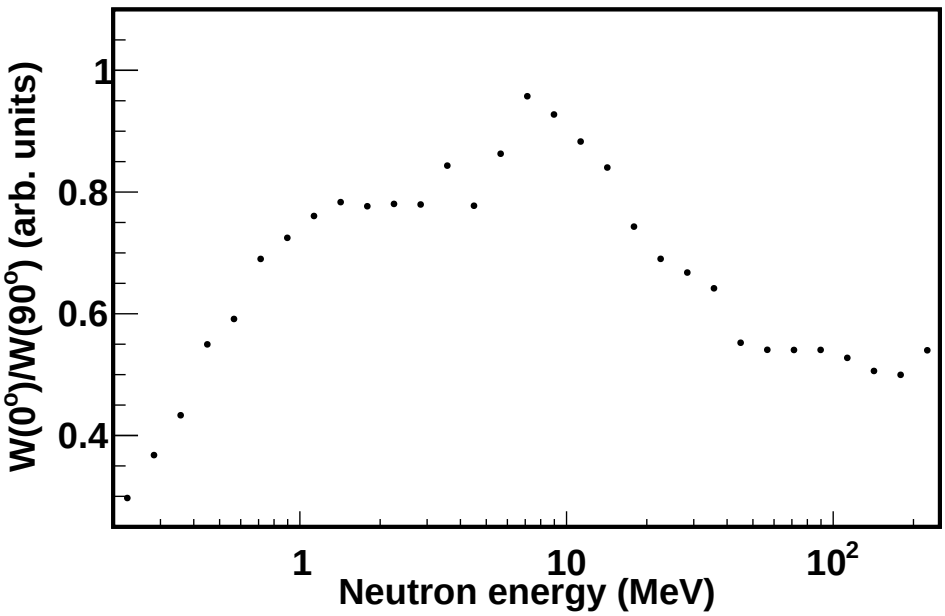

(a) Present work

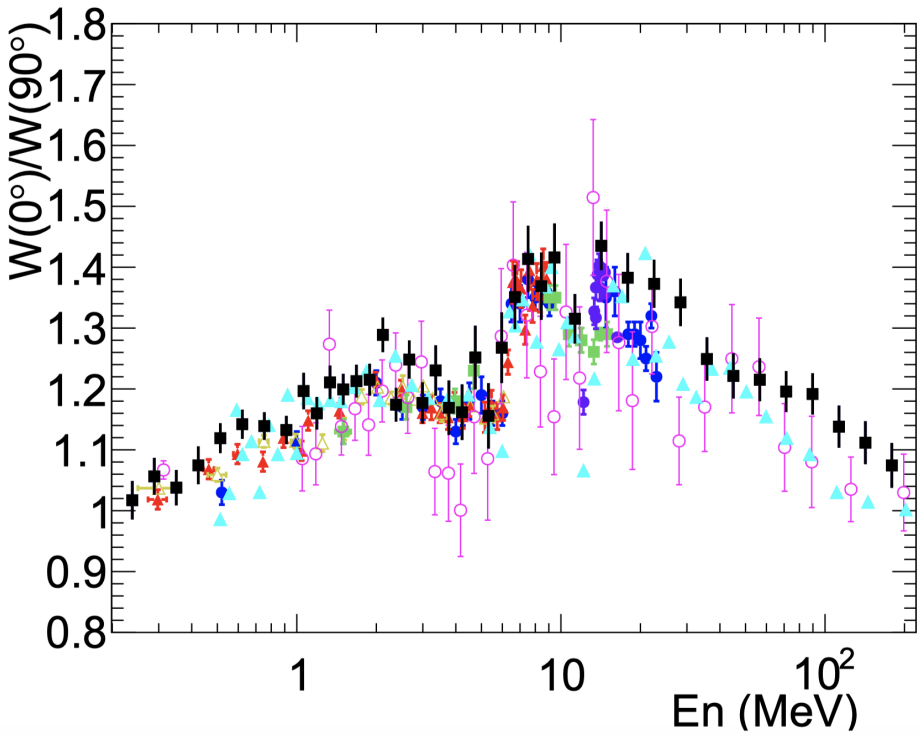

(b) Previous measurements [68]

Figure 2.6: Angular distribution of the ^{235}U target from the EAR-1 measurement. In the top plot the angular distribution of the present work is presented in arbitrary units, while in the second plot the angular distribution measurements from [23], presented in absolute units.

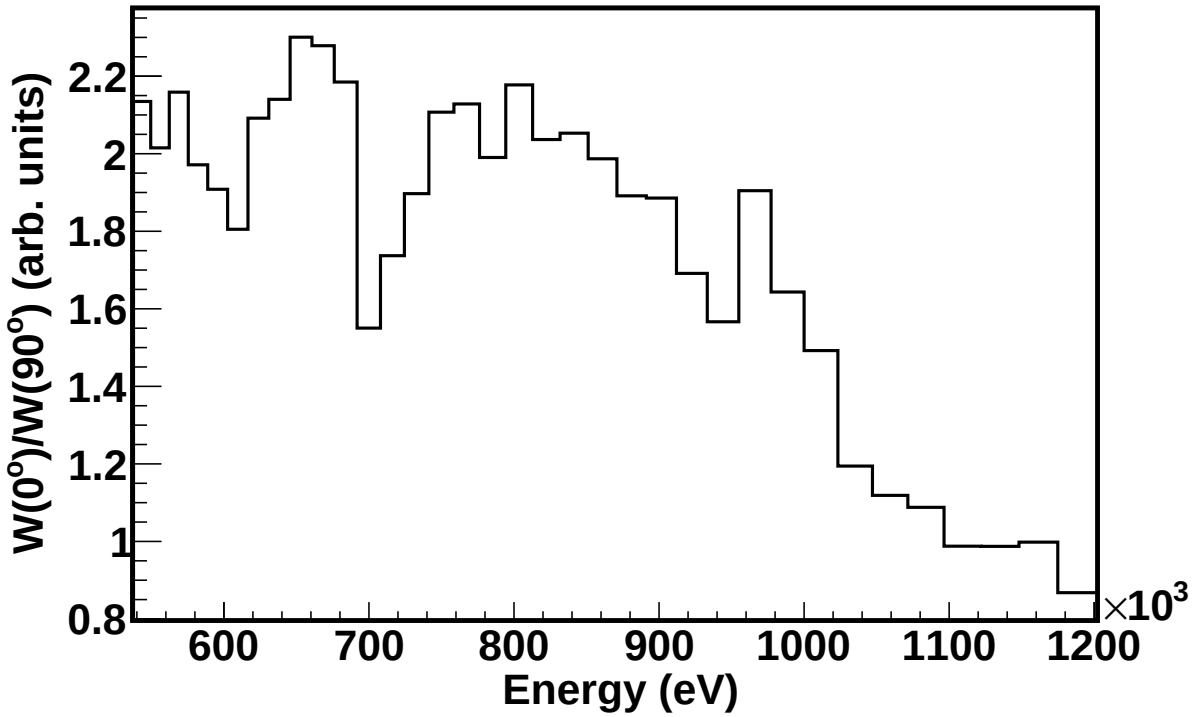

(a) Low energy region

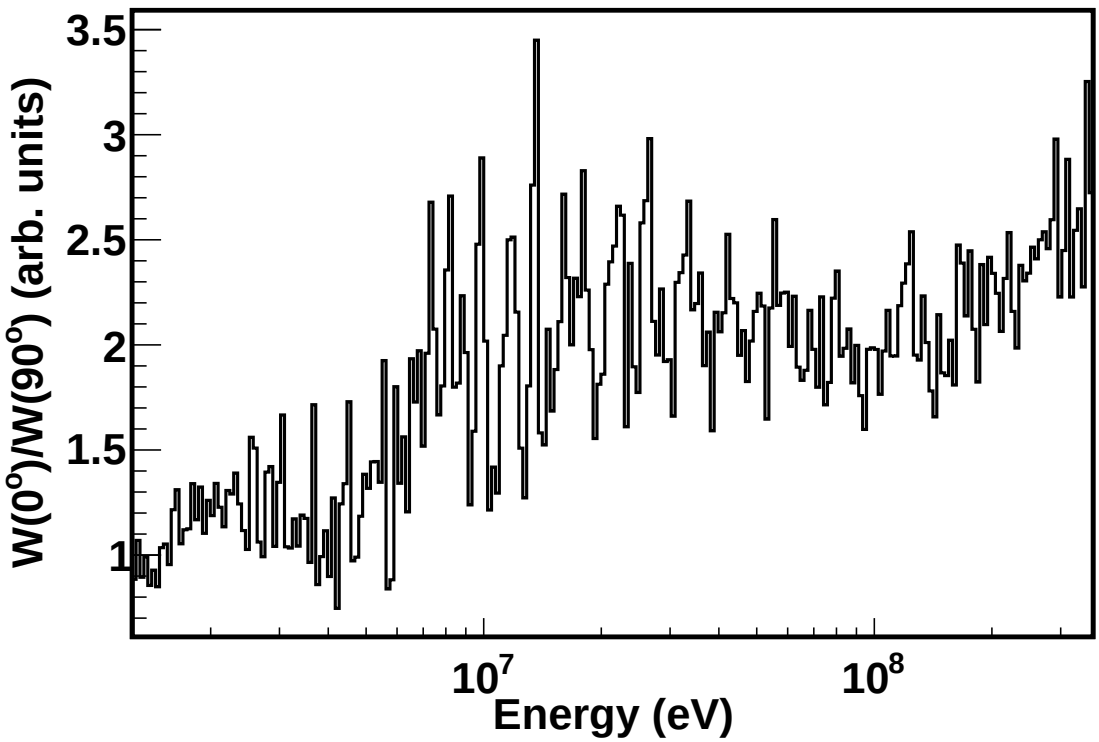

(b) High energy region

Figure 2.7: Angular distribution of the ^{230}Th target from the EAR-1 measurement, in arbitrary units. In the top plot the angular distribution in the vicinity of the resonance is shown, while in the second plot the angular distribution of the higher energy region is presented.

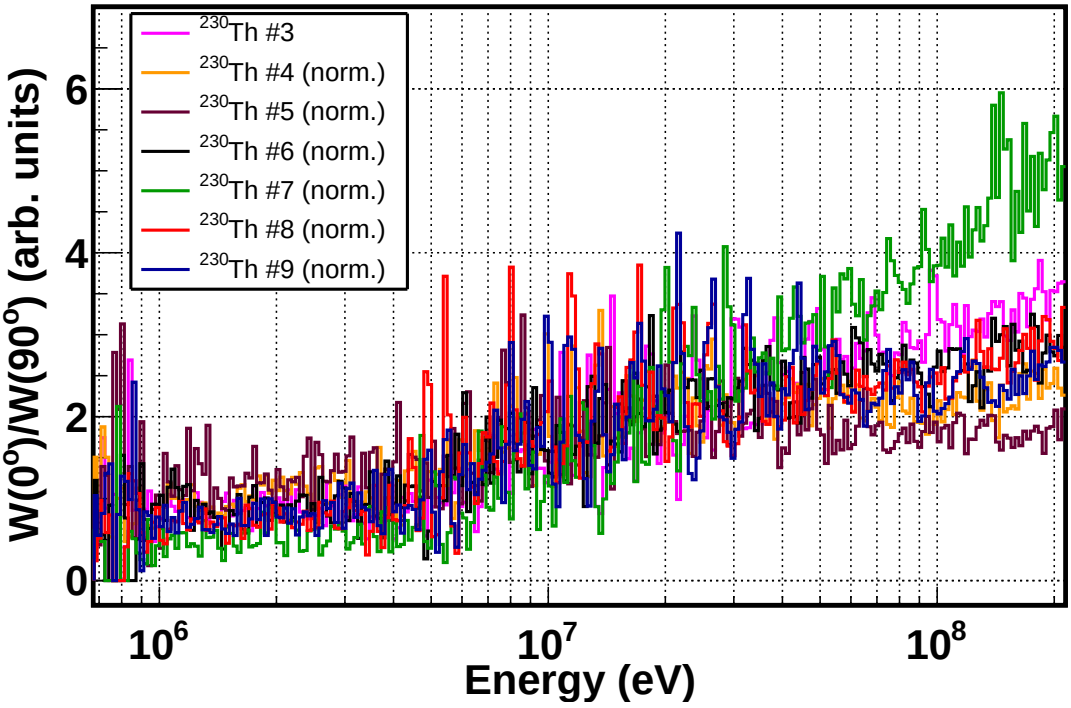

Figure 2.8: Angular distributions for all ^{230}Th targets from the EAR-1 measurement, normalized to ^{230}Th #3. The units in the y-axis are arbitrary.

Only a few measurements for the angular distribution of the ^{230}Th(n,f) reaction data exist in the Experimental Nuclear Reaction Data Library EXFOR [3]. The oldest data are from Simmons and Henkel in 1960 [69], covering the energy range from 1 to 9 MeV. The rest of the existing data cover narrower energy ranges in the region of the resonance. Specifically, the data of Yuen *et al.* [70] are in the energy region 0.68 to 1 MeV, the data of James *et al.* [30] are in the energy region 0.7 to 0.95 MeV and the data of Boldeman and Walsh [28] in the energy range from 0.68 to 0.78 MeV. The data of Simmons and Henkel are the only ones in a wide energy range. Thus, the angular distributions from the present work are compared only to these data, which are presented in figure 2.9.

A similar behavior in the angular distributions shape is observed between the data from the present work and the data of Simmons and Henkel. More specifically, an increase in the $W(0^o)/W(90^o)$ ratio is observed in both datasets at $\sim$2 MeV, which decreases smoothly to a minimum at $\sim$4 MeV and arrives again to a maximum value at $\sim$7 MeV.

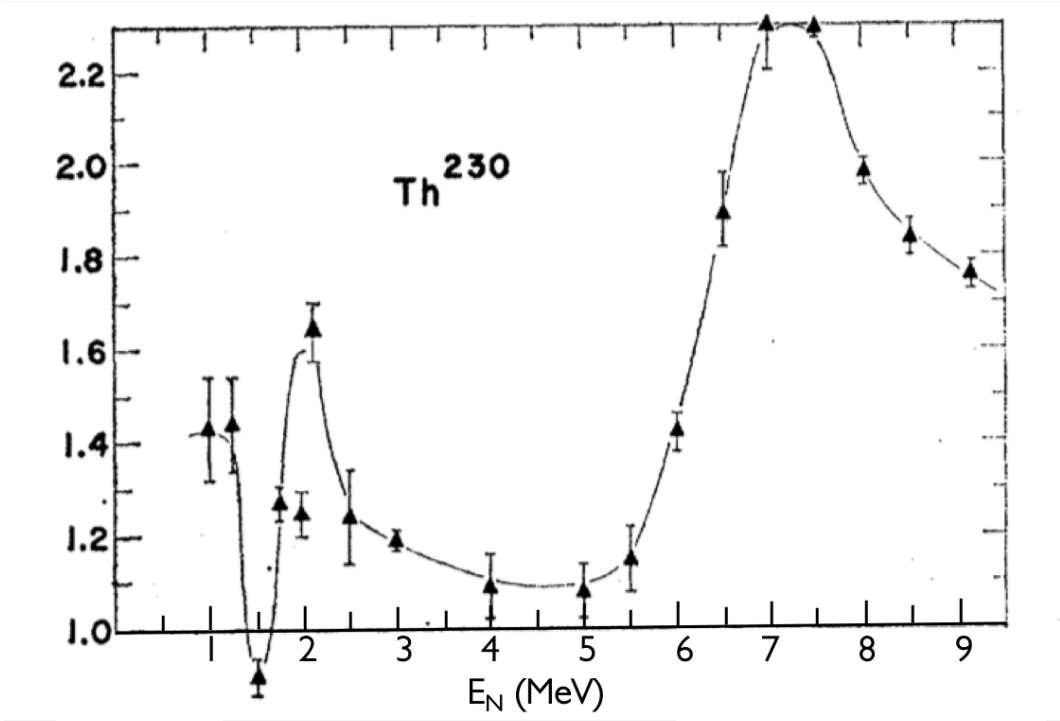

Figure 2.9: Angular distribution for ^{230}Th from Simmons and Henkel [69].

2.2 Data quality checks and data selection

The pulse shape analysis procedure, where a first selection of fission events is made, is followed by additional data quality checks and data selection. Various parameters of the recognized pulses are checked, in order to validate that the pulses correspond to fission events, the arrival time of the γ-flash is estimated correctly etc. Additional cuts are applied to the recognized signals in order to reject noise, bad runs etc. The offline analysis of the experimental data is carried out using ROOT [19].

2.2.1 Detector stability

An important check is the verification of the detector stability, in order to be sure that the gain of the detectors remains constant throughout the measurements. This is achieved by taking beam-off spectra during the measurements, where the data are recorded in bunches, while the trigger for the acquisition is given externally and independent from the beam trigger. In the beam-off spectra the fission fragment signals are absent since there is no beam and only the alpha signals from the radioactivity of the targets are recorded. In figure 2.10 two beam-off spectra are depicted, one from the beginning and one from the end of the measurement in EAR-1, normalized to the number of bunches, for one of the ^{230}Th samples. As seen in the figure the gain of the detector is stable, since the end of the alpha signals is in the same channel for both spectra. The stability of all detectors in both EAR-1 and EAR-2 measurements was checked in the same way and no gain shift was observed.

An additional information from the beam-off spectra in figure 2.10 is the channel where the alpha signals end. Pulses from the beam-on spectra with amplitude lower

than the alpha signals are excluded from the analysis even though they might correspond to fission events. This way it is ensured that no alpha signals are counted as fission events, but the low energy fission fragment signals are lost. The estimation of the lost fission fragments is achieved via Monte Carlo simulations, as described in section 2.3.4.

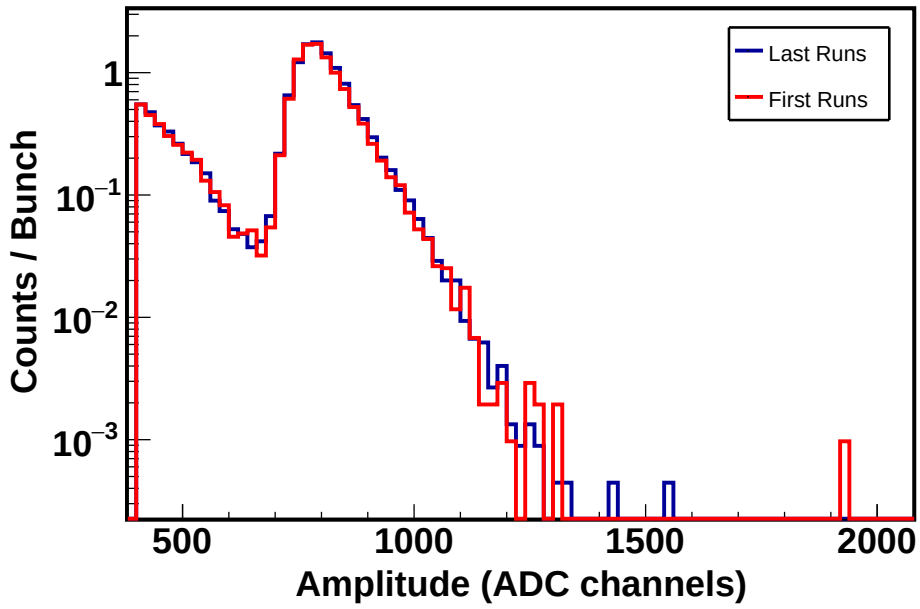

Figure 2.10: Beam-off spectra from the beginning (red line) and end (blue line) of the EAR-1 measurement for one of the ^{230}Th targets. The stability of the detector is verified, since no gain shift is observed between the two spectra.

2.2.2 γ-flash arrival

The accurate recognition of the γ-flash is a crucial step in the analysis procedure, since the time-of-flight of each fission event is estimated relative to the γ-flash arrival. In the pulse shape analysis routine the γ-flash is identified as the first peak that crosses a specific threshold and has a width larger than a user-defined value. Special attention has to be given to false recognition of the γ-flash, related to proton pre-pulses from the PS. These pre-pulses generate neutrons, which can cause a fission event in one or more targets. The fission signal can sometimes be falsely identified as the γ-flash resulting in wrong timing. In the movies where the arrival time in one of the detectors is outside the narrow peak expected, the whole event is discarded. The distributions of the arrival times of the γ-flash for one of the ^{230}Th targets at the EAR-1 measurement are shown in figure 2.11. As seen in the figure two distributions are observed, corresponding to the difference arrival times of the γ-flash for the dedicated (red distribution) and the parasitic (blue distribution) pulses respectively. The difference in the arrival times does not affect the timing of the fission fragment pulses, since it is estimated relative to the arrival of the γ-flash on a bunch-by-bunch basis.

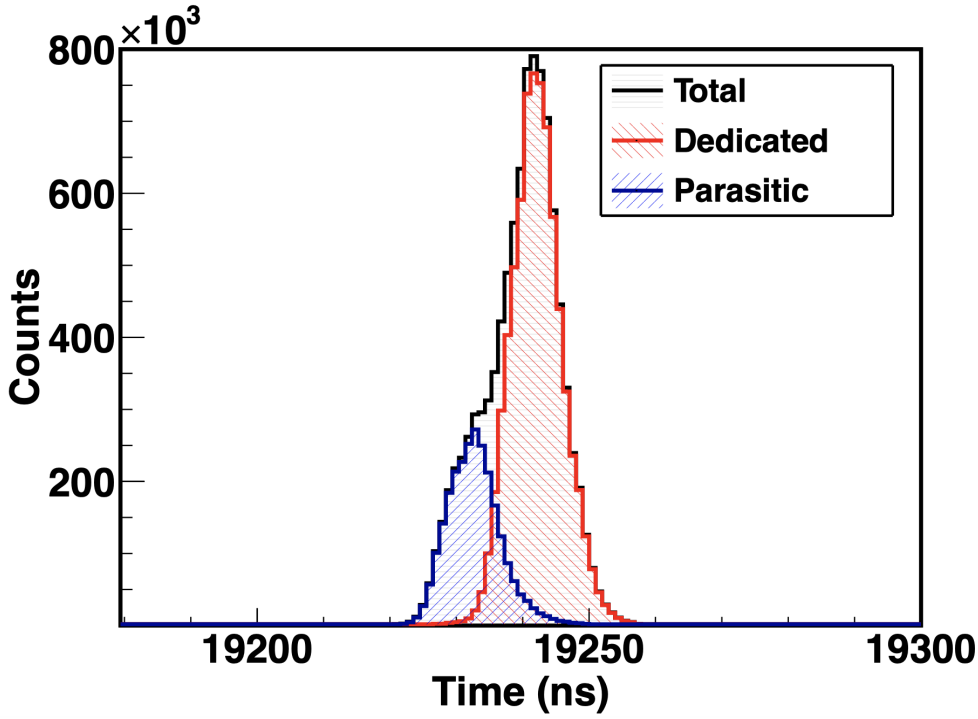

Figure 2.11: Distributions of the arrival time of the γ-flash for the total (black), dedicated (red) and parasitic (blue) pulses.

2.2.3 Noise rejection

In some cases noise is recorded in the movie and can be falsely recognized as a pulse. The noise is rejected in two steps, firstly in the pulse shape analysis routine and secondly in the offline analysis. In the first step various constrains are applied to the recognition of the pulses (area to amplitude, fwhm etc.) in order to avoid recording the noise as a pulse. Nevertheless, still noise signals are recognized as fission pulses. In the offline analysis, additional cuts are applied to the recognized pulses, in order to reject the remaining noise ones. Specifically, if a saturated pulse and/or a pulse with very high amplitude (much higher than the amplitude expected for fission fragments) is observed in one of the detectors, the whole event is discarded for all detectors. An example of noise recorded in the signal for two of the detectors simultaneously is seen in figure 2.12. It is interesting to note that in many cases noise is recorded simultaneously in all detectors. This can be used as an advantage in noise rejection, because even if noise is recognized as true pulses from one of the detectors if the noise is recognized in one of the other 9 detectors the whole event is discarded.

Another cause for noise recognition as pulse in the high energy region, is the γ-flash residuals as mentioned in section 2.1.1. This can be clearly seen in figure 2.13, where the amplitude of the pulses recognized is plotted as a function of the neutron energy for the ^{235}U target of the EAR-1 measurement. In the low energy region low amplitude pulses are detected, which correspond to the natural radioactivity of the targets. At higher energies the rate of the pulses from the radioactivity of the targets per energy bin is decreasing, since each energy bin corresponds to smaller time intervals. On the other hand, the residuals from the γ-flash increase at higher

energies, because at smaller time-of-flights the description of the γ-flash is worse, as already seen in section 2.1.1.

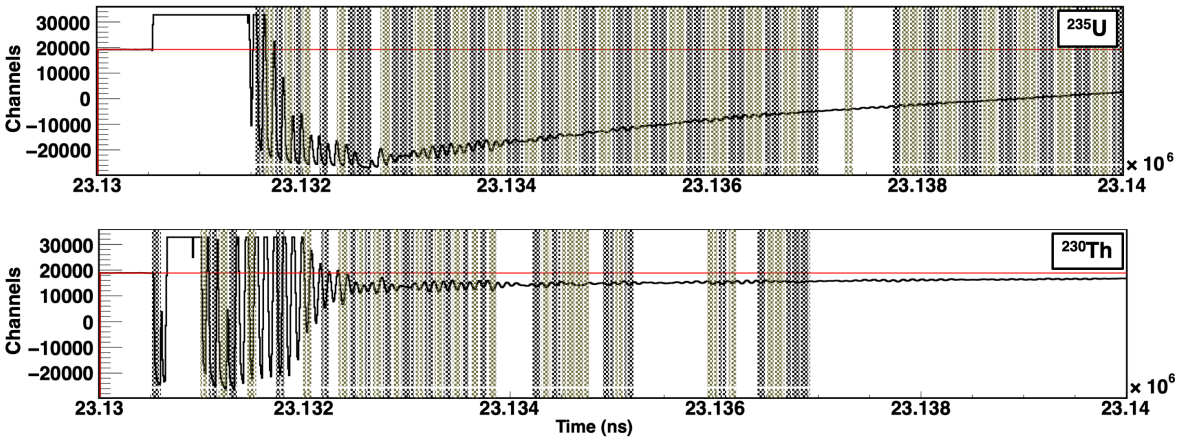

Figure 2.12: Noise recorded in the signal simultaneously in two of the detectors.

In order to treat this increase in the noise at higher neutron energies the amplitude cut applied to the pulses is increased in order to reject the additional noise. The amplitude cut applied in two different energy regions is shown in figure 2.14, for the ^{235}U (figure 2.14a), ^{230}Th #3 (2.14b) and ^{238}U (figure 2.14c) targets. The amplitude spectra from lower energies are shown in blue and at higher energies in red, respectively. The blue and red dashed lines represent the amplitude cut applied in the lower and in the higher energy region, respectively. The spectra from each target are normalized to the integral of the lowest count spectrum for visualization purposes. As seen in the figures, with the use of a lower amplitude cut a rejection of the alpha particles originating from the radioactivity of the samples for low energies is achieved. At higher energies a higher amplitude cut is implemented in order to reject the additional noise recorded. Regarding the ^{238}U target, an additional amplitude spectrum is depicted in the figure in green. As seen in the figure, this high energy spectrum is distorted in shape, preventing this way to reach energies higher than 160 MeV. This can be explained by the lower mesh voltage applied in the Micromegas detector of ^{238}U, in order to avoid the saturation of the γ-flash, at the cost of having lower amplitude pulses. This worst response of the ^{238}U target to the γ-flash can be attributed to the thickness of this target leading to higher counting rates at the higher energy region. The pulses of lower amplitude do not affect the analysis of the lower energies, but for higher energies where the effects of the γ-flash are significant, the recognition becomes challenging.

In order to validate whether the higher amplitude cut applied alters the results, an additional check is implemented. The analysis is performed with two different amplitude cuts (the lower one used in the analysis and the highest one). Up to a certain energy, the results are expected to differ by a scaling factor, due to the different portion of the amplitude spectra being counted as fission fragments. With the increase in energy, noise is added in the signal, resulting in deviations between the spectra with different amplitude cuts. This can be seen in figure 2.15. The agreement between the counting spectra of the ^{235}U, the ^{230}Th #3 and the ^{238}U targets confirms that a higher amplitude cut does not alter the analysis, as long as the lost counts

are accounted for. The deviation at higher energies, shows the necessity of a higher amplitude cut at higher energies to reject the additional noise. The method used for the amplitude cut correction is presented in section 2.3.4.

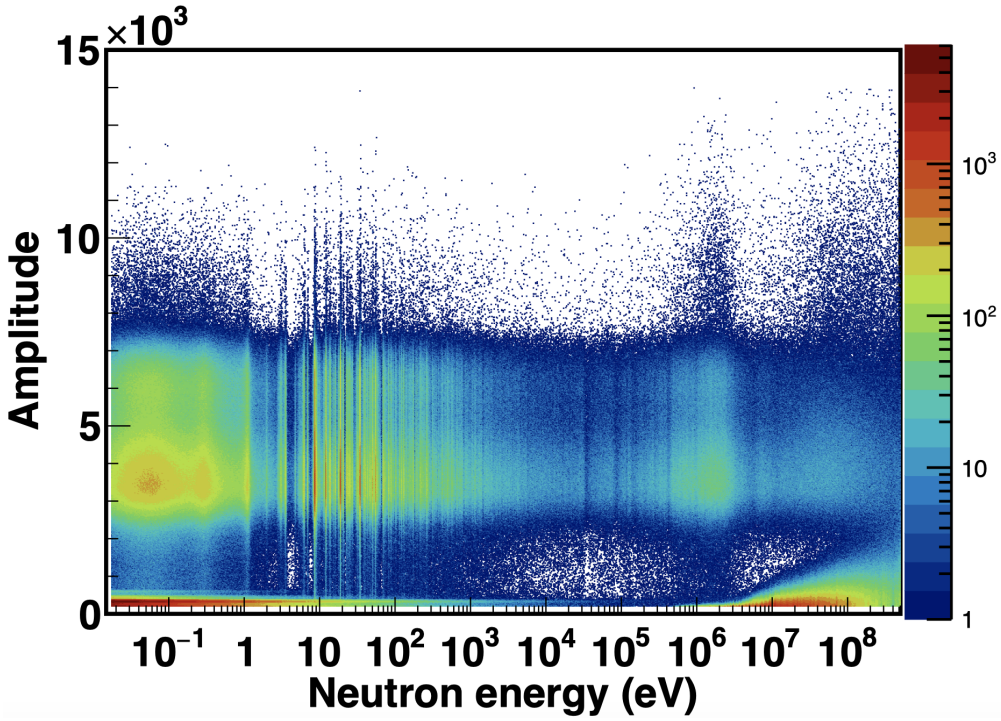

(a) Full scale

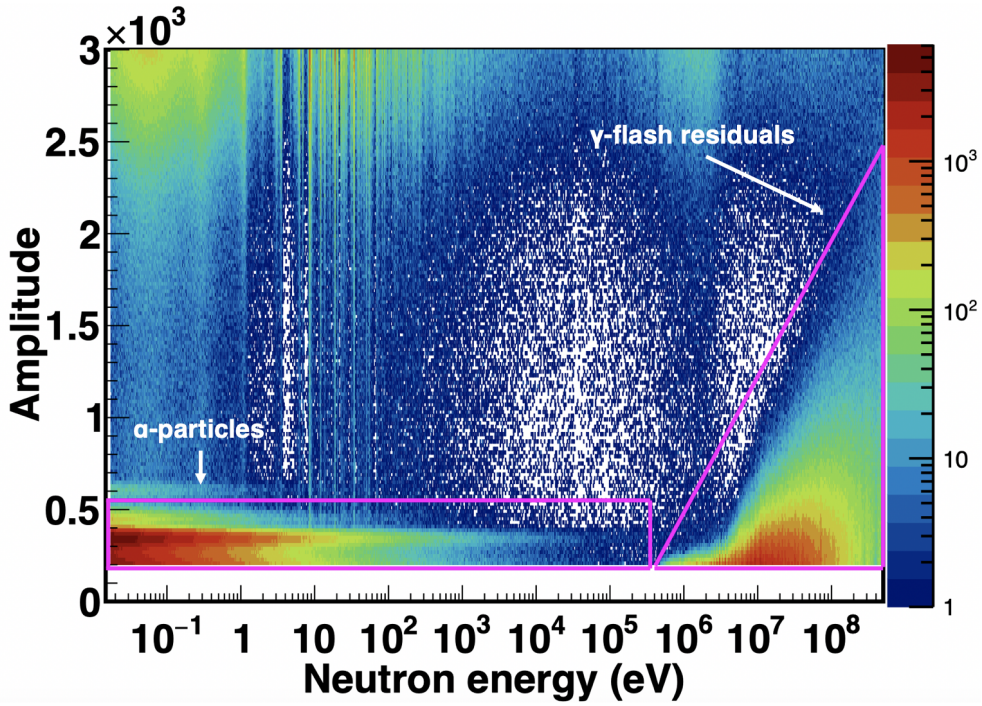

(b) Amplitude (y-scale) zoom

Figure 2.13: Distribution of the amplitude of the signals as a function of the neutron energy for the ^{235}U target of EAR-1 in (a) full scale and (b) focusing on the smaller amplitudes. The a-particles from the natural radioactivity of the target are present in the low energy region and the γ-flash residuals, increasing with energy, are present in the high energy region.

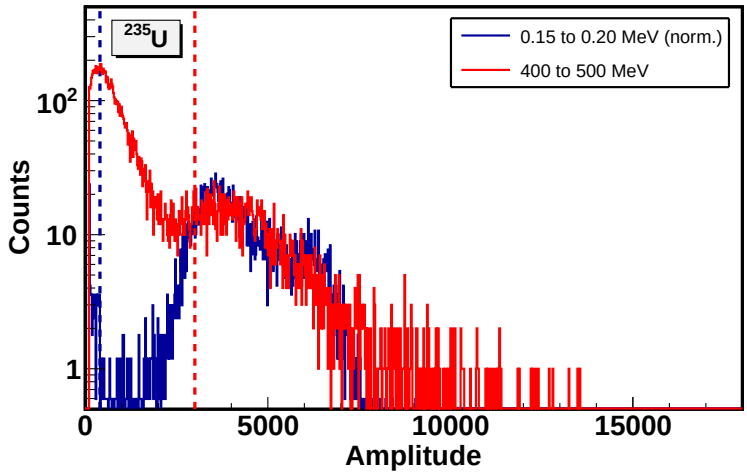

(a) Amplitude spectra for the ^{235}U target of the EAR-1 measurement.

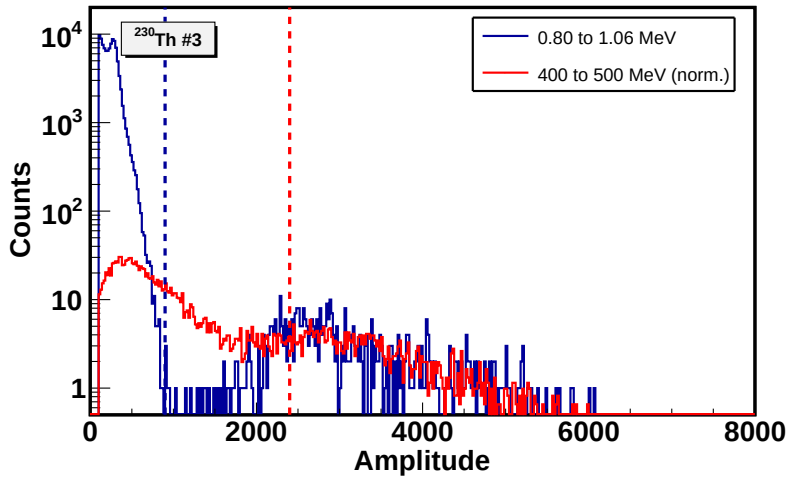

(b) Amplitude spectra for the ^{230}Th target of the EAR-1 measurement.

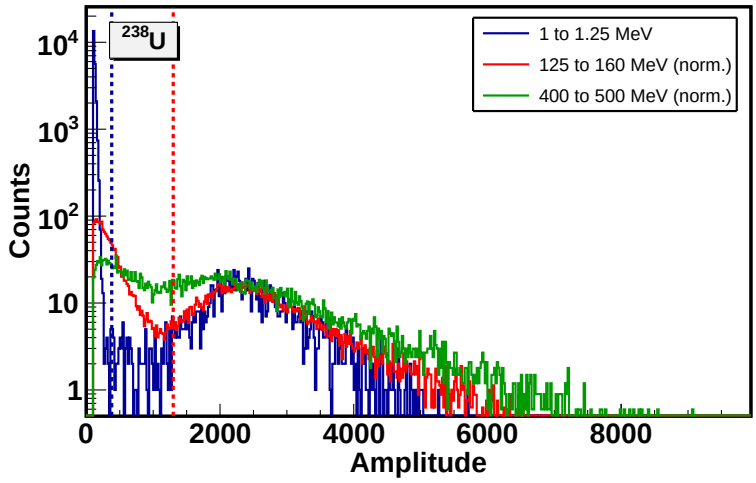

(c) Amplitude spectra for the ^{238}U target of the EAR-1 measurement.

Figure 2.14: Amplitude spectra at different energy regions for the ^{235}U (a) ^{230}Th #3 (b) and ^{238}U (c) targets. The blue dashed line represents the lower amplitude cut implemented in the analysis, for the rejection of the alpha particles. The red dashed line represents the high amplitude cut implemented in the analysis, in order to reject the additional noise at higher energies. For the ^{238}U target an additional amplitude spectrum is shown (green line) to demonstrate the distortion of the amplitude spectra at higher energies.

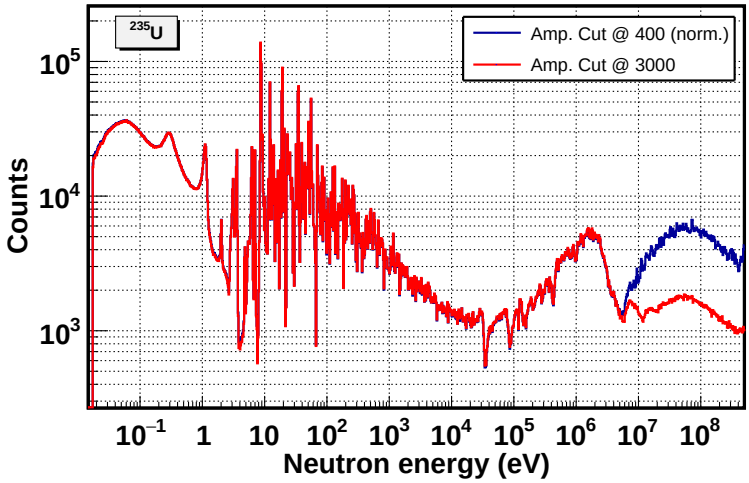

(a) Counting spectra for the ^{235}U target of the EAR-1 measurement.

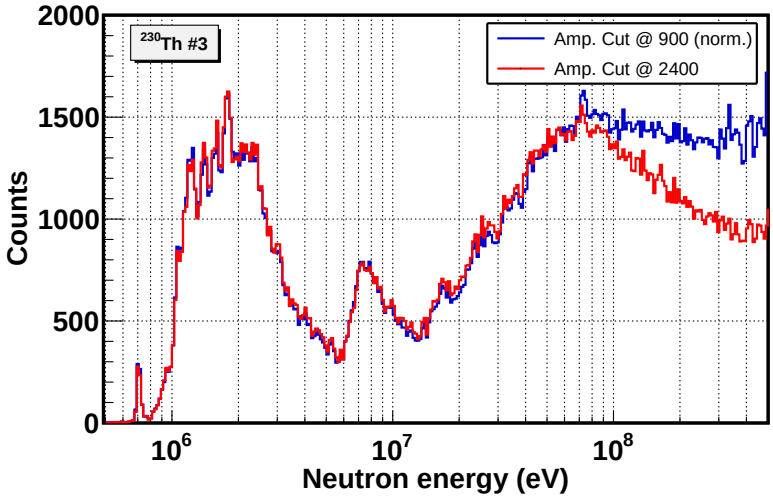

(b) Counting spectra for the ^{230}Th target of the EAR-1 measurement.

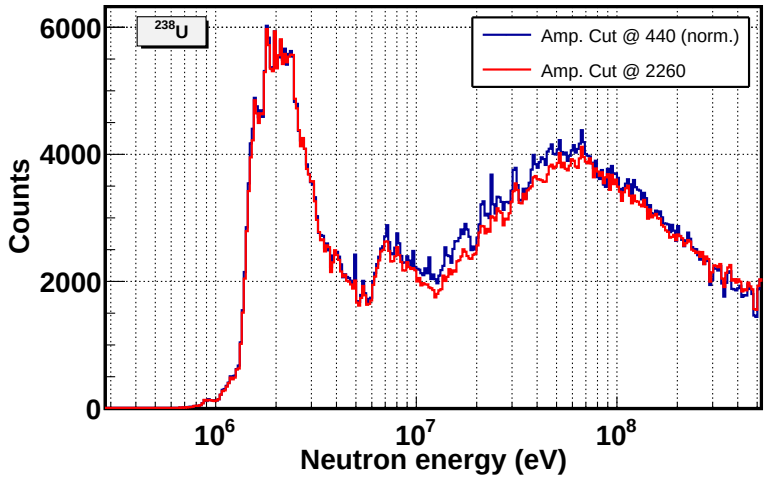

(c) Counting spectra for the ^{238}U target of the EAR-1 measurement.

Figure 2.15: Counting spectra obtained with different amplitude cuts, a low one (blue line) and a higher one (red line) for the ^{235}U (a) the ^{230}Th (b) and the ^{238}U (c) targets of the EAR-1 measurement. The counts are normalized in the low energy region of each target.

2.2.4 Dedicated and parasitic pulses

Two types of pulse bunch exist in the n_TOF facility at CERN, the dedicated ones corresponding to the nominal intensity of the proton bunch and the parasitic corresponding to a low intensity (approximately half of the nominal). An additional important quality check of the data is the agreement between dedicated and parasitic pulses, when normalized to the number of protons. This way, the data analysis methodology is validated, confirming that the various steps of the analysis procedure, such as the γ-flash subtraction, the dead time correction etc. is performed in a consistent way for both pulse modes.

Concerning the EAR-1 measurement the comparison between the counts normalized to the number of protons between the dedicated and the parasitic pulses is presented in figure 2.16. Specifically, in figure 2.16a the comparison between the two pulses modes is presented for the ^{235}U target. It is observed that in the low energy region the counts from the dedicated pulses are higher than the parasitic ones. This is also observed in other measurements of n_TOF Phase-III, which indicates a slightly different neutron beam flux in the low energy region between dedicated and parasitic pulses. For energies higher than $\sim$ 1 keV the agreement between dedicated and parasitic pulses is very good, indicating that the analysis procedure is equivalent for both pulse modes and no significant dead time is observed for the ^{235}U target. Concerning the ^{230}Th #3, as seen in figure 2.16b, the comparison between the counts from dedicated and parasitic pulses is very good for the whole energy region. At energies higher that $\sim$ 300 MeV the normalized counts of the parasitic pulses are slightly higher than the dedicated ones, indicating counting losses due to pile-up, which are accounted for, as presented in section 2.3.1. Regarding the ^{238}U target, as seen in figure 2.16c, for energies up to $\sim$ 50 MeV the counts from the parasitic pulses are in very good agreement with the counts from the dedicated ones. For higher energies the counts from the parasitic pulses are higher than the dedicated ones, while this difference is increasing with the neutron energy. The cause behind this deviation is again counting losses due to pile-up. The corrections regarding these counting losses are presented in section 2.3.1.

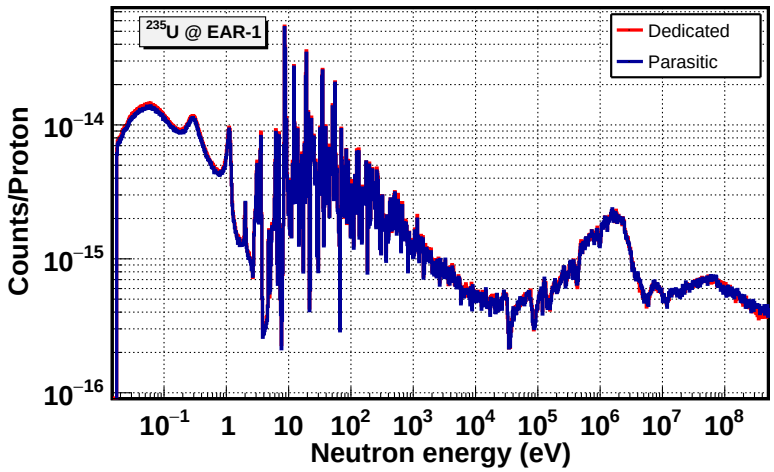

(a) ^{235}U target of the EAR-1 measurement

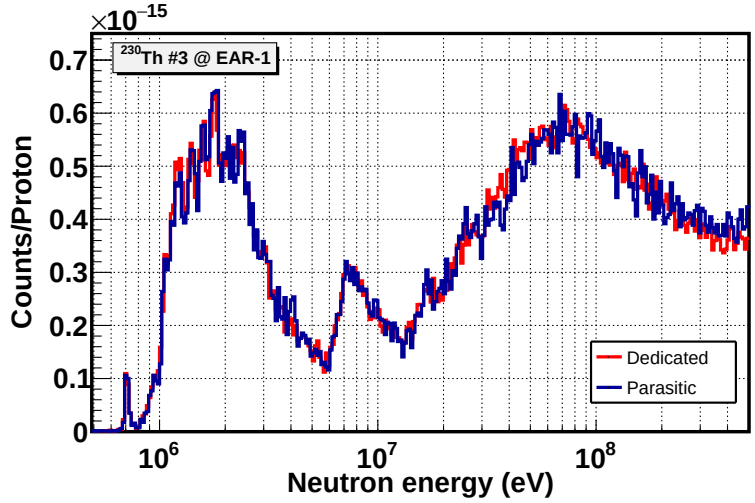

(b) ^{230}Th #3 target of the EAR-1 measurement

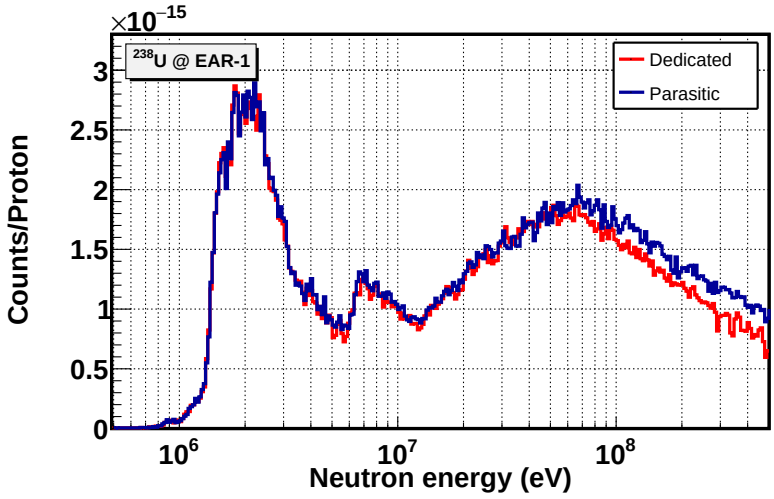

(c) ^{238}U target of the EAR-1 measurement

Figure 2.16: Comparison of the dedicated (red line) and the parasitic (blue line) counts normalized to the number of protons for the EAR-1 measurement.

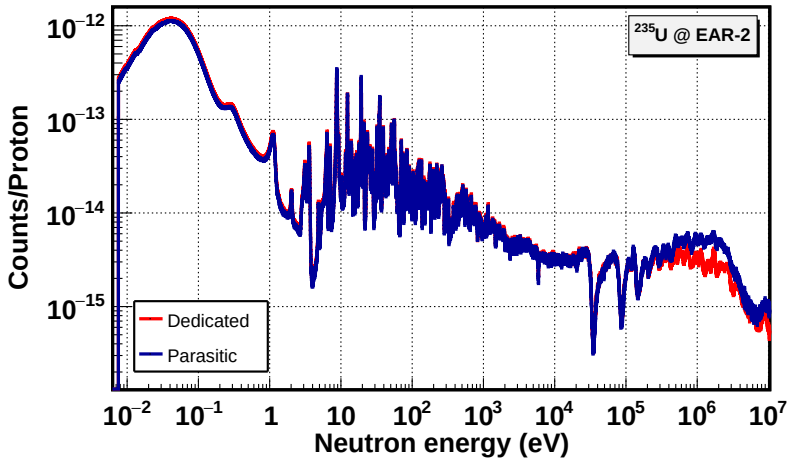

(a) ^{235}U target of the EAR-2 measurement

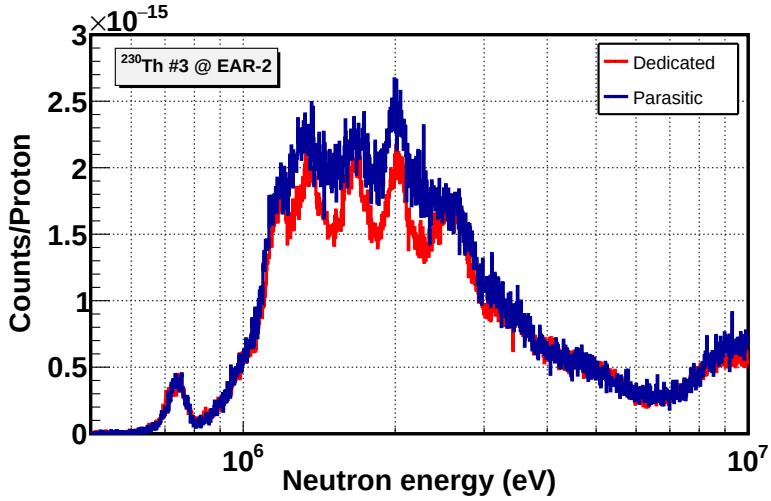

(b) ^{230}Th #3 target of the EAR-2 measurement

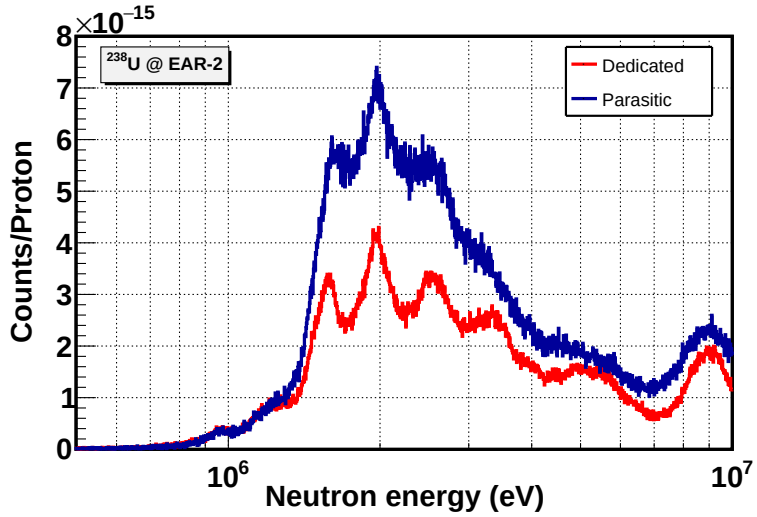

(c) ^{238}U target of the EAR-2 measurement

Figure 2.17: Comparison of the dedicated (red line) and the parasitic (blue line) counts normalized to the number of protons for the EAR-2 measurement.

The comparison between the dedicated and the parasitic pulses normalized to the number of protons for the EAR-2 measurement is shown in figure 2.17. As seen in the figure many deviations are observed between the dedicated and the parasitic pulses for all targets. The reason behind this effect is severe counting losses due to high counting rates. This was expected prior to the experiment since the masses of all the targets were optimized for the EAR-1 measurement. The expectation from the EAR-2 measurement was aiming for the energy region below the fission threshold of ^{230}Th, where no data exist in literature and the cross-section is expected to be very low. However, as it will be discussed in section 2.3.2, the contamination of Pu isotopes in the targets was strong enough, to prevent from distinguishing counts originating from the ^{230}Th(n,f) reaction. Regarding the ^{235}U target, as seen in figure 2.17a the deviation between dedicated and parasitic pulses starts at $\sim$ 300 keV, which is a lower energy than the ^{230}Th fission threshold. As a result, since - as shown in section 2.3.1 - it is not possible to correct for these high counting losses, there is no overlapping region where both the ^{235}U target and the ^{230}Th targets have useful counts in the EAR-2 measurement. For the ^{230}Th #3 target differences are seen between the dedicated and the parasitic pulses in the energy region 1 to 3 MeV. Similar results are observed in all ^{230}Th samples, except for the two targets having a lower mass (namely ^{230}Th #5 and #6) where no disagreement is observed between the two pulse modes. Concerning the ^{238}U target, the agreement between the counts of the dedicated and the parasitic pulses is up to $\sim$ 1.2 MeV. For higher energies large deviations are observed in the counts of the two pulse modes, due to the high counting rates in this energy region. As a result, in the EAR-2 measurement, cross-section results for ^{230}Th using the ^{238}U(n,f) reaction is achieved only up to 1.2 MeV.

2.2.5 Comparison of ^{230}Th targets

The last quality check on the data is the comparison of counts of the ^{230}Th targets, normalized to the energy region 1 - 5 MeV. The comparison is presented in figure 2.18 in two subplots, with only the statistical uncertainties depicted in the plots. At the top figure the comparison of the counts of all ^{230}Th targets is presented in 50 bpd from the fission threshold up to 20 MeV. The higher energy region is shown in the bottom plot of the figure in 10 bpd up to 500 MeV.

As seen in figure 2.18a, very good agreement is achieved between all seven ^{230}Th targets. It is important to note that no systematic deviation is observed between them. At higher energies the dispersion between the ^{230}Th targets is higher, but again no systematic uncertainty is observed between the targets. These higher differences at higher energies are a result of the complexity of the analysis at the high energy region and leads to a higher uncertainty in the final results obtained there. The maximum difference of the mean value between the ^{230}Th targets up to 400 MeV is lower than 10%. At energies higher than 400 MeV the differences between the ^{230}Th targets are increasing, indicating that the analysis may not be reliable in this region.

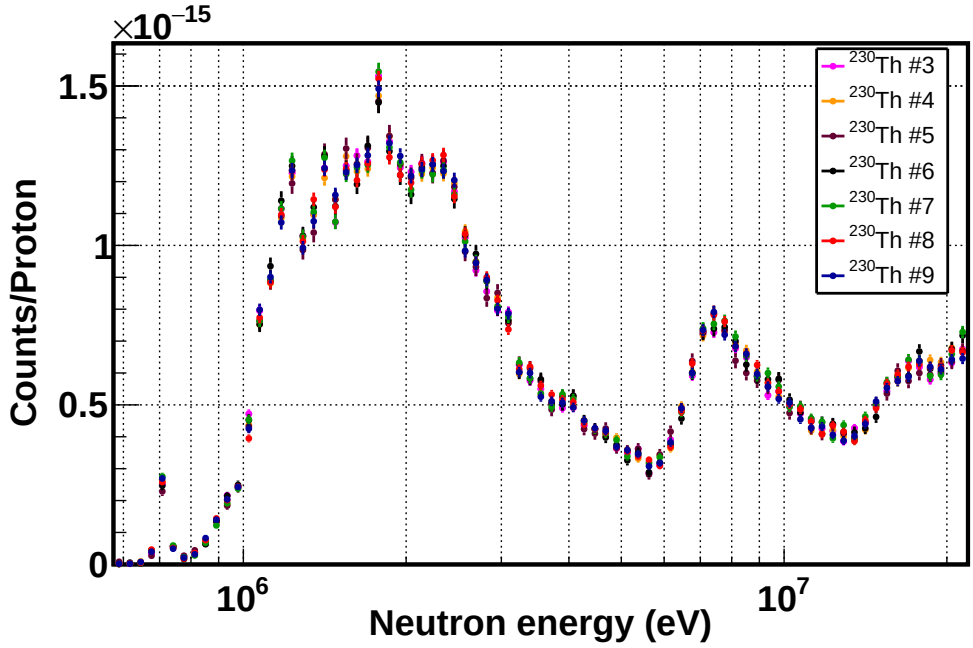

(a) Lower energy region in 50 bpd

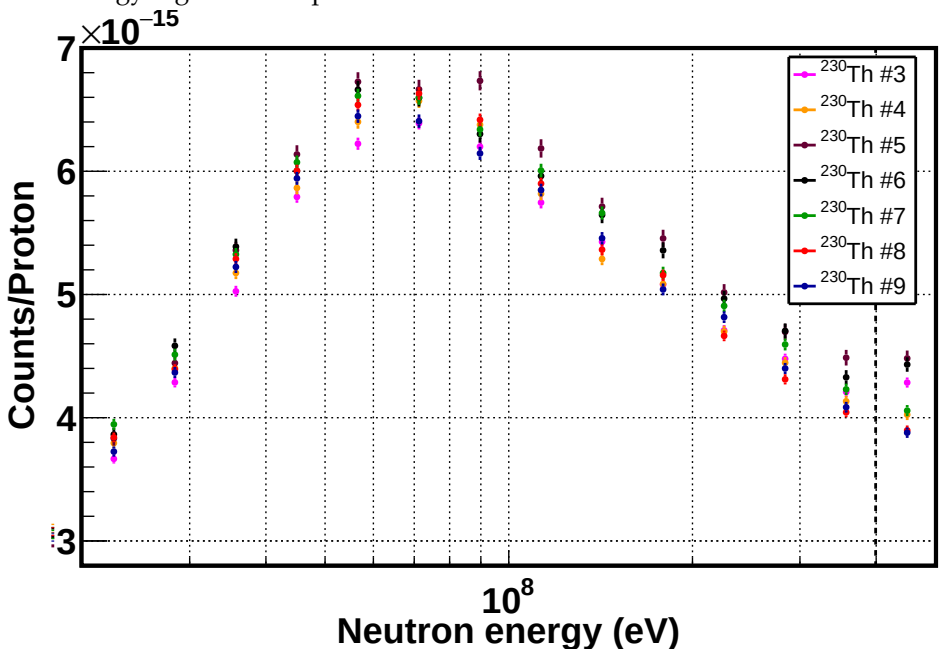

(b) Higher energy region in 10 bpd

Figure 2.18: Comparison of the counts normalized to the number of protons of the ^{230}Th targets of the EAR-1 measurement. In the top plot (a) the lower energy region is presented in 50 bpd, from the fission threshold up to 20 MeV. In the bottom (b) the higher energy region is presented in 10 bpd from 20 MeV up to 500 MeV. The dashed line represents the maximum energy where the agreement between the targets is acceptable. The counts are normalized to each other in the energy region 1 to 5 MeV.

2.3 Corrections

In this section the corrections on the fission counts are presented. These corrections are necessary to account for pulses lost due to high counting rates, counts lost due to the amplitude cut applied to the fission spectra and counts which originate from the contaminants present in the targets. In addition, the methodology for the estimation of the effective flight path length is presented, an essential quantity for the conversion of the neutron time-of-flight to energy.

2.3.1 Dead time

A necessary correction in the counting spectra is the dead time correction, in order to account for lost fission fragment counts. In order to discriminate between two successive pulses, a minimum time interval must exist between the two events. At low counting rates there is always a small probability to lose an event because it is too close to a previous one. With increasing counting rates, these counting losses can become very severe and it is necessary to account for them.

Two models of dead time behavior are used to describe the response of the detector when two events occur close in time with each other, the paralyzable and the nonparalyzable one [20]. A fixed dead time τ is assumed to be the time the detector is not recording any new events after a preceding one. In the paralyzable model when an event occurs during this time the dead time is extended for an additional time τ. In the nonparalyzable model an event occurring during the dead time is lost and has no affect in the behavior of the detector. The graphical representation of the paralyzable and nonparalyzable behavior of a detector is shown in figure 2.19.

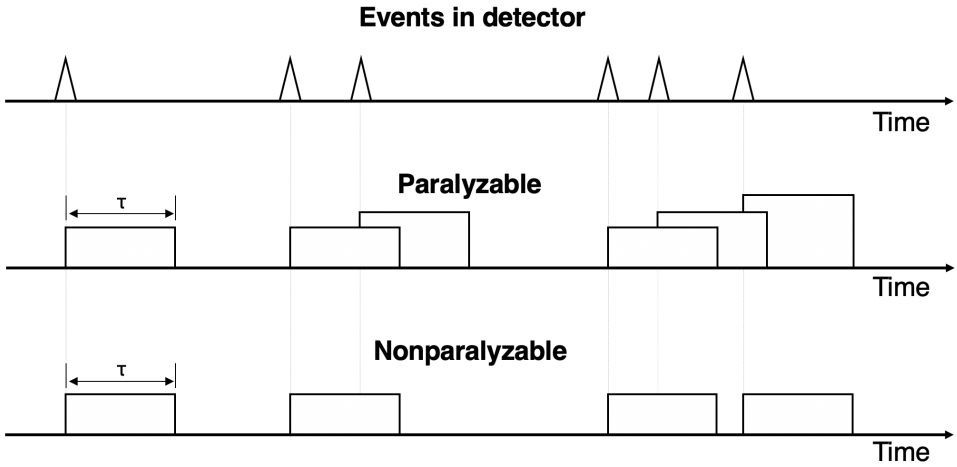

Figure 2.19: Graphical representation of the behavior of the detector in the paralyzable and nonparalyzable model.

In the case of the Micromegas, the detector does not follow either the paralyzable or the nonparalyzable model. When an event occurs close in time with a preceding one, it is recorded in the signal. Depending on how close in time the two events are, as well as their relative amplitudes, the two events can sometimes be recognized as two

single events or as one event with amplitude equal to the sum of their amplitudes or one of two events can be recognized with its true amplitude and the second one be totally missed from the pulse shape analysis routine. As a result, the first step in order to apply the dead time correction for the Micromegas detectors is to apply a selection on the recorded signals in order to follow the nonparalyzable model. In order to do so, when a number of pulses are closer in time than the fixed dead time τ, assumed to be equal with the FWHM of the pulses, and they are recognized by the pulse shape analysis routine, the pulses later in time are discarded from the analysis. So, following the nonparalyzable case, the true interaction rate n in the detector is given by the following equation

$$n = \frac{m}{1 - m\tau} \tag{2.1}$$

where m is the recorded counting rate. The correction is applied independently for the dedicated and the parasitic pulses, since the experimental counting rate is different between the two pulse modes.

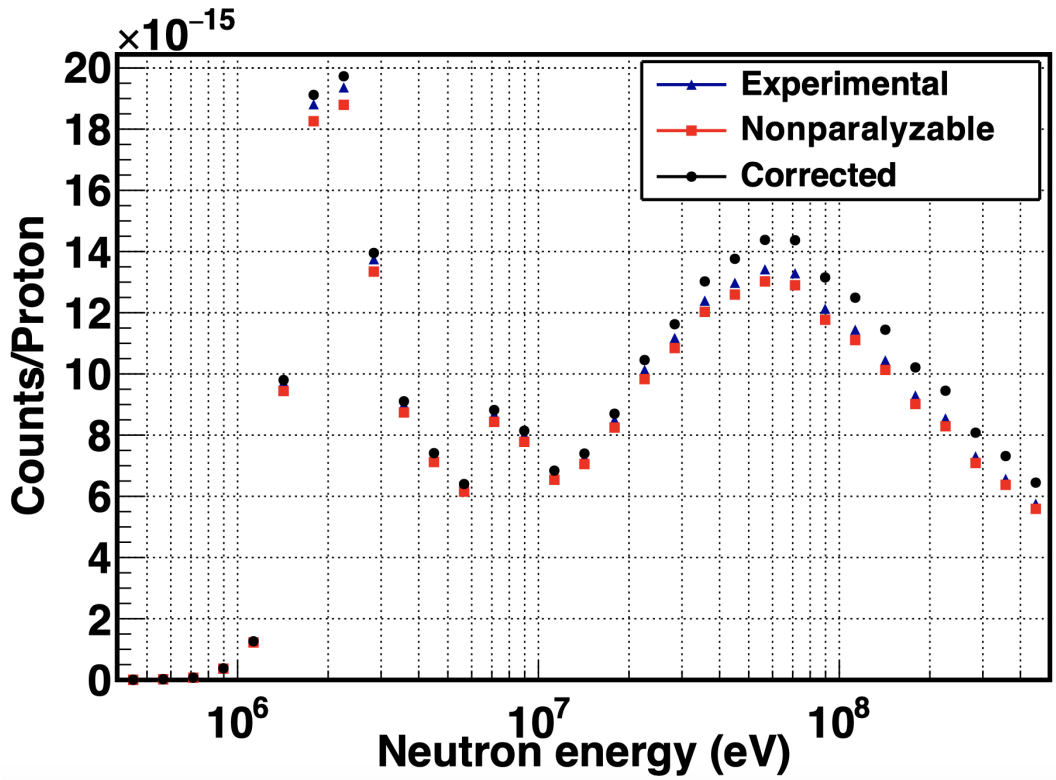

Figure 2.20: The procedure of the correction of the counts due to dead time for the ^{238}U target of EAR-1. The blue triangles are the experimental points, the red squares are the experimental points corrected to follow the nonparalyzable model and the black circles are the points corrected for the dead time.

In figure 2.20 the steps in which the dead time correction is applied to the counts from the dedicated pulses of the ^{238}U target of the EAR-1 measurement are presented. The blue triangles represent the experimental counts, as estimated from the pulse shape analysis routine. The red squares represent the experimental counts

converted to follow the nonparalyzable model, which, as expected, are lower than the experimental ones. The black circles are the corrected counts, estimated via equation 2.1. The same corrections are estimated for the dedicated and parasitic pulses of all targets of the EAR-1 and EAR-2 measurements.

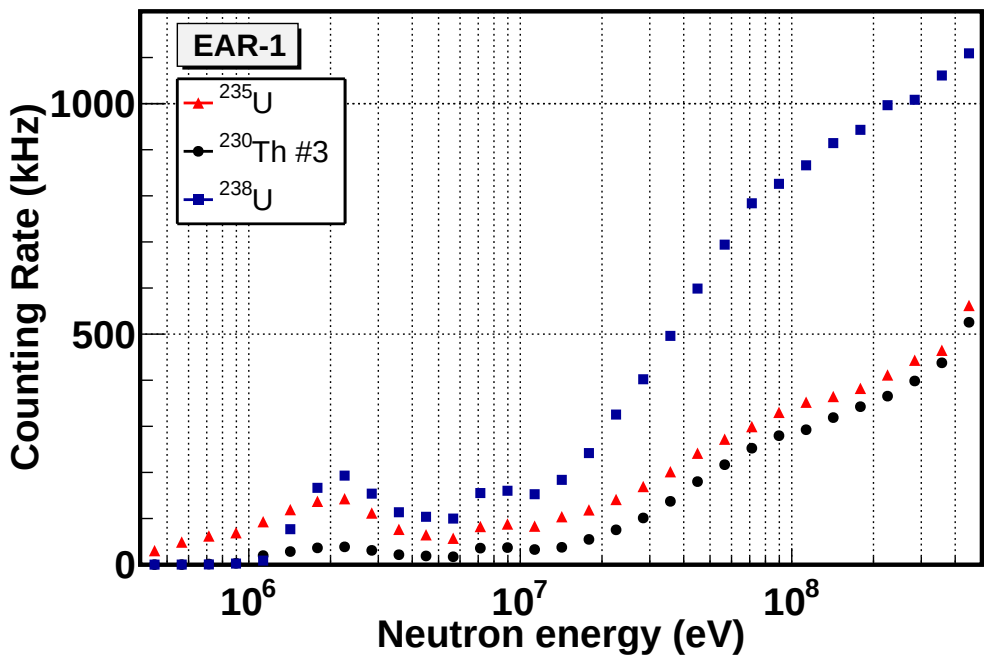

(a) Counting rates of the EAR-1 measurement.

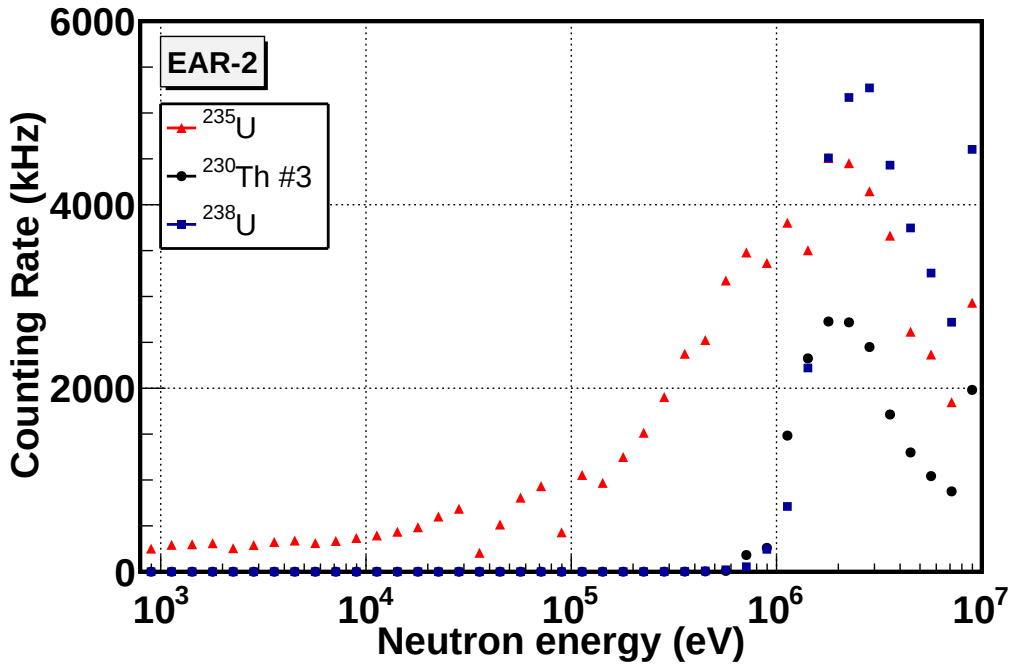

(b) Counting rates of the EAR-2 measurement.

Figure 2.21: Experimental counting rates of the dedicated pulses for the ^{235}U (red triangle), the ^{230}Th #3 (black circle) and the ^{238}U (blue square) targets for the EAR-1 measurement at the top (a) and the EAR-2 measurement at the bottom (b).

While the experimental counting rates of all targets from the EAR-1 measurement are low enough to permit the adequate correction of the lost pulses, this is not the case for the EAR-2 targets. The experimental counting rates of the targets of EAR-1 and EAR-2 for the dedicated pulses are shown in figure 2.21. As seen in the figure, the highest counting rate from the EAR-1 measurement is observed in the high energy region of the ^{238}U target to be ~1100 kHz. On the other hand, the counting rates from the EAR-2 measurements are higher, going up to ~6000 kHz. The correction for dead time for these high counting rates was not possible with this approach. Methodologies for dead time correction for high counting rates exist in literature [71, 72], but in the case of the EAR-2 data, even though a more sophisticated approach on the dead time correction would manage to extend the high energy reached in the EAR-2 experiment, it was decided not to proceed to such correction in the context of the present work. The reason behind this is that the results for the high energy region are already acquired from the EAR-1 measurement with better energy resolution than what can be accomplished at EAR-2.

2.3.2 Contaminants

As described in section 1.2.1 Pu isotopes are present in the ^{230}Th samples. The total contribution of the contaminants is negligible for energies higher than the fission threshold. This can be seen in figure 2.22, where the expected counts per proton for ^{230}Th are plotted in comparison with the expected counts from all the Pu isotopes in the same target, for the EAR-1 measurement. As can be seen in the figure, above the fission threshold the contribution from all the Pu contaminants is negligible.

However, this is not the case in the low energy region. The expected counts from all the Pu isotopes are estimated, taking into account each isotope cross-section and the evaluated flux of EAR-2 in 1000 bpd. Then the expected counts are normalized to the experimental ones, in the energy region between 4 eV to 3 keV. As seen in figure 2.23 there are no counts that can be attributed to the ^{230}Th target. By investigating the resonances, it is seen that all the peaks present in the spectrum can be attributed to the Pu isotopes. In addition, the thermal point matches the expected one from the Pu isotopes. As a result, only an estimation of the minimum value of the fission cross-section of ^{230}Th can be made below the fission threshold.

The contribution from each Pu isotope to the total Pu counts per proton, taking into account the mass of each isotope in the sample, the cross-section of each isotope and the EAR-2 evaluated flux is presented in figure 2.24. As seen in the figure from 0.02 eV to ~200 keV the main contributor to the total Pu counts, is ^{239}Pu with contributions from ^{240}Pu, ^{241}Pu and ^{242}Pu at distinct resonances of each isotope. While, at higher energies the contribution from ^{240}Pu and ^{242}Pu is significant.

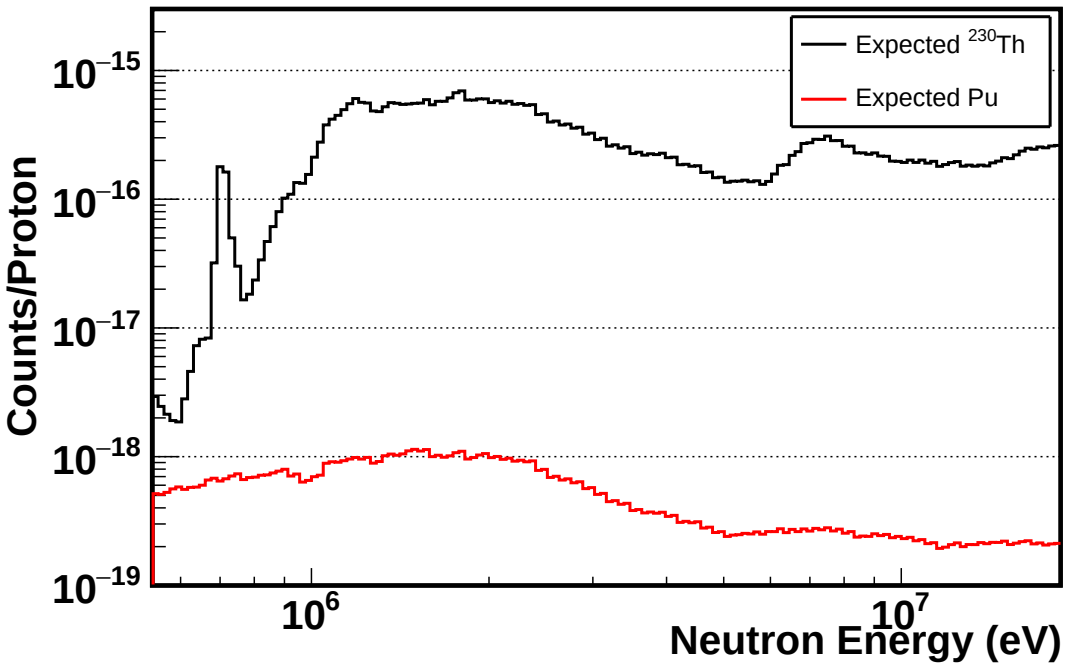

Figure 2.22: Expected counts per proton for ^{230}Th (black line) and for all the Pu isotopes present in the ^{230}Th target (red line), for the EAR-1 measurement.

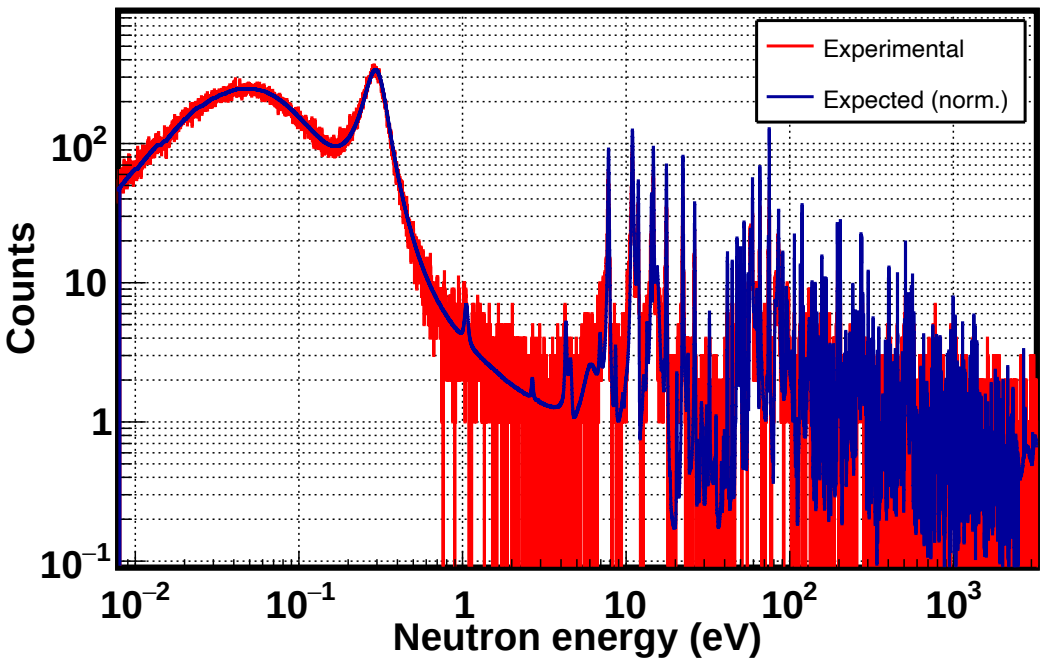

Figure 2.23: Comparison between experimental counts (red line) and expected counts (blue line) of the ^{230}Th target of the EAR-2 measurement, taking into account the Pu isotopes present. The expected counts are normalized to the experimental ones in the energy region between 4 eV and 3 keV.

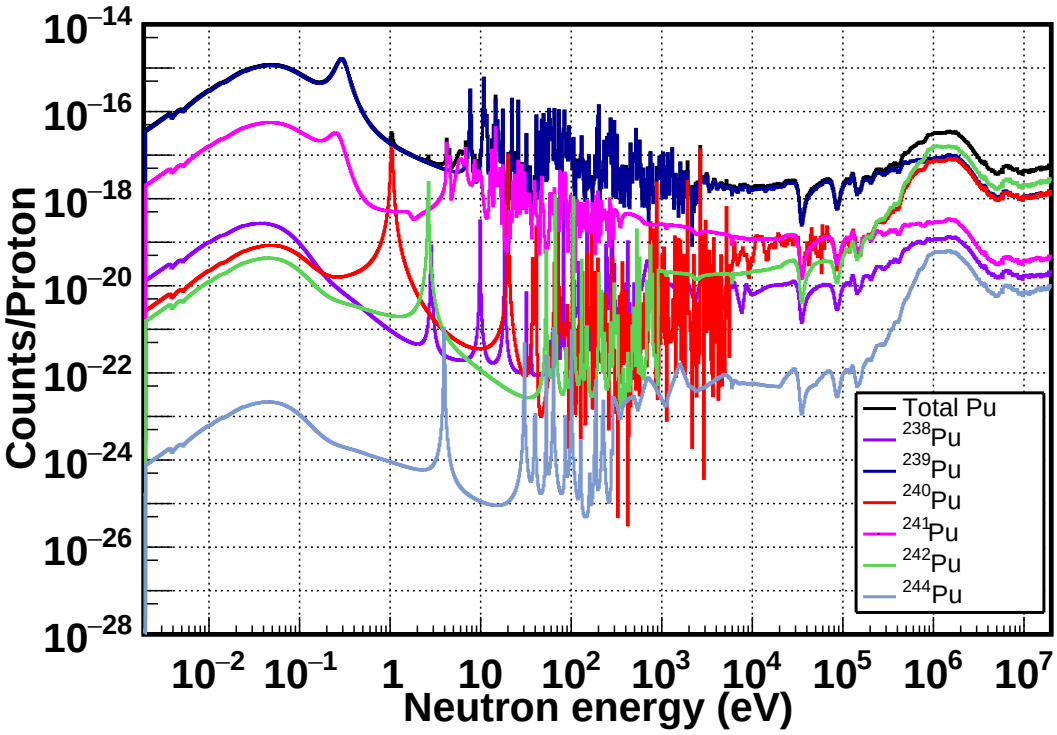

Figure 2.24: Expected Pu counts per proton in each ^{230}Th target, estimated taking into account the evaluated flux of EAR-2 and the mass and cross-section of each isotope.

2.3.3 Flight path length

The flight path length is a very important quantity for the accurate conversion of the time-of-flight to energy. The first step in the calculation of the flight path length for each energy is the estimation of geometrical distance L_{geom}, taking into account the resonances of the ^{235}U target. To achieve that, various distances were tried to calculate the expected counts of the ^{235}U target (calculated with the convolution of the evaluated flux and the reference cross-section) to determine the distance with which the best reproduction of the energy of the resonances is achieved.

The next step is the estimation of the effective flight path length, as described in section 1.1.3. However, regarding the EAR-1 measurement, the correction of the energy by taking into account the mean value of the moderation length is less than 0.7% for all energies, as it is shown in figure 2.25. As a result, the correction for the moderation length is negligible for the EAR-1 measurement.

Specifically, the cross-section of ^{235}U was calculated using the ^{10}B target as reference, with a constant flight path for the whole energy region in 1000 bpd. The cross-section results, normalized to ENDF/B-VIII.0 are shown in figure 2.26, along with the ENDF/B-VIII.0 cross-section in the energy region 0.5 eV to 26 eV. As seen in the figure, the energies of the ^{235}U resonances are reproduced with great accuracy. However, this alone is not adequate to prove that a constant flight path length would be sufficient for the conversion from time-of-flight to energy for the EAR-1 measurement. For this reason, the same test was performed with the same constant flight path, implementing the ^{230} Th #3 target. The cross-section results are compared to ENDF/B-VIII.0 evaluated ones in the vicinity of the resonance and for 1000 bpd,

normalized to the integral of the resonance. As seen from the comparison in figure 2.27, the conversion of the time-of-flight to energy is very good, reproducing the energy range of the resonance, which has been measured by various experimental campaigns in EXFOR.

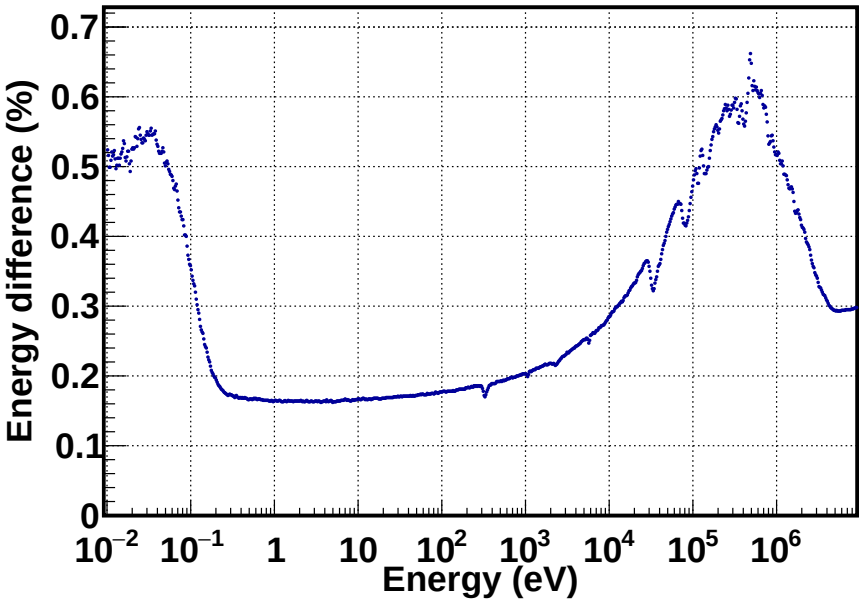

Figure 2.25: The percentage in the energy difference calculated for the EAR-1 measurement, when the energy conversion from time-of-flight is carried out by the geometric flight path length and by taking into account the mean path of the moderation length for each energy.

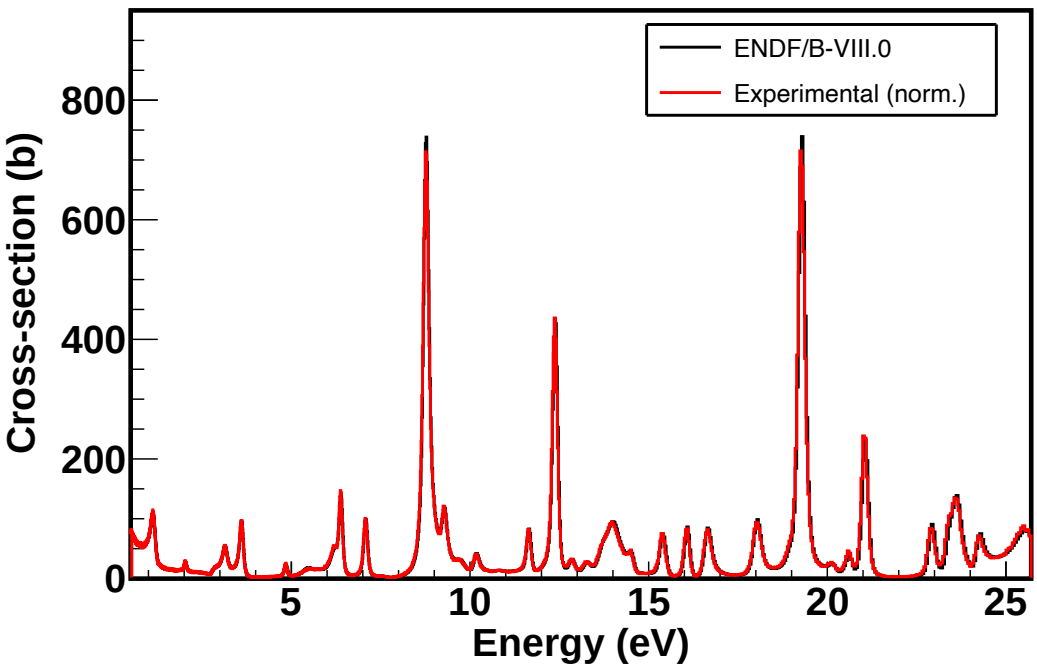

Figure 2.26: Cross-section of ^{235}U(n,f) estimated using ^{10}B(n,a) as reference (red line) from the EAR-1 measurement, normalized to ENDF/B-VIII.0 (black line) in the energy region 0.5 to 26 eV.

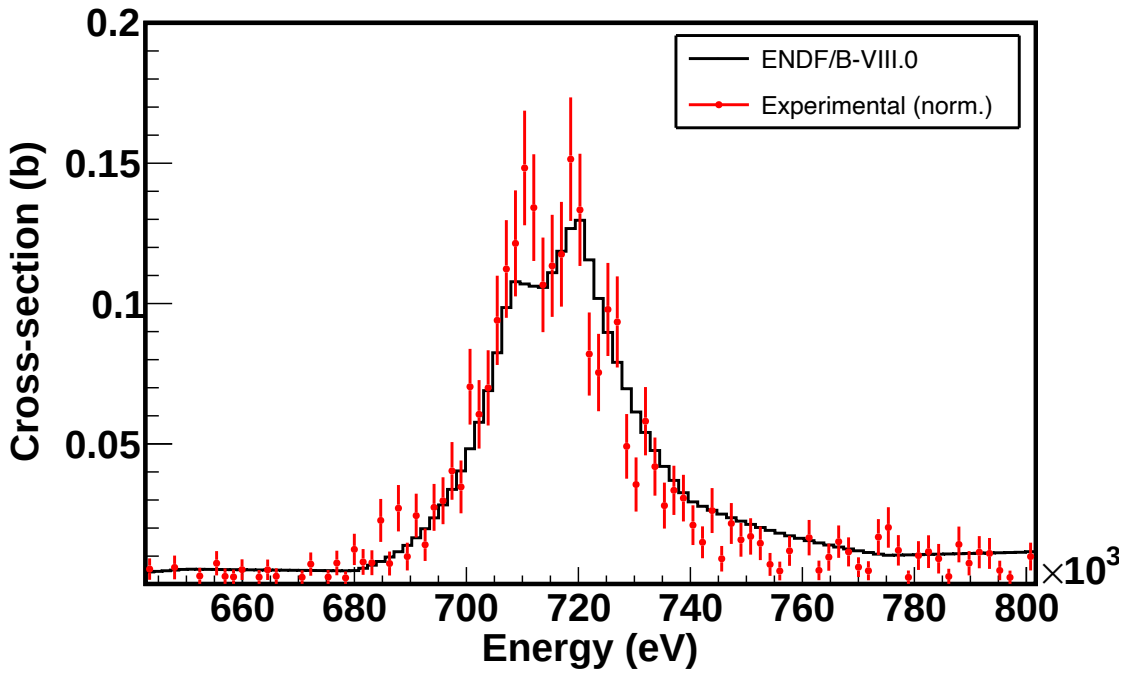

Figure 2.27: Cross-section of ^{230}Th(n,f) estimated using ^{235}U(n,f) as reference (red points) from the EAR-1 measurement, normalized to ENDF/B-VIII.0 (black line) in the integral of the resonance.

For the above mentioned reasons, a constant length is adopted for the conversion of the measured time-of-flight to energy for all the energy region of the EAR-1 measurement. The constant length used for each target is shown in table 2.1. The different lengths are estimated via the geometrical distances of the targets inside the fission chamber.

Table 2.1: Flight path lengths used for the conversion of the time-of-flight to energy for the targets of the EAR-1 measurement.

Target	Distance (m)
^{235}U	183.40
^{230}Th #3	183.42
^{230}Th #4	183.43
^{230}Th #5	183.45
^{230}Th #6	183.46
^{230}Th #7	183.48
^{230}Th #8	183.50
^{230}Th #9	183.51
^{238}U	183.53

Concerning the EAR-2 measurement the same simplified approach related the conversion of time-of-flight to neutron energy is implemented. However, a constant flight path length is not adequate for the whole energy region. Two constant flight path lengths are adopted for the analysis of the EAR-2 measurement. The first flight path length is for the low energy region, in order to estimate the contribution of the Pu contaminants, as presented in section 2.3.2. The second flight path length is for the energy region from the fission threshold of ^{230}Th up to 1 MeV, where the fission cross-section is deduced for the EAR-2 measurement. In figure 2.28 the experimental counts per proton pulse of ^{235}U are plotted in comparison with the expected counts. The time-of-flight conversion to energy is performed with a constant flight path, while for the calculation of the expected counts the evaluated flux for the capture collimator of experimental EAR-2 [9] is combined with the evaluated cross-section of ^{235}U from ENDF/B-VIII.0 [25]. As seen in the figure, the position of the energy of the resonances is reproduced quite well with a constant flight path from the thermal region up to ∼100 keV. Small differences in the counting spectrum shape can be attributed to the use of the evaluated flux of the capture collimator, even though the fission collimator was used in the experiment. The same comparison is presented in figure 2.29 for the ^{230}Th #3 target in the resonance at the threshold of the ^{230}Th(n,f) cross section, for a different flight path. As seen in the figure the energy center of the resonance in the experimental counts shows a good agreement with the expected ones, while the significant difference in shape is due to the neutron energy resolution in the region. The two flight paths adopted for each energy region are presented in table 2.2.

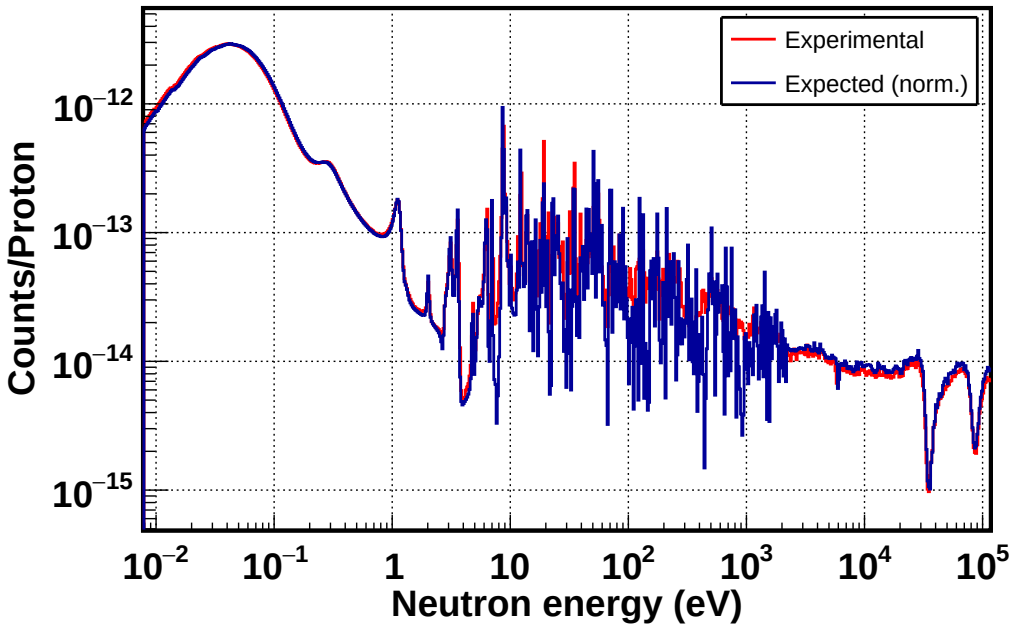

Figure 2.28: Comparison between experimental counts (red line) and expected counts per proton (blue line) for the ^{235}U target of the EAR-2 measurement. The expected counts are normalized to the experimental ones.

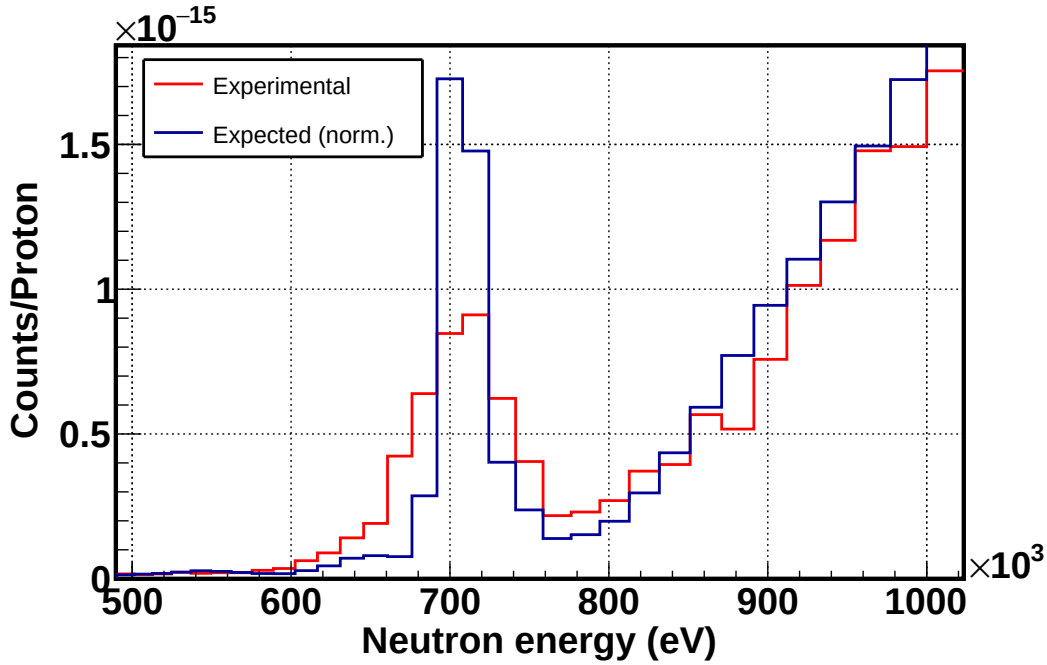

Figure 2.29: Comparison between experimental counts (red line) and expected counts per proton (blue line) for the ^{230}Th #3 target of the EAR-2 measurement. The expected counts are normalized to the experimental ones.

Table 2.2: Flight path lengths used for the conversion of the time-of-flight to energy for the targets of the EAR-2 measurement. Two flight path lengths are used for each target, one for the low energy region and one for the energy region of the ^{230}Th resonance.

Target	Distance low (m)	Distance resonance (m)
^{235}U	19.20	18.78
^{230}Th #3	19.22	18.80
^{230}Th #4	19.23	18.81
^{230}Th #5	19.25	18.83
^{230}Th #6	19.26	18.84
^{230}Th #7	19.28	18.86
^{230}Th #8	19.30	18.88
^{230}Th #9	19.31	18.89
^{238}U	19.33	18.91

2.3.4 FLUKA simulations

The behavior of the energy deposition on the Micromegas detector was studied by means of Monte-Carlo simulations performed with FLUKA [21, 22] through the graphical interface FLAIR [73] using the GEF ("GEneral description of Fission observables") code [23, 74, 75] as a fission event generator. For the description of the sample-detector setup a simple geometry is implemented. The actinide sample is described by a cylindrical volume, with a diameter equal to the known diameter of the samples (8 cm). Concerning the composition of the samples, it has been observed to vary at different points of the samples [76], so it cannot be considered as known. A composition consisting of various elements (O, Al, C, etc.) in addition to the main isotope is considered and the equivalent thickness of each target is adjusted respectively, in order to achieve the reproduction of the experimental amplitude spectra via the simulations. The gas of the Micromegas detector is described as another cylindrical volume with a diameter equal to the mesh diameter (9.5 cm), the thickness of the drift gap (6 mm) and the composition Ar:CF_4:isoC_4H_{10} (88:10:2), with a density estimated for a gas pressure of 1 bar (0.00198706 g/cm^3).

The fission fragments are generated via a user-defined source routine, within the FLUKA code. The output information from the GEF code, namely the atomic and mass numbers and the kinetic energy of the fission fragments are given to describe the beam characteristics of the simulation. An example of the mass and energy distributions of fission fragments obtained by the GEF code is given in figure 2.30. In addition, the direction cosines are defined, in order to assume an isotropic emission of the fission fragments at a 4π solid angle, by the following equations:

$$\begin{aligned} \cos x &= \sqrt{1-\cos^2 z} \times (-1 + 2 \cdot \mathrm{Rand}) \\ \cos y &= \sqrt{1-\cos^2 z} \times (-1 + 2 \cdot \mathrm{Rand}) \\ \cos z &= -1 + 2 \cdot \mathrm{Rand} \end{aligned} \tag{2.2}$$

where Rand is a random number between 0 and 1.

In order to generate the fission fragments evenly distributed in the volume of the sample two random numbers (r_1 and r_2) are generated in the square inscribing a circle with a diameter equal to the diameter of the samples (R). If the random numbers generated are inside the circle (${r_1}^2 + {r_2}^2 \leq R^2$) the generated random numbers are used as the x and y coordinates, and the z coordinate is randomly estimated within the thickness of the target. The output of the FLUKA simulations is the energy deposition in the detector gas from the fission fragments generated in the actinide target, as shown in figure 2.31. The energy deposition spectrum in the detector is presented in figure 2.32, where the contributions from the light and heavy fragments are shown in red and blue respectively.

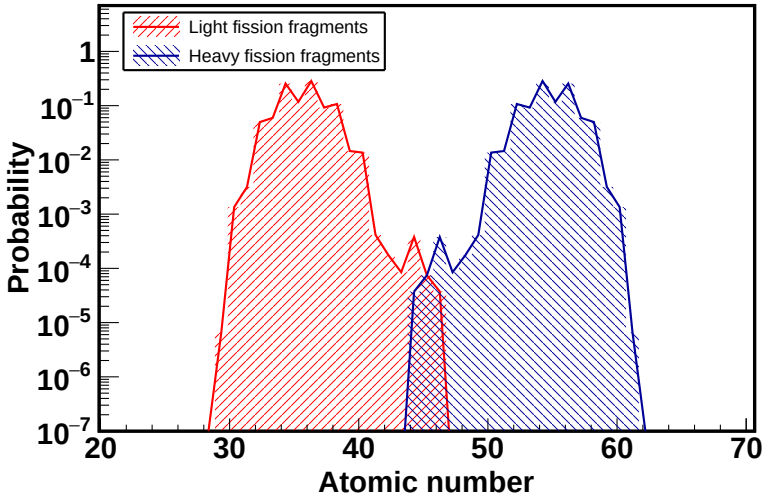

(a) Atomic mass distributions

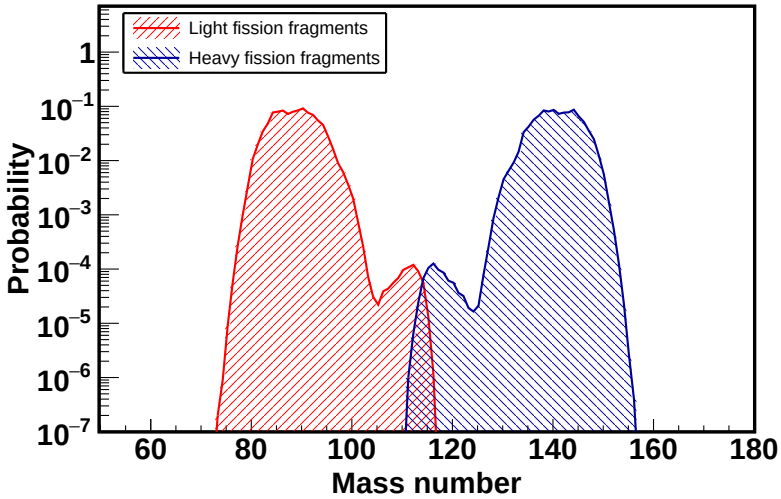

(b) Mass number distributions

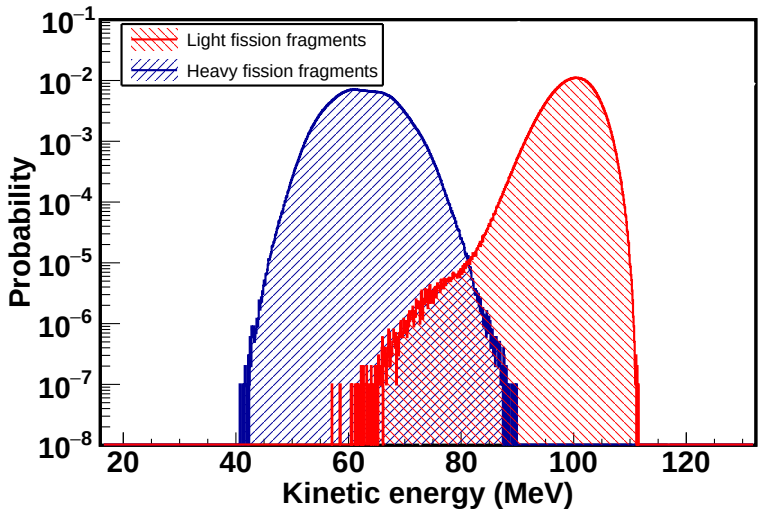

(c) Kinetic energy distributions

Figure 2.30: Atomic mass (a), mass number (b) and kinetic energy (c) distributions of ^{230}Th light (red line) and heavy (blue line) fission fragments for neutron energy 1 MeV, obtained by the GEF code.

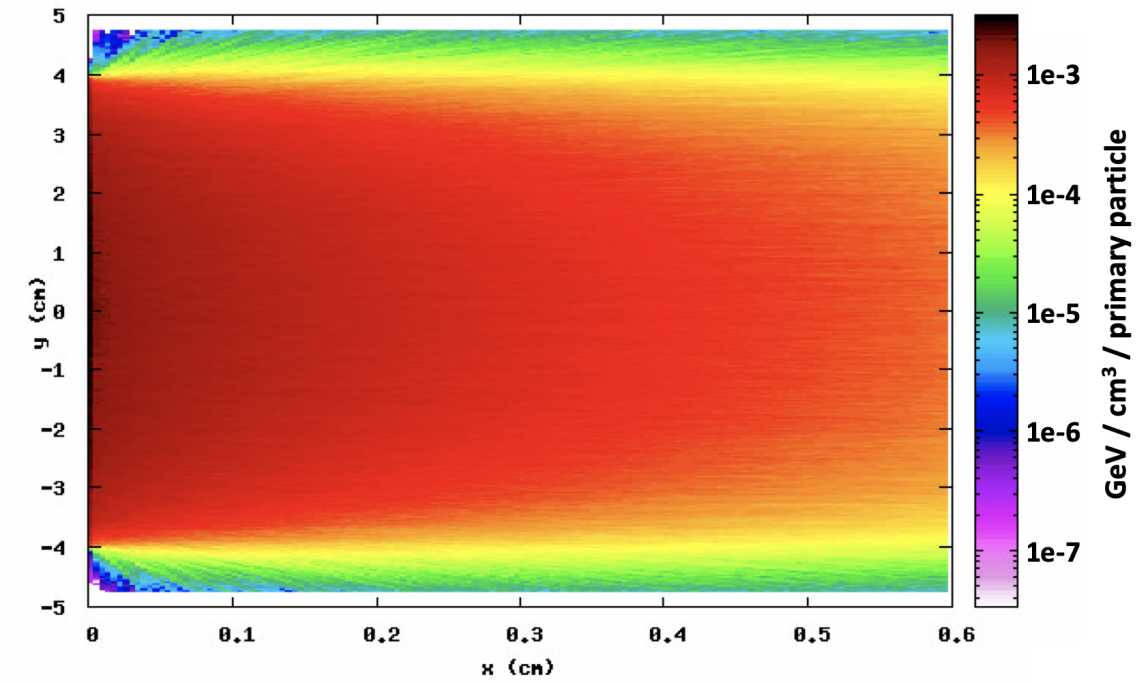

Figure 2.31: Simulated energy deposition of fission fragments from a ^{230}Th sample (placed at y = 0) in the Micromegas detector. The fission fragments characteristics are imported from the GEF code and the emission is assumed to be isotropic.

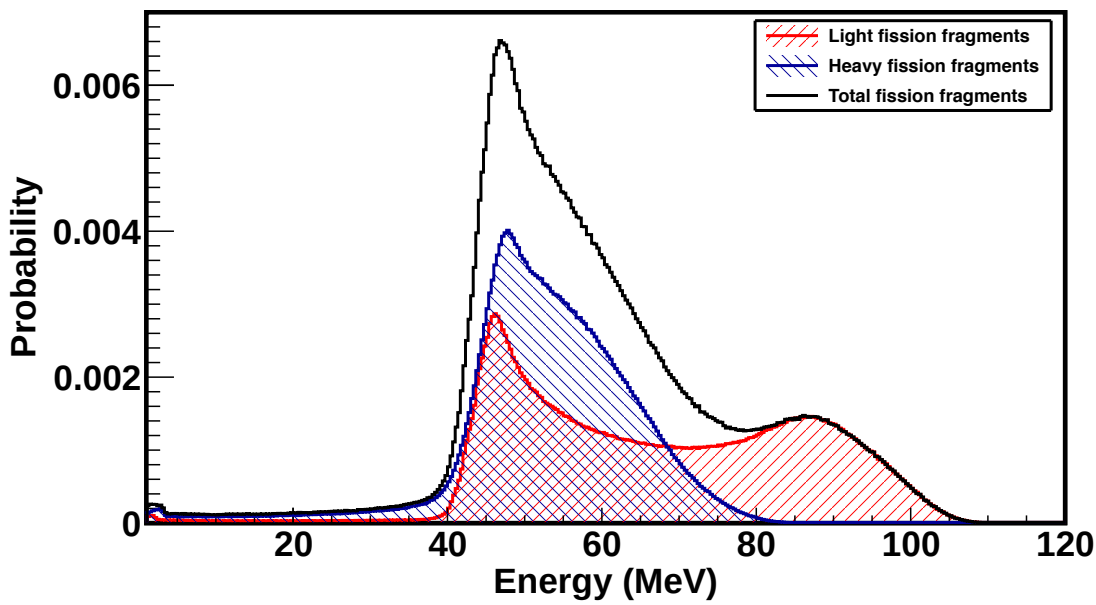

Figure 2.32: Simulated energy deposition of fission fragments in the Micromegas detector from a ^{235}U target. The fission fragment characteristics are imported from the GEF code and the emission is assumed to be isotropic. The red line corresponds to the energy deposition of the light fission fragments, the blue line corresponds to the energy deposition of the heavy fission fragments, while the black line corresponds to the total energy deposition, from both the light and heavy fission fragments.

The total energy deposition in the detector gas (black line of figure 2.32) can be described by two distinct peaks and a tail in the lower energy region. The higher energy peak is a result of the energy deposition of the light fission fragments emitted at angles close to 90° from the edge of the target with direction towards the detector gas, making it possible for a significant part of the initial kinetic energy to be deposited in the gas. However, light fission fragments emitted at smaller angles or at higher angles from the edges of the target with a direction opposite to the detector gas, deposit a small part of their energy in the detector gas, contributing this way in the lower energy peak of the spectrum. Thus, the lower energy peak of the spectrum originates from heavy fission fragments and light fission fragments which deposit smaller energies in the detector gas. This explains the difference in the shape and amplitude of these two peaks. Concerning the low energy tail, it is a result of very small energy deposition in the detector gas, while the main contribution in the tail comes from the heavy fission fragments. The height of the tail is related to the thickness of the actinide sample. With an increase in the thickness of the target the low energy tail increases in height. However, since as mentioned above the composition of the target is not explicitly known, the thickness of the target cannot be estimated as well. Thus, with a specific composition provided in the simulations the thickness of the targets is adjusted in order to match the experimental spectra with the simulated ones. The adjustment of the target thickness is a process of importance, since the part of the fission fragments lost from the spectrum are the ones absorbed by the sample itself.

The simulations performed with the FLUKA code are used for the estimation of the fission fragments lost inside the sample itself, as well as the fission fragments entering the detector gas which are discarded from the analysis due to the amplitude cut applied. The calculation of the fission fragments lost inside the target is a straightforward one, and is accomplished by dividing the primary particles which deposit energy in the detector to the total number of the primary particles used in the simulation. The correction varies, depending on the thickness of the sample, from 6.2% for the ^{238}U target to less than 2% for the rest of the targets. For the correction of the fission fragments rejected by the analysis procedure, due to the amplitude cut applied, the comparison between the experimental amplitude spectra with the simulated ones is required. To achieve that, the calibration of the simulated spectra is needed in order to convert the x-axis from energy to channels to compare with the experimental spectra. In addition, a skewed gaussian response function is assumed for the convolution of the calibrated simulated spectra. The mean value of the gaussian distribution is the center of each bin and the standard deviation is selected constant for all bins and a very good reproduction of the experimental spectra is achieved. The standard deviation is 28 channels for all the ^{230}Th targets, 25 channels for the ^{235}U target and 35 channels for the ^{238}U target. The comparison between the experimental (blue line) and the calibrated and simulated (red line) spectra, is presented in figure 2.33 for the ^{235}U (2.33a), the ^{230}Th #3 (2.33b) and the ^{238}U (2.33c) samples.

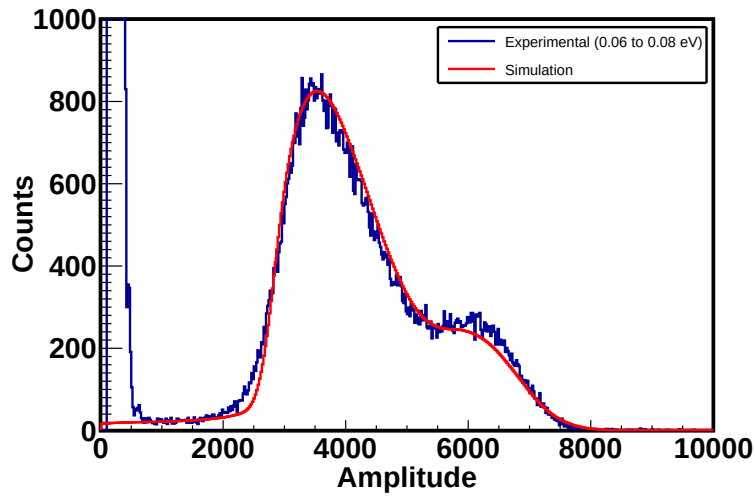

(a) ^{235}U

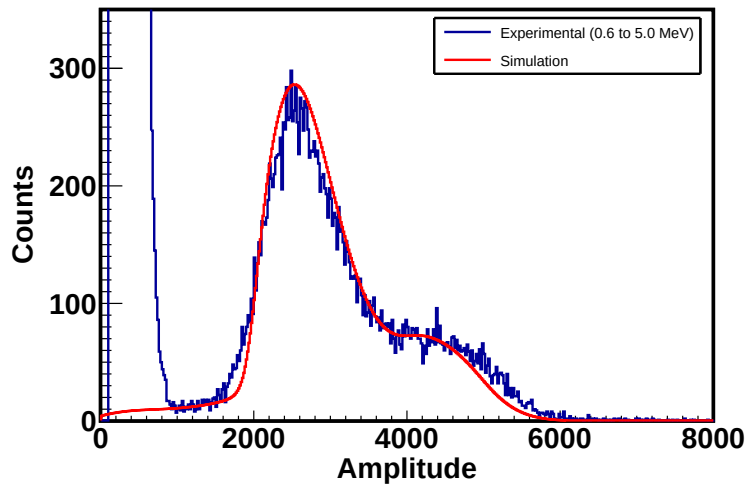

(b) ^{230}Th #3

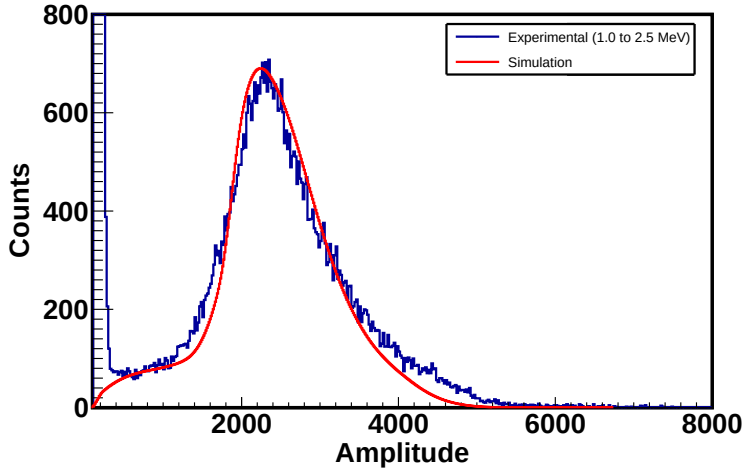

(c) ^{238}U

Figure 2.33: Comparison between experimental from the EAR-1 measurement (blue line) and simulated (red line) spectra for the (a) ^{235}U, (b) ^{230}Th and (c) ^{238}U targets, after the calibration and application of a skewed gaussian response function.

It is interesting to note the similar amplitude spectra between the ^{230}Th and the ^{235}U targets. This is a result of the similar thickness of the targets, in addition to the same voltages applied to the electrodes during the experiment, while the difference in the amplitude spectrum of the ^{238}U target is due to the lower voltage applied to the mesh electrode and because the ^{238}U is thicker. The result is to be able to distinguish the low energy depositions in the detector gas. Because of this, an alternative method for the estimation of the lost fission fragments can be adopted, by assuming that the low energy depositions extend linearly to zero. Then the ratio of the corrected ^{230}Th counts to the corrected ^{235}U counts from this method, deviates less than 1% compared to the same ratio estimated via the FLUKA simulations. Also, the same amplitude cut can be assumed for all targets with no additional correction. With this approach, again the difference of the results compared to the correction estimated via the FLUKA simulations is less than 0.8% for all ^{230}Th targets. These alternative approaches for the amplitude cut correction validate the accuracy of the FLUKA simulation results and at the same time provide an estimation of the systematic uncertainty related to the lost fission fragments correction, which is less than 1% for all ^{230}Th targets.

The FLUKA simulations are used for the estimation of the lost fission fragments at lower energies, where the residuals from the γ-flash subtraction are not yet present in the amplitude spectra. As mentioned in section 2.12 a higher amplitude cut is adopted at higher energies in order to compensate for the increase of noise. The estimation of the fission fragments lost under the noise signals is estimated from the comparison of the analysis with a lower amplitude cut to the analysis with a higher amplitude cut. Specifically, the analysis is performed with a low and a high amplitude cut. Then a correction factor is estimated from the ratio of an integrated region of the counting spectrum of the lower amplitude cut to the higher one. The region is chosen in order to have clean amplitude spectra with both amplitude cuts. This correction is valid, given that the shapes of the amplitude spectra are invariant in the above mentioned energy regions. Even though this applies to the ^{235}U and ^{238}U targets, this is not the case for the ^{230}Th targets. For energies higher than 25 MeV, the shape and position of the amplitude spectra are different with respect to the lower energies. This can be treated, by estimating the correction factor between two different shapes of amplitude spectra, by implementing an amplitude cut at both which lies in the low energy background. Then, since the background is the same for both spectra, the correction factor can be estimated without a problem. Then, for reaching higher energies the corrected and changed in shape amplitude spectra are compared to the spectra taken at higher energies, which have partially the same shape.

2.3.5 MCNP simulations

Monte Carlo simulations were performed with the MCNP5 code [24] for the estimation of the variation in the neutron fluence between the targets. The geometry of the experimental setup, consisting of the fission chamber filled with Ar:CF_4:isoC_4H_{10} (88:10:2), the Micromegas detectors and the actinide targets with the target holders is implemented in the MCNP5 code, as seen in figure 2.34. The neutron source is described as a mono-directional disk source with a histogram of energies, following

the experimental flux of EAR-1 and EAR-2, as seen in figure 1.2 of section 1.1. The diameter of the disk equals the fission collimator of each experimental area, the energy binning of the histogram is the isolethargic energy binning of the experimental flux for 100 bpd, while the weight for each energy used for the simulations is calculated by dividing the absolute value of the experimental flux at each energy bin to the integral of the flux in the whole energy region.

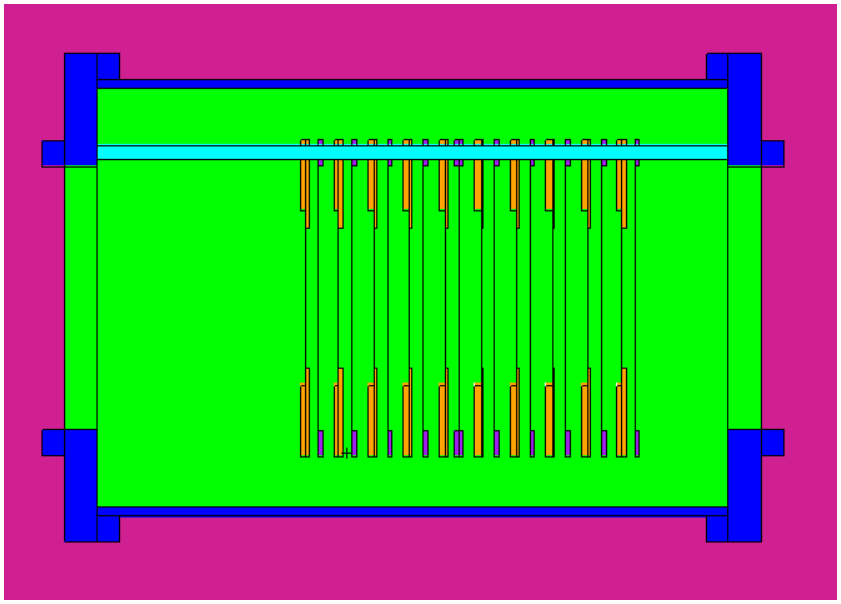

Figure 2.34: The geometry of the experimental setup used for the MCNP5 simulations. The fission chamber is depicted in blue, the air in the experimental area in magenta, the gas of the Micromegas detector in green, the sample holders in orange and the support of the Micromegas detectors in purple.

The results from the Monte Carlo simulations with the MCNP5 code, namely the ratio of the simulated flux between the reference target used in each area to the two ^{230}Th targets placed at the extreme positions with respect to the neutron beam direction, are presented in figure ref 2.35. The results are presented in the energy regions where the cross-section results are deduced for each experimental area. As seen in figure 2.35a, the correction due to the different positions of the ^{230}Th targets with respect to the reference target is less than 1% for all energy regions. It is interesting to note that the further away the target is placed from the direction of the beam, and consequently to the ^{235}U target which is the second target placed in the fission chamber, the greater the correction difference is with respect to the ^{235}U reference target. At lower energies this difference is higher (0.9%) and it decreases with energy down to 0.2% after 100 MeV. For the ^{230}Th target closer to the ^{235}U target the difference is negligible. As a result, the lower energies seem to be more affected than the higher ones, since the probability of interaction with the materials present in the path of the beam is higher. Concerning the EAR-2 ratio, as seen in figure 2.35b, the difference between the reference target ^{238}U and the ^{230}Th targets, is less than 1% in all cases, while at the energy region of interest it is fairly constant for each target. In conclusion, the correction due to the variations of the neutron fluence is very small (less than 1% for all cases), but it is not systematic in the whole energy region of interest and between the ^{230}Th targets. So, it is important to be taken into account in order

to improve the accuracy of the cross-section results and the agreement between the ^{230}Th targets.

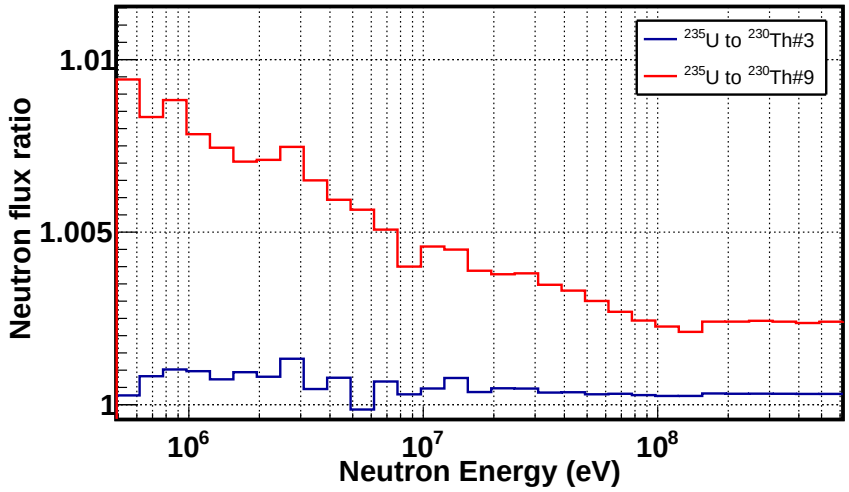

(a) EAR-1

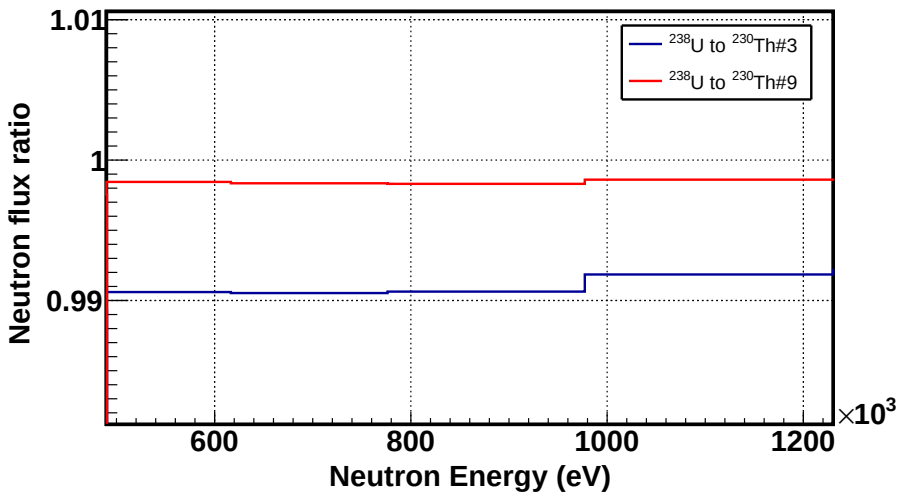

(b) EAR-2

Figure 2.35: Ratio of the simulated flux with the MCNP5 code of the reference target used in each experimental area, namely ^{235}U for EAR-1 and ^{238}U for EAR-2, to the ^{230}Th placed closer to the direction of the beam (blue line) and further away (red line).

Chapter 3

Results

In this chapter the cross-section is calculated, from the fission counts estimated as presented in Chapter 2 applying all the necessary corrections.

3.1 Cross-section calculation

The cross-section at each energy bin is calculated relative to the reference target, via the expression:

$$\sigma(E) = \frac{N(E)}{N^{ref}(E)} \cdot \frac{f_{abs}}{f_{abs}^{ref}} \cdot \frac{f_{amp}(E)}{f_{amp}^{ref}(E)} \cdot \frac{f_{dt}(E)}{f_{dt}^{ref}(E)} \cdot \frac{f_{cont}(E)}{f_{cont}^{ref}(E)} \cdot f_{flux}(E) \cdot \frac{n}{n^{ref}} \cdot \sigma^{ref}(E) \quad (3.1)$$

where N are the recorded counts, f_{abs} is the correction factor for the fission fragments which do not succeed in entering the Micromegas gas, f_{amp} is the correction factor for the amplitude cut, f_{dt} is the correction factor for the dead time, f_{cont} is the correction factor for the contribution of the contaminants, f_{flux} is the correction factor for the difference in the flux between the target and the reference sample, n is the areal density of the samples in atoms per barn and σ^{ref} is the cross-section of the reference target, while the superscript 'ref' refers to the reference sample.

3.1.1 Reproduction of the ^{238}U(n,f) cross-section

In order to test and validate the analysis procedure described in chapter 2, the neutron induced fission cross-section of ^{238}U using ^{235}U as reference is estimated via equation 3.1 up to 160 MeV. The reference cross-section of ^{235}U is standard, taken from ENDF/B-VIII.0 [25] from 0.15 up to 30 MeV, with the cross-section uncertainty varying from 1.5 to 1.8% in this energy region. For energies between 30 and 200 MeV the cross-section is also considered as standard, taken from the IAEA 2017 Neutron Data Standards library [26], with an uncertainty given between 2.2 and 4.8%, with the tendency to increase at higher energies. For energies higher than 200 MeV, the cross-section values are taken from the IAEA Report [27], with the uncertainty estimated to be 5.0% at 300 MeV, 7.1% at 400 MeV and 5.7% at 500 MeV. The ^{238}U(n,f) cross-section is taken from ENDF/B-VIII.0 for energies from 0.5 up to 30 MeV with the uncertainty being between 9.6 and 10.4% for this energy region. The

cross-section for the higher energy region, from 30 to 200 MeV, is again taken from the IAEA 2017 Neutron Data Standards library, with the uncertainty ranging from 1.9 to 4.9%. The cross-section results for the ^{238}U(n,f) reaction, as estimated from this work, are presented in figure 3.1 (black circles) along with the reference (red line). As seen in the figure, the reproduction of the reference cross-section is very good up to 30 MeV. For the energy region 30 to 50 MeV the cross-section estimated from this work is lower than the reference, with the difference being less than 5% at all energies. At higher energies the agreement between this work and the reference is very good, up to 160 MeV. Taking into account the uncertainties of the reference reactions the agreement between the cross-section estimated from this work and the reference is very good, thus validating the accuracy of the analysis procedure used to deduce the cross-section results.

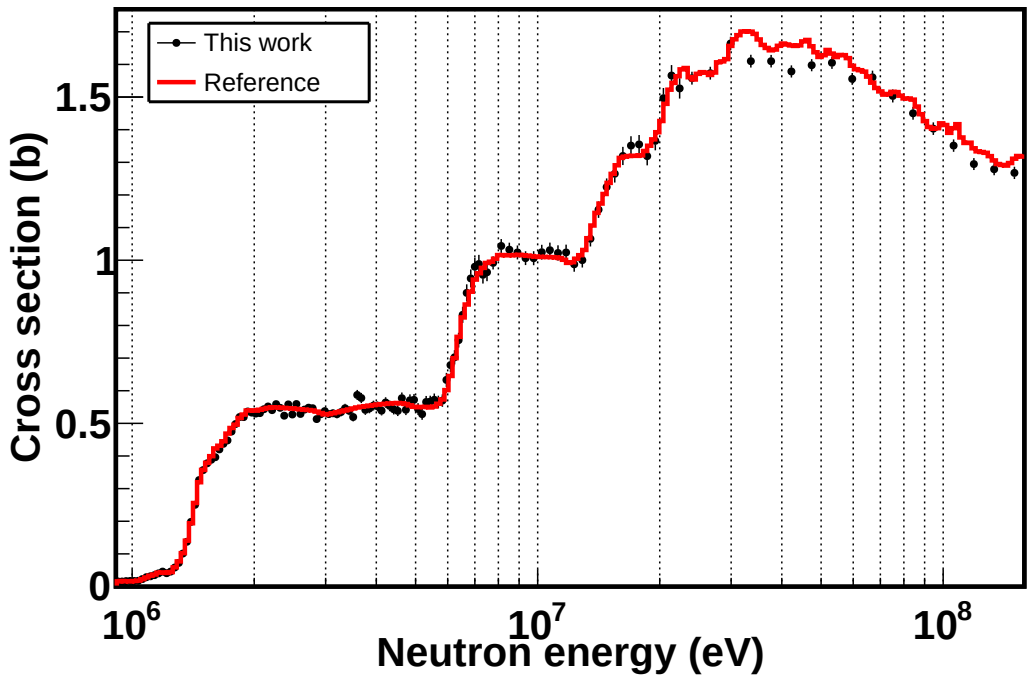

Figure 3.1: Cross-section of the ^{238}U(n,f) reaction (black circle) from the EAR-1 measurement, estimated using the ^{235}U(n,f) reaction as reference, plotted along with the reference cross-section of ^{238}U(n,f) (red line).

3.1.2 Cross-section results for the ^{230}Th(n,f) reaction

The cross-section results, of all seven ^{230}Th targets estimated using the ^{235}U(n,f) reaction as reference, are presented in figure 3.2. In general, the seven ^{230}Th target results are in very good agreement with each other, since no systematic difference is observed between them. The final cross-section results are estimated as a mean value of the seven ^{230}Th targets, as presented in figure 3.3, along with the previous datasets, while only the statistical uncertainties are shown in the figure.

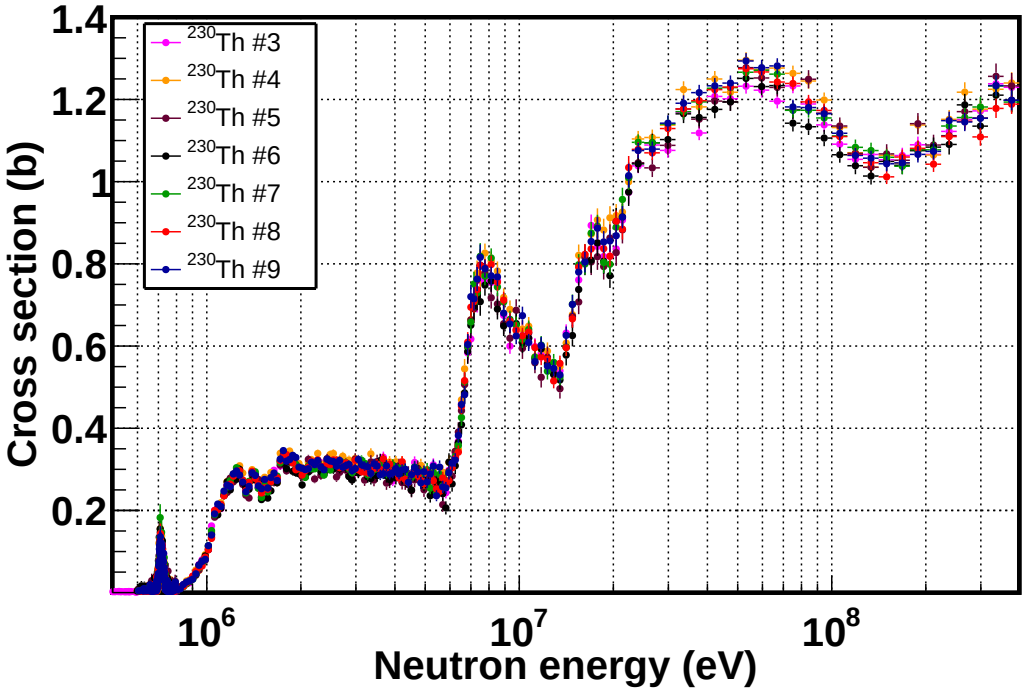

Figure 3.2: Cross-section of the ^{230}Th(n,f) reaction from the EAR-1 measurement, estimated using the ^{235}U(n,f) reaction as reference, for the seven ^{230}Th targets. Only the statistical uncertainties are shown in the figure.

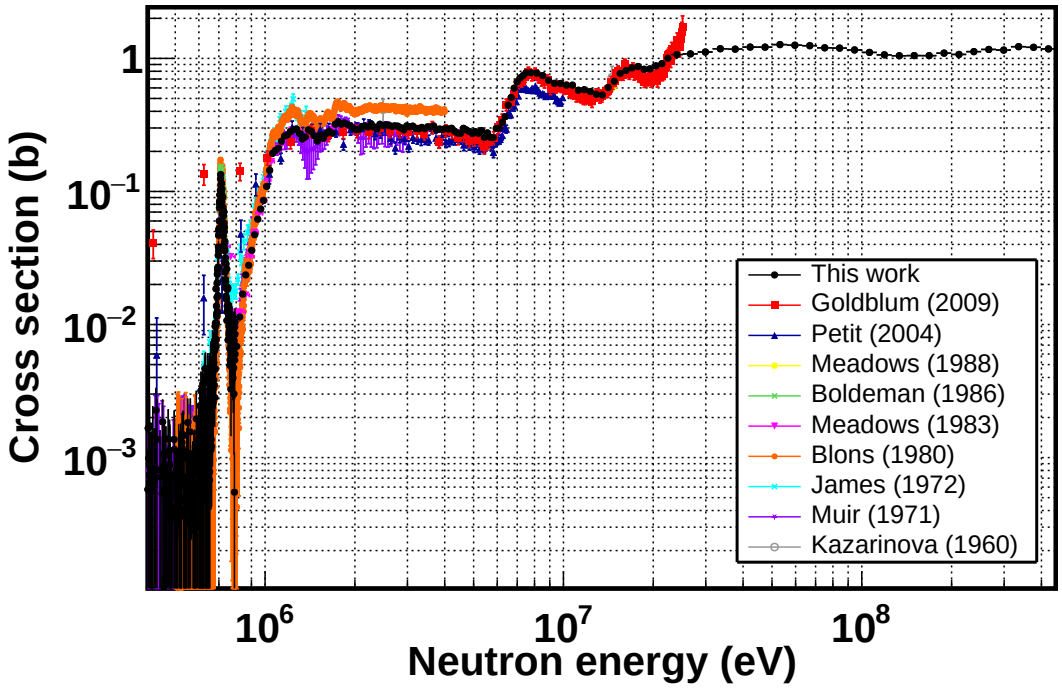

Figure 3.3: Cross-section of the ^{230}Th(n,f) reaction (black circle) from the EAR-1 measurement, estimated using the ^{235}U(n,f) reaction as reference, plotted along with the previous datasets. Only the statistical uncertainties are shown in the figure.

Specifically, the results of the ^{230}Th(n,f) reaction in the resonance region are presented in figure 3.4 along with the previous datasets. The adopted binning in this energy region is isolethargic with 2000 bpd. As seen in figure 3.4, a structure appears in the energy region of 710 keV, also seen in the data of Boldeman and Walsh [28], Blons *et al.* [29], James *et al.* [30] and Muir and Veeser [31]. However, the absolute value of the cross-section of the resonance in this work is lower than the data of Boldeman and Walsh, Blons *et al.* and James *et al.* and higher than that of Muir and Veeser. However, it is important to note that the data of Blons *et al.* and James *et al.* are normalized to the value of 0.37 b at 1.4 MeV after private communication with J.E. Evans and G.A. Jones and they are systematically higher than the other datasets at higher energies. Regarding the data from the surrogate method of Goldblum *et al.* and Petit *et al.*, large deviations are observed between them and this work, as well as the previous datasets. The energy resolution of the data by Blons *et al.*, is superior to all the other existing measurements and reveals two maxima centered at ∼709 and ∼719 keV respectively. The present data tend to confirm this structure, though with lower cross section values.

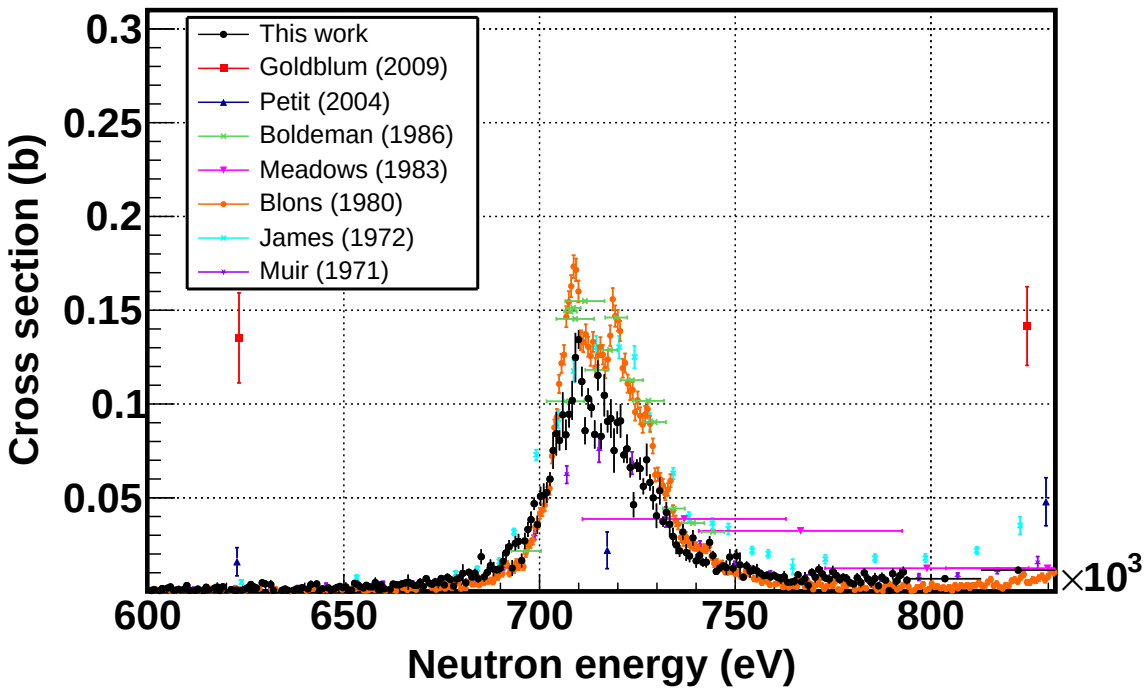

Figure 3.4: Cross-section of the ^{230}Th(n,f) reaction (black circle) from the EAR-1 measurement, determined using the ^{235}U(n,f) reaction as reference, plotted along with the previous datasets in the resonance region. The binning used is isolethargic with 2000 bpd. Only the statistical uncertainties are shown in the figure.

The cross-section of the EAR-1 measurement from the fission threshold up to 1 MeV in comparison with the cross-section at the same energy region for the EAR-2 measurement is presented in figure 3.5. The cross-section results are the mean value of the ^{230}Th #5 and ^{230}Th #6 targets, selected because the beam has a different diameter in EAR-1 and EAR-2 (8 and 6.7 cm respectively) and the targets are highly inhomogeneous, with the exception of these two ^{230}Th targets. As seen in the figure, the

agreement between the two areas is fairly good after the resonance, while comparing the integral of the resonance a difference of the order of 16% is estimated. The reason behind this high difference is not understood very well, but it could be a result of various components. Firstly, the energy resolution of the EAR-2 measurement is worser than the corresponding EAR-1 measurement, as seen in the figure from the wider peak of the resonance, as a result of the much shorter flight path of EAR-2 in combination with the lower voltages applied in the mesh electrodes making the resolution of the Micromegas itself worse. So, the counts from the resonance peak could be scattered at lower and higher energies and not being accounted for. The abrupt changes in the cross-section values of the resonance highlight the difference in energy resolution of the two experimental areas. In addition the ^{238}U(n,f) cross-section is not known with very high accuracy in this energy region. The ENDF/B-VIII.0 [25] evaluation estimates the uncertainty in this energy region in the order of ∼10%. While the uncertainty given in the evaluated libraries JENDL-4.0 [49] and JEFF-3.3 [50] is lower, differences in the cross-section values of the ^{238}U(n,f) reaction in this energy region are up to 20%. Unfortunately, the ^{235}U(n,f) reaction could not be used for the EAR-2 measurement for this energy region due to the very high counting rate, as presented in figure 2.21b.

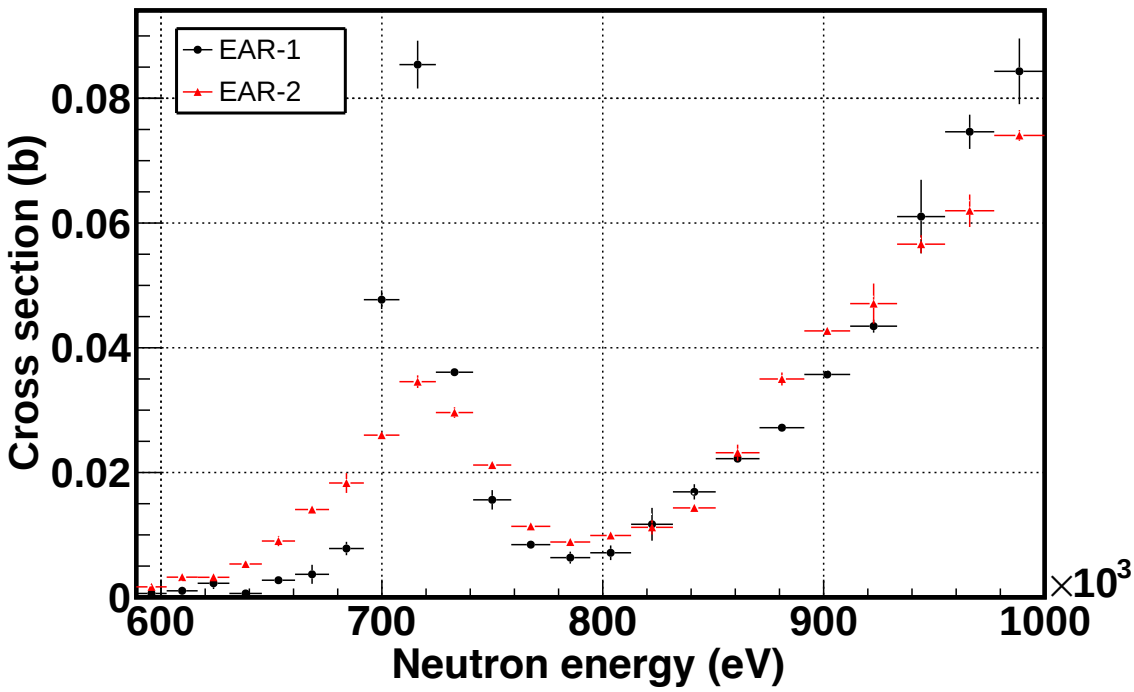

Figure 3.5: Cross-section of the ^{230}Th(n,f) reaction (black circle) from the EAR-1 measurement deduced using the ^{235}U(n,f) reaction as reference, in comparison with the cross-section of the EAR-2 measurement (red triangle) deduced using the ^{238}U(n,f) reaction as reference in the same energy region. The binning used is isolethargic with 100 bpd. Only the statistical uncertainties are shown in the figure.

The cross-section results of the ^{230}Th(n,f) reaction from 0.8 up to 1.5 MeV, are presented in figure 3.6, along with the previous datasets in this energy region. As seen in the figure, the data from the present work are in very good agreement with the data of Meadows and Muir and Veeser, as well as with the surrogate data from Goldblum *et al.* and Petit *et al.* for energies higher than 1.2 MeV. Good agreement within the given uncertainties is observed also with the data of Blons *et al.* up to 0.9 MeV. However, the data from Blons *et al.* for energies higher than 0.9 MeV and the data from James *et al.* have higher cross-section values than the data from the present work. These higher cross-section values could be a result of the normalization of both datasets to the same cross-section value at 1.4 MeV.

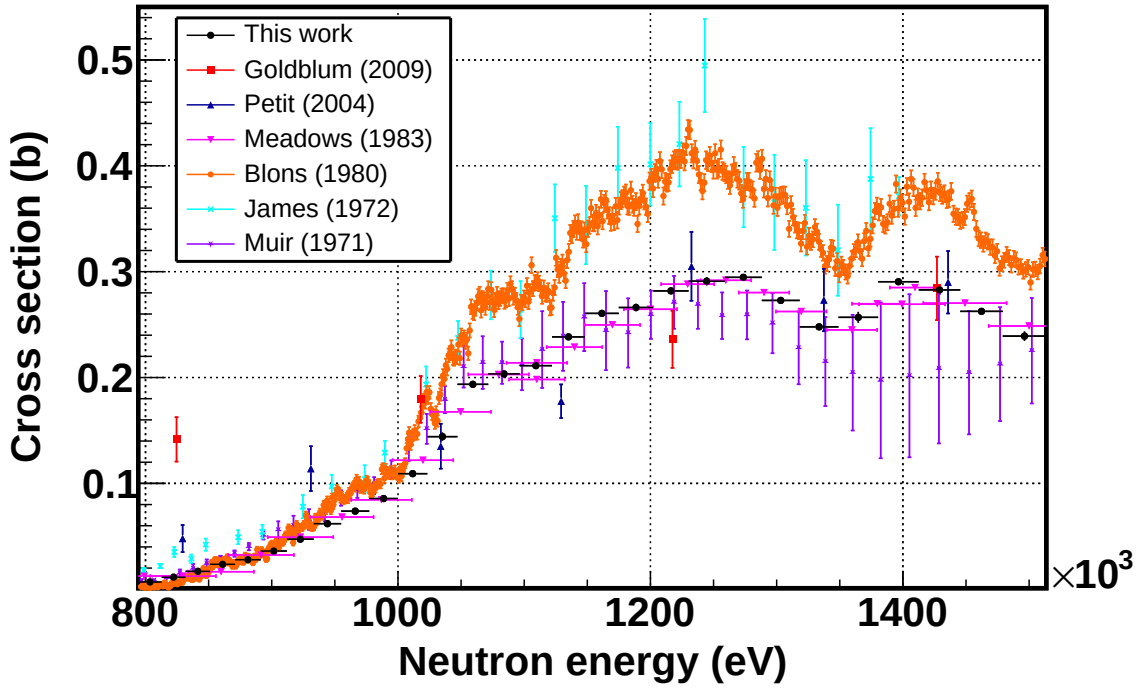

Figure 3.6: Cross-section of the ^{230}Th(n,f) reaction (black circle) from the EAR-1 measurement, deduced using the ^{235}U(n,f) reaction as reference, plotted along with the previous datasets between 0.8 and 1.5 MeV. The binning used is isolethargic with 100 bpd. Only the statistical uncertainties are shown in the figure.

The cross-section results of the ^{230}Th(n,f) reaction in the energy region of the fission plateau, between 1.5 and 6 MeV are presented in figure 3.7, along with the previous datasets in this energy region. As seen in the figure, the data from this work are in very good agreement with the data of Goldblum *et al.*, Meadows and Muir and Veeser. Regarding the data of Blons *et al.* and Kazarirova *et al.* [34], they are in agreement with each other and systematically higher than the data of the present work and the other datasets, a behavior which is observed in the data of Blons *et al.* also at lower energies. Concerning the data of Petit *et al.* they do not follow the trend of increase in the cross-section at around 1.8 MeV and even though they are in agreement within uncertainties in this energy region with the previous datasets, they are in general systematically lower.

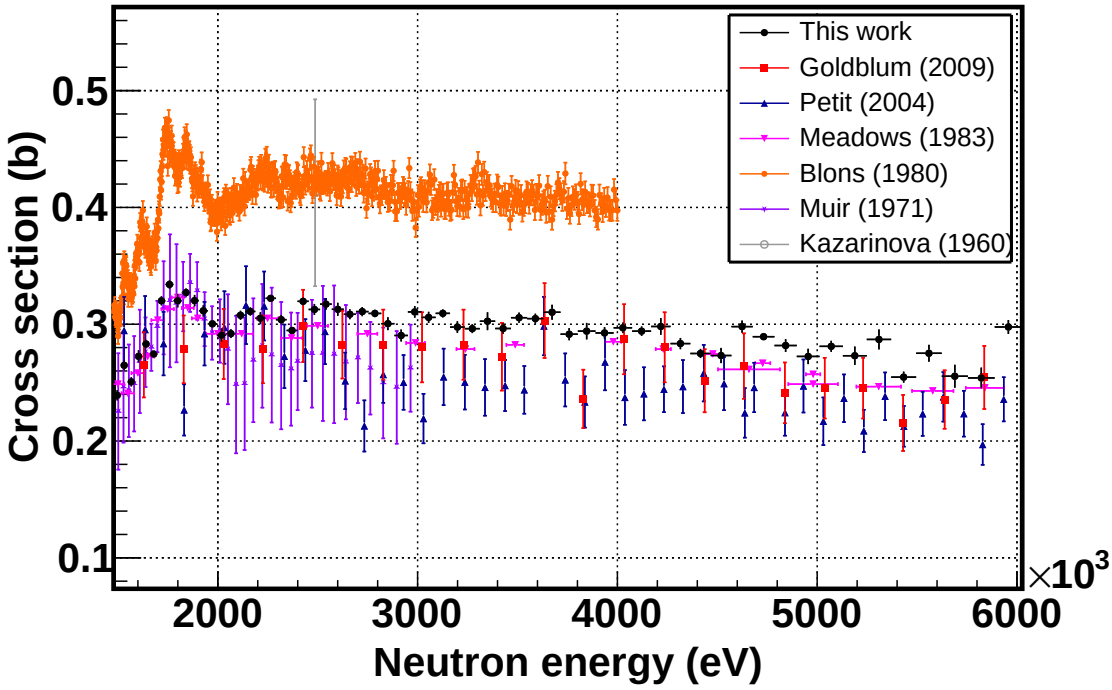

Figure 3.7: Cross-section of the ^{230}Th(n,f) reaction (black circle) from the EAR-1 measurement, deduced using the ^{235}U(n,f) reaction as reference, plotted along with the previous datasets between 1.5 and 6.0 MeV. The binning used is isolethargic with 100 bpd. Only the statistical uncertainties are shown in the figure.

In the higher energy region the cross-section results of the ^{230}Th(n,f) reaction from this work are presented in figure 3.8 along with the previous datasets in the same energy region. As seen in the figure, the cross-section results from this work are in very good agreement with the data from Goldblum *et al.*, Meadows and Kazarinova *et al.*, while the data from Petit *et al.* are systematically lower, following the trend of the previous energy region. For energies higher than 14 MeV, only the data of Goldblum *et al.* exist in literature and for energies higher than 17 MeV differences are observed between the data of the present work and Goldblum *et al.* in the cross-section shape as well as in the cross-section value. It is interesting to note that peaks from higher chance fission cross-section are present in the data at ∼7.6 MeV, ∼17.5 MeV and ∼23 MeV for the second, third and fourth chance fission respectively.

For energies higher than 25 MeV, no datasets exist in literature. The ^{230}Th(n,f) cross-section is measured for the first time in this work for energies from 30 MeV up to 400 MeV, extending this way the energy range of the previous data. The cross-section results are shown in figure 3.9.

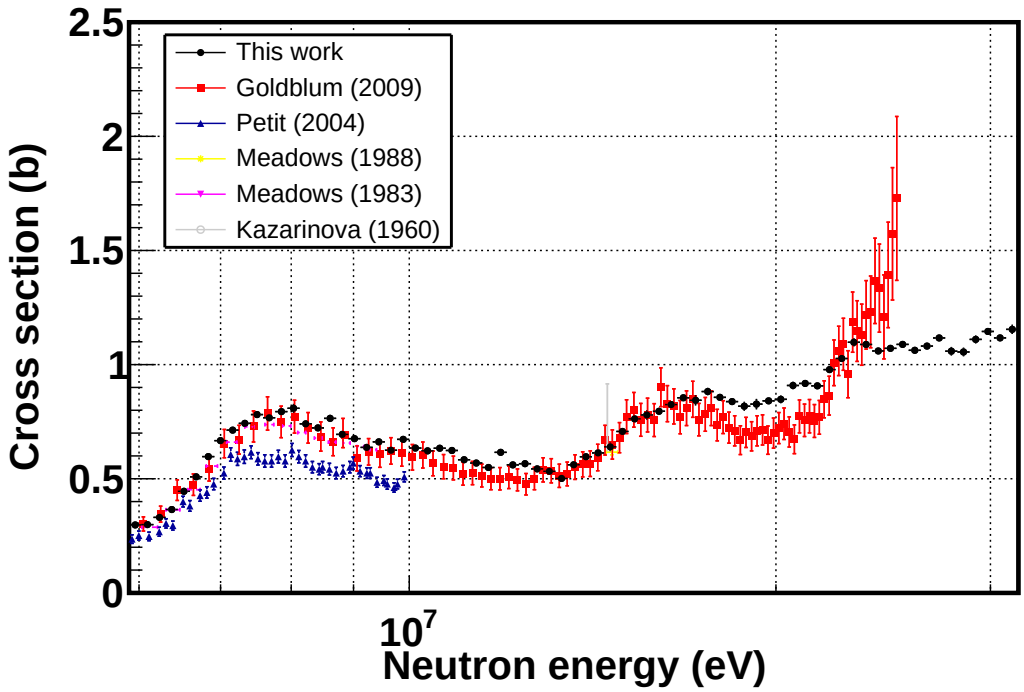

Figure 3.8: Cross-section of the ^{230}Th(n,f) reaction (black circle) from the EAR-1 measurement, deduced using the ^{235}U(n,f) reaction as reference, plotted along with the previous datasets between 6.0 and 30.0 MeV. The binning used is isolethargic with 100 bpd. Only the statistical uncertainties are shown in the figure.

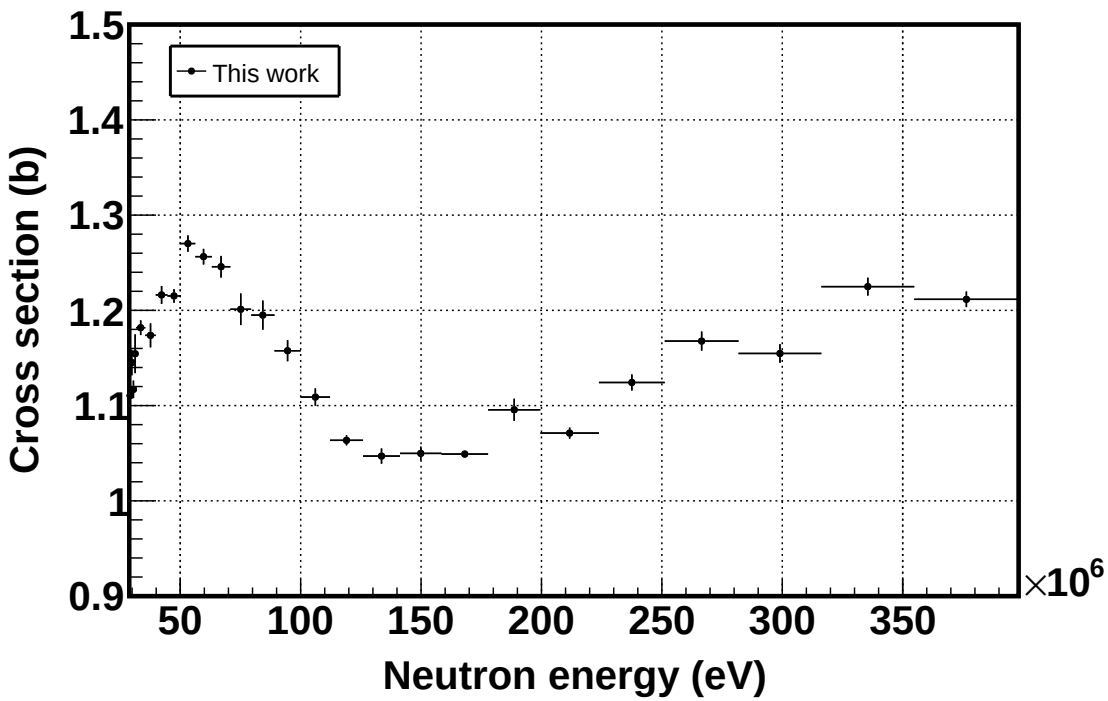

Figure 3.9: Cross-section of the ^{230}Th(n,f) reaction (black circle) from the EAR-1 measurement, deduced using the ^{235}U(n,f) reaction as reference, for energies between 30.0 and 400.0 MeV. The binning used is isolethargic with 20 bpd. Only the statistical uncertainties are shown in the figure.

In figure 3.10 the cross-section results of the ^{230}Th(n,f) reaction are shown in comparison with the latest evaluated libraries ENDF/B-VIII.0 which adopts the JENDL-4.0 [49] library (red), JEFF-3.3 [50] (blue) and TENDL-2019 [51] (green). As seen in the figure, the data of this work are in very good agreement with the JENDL-4.0 evaluation from the fission threshold and the resonance up to 7 MeV, while at higher energies the JENDL-4.0 evaluation underestimates the cross-section values. Regarding the JEFF-3.3 evaluation the resonance seems to be underestimated, as well as the cross-section values, even though the shape of the cross-section is generally reproduced. Concerning, the TENDL-2019 evaluation, which is the only one for energies higher than 20 MeV, it is not reproducing the cross-section results neither in shape nor in the cross-section values. Especially, below 5 and above 22 MeV the discrepancies with the present data are significant.

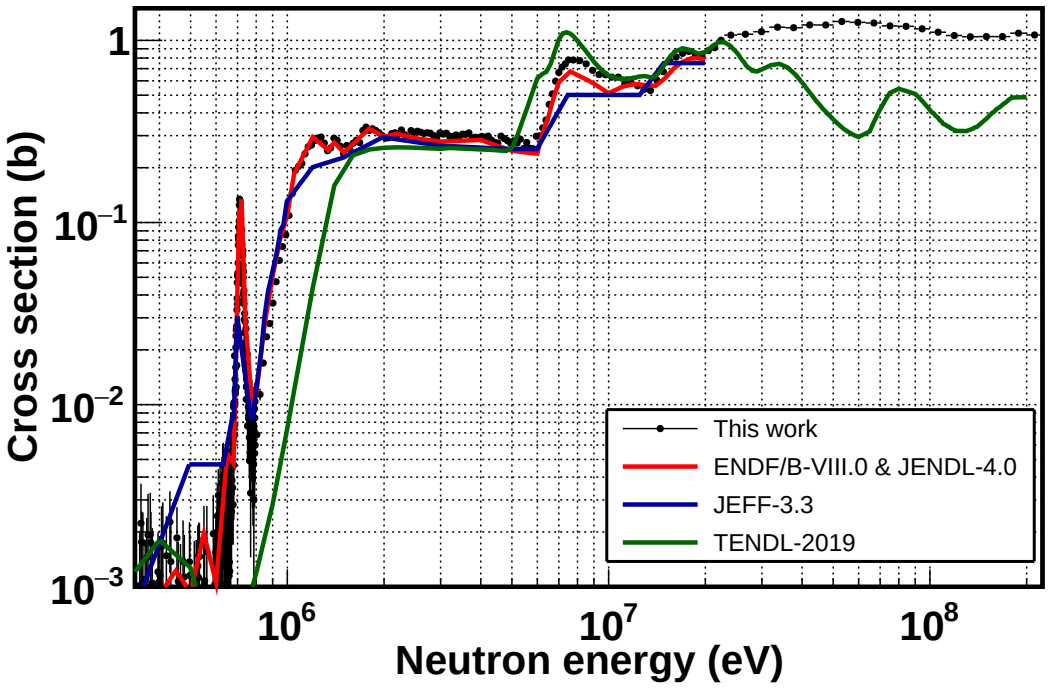

Figure 3.10: Cross-section of the ^{230}Th(n,f) reaction from this work (black circle) (EAR-1 measurement) in comparison to the latest evaluated libraries ENDF/B-VIII.0 which adopts the JENDL-4.0 library (red), JEFF-3.3 (blue) and TENDL-2019 (green). Only the statistical uncertainties are shown in the figure.

3.1.3 Uncertainties

The statistical uncertainty of the ^{230}Th(n,f) cross-section, is shown in figure 3.11 for energies higher than 0.8 MeV, which is the mean value of the seven ^{230}Th targets. The statistical uncertainty is a result of the statistical uncertainty of the ^{230}Th targets, the statistical uncertainty of the ^{235}U target used as reference for the estimation of the cross-section, as well as the choice of binning used for the results. As seen in figure 3.11, the statistical uncertainty is less than 4.5% for energies higher than 0.8 MeV. In the resonance peak the statistical uncertainty is less than ∼7%, but increases at the edges of the peak, as a result of the low statistics due to the fine binning selected

in the region, in combination with the decrease of the cross-section. While, this is a result of a selected binning in the region and a coarser binning would improve the statistical uncertainty, it would come at the cost of worse energy resolution, which is crucial in the region of the resonance in order to describe in as much detail as possible the structures of the resonance.

Concerning the systematic uncertainty of the ^{230}Th(n,f) cross-section, it is a result of several factors involved in the cross-section calculation, listed in table 3.1. Firstly, the systematic uncertainty on the mass of the ^{230}Th target which is of the order of 1%, originating from the α-spectroscopy measurements implemented to estimate the mass of the targets. The corrections from the FLUKA simulations, namely the correction for the amplitude cut applied in the analysis and the correction for the fission fragments which do not manage to enter the detector gas, introduce systematic uncertainties in the analysis. In order to estimate the systematic uncertainty from this correction the following method was employed: the final cross-section results were calculated in two independent ways, the first one as described in section 2.3.4 with the use of the FLUKA simulations and the second one assuming the same thickness for all targets (the seven ^{230}Th and the ^{235}U) and applying the same amplitude cut in all targets (selected from the amplitude cut spectra). As a result, the systematic uncertainty of the amplitude cut correction is estimated from the difference in the final cross-section values of the two methods to be less than 2.2%.

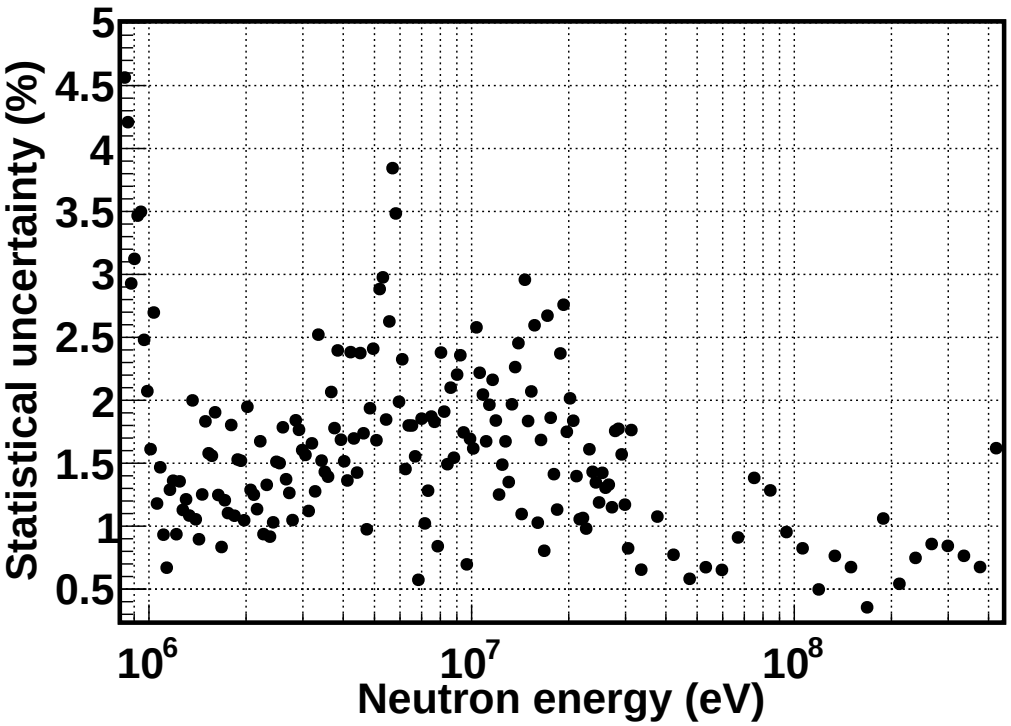

Figure 3.11: Statistical uncertainty of the ^{230}Th(n,f) cross-section from the EAR-1 measurement, for energies higher than 0.8 MeV, in isolethargic variable binning (100 bpd and 20 bpd varying at different energy regions).

Table 3.1: Systematic uncertainties of the ^{230}Th(n,f) cross-section calculation.

Contribution	Uncertainty
Sample mass	1%
Amplitude cut correction	< 2.2%
^{235}U(n,f) cross-section	1.3 - 5%
Dead time	< 1%
Neutron beam fluence	< 1%

Another factor contributing to the systematic uncertainty of the cross-section, is the uncertainty of the ^{235}U(n,f) cross-section used as reference. The uncertainty dependents on the neutron energy, as shown in figure 3.12. As seen in the figure, the uncertainty is less than 1.5% for energies up to 20 MeV, less than 3% for energies up to 80 MeV and less than 5% for energies up to 400 MeV.

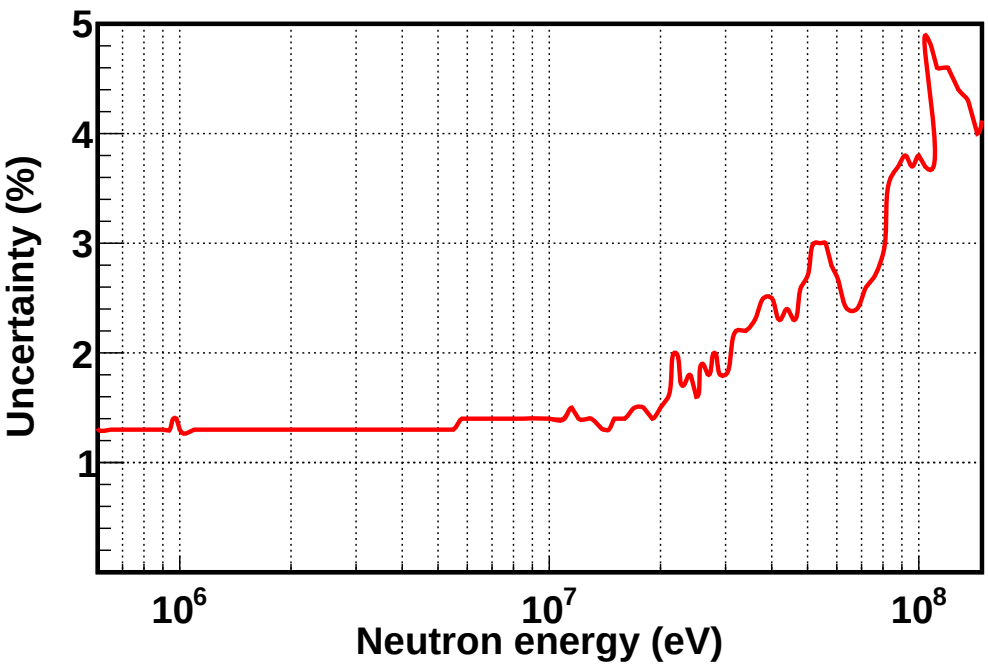

Figure 3.12: Cross-section uncertainty of the ^{235}U(n,f) reaction [25, 26, 27], used as a reference for the calculation of the fission cross-section of ^{230}Th.

Finally, the contributions to the systematic uncertainty of the dead time correction and the MCNP simulation for the different neutron fluence between the targets are considered negligible (< 1%) because the corrections are very small and a similar behavior is observed between the ^{235}U target and the ^{230}Th targets.

Chapter 4

Theoretical investigation

A theoretical investigation of the ^{230}Th(n,f) cross section was performed with the use of the EMPIRE code, in order to reproduce the experimental results of this work via statistical model calculations. To this end, various fission parameters of the thorium isotopes were adjusted in the EMPIRE calculations (fission barrier heights and widths, asymptotic level density parameter) in order to achieve a good reproduction of the experimental cross section.

4.1 Nuclear fission

Fission was discovered in an effort originating from Enrico Fermi and his co-workers to produce nuclei with increasing atomic numbers by bombarding them with neutrons. But it was Hahn and Strassmann [77] who managed to separate barium from uranium bombarded with neutrons. Based on this evidence, Meitner and Frisch [78] in 1939 offered an explanation on the basis of the liquid drop model (LDM), proposing that the uranium nuclei after neutron capture are unstable and fission (a term borrowed from biology). Bohr and Wheeler [79], provided a full theoretical description of the fission mechanism, which is the basis on the understanding of the fission process until today. A description of the fission mechanism is given in Wagemans [80] and Vandenbosch and Huizenga [81].

In the LDM the nucleus is described as a charged liquid droplet, while the shell model deals with individual nucleons. The two nuclear models are combined to form the semiempirical mass formula (equation 4.1) for the binding energy of the nucleus, with the LDM claiming the first three terms and the shell model the last two terms of the formula.

$$\begin{aligned} E &= E_v + E_s + E_C + E_{sym} + E_p \\ &= a_v A - a_s A^{2/3} - a_C \frac{Z(Z-1)}{A^{1/3}} - a_{sym} \frac{(N-Z)^2}{A} + \delta \end{aligned} \tag{4.1}$$

In the semiempirical mass formula the first term, called the volume term, assumes each nucleon attracts only its closest neighbors. The second term, named surface term, takes into account the less tightly bound nucleons of the nuclear surface, contributing less than those in the center. Thus, the surface term is proportional to the

nuclear surface and it is subtracted from the formula. The third term, represents the Coulomb repulsion of the protons, hence it is called the Coulomb term. The Coulomb term tends to make the nucleus less bound, so it has a negative sign. The fourth term, called the symmetry term, is implemented in order to describe realistic nuclei which are stable when Z $\approx$ A/2, which is important for light nuclei, while its importance is reduced for heavier ones (which require additional neutrons for nuclear stability). Finally, the last term, named the pair term, takes into account the tendency of like nucleons to couple pairwise to stable configurations. So, $\delta = \pm a_p A^{-3/4}$, where the plus sign is used for even-even nuclei, the minus sign is used for odd-odd nuclei and $\delta = 0$ when A odd.

In the case an initial spherical nucleus starts to deform, it can be assumed that the volume remains constant, while the surface and Coulomb terms are affected by the deformation. The deformed nucleus can be described by an ellipsoid of revolution, where α is the semimajor axis and b is the semiminor one. Then the deviation of the ellipsoid from a sphere with radius R is given by equation 4.2, where ϵ is the distortion parameter related to the deformation parameter β ($\epsilon = \beta\sqrt{5/4\pi}$).

$$\begin{aligned} \alpha &= R(1+\epsilon) \\ b &= R(1+\epsilon)^{-1/2} \end{aligned} \tag{4.2}$$

The condition of the volume of the nucleus remaining constant is satisfied, since the volume of the spherical nucleus is equal to the volume of the nucleus as it deforms into an ellipsoid ($V = 4/3\pi R^3 = 4/3\pi\alpha b^2$). The surface of the ellipsoid increases as seen in equation 4.3.

$$S = 4\pi R^2(1 + \frac{2}{5}\epsilon^2 + \dots) \tag{4.3}$$

and consequently, the surface term of equation 4.1 increases accordingly. At the same time, with the protons being further apart inside the nucleus due to the deformation, the Coulomb term of equation 4.1 decreases as:

$$E_C = a_C \frac{Z(Z-1)}{A^{1/3}}(1 - \frac{1}{5}\epsilon^2 + \dots) \tag{4.4}$$

By the changing of surface and Coulomb terms of the semiempirical mass formula (equation 4.1) the difference of the binding energy between the spherical and the ellipsoid nucleus is presented in equation 4.5.

$$\begin{aligned} \Delta E &= E(\epsilon) - E(\epsilon = 0) \\ \Delta E &= -a_s A^{2/3}(1 + \frac{2}{5}\epsilon^2 + \dots) - a_C \frac{Z(Z-1)}{A^{1/3}}(1 - \frac{1}{5}\epsilon^2 + \dots) \\ &\quad + a_s A^{2/3} + a_C \frac{Z(Z-1)}{A^{1/3}} \\ \Delta E &\approx (-\frac{2}{5}a_s A^{2/3} + \frac{1}{5}a_C \frac{Z(Z-1)}{A^{1/3}})\epsilon^2 \end{aligned} \tag{4.5}$$

When the second term of equation 4.5 is larger than the first, the nucleus gains energy as it deforms from spherical to ellipsoid, so it continues to deform gaining more energy. These nuclei are unstable against fission and will eventually separate into two parts, without any additional energy provided to the nucleus. This condition is met when $E_C/2E_s > 1$, with the corresponding ratio x (equation 4.6) named as the fissility parameter.

$$x = \frac{E_C}{2E_s} \tag{4.6}$$

The condition of the fissility parameter being larger than one, meaning as already mentioned that fission will occur, is equivalent after calculations with the following condition:

$$\frac{Z^2}{A} > 50 \tag{4.7}$$

This implies that nuclei with Z>125 would spontaneously fission immediately after their creation. In the case of ^{230}Th the value of Z^2/A is 35.2 with $x = 0.69$.

4.1.1 The double-humped fission barrier

Within the framework of the LDM, the fission process is described as a single-humped barrier penetration. However, this approach fails to explain effects caused by the shell structure of the nucleus, such as the symmetric and asymmetric modes for the mass distribution of the fission fragments [82, 83], the different thresholds and angular anisotropies for these two modes [84, 85], the barrier heights [86] and the fission isomers [87, 88]. This resulted in adding shell and pairing corrections in the estimation of the fission barriers. In 1967 Strutinsky [89, 90] added a shell correction term, which indicated an oscillation of the energy curve of actinides as they get deformed, generating this way a double-humped fission barrier. A detailed description of the double-humped fission barrier is given by Bjørnholm and Lynn [91], while in figure 4.1 a double-humped fission barrier is shown, along with the corresponding liquid drop model single-humped fission barrier with no shell corrections. The states of the first well are closely spaced and called Class-I states, while the states of the second well are broader and sparsely spaced, called Class-II states. The structure of the secondary well was able to explain fission isomers and structures in the subthreshold fission cross-section.

Fission isomers are states with very long half-lives for spontaneous fission. These isomers are explained as states of the second potential well, which can either undergo fission penetrating a thin barrier, instead of decaying by γ-emission to the ground state. In addition, the double-humped fission barrier can explain the structure of the resonances in the fission cross-section. Individual fission resonances in

the eV-keV region are explained as excited states from the first potential well, originating from the compound nucleus at normal deformation. Additional fission resonances, with significant fission cross-section appear in clusters. Each cluster corresponds to a Class-II state of the second potential well, while the narrower and closely spaced resonances correspond to Class-I states of the first potential well.

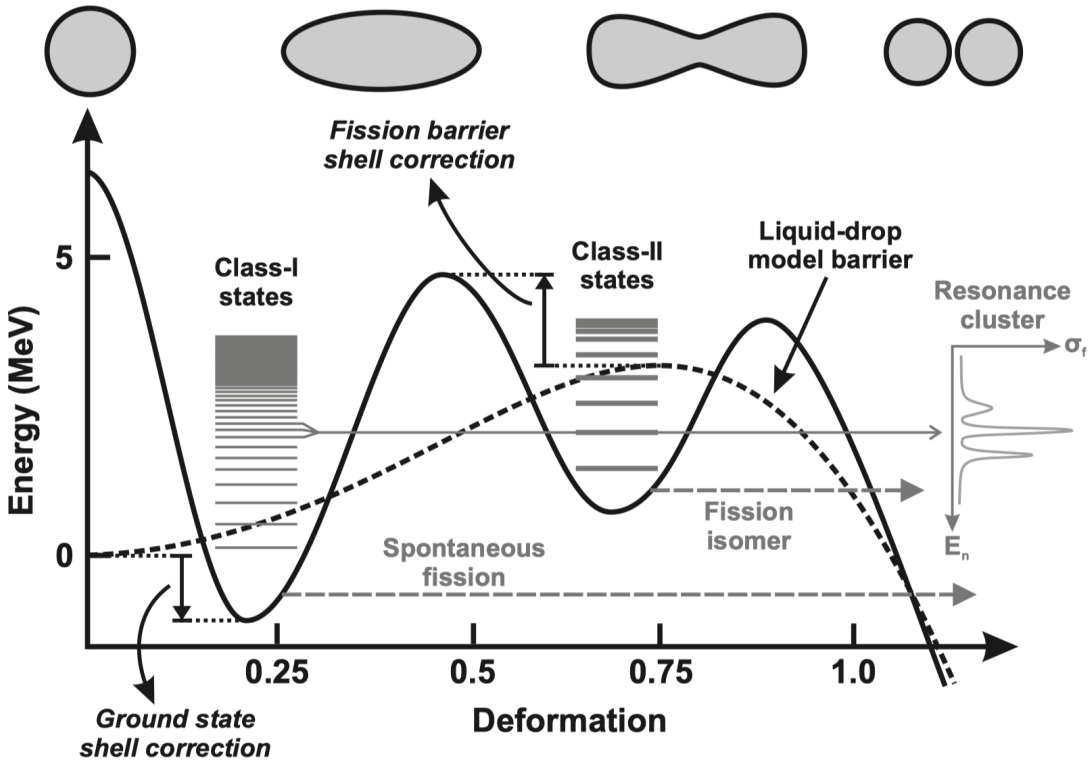

Figure 4.1: Schematic representation of the double-humped fission barrier (black line), with the corresponding liquid drop model single-humped fission barrier with no shell corrections (dashed line). Fission resonances are a result of a coupling in energy and spin-parity of the Class-I states with the Class-II ones. When a nucleus is excited in a Class-I state of the first potential barrier that is coupled with a Class-II state of the second potential barrier, the fission probability is higher, since only one barrier must be penetrated to fission, and a resonant structure is seen in the fission cross-section. The axis values are indicative [92].

4.1.2 Thorium anomaly

The double-humped fission barrier approach fails to explain narrow resonances and fine structures in the threshold region of the fission cross-section, something known as the thorium anomaly. The existence of these resonances implies that the second barrier is dominant. In order to explain the presence of the resonances, Möller and Nix [93] performed calculations indicating the splitting of the outer barrier peak creating this way a shallow (rougly 1 MeV deep) third well, forming a triple-humped barrier. This third well allows the existence of Class-III vibrational states, that could explain the structures found near the fission threshold. A schematic representation of the triple-humped barrier is shown in figure 4.2. Calculations made with a model incorporating the triple-humped fission barriers for the ^{232}Th and ^{231}Pa nuclei were

able to reproduce the resonant structure in the first-chance neutron-induced fission cross sections [94].

Based on the large and well isolated resonance, as well as the fine structures present in the ^{230}Th(n,f) cross-section, Blons *et al.* [48] supported the triple-humped barrier approach concluding in the presence of two rotational bands with the same quantum number but opposite parities (which is the result of a pear-like octapule deformation) combined with the low value of the moment of inertia (which implied larger quadrupole deformation than the one associated with the second barrier). Another approach by Boldeman *et al.* [95], within the triple-humped barrier model, interprets the resonant structure in the ^{230}Th(n,f) cross-section as a pure vibrational resonance in the third well. A more recent study by Mirea *et al.* [96] provides another origin for the fine structure of the resonance in the threshold region of the ^{230}Th(n,f) cross-section, within the hybrid model taking into account dynamical particle effects, within the double-humped potential.

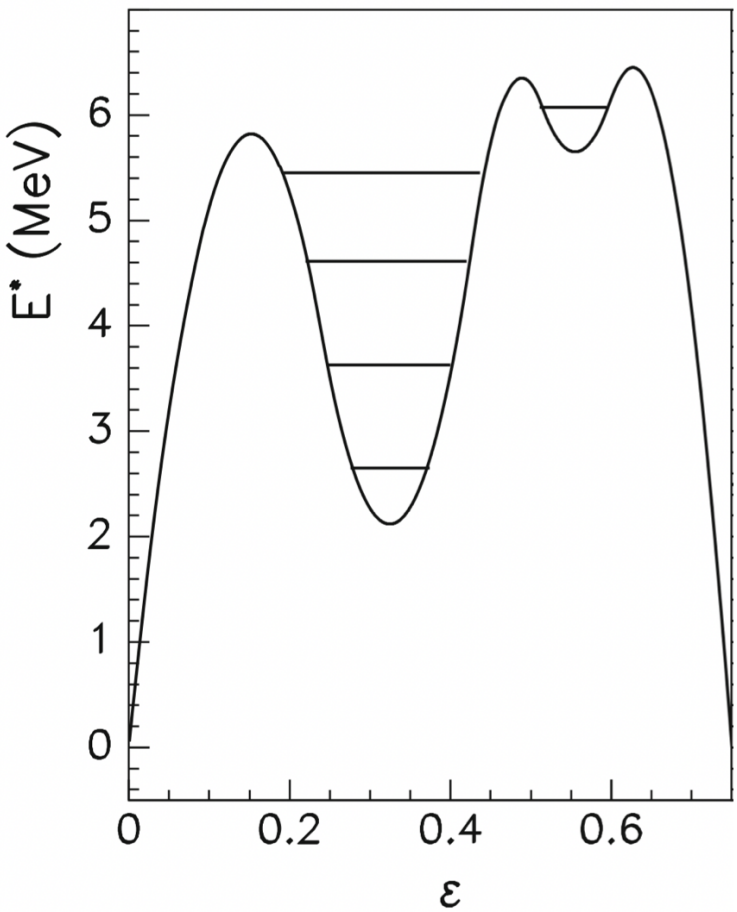

Figure 4.2: Schematic representation of the triple-humped fission barrier as function of the elongation variable [7]. The parameters of the barrier are for the nucleus ^{232}Th [94].

In the attempt to explain the resonances and fine structures present in the fission cross-section of light actinides various publications exist in literature. Theoretical calculations have been performed for the ^{230}Th(n,f) cross-section structure for a double-humped fission barrier [30, 96, 70] or a triple-humped fission barrier [48, 97, 29, 28, 95, 98, 99], many of them reproducing very well the fine structures of

the ^{230}Th(n,f) resonance. In order to constrain the theoretical models more detailed fission cross-section measurements and angular distributions are required [99]. Indeed, fission fragment angular distributions and anisotropies have been measured by Boldeman *et al.* for the energy range 680-1100 keV [95], James *et al.* for the energy range 625-1400 keV, Yuen *et al.* at 682, 715, 730, 740, 750 and 1000 keV and Simmons and Henkel [69] in the energy range 1 to 9 MeV. The analysis of the data in the region of the resonance revealed the simultaneous presence of two rotational bands with opposite parities but the same quantum number K and a low value of the associated moment of inertia parameter, indicating an asymmetric, pear-like octupole deformation in the third well [95].

4.1.3 Fission modes

During the process of nuclear fission a single nuclear system transits to two separated fragment nuclei. The shape of the fissioning nuclei evolves from a single shape corresponding to the nuclear ground state to the scission point corresponding to two touching fission fragments. Two fission modes can occur, the asymmetric and the symmetric, according to the observed fragment mass distribution. In order to describe realistically the fission process and explain the characteristic features of fission the structure of the fission potential-energy surface is required.

Nuclei below the actinide region exhibit both the symmetric and assymetric fission modes, while at certain excitation energies, the combination of the two modes results in a three-peaked structure of the mass distribution of the fission fragments. Nuclei at the upper end of the actinide region sometimes display two-mode fission in the same nucleus. Nuclei in the actinide region below Fm, divide into a heavy fragment with mass near 140 and a light fragment with a mass that shifts according to the mass of the fissioning nuclei, a behavior explained by shell structure effects.

For the explanation of these fission characteristics a five-dimensional potential-energy surface approach has been proposed [100, 101]. The five independent shape parameters for the potential energy calculations being the elongation, mass asymmetry (M1-M2)/M1+M2) of the two pre-scission, still connected, fragments, left and right fragment deformation and neck, as seen in figure 4.3. The total potential surface in these calculations, has "valleys" in the space of elongation and "ridges" that are higher than the saddles and inhibit the movement between "valleys". Coexistence of two fission modes (the symmetric and asymmetric fission fragment mass distribution), can cause for example two separate peaks in kinetic energy distributions and separate energy thresholds for the onset of symmetric and asymmetric fission. In the case of ^{232}Th, the symmetric and asymmetric fission paths are well separated by a high ridge from saddle to scission, as seen in figure 4.4, thus verifying that at low excitation energies two fission paths exist with little or no overlap, which is a more general feature in light actinides.

The theoretical investigation of the fission process is still ongoing and even after 80 years since the discovery of this phenomenon, many of its aspects remain unresolved.

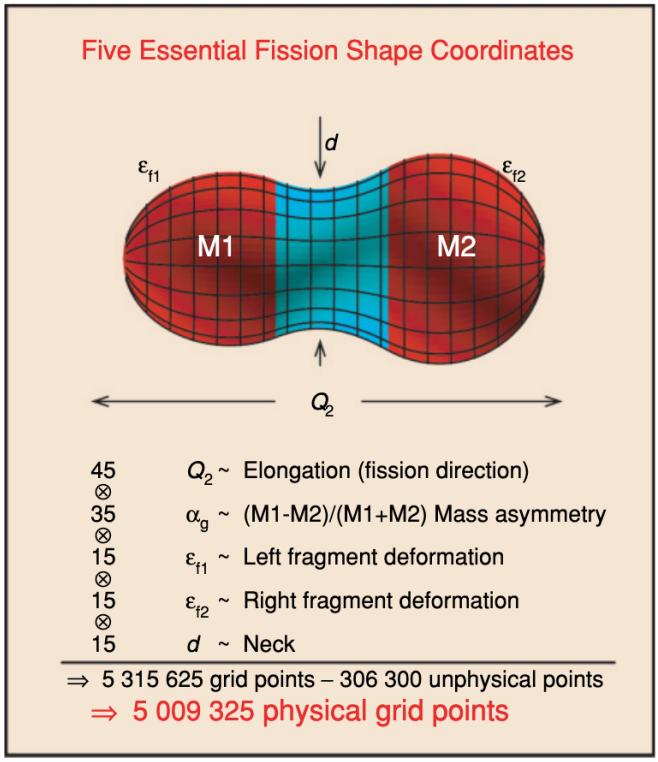

Figure 4.3: Representation of the shape of the elongated nucleus, at the pre-scission phase [101].

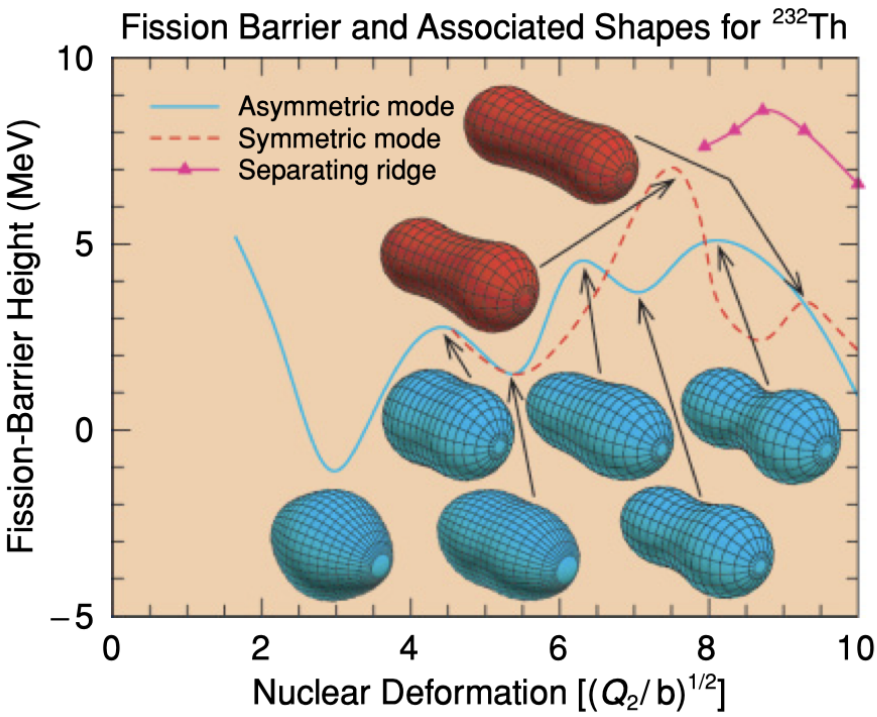

Figure 4.4: Fission barriers for ^{232}Th calculated for two different fission modes (symmetric and asymmetric) well separated by a high ridge. Shapes associated with the barrier curves are also displayed for representative points [101].

4.1.4 Fission fragment angular distributions

The angular distribution of fission fragments is a result of two quantities: the angular momentum of the projectile and the fraction of this angular momentum that converts to orbital angular momentum between the fission fragments. This fraction is characterized by a parameter K, where K is the component of the total angular momentum of the deformed nucleus along the nuclear symmetry axis. In the process the compound nucleus transits to the saddle point, suffers vibrations and changes in shape, while its energy and angular momentum are being redistributed in many ways. This is implemented in such a way that the K value of the transitional nucleus is unrelated to the initial K value of the compound nucleus. A schematic representation of the angular momentum coupling scheme is shown in figure 4.5. An overview on the angular distributions of fission fragments is presented in [81].

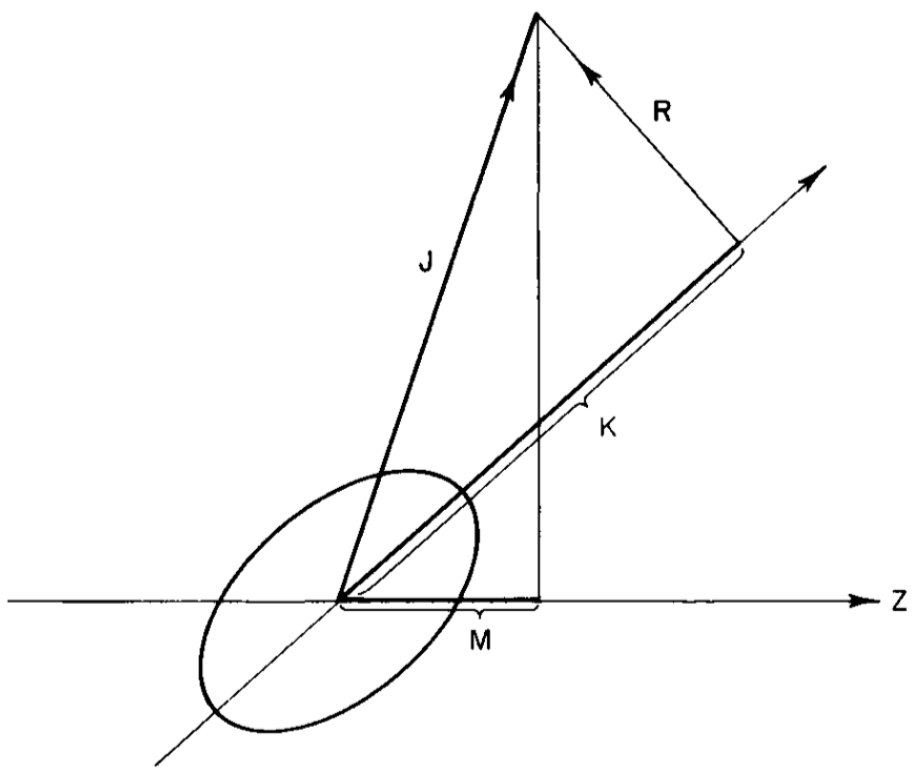

Figure 4.5: Schematic representation of a compound nucleus, where J is the total angular momentum, and M, K and R are the projections of the angular momentum on the space fixed axis Z (beam direction), on the symmetry axis of the compound nucleus and on an axis perpendicular to K [81].

A periodic structure often present in the fission fragment anisotropy data as a function of projectile energy is a result of multichance fission, as also seen in the anisotropy data in this work for the anisotropy of the ^{230}Th(n,f) reaction (figure 2.7). The compound nucleus can decay either by neutron emission or by fission. If neutron emission occurs, the competition between fission and neutron emission continues until the excitation energy is smaller than the neutron binding energy and the fission

threshold. The fragment anisotropy of the second chance fission (when fission occurs after one neutron emission from the compound nucleus) can be very large, especially for even-even target nuclei, where the effect of pairing lowers the threshold energy of the second chance fission. The peak at each multichance fission can be explained by the temperature decrease after neutron emission, leading to the drop of K [102]. In general, the structure of the anisotropy is correlated with the structure of the total cross-section, as can be also seen in the cross-section data of this work (figure 3.3). As higher chance fission is energetically possible, an increase is observed in the total fission cross-section, which then decreases until another higher chance fission becomes energetically possible.

At low excitation energies, near the fission barrier, fission occurs through states in the transitioning nucleus. Most of the excitation energy of the compound nucleus is used for the deformation of the transitioning nucleus. As a result, the nucleus is thermodynamically cold, thus having a spectrum of excited states. Information on the level structure of the transitioning nuclei, for excitation energies near the fission barrier, can be obtained from the angular distributions of the fission fragments.

4.2 The EMPIRE code

The EMPIRE code [37] is a modular system of nuclear reaction codes, containing various nuclear models and can be used in a wide energy range and for several interacting particles. The code is suitable for the theoretical investigation of nuclear reactions and for nuclear data evaluations. EMPIRE contains the major nuclear reaction models, such as the optical model (also for fission), Coupled Channels and DWBA, Multi-step Direct, Multi-step Compound, exciton model for pre-equilibrium emission, hybrid Monte Carlo simulation, and the full Hauser-Feshbach statistical model including width fluctuations for gamma decay of the compound nucleus.

4.2.1 Hauser-Feshbach statistical model

The theoretical calculations in this work were performed within the Hauser-Feshbach model. Based on Bohr's assumption, the probability for creation of the compound nucleus in a particular state is independent from the probability of decay in a particular decay channel. In the Hauser-Feshbach statistical model the (α,b) reaction cross-section is given by:

$$\sigma_{\alpha,b}(E) = \sum_{J\pi} \sigma_a(E, J\pi) P_b(E, J\pi) \tag{4.8}$$

where $\sigma_a(E, J\pi)$ is the cross-section for the formation of the compound nucleus in a state of spin and parity $J\pi$ and $P_b(E, J\pi)$ represents the decay probability of the compound nucleus in channel b. If the compound nucleus is excited in a state with energy E^* in channel b, the decay probability is given in terms of transmission coefficients

$$P_b(E, J\pi) = \frac{T_b(E^*, J\pi)}{\sum_c T_c(E_C^*, J\pi)} \tag{4.9}$$

where T_b is the transmission coefficient of channel b, while the denominator is the sum of all other possible exit channels, which might include particle emission, photon emission or fission. The transmission coefficient of channel b depends on the level density model, the optical model and the gamma-ray strength function.

In case the residual nucleus is left in an excited state E_B^* with a density of states $\rho_B(E_B^*)$ equation 4.9 can be written as

$$P_b^{l_\pi} = \frac{T_l(\epsilon_b)\rho_B(E_B^*)}{\sum_\gamma T_{\gamma,l}\rho_c(E_C^*, J\pi)} \tag{4.10}$$

In case spin is taken into account the cross-section of the entrance channel is calculated by the Optical Model, considering the interaction of the particle beam and the target nucleus as scattering of light on a dark sphere. As a result, the final cross-section of the reaction channel, taking into account the sum over all the possible spin additions in the entrance (allowed by the energy conservation and selection rules) and exit channel, is shown in the following equation

$$\sigma_{\alpha,b}(E) = \frac{\pi}{k^2}\sum_J \frac{2J+1}{(2s+1)(2S+1)} \frac{\sum_{l,j,l',j'} T_l(E)T_{l'(\epsilon_b)}\rho_B(E_B^*, S')}{\sum_{\gamma,l'',j''} T_{\gamma,l''}\rho_C(E_C^*)} \tag{4.11}$$

where j and J are the angular momenta of the entrance channel and of the compound nucleus respectively, s, S and S$'$ are the spins of the incident particle, the target nucleus and residual nucleus respectively.

The fission cross-section within the Hauser-Fesbach model, is described as a decay channel of the compound nucleus. The optical model for fission can be used from sub-barrier excitation energies up to 200 MeV and it describes the transmission through multi-humped fission barriers [103]. With the use of the optical model for fission the different degrees of damping of the vibrational states within the wells are taken into account.

It is important to note that different combinations for the barrier heights and for the level densities can give the same cross-section value [7]. For this reason additional experimental quantities, such as competing reaction channels, angular distribution of fission fragments, distribution of the total angular momentum in the primary fragments, isomer excitation, mass distributions of fission fragments, etc. can assist in order to constrain the theoretical models. Unfortunately, for the study of the ^{230}Th fission cross-section no complementary experimental data, such as other reaction channels, exist in literature. Some angular distribution data around the resonance exist, however EMPIRE in its present version has not implemented statistical models for the angular distributions of the fission fragments.

4.2.2 Models for the EMPIRE calculation

As already mentioned in section 4.1.2 various approaches exist in literature to reproduce the fission cross-section data of ^{230}Th, based either on the double-humped barrier, or on the triple-humped barrier. It is important to note, that for the case of the fission cross-section of ^{232}Th the gross resonant structure was reproduced very well in the triple-humped barrier approach within the optical model for fission, attributed to partially damped vibrational states in the second well and undamped vibrational states in the third well [94]. However, in this work, the double-humped fission barrier was chosen for the calculations with the EMPIRE code in order to reproduce the general trend of the fission cross section. Even though, the triple-humped barrier might be able to reproduce in a better way the resonance and fine structures of the fission cross-section of ^{230}Th, the energy resolution of this work and the statistical uncertainty in the resonance region was not as good as the previous measurement by Blons *et al.* to justify this more complicated approach. In addition, a detailed theoretical study of the fission process and the barrier characteristics lies beyond the scope of the present work, that used for theoretical calculations a phenomenological approach in order to reproduce the gross shape of the cross-section, in the framework of an experimental work for the measurement of the ^{230}Th(n,f) cross-section.

For the present calculation of the ^{230}Th fission cross-section the EMPIRE code (version 3.2.3 Malta) was used. The decay channels with charged particles were neglected, so in addition to fission the (n,el), (n,inl), (n,γ) and (n,xn) channels were taken into account for the calculations. The optical model parameters were taken from the Reference Input Parameter Library (RIPL-3) [38] for the inelastic (direct) channel and for the inverse neutron channel. The optical model potential used, with RIPL catalog number 2408 [39], is a global dispersive coupled-channel optical model for the description of neutron and proton interactions with actinide nuclei for energies between 0.001 to 200 MeV [104]. The phenomenological model PCROSS (with parameter 1.5) was used for the preequilibrium mechanism, which is described by the classical exciton model including nucleon, cluster and gamma emissions [40, 41]. For the modeling of the γ-ray strength functions the modified Lorentzian MLO1 was used [42]. The level densities in the continuum of the normal states corresponding to the equilibrium deformation were estimated with the Enhanced Generalized Superfluid Model (EGSM) (including an adjustment to discrete levels) [43], which is the default level density model in EMPIRE. The EGSM, uses the super-fluid model below the critical excitation energy and the Fermi Gas model above, while it includes a more accurate treatment of high angular momenta than the Generalized Superfluid model. The same model (EGSM) was used for describing the level densities for the deformations to the saddle points (level densities of the transition states). In addition for the calculations with EMPIRE only single modal fission was considered, no discrete states above the fission barrier were taken into account, while subbarrier effects were taken into account.

Concerning the fission barriers taken into account for the calculation, as already mentioned above, the double-humped barrier approach was implemented. However, the already existing RIPL-3 fission barriers and fission widths had to be adjusted in order to be able to reproduce the experimental results. In addition, no fission barriers exist in the RIPL-3 library, for the thorium isotopes with mass number lower than 230. However, these fission barriers are required as input in the calculations in order to take into account multichance fission, in order to reproduce the structures in the fission cross-section at higher energies, as well as the competing (n,xn) channels. So, these fission barriers were adjusted in order to reproduce the experimental fission cross-section of this work.

The default EMPIRE calculation up to 200 MeV is presented in figure 4.6, along with the experimental data of the present work. As seen in the figure, the default calculations underestimate the slope and the value of the subthreshold fission cross-section. They also underestimate the fission plateau and the corresponding fission slope. In the higher energy region, the multichance fission cross-sections are also underestimated up to 75 MeV. At higher energies the cross-section is overestimated by the EMPIRE calculation.

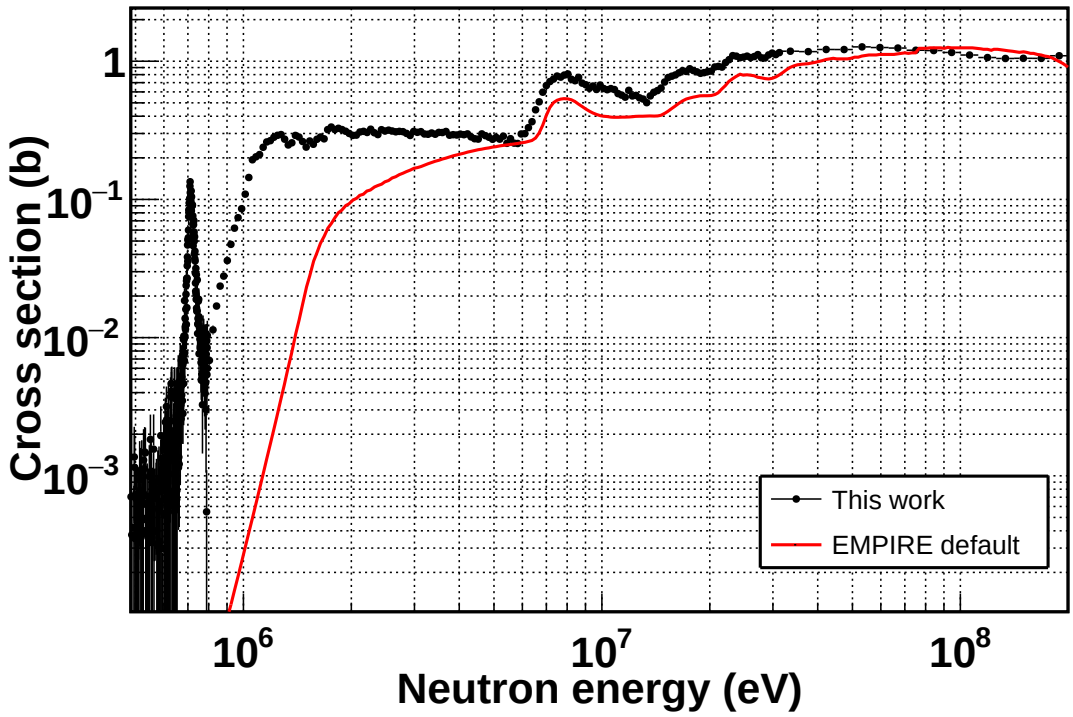

Figure 4.6: EMPIRE calculation from the fission threshold up to 200 MeV with the default parameters (red line) along with the experimental data of this work (black points), for the ^{230}Th fission cross-section.

As with the EMPIRE code calculation, the default calculation with the TALYS code (version 1.95) [105] was attempted. The default optical model potentials in TALYS of Koning and Delaroche [106] were used for the calculations. The fission barriers and widths of the calculation were within the double-humped barrier approach, taken from the RIPL-3 library. Concerning the level densities, the model implemented in

the calculations was the generalized superfluid model. As for the γ-ray strength function the Kopecky-Uhl generalized Lorentzian was used [107]. In addition to the above-mentioned calculation with the TALYS code, the calculation with the best card enabled was held. This is a set of adjusted nuclear model parameters which reproduce the optimal fit for measurements of all reaction channels of the nuclide of interest.

The calculations with the TALYS code, both with the default and best parameters from the fission threshold up to 200 MeV are presented in figure 4.7, along with cross-section results of this work. As seen in the figure, the fission cross-section of the TALYS default calculation is lower than the experimental data for the whole energy region, while it fails to reproduce the shape of the cross-section in the fission threshold, the second chance fission, as well as the high energy region. Regarding the TALYS best calculation, it fails to reproduce the fission threshold, while for energies from 1.5 to 22 MeV the shape of the cross-section is reproduced quite well. Though for energies lower than 5 MeV the cross-section values are lower than the experimental data, for energies from 5 to 9.5 MeV the cross-section values are higher than the experimental data while the position of the second chance fission peak lies at lower energy compared to the experimental data.

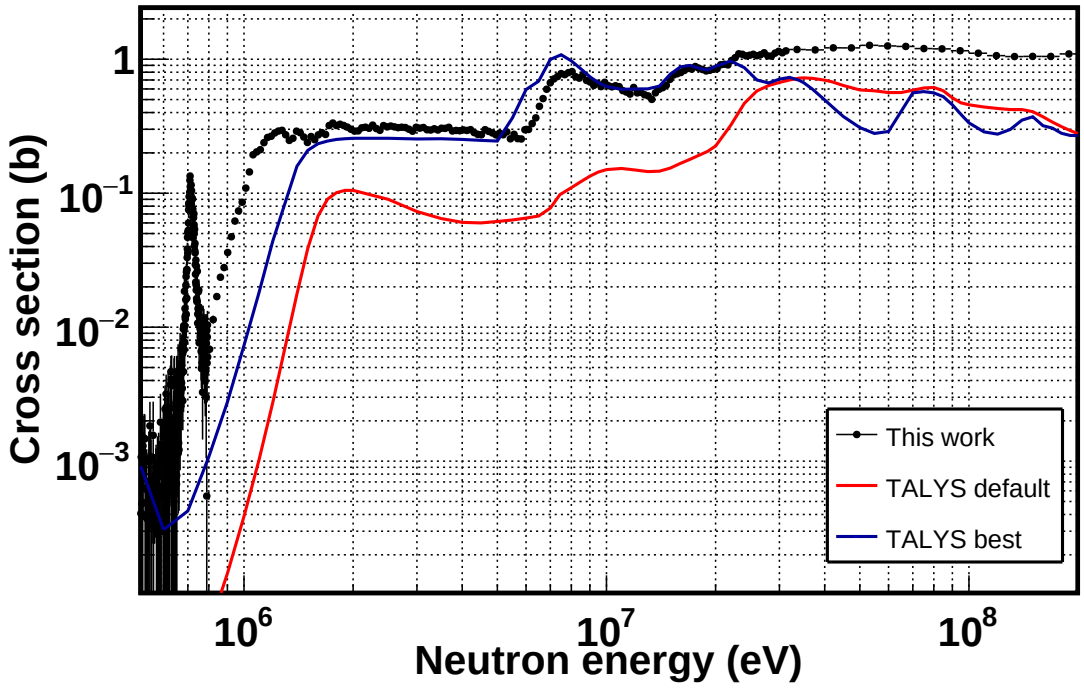

Figure 4.7: TALYS calculation from the fission threshold up to 200 MeV with the default parameters (red line) and the best parameters of the TALYS code (blue line), along with the experimental data of this work (black points), for the ^{230}Th fission cross-section.

Both the EMPIRE and TALYS calculations do not reproduce in a satisfactory way the fission cross-section of ^{230}Th. However, in the TALYS-1.95 manual it is stated that in order to obtain very satisfactory fits to fission data, many adjustable input parameters are required [107]. On the contrary, with the EMPIRE code, satisfactory reproduction of the fission experimental data can be achieved by adjusting only the

fission barrier heights, the fission barrier widths and the asymptotic level density parameter. For this reason, the theoretical study, in a phenomenological framework, of the fission cross-section of ^{230}Th of this work was performed via the EMPIRE code.

4.2.3 Modified EMPIRE calculation

In an attempt to improve the agreement between the EMPIRE calculations and the experimental data of this work, with the scope of describing the gross structure of the fission cross-section, various adjustments were made in the fission barrier heights and widths, as well as the level density parameters of the thorium isotopes. Specifically, the second fission barrier height and the corresponding width of ^{231}Th were reduced by 8% and 28%, respectively, while the first fission barrier height was reduced by 3%. With these adjustments the description of the fission cross-section was improved up to 1.5 MeV, failing however to describe the fine structures for energies higher than 1.2 MeV. The asymptotic level density parameter of ^{230}Th was increased by 25% in order to decrease the fission cross-section in the energy region from 1.5 to 6 MeV. The second fission barrier height of ^{230}Th was decreased by 6% in order to better describe the first chance fission cross-section. Although, the shape and value of the cross-section are not reproduced in the energy region from 8.5 to 13 MeV. For the higher energy region, the fission barrier heights and widths were chosen in order to prevent abrupt shapes in the fission cross-section shapes. Then the asymptotic level density parameter of ^{229}Th was decreased by 17%, in order to increase the cross-section for energies higher than 10 MeV and better describe the gross cross-section shape and values. The values of the fission barrier heights and widths of the thorium isotopes implemented in the calculations are presented in table 4.1. Comparing the barrier heights used for the calculations in the present work with the calculated barrier heights for Th isotopes in the work of Möller *et al.* [101], it can be seen that the first barrier height of the present work has higher values than Möller *et al.*, which are closer to the values proposed by the Reference Input Parameter Library (RIPL-3) [38]. While for the second barrier heights, both the heights of the present work and Möller *et al.* are lower than RIPL-3, but still the barriers of the present work have higher values compared to Möller *et al.*

The modified EMPIRE calculation with the adjustments previously stated, is presented in figure 4.8. As seen in the figure, the agreement between the EMPIRE calculations and the data has been improved. However, only the gross structure of the cross-section is reproduced. Fine structures at approximately 1.0 to 2.0 MeV in the fission plateau are not reproduced by the calculations. In addition, the shape and value of the cross-section in the energy region 8.0 to 13.0 MeV is also not described in a sufficient way. In the energy region 13 to 75 MeV the cross-section is reproduced quite well, failing however to match the higher chance fission shapes. For energies greater than 75 MeV, the cross-section value is overestimated and the cross-section shape is not reproduced well by the calculations.

Table 4.1: Fission barrier height and widths for the thorium isotopes used for the modified EMPIRE calculations. In bold, the values which are modified from the default ones are presented, while in italics the values which do not exist at all in RIPL-3 and are selected for the calculations.

Isotope	First barrier		Second barrier	
	V_A	$\hbar\omega_A$	V_B	$\hbar\omega_B$
^{223}Th	*6.00*	*0.90*	*6.70*	*0.60*
^{224}Th	*6.60*	*0.90*	*7.30*	*0.60*
^{225}Th	*6.60*	*0.90*	*7.30*	*0.60*
^{226}Th	*6.60*	*0.90*	*7.30*	*0.60*
^{227}Th	*6.60*	*0.90*	*7.30*	*0.60*
^{228}Th	*6.10*	*0.90*	*6.80*	*0.60*
^{229}Th	*6.10*	*0.90*	*6.30*	*0.60*
^{230}Th	6.10	0.90	**6.37**	0.60
^{231}Th	**5.80**	0.70	**6.15**	**0.36**

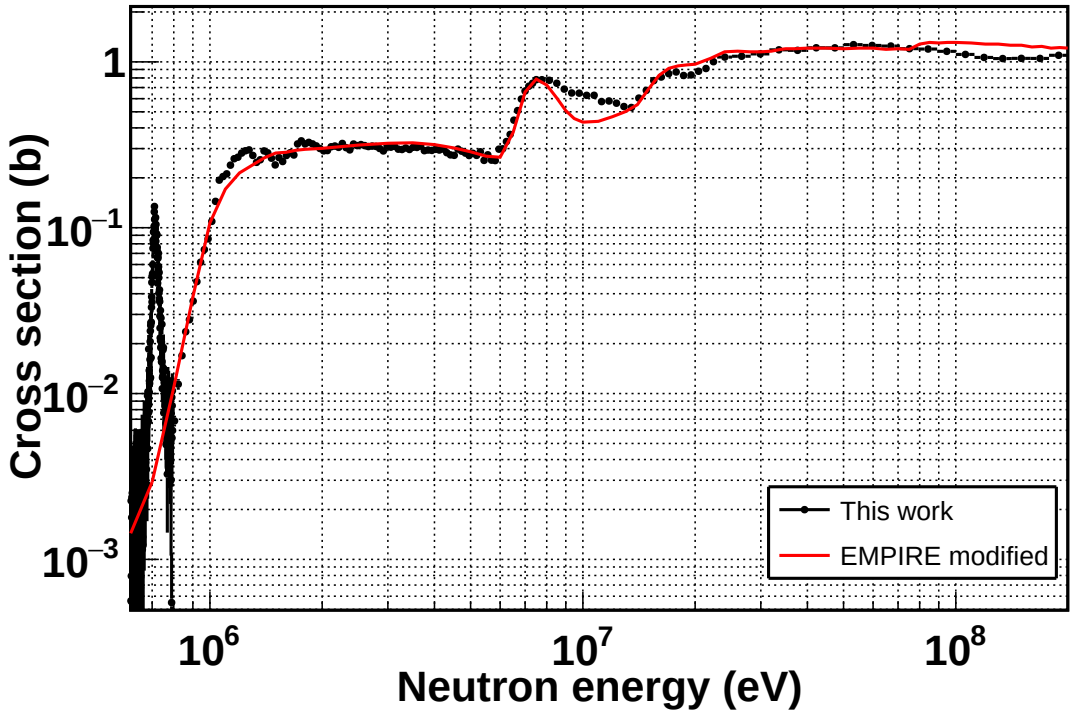

Figure 4.8: EMPIRE calculation from the fission threshold up to 200 MeV with the modified parameters (red line) along with the experimental data of this work (black points), for the ^{230}Th fission cross-section.

Along with the total fission cross-section of ^{230}Th the higher chance fission cross-sections are estimated individually in the EMPIRE calculation. As seen in figure 4.9 the (n,f) channel is dominant up to 6 MeV, while at higher energies the (n,nf) channel is the more important one, with contributions from the (n,2nf) and the (n,3nf) at 18 and 25 MeV, respectively. The contribution from higher chance fission is also present in the experimental data, where very good agreement is seen in the position of the peaks from higher chance fission between the EMPIRE calculations and the experimental data. The cross-sections for higher chance fission, are at least one order of magnitude lower than the total fission cross-section, thus having a negligible effect is the total fission cross-section results. It is interesting to note that the (n,nf) channel, according to the EMPIRE calculation, seems to be the dominant one for energies higher than 6 MeV, while its fission cross-section has an increase with the increase of energy. A similar behavior is observed also in the calculations of Maslov [108, 109] and Maslov *et al.* [110] for ^{230}Th and ^{232}Th, where even though the cross-section calculations for multichance fission are up to 20 MeV, an increase in the fission cross-section of (n,nf) is seen after the second chance fission peak.

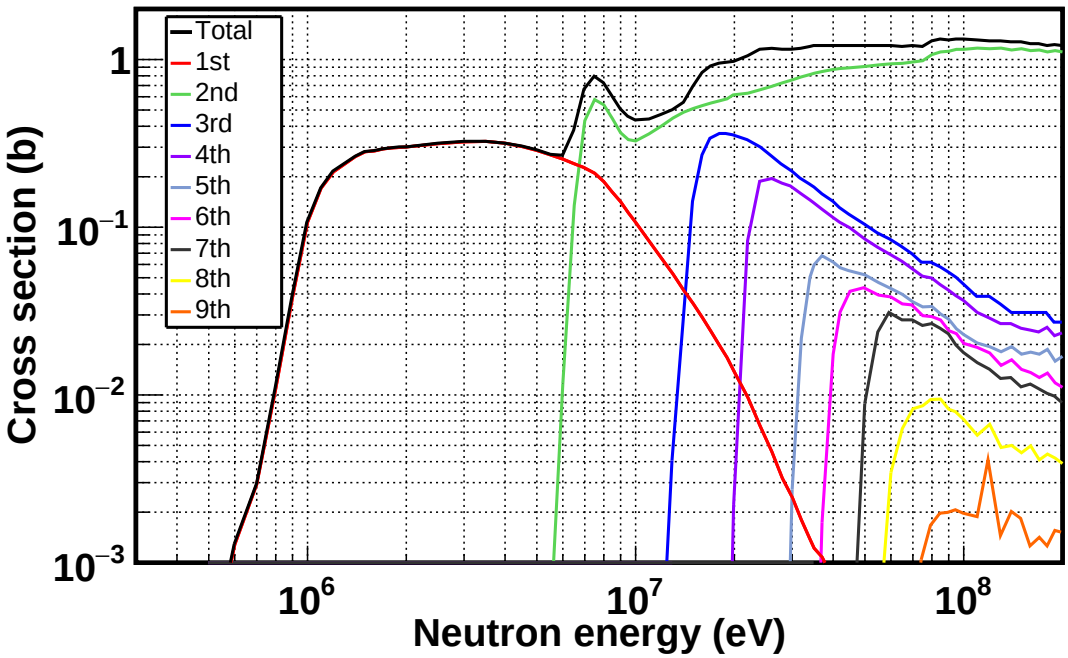

Figure 4.9: Multi-chance fission cross-sections, as calculated from the EMPIRE code with the modified parameters.

The effect of the modifications in the fission barrier characteristics and the asymptotic level density parameters on the thorium isotopes does not seem to significantly affect the other neutron induced reaction channels as seen in figure 4.10. As seen in figure 4.10a the ^{230}Th(n,tot) cross-section is not affected by the changes as expected. The total cross-section, calculated by the EMPIRE calculations, is divided into two components: the elastic part and the reaction part. The elastic part, presented in figure 4.10b, remains unaltered by the modifications, as anticipated since no parameters related to the elastic channel have been modified. The large scale structure seen in the elastic cross-section, dominating also the total cross-section, is a result

of the interference between the incident wave function and the wave transmitted through the nuclear potential [111]. The remaining reaction channels in the default EMPIRE calculation, are seen in figures 4.10c and 4.10d. As presented in the figures both the capture and inelastic cross-sections are reduced by the modified parameters. The modified parameters used for the EMPIRE calculations are selected in order to increase the fission cross-section of the default EMPIRE calculation, in order to achieve a better agreement between the experimental data and the calculations. This increase in the fission cross-section, results in a decrease in the other reaction channel cross-sections.

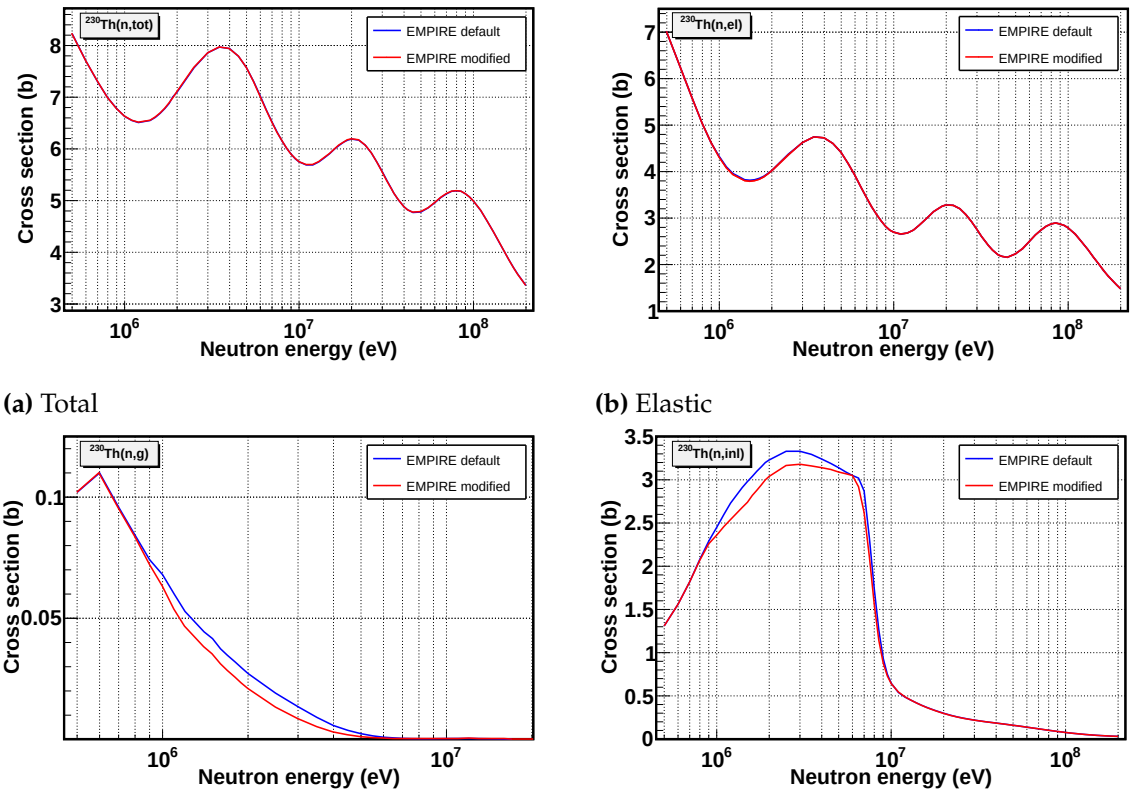

(a) Total

(b) Elastic

(c) Capture

(d) Inelastic

Figure 4.10: Total (a), elastic (b),capture (c) and inelastic (d) neutron induced cross-sections for ^{230}Th. The blue line is the theoretical predictions with the default EMPIRE parameters, while the red line with the modified parameters.

The ^{230}Th(n,xn) reaction channels were estimated in the modified EMPIRE calculation and are presented in figure 4.11. As seen in the figure the (n,2n), (n,3n) and (n,4n) channels have a significant cross-section, which is reducing at higher energies. As mentioned above, it is unfortunate that no available experimental data exist in literature for these reactions in order to validate the EMPIRE calculations and constrain the theoretical model.

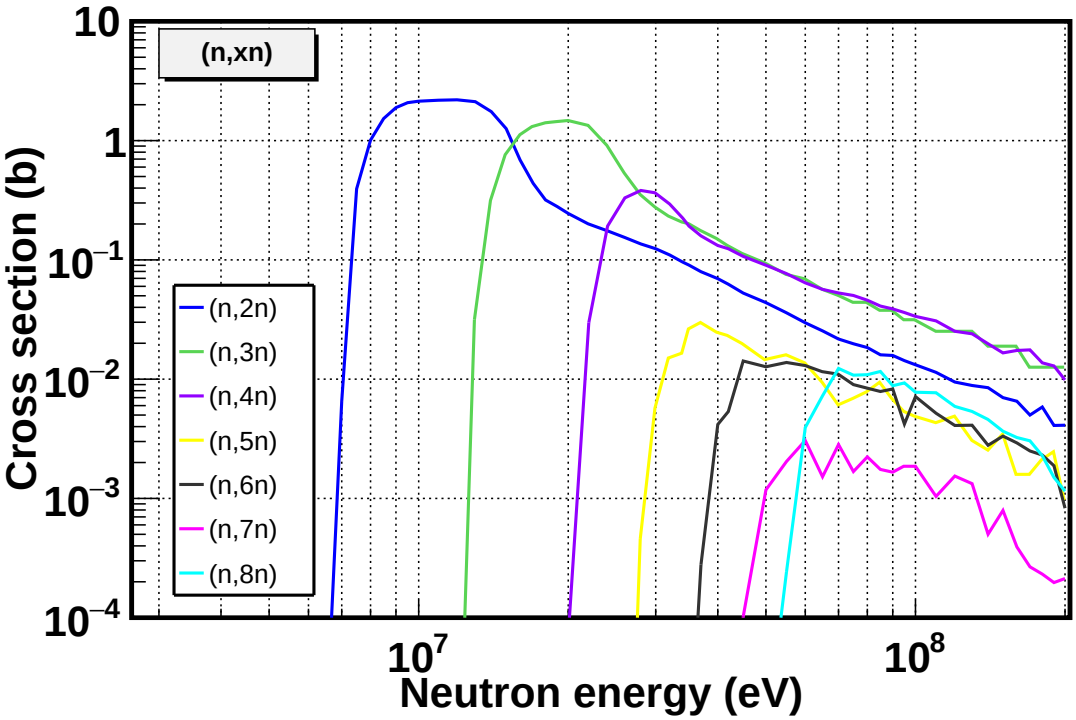

Figure 4.11: Cross-section for the (n,xn) channels from the EMPIRE calculation with the modified parameters.

Chapter 5

Conclusions and future perspectives

The scope of the present thesis was the study of the ^{230}Th(n,f) reaction, within the framework of the n_TOF collaboration at CERN, in order to provide high accuracy data over a wide energy range. These data might help in resolving the discrepancies between the previous datasets and also provide useful information for the study of the fission process itself. In addition, neutron induced cross-section data are needed for the design and study of New Generation Nuclear Reactors.

In this work the fission cross-section of ^{230}Th using ^{235}U as reference was estimated from the fission threshold up to 400 MeV (EAR-1 measurement), providing for the first time in literature data for energies higher than 25 MeV. The improvement of the experimental setup and electronics made it possible to reach this high energy region, for the first time with the use of Micromegas detectors at the first experimental area EAR-1 of n_TOF. A comparison of the experimental data between EAR-1 and EAR-2, in the energy region from the fission threshold to 1 MeV, was achieved, resulting to fairly good agreement between the results (taking into account the difficulties encountered in the analysis of the EAR-2 data, namely the contaminants, high counting rates etc.)

The analysis procedure was detailed and thorough, in order to ensure the correct counting of the fission pulses and the accurate conversion from time-of-flight to energy. This included a detailed study of the γ-flash pulse, a methodology for the rejection of noise at higher energies, detailed Monte Carlo simulations for reproducing the experimental amplitude spectra etc. In addition, a simplified approach was attempted for the estimation of a gross angular distribution of the fission fragments for the first time with this type of Micromegas detectors. The angular distribution methodology gave promising results, but, more importantly, the motivation for measuring the angular distribution of the ^{230}Th(n,f) reaction in a wide energy range, with a more accurate detection system for this kind of measurements (as PPACs).

Finally, a theoretical study of the ^{230}Th(n,f) reaction was carried out with the EMPIRE code. The double-humped fission barrier was used for the calculations, while fission barrier heights and widths of the thorium isotopes were adjusted and/or added to the existing RIPL-3 fission data, in order to improve the agreement between the EMPIRE calculations and the gross structure of the experimental cross-section results. Further theoretical investigation with the triple humped potential

might be able to reproduce the resonance in the threshold region, as indicated from previous studies on the ^{232}Th(n,f) reaction.

This theoretical study stressed out the need of new experimental measurements in order to constrain the theoretical models. The shape of the fission cross-section of thorium isotopes, known as the thorium anomaly, has not yet been explained theoretically. Additional experimental measurements of the angular distributions of fission fragments can assist in the study of the fission process. In addition, cross-section measurements of competing channels, which for ^{230}Th do not exist in literature, can also provide useful information for the theoretical study of nuclear reactions. Regarding the low energy region, measurements with ^{230}Th targets with less impurities can assist in the determination of the cross-section below the fission threshold.

In addition, new high resolution measurements in the resonance, can be of great importance in order to confirm the data of Blons *et al.* [29], which are the only existing high resolution data in the region. A confirmation of the fine structures and the value of the resonance can assist in the theoretical study of the reaction and can verify the absolute value of the maximum cross-section at the resonance peak which is overestimated by Boldeman and Walsh [28] and by the normalized data of Blons *et al.* [29] and James *et al.* [30] according to the present data.

In conclusion, for the study of the fission process, additional experimental data would be of great help in order to constrain and evolve the theoretical models. Competing reactions, angular distributions of fission fragments and other experimental values related to the fission process would be the next step, in order to better understand the fission mechanism and offer an explanation for the fine structures present in the fission cross-section of the thorium isotopes, known as the thorium anomaly.

Bibliography

[1] Suglobov, D. N., Yakovlev, R. M. & Myasoedov, B. F. Thorium-uranium fuel cycle for heat and power engineering. *Radiochemistry* **49**, 441–448 (2007). URL https://doi.org/10.1134/S1066362207050013.

[2] Generation-IV International Forum URL https://www.gen-4.org/gif/.

[3] Zerkin, V. V. & Pritychenko, B. The experimental nuclear reaction data (EXFOR): Extended computer database and Web retrieval system. *Nucl. Instrum. Meth. A* **888**, 31–43 (2018). URL https://doi.org/10.1016/j.nima.2018.01.045.

[4] Rubbia, C. *et al.* A high resolution spallation driven facility at the CERN-PS to measure neutron cross sections in the interval from 1 eV to 250 MeV. Tech. Rep. CERN-LHC-98-002-EET, CERN (1998). URL cds.cern.ch/record/357112.

[5] Abbondanno, U. *et al.* CERN n_TOF facility : Performance report. Tech. Rep. CERN-SL-2002-053-ECT, CERN, Geneva (2002). URL cds.cern.ch/record/601511.

[6] Berthoumieux, E. The neutron Time-Of-Flight facility, n_TOF, at CERN (I): Technical Description. Tech. Rep. n_TOF-PUB-2013-001, CERN, Geneva (2013). URL cds.cern.ch/record/1514680.

[7] Colonna, N. *et al.* The fission experimental programme at the CERN n_TOF facility: status and perspectives. *Eur. Phys. J. A* **56**, 48 (2020). URL https://doi.org/10.1140/epja/s10050-020-00037-8.

[8] Barbagallo, M. *et al.* High-accuracy determination of the neutron flux at n_TOF. *Eur. Phys. J. A* **49**, 156 (2013). URL https://doi.org/10.1140/epja/i2013-13156-x.

[9] Sabaté-Gilarte, M. *et al.* High-accuracy determination of the neutron flux in the new experimental area n_TOF-EAR2 at CERN. *Eur. Phys. J. A* **53**, 210 (2017). URL https://doi.org/10.1140/epja/i2017-12392-4.

[10] Shekhtman, L. Micropattern gaseous detectors. *Nucl. Instrum. Meth. A* **494**, 128–141 (2002). URL https://doi.org/10.1016/S0168-9002(02)01456-0.

[11] Andriamonje, S. *et al.* Development and performance of Microbulk Micromegas detectors. *J. Instrum.* **5**, P02001 (2010). URL https://doi.org/10.1088/1748-0221/5/02/p02001.

[12] Oed, A. Micro pattern structures for gas detectors. *Nucl. Instrum. Meth. A* **471**, 109–114 (2001). URL https://doi.org/10.1016/S0168-9002(01)00966-4.

[13] Sauli, F. Micro-pattern gas detectors. *Nucl. Instrum. Meth. A* **477**, 1–7 (2002). URL https://doi.org/10.1016/S0168-9002(01)01903-9.

[14] Hoch, M. Trends and new developments in gaseous detectors. *Nucl. Instrum. Meth. A* **535**, 1–15 (2004). URL https://doi.org/10.1016/j.nima.2004.07.265.

[15] Giomataris, Y., Rebourgeard, P., Robert, J. & Charpak, G. MICROMEGAS: a high-granularity position-sensitive gaseous detector for high particle-flux environments. *Nucl. Instrum. Meth. A* **376**, 29–35 (1996). URL https://doi.org/10.1016/0168-9002(96)00175-1.

[16] Giomataris, Y. Development and prospects of the new gaseous detector "Micromegas". *Nucl. Instrum. Meth. A* **419**, 239–250 (1998). URL https://doi.org/10.1016/S0168-9002(98)00865-1.

[17] Andriamonje, S. *et al.* A Transparent Detector for n_TOF Neutron Beam Monitoring. *J. Korean Phys. Soc.* **59**, 1597–1600 (2011). URL https://doi.org/10.3938/jkps.59.1597.

[18] Stamatopoulos, A. *Study of the ^{240}Pu(n,f) and ^{237}Np(n,f) reaction cross sections at the new experimental area (EAR2) of the CERN n_TOF facility*. Ph.D. thesis, National Technical University of Athens (2019).

[19] Brun, R. & Rademakers, F. ROOT: An object oriented data analysis framework. *Nucl. Instrum. Meth. A* **389**, 81–86 (1997). URL https://doi.org/10.1016/S0168-9002(97)00048-X.

[20] Knoll, G. F. *Radiation detection and measurement* (Wiley New York, 1989), 2nd edn.

[21] Böhlen, T. T. *et al.* The FLUKA Code: Developments and Challenges for High Energy and Medical Applications. *Nucl. Data Sheets* **120**, 211–214 (2014). URL https://doi.org/10.1016/j.nds.2014.07.049.

[22] Battistoni, G. *et al.* The FLUKA code: description and benchmarking. *AIP Conf. Proc.* **896**, 31–49 (2007). URL https://doi.org/10.1063/1.2720455.

[23] Schmidt, K.-H., Jurado, B., Amouroux, C. & Schmitt, C. General Description of Fission Observables: GEF Model Code. *Nucl. Data Sheets* **131**, 107–221 (2016). URL https://doi.org/10.1016/j.nds.2015.12.009.

[24] X-5 Monte Carlo Team. *MCNP — A General Monte Carlo N-Particle Transport Code, Version 5 (LA-UR-03-1987)* (2005).

[25] Brown, D. A. *et al.* ENDF/B-VIII.0: The 8th Major Release of the Nuclear Reaction Data Library with CIELO-project Cross Sections, New Standards and Thermal Scattering Data. *Nucl. Data Sheets* **148**, 1–142 (2018). URL https://doi.org/10.1016/j.nds.2018.02.001.

[26] Carlson, A. D. *et al.* Evaluation of the Neutron Data Standards. *Nucl. Data Sheets* **148**, 143–188 (2018). URL https://doi.org/10.1016/j.nds.2018.02.002.

[27] Marcinkevicius, B., Simakov, S. & Pronyae, V. ^{209}Bi(n,f) and ^{nat}Pb(n,f) Cross Sections as a New Reference and Extension of the ^{235}U, ^{238}U and ^{239}Pu(n,f) Standards up to 1 GeV. *IAEA INDC(NDS)0681* (2015). URL https://www-nds.iaea.org/standards/.

[28] Boldeman, J. W. & Walsh, R. L. Neutron fission of thorium-230 revisited. *Radiat. Eff.* **92**, 317–321 (1986). URL https://doi.org/10.1080/00337578608208342.

[29] Blons, J., Mazur, C., Paya, D., Ribrag, M. & Weigmann, H. Proc. Int. Winter Meeting on nuclear physics. *Bormio* (1980).

[30] James, G. D., Lynn, J. E. & Earwaker, L. G. Nuclear spectroscopy of highly deformed ^{231}Th. *Nucl. Phys. A* **189**, 225–249 (1972). URL https://doi.org/10.1016/0375-9474(72)90292-8.

[31] Muir, D. W. & Veeser, L. R. Tech. Rep. 71301 (1971).

[32] Meadows, J. W. The fission cross sections of some thorium, uranium, neptunium and plutonium isotopes relative to ^{235}U. Tech. Rep. ANL/NDM-83 (1983). URL https://doi.org/10.2172/5539010.

[33] Meadows, J. W. The fission cross sections of ^{230}Th, ^{232}Th, ^{233}U, ^{234}U, ^{236}U, ^{238}U, ^{237}Np, ^{239}Pu and ^{242}Pu relative to ^{235}U at 14.74 MeV neutron energy. *Ann. Nucl. Energy* **15**, 421–429 (1988). URL https://doi.org/10.1016/0306-4549(88)90038-2.

[34] Kazarinova, M. I., Zamyatnin, Y. S. & Gorbachev, V. M. Fission cross sections for Th^{230}, Pu^{240}, Pu^{241}, and Am^{241} by neutrons with energies of 2.5 and 14.6 MeV. *Sov. At. Energy* **8**, 125–127 (1961). URL https://doi.org/10.1007/BF01481207.

[35] Goldblum, B. L. *et al.* Indirect determination of the ^{230}Th(n,f) and ^{231}Th(n,f) cross sections for thorium-based nuclear energy systems. *Phys. Rev. C* **80**, 044610 (2009). URL https://doi.org/10.1103/PhysRevC.80.044610.

[36] Petit, M. *et al.* Determination of the ^{233}Pa(n,f) reaction cross section from 0.5 to 10 MeV neutron energy using the transfer reaction ^{232}Th(^{3}He,p)^{234}Pa. *Nucl. Phys. A* **735**, 345–371 (2004). URL https://doi.org/10.1016/j.nuclphysa.2004.02.017.

[37] Herman, M. *et al.* EMPIRE: Nuclear Reaction Model Code System for Data Evaluation. *Nucl. Data Sheets* **108**, 2655–2715 (2007). URL https://doi.org/10.1016/j.nds.2007.11.003.

[38] Capote, R. *et al.* RIPL – Reference Input Parameter Library for Calculation of Nuclear Reactions and Nuclear Data Evaluations. *Nucl. Data Sheets* **110**, 3107–3214 (2009). URL https://doi.org/10.1016/j.nds.2009.10.004.

[39] Capote, R., Soukhovitskii, E., Quesada, J. M. & Chiba, S. Lane consistency of the dispersive coupled-channel optical model potential. *EDP Sciences* 239–242 (2008). URL https://doi.org/10.1051/ndata:07765. Proceedings of the International Conference on Nuclear Data for Science and Technology, April 22-27, 2007, Nice, France.

[40] Griffin, J. J. Statistical Model of Intermediate Structure. *Phys. Rev. Lett.* **17**, 478–481 (1966). URL https://doi.org/10.1103/PhysRevLett.17.478.

[41] Cline, C. K. The Pauli exclusion principle in pre-equilibrium decay. *Nucl. Phys. A* **195**, 353–360 (1972). URL https://doi.org/10.1016/0375-9474(72)91063-9.

[42] Plujko, V. A. A New Closed-Form Thermodynamic Approach for Radiative Strength Functions. *Acta Phys. Pol.B* **31**, 435 (2000).

[43] D'Arrigo, A., Giardina, G., Herman, M., Ignatyuk, A. V. & Taccone, A. Semi-empirical determination of the shell correction temperature and spin dependence by means of nuclear fission. *J. Phys. G: Nucl. Part. Phys.* **20**, 365–376 (1994). URL https://doi.org/10.1088/0954-3899/20/2/015.

[44] Krane, K. S. *Introductory nuclear physics* (Wiley, New York, NY, 1988).

[45] Abbondanno, U. *et al.* Measurements of Fission Cross Sections for the Isotope relevant to the Thorium Fuel Cycle. *CERN/INTC 2001-025 INTC/P-145* (2001).

[46] International Atomic Energy Agency (IAEA). Thorium fuel cycle — Potential benefits and challenges. *IAEA-TECDOC-1450* (2005).

[47] Greneche, D. & Chhor, M. *Development of the thorium fuel cycle*, 177–202 (2012). URL https://doi.org/10.1533/9780857096388.2.177.

[48] Blons, J., Mazur, C., Paya, D., Ribrag, M. & Weigmann, H. On the existence of triple-humped fission barriers in ^{231,233}Th. *Nucl. Phys. A* **414**, 1–41 (1984). URL https://doi.org/10.1016/0375-9474(84)90494-9.

[49] Shibata, K. *et al.* JENDL-4.0: A New Library for Nuclear Science and Engineering. *J. Nucl. Sci. Technol.* **48**, 1–30 (2011). URL https://doi.org/10.1080/18811248.2011.9711675.

[50] Plompen, A. *et al.* The joint evaluated fission and fusion nuclear data library, JEFF-3.3. *Eur. Phys. J. A* **56**, 181 (2020). URL https://doi.org/10.1140/epja/s10050-020-00141-9.

[51] Koning, A. J. *et al.* TENDL: Complete Nuclear Data Library for Innovative Nuclear Science and Technology. *Nucl. Data Sheets* **155**, 1–55 (2019). URL https://doi.org/10.1016/j.nds.2019.01.002.

[52] Zanini, L. *et al.* Study of the background in the measuring station at the n_TOF facility at CERN: sources and solutions. Tech. Rep. SL-Note-2001-046-EET, CERN, Geneva (2001). URL http://cds.cern.ch/record/702679.

[53] Ferrari, A., Rubbia, C. & Vlachoudis, V. A comprehensive study of the n_TOF Background. Tech. Rep. SL-Note-2001-036-EET, CERN, Geneva (2002). URL `cds.cern.ch/record/702671`.

[54] Guerrero, C. *et al.* Performance of the neutron time-of-flight facility n_TOF at CERN. *Eur. Phys. J. A* **49**, 1–15 (2013). URL `https://doi.org/10.1140/epja/i2013-13027-6`.

[55] Chiaveri, E. Proposal for n_TOF Experimental Area 2 (EAR-2). Tech. Rep. CERN-INTC-2012-029/ INTC-O-015, CERN, Geneva (2012). URL `cds.cern.ch/record/1411635`.

[56] Weiß, C. *et al.* The new vertical neutron beam line at the CERN n_TOF facility design and outlook on the performance. *Nucl. Instrum. Meth. A* **799**, 90–98 (2015). URL `https://doi.org/10.1016/j.nima.2015.07.027`.

[57] Lorusso, G. *et al.* Time–energy relation of the n_TOF neutron beam: energy standards revisited. *Nucl. Instrum. Meth. A* **532**, 622–630 (2004). URL `https://doi.org/10.1016/j.nima.2004.04.247`.

[58] Chu, S. Y. F., Ekström, L. P. & Fireston, R. B. *Lund/LBNL Nuclear Data Search* (Lawrence Berkeley National Laboratory). URL `http://nucleardata.nuclear.lu.se/toi/`.

[59] Giomataris, I. MICROMEGAS: results and prospect. *ICFA Instrum. Bul.* **19** (2004). URL `www.slac.stanford.edu/pubs/icfa/fall99/paper1/paper1a.html`.

[60] Tsinganis, A. *et al.* Measurement of the ^{242}Pu(n,f) cross section at n_TOF. *EPJ Web Conf.* **66**, 03088 (2014). URL `https://doi.org/10.1051/epjconf/20146603088`.

[61] Stamatopoulos, A. *et al.* Investigation of the $^{240}\mathrm{Pu}(n,f)$ reaction at the n_TOF/EAR2 facility in the 9 meV–6 MeV range. *Phys. Rev. C* **102**, 014616 (2020). URL `https://doi.org/10.1103/PhysRevC.102.014616`.

[62] Abbondanno, U. *et al.* The data acquisition system of the neutron time-of-flight facility n_TOF at CERN. *Nucl. Instrum. Meth. A* **538**, 692–702 (2005). URL `https://doi.org/10.1016/j.nima.2004.09.002`.

[63] CASTOR: CERN Advanced STORage manager URL `castor.web.cern.ch`.

[64] Žugec, P. *et al.* Pulse processing routines for neutron time-of-flight data. *Nucl. Instrum. Meth. A* **812**, 134–144 (2016). URL `https://doi.org/10.1016/j.nima.2015.12.054`.

[65] Tarrío, D. *et al.* Measurement of the angular distribution of fission fragments using a PPAC assembly at CERN n_TOF. *Nucl. Instrum. Meth. A* **743**, 79–85 (2014). URL `https://doi.org/10.1016/j.nima.2013.12.056`.

[66] Warren, S. *Development of the STEFF detector for the neutron Time Of Flight facility (n_TOF), CERN*. Ph.D. thesis, The University of Manchester (2016).

[67] Urlass, S. *et al.* Measurement of the ^{16}O(n,α) cross-section using a Double Frisch Grid Ionization Chamber. *EPJ Web Conf.* **239**, 01030 (2020). URL https://doi.org/10.1051/epjconf/202023901030.

[68] Leal-Cidoncha, E. *et al.* Fission Fragment Angular Distribution measurements of ^{235}U and ^{238}U at CERN n_TOF facility. *EPJ Web Conf.* **111**, 10002 (2016). URL https://doi.org/10.1051/epjconf/201611110002.

[69] Simmons, J. E. & Henkel, R. L. Angular Distribution of Fragments in Fission Induced by MeV Neutrons. *Phys. Rev.* **120**, 198–210 (1960). URL https://doi.org/10.1103/PhysRev.120.198.

[70] Yuen, G., Rizzo, G. T., Behkami, N. & Huixenga, J. R. Fragment angular distributions of the neutron-induced fission of ^{230}Th. *Nucl. Phys. A* **171**, 614–624 (1971). URL https://doi.org/10.1016/0375-9474(71)90607-5.

[71] Stamatopoulos, A. *et al.* An alternative methodology for high counting-loss corrections in neutron time-of-flight measurements. *Nucl. Instrum. Meth. A* **913**, 40–47 (2019). URL https://doi.org/10.1016/j.nima.2018.10.032.

[72] Guerrero, C., Cano-Ott, D., Mendoza, E., Wright, T. & The n_TOF Collaboration. Correction of dead-time and pile-up in a detector array for constant and rapidly varying counting rates. *Nucl. Instrum. Meth. A* **777**, 63–69 (2015). URL https://doi.org/10.1016/j.nima.2014.12.008.

[73] Vlachoudis, V. FLAIR: A Powerful But User Friendly Graphical Interface For FLUKA. *Proc. Int. Conf. on Mathematics, Computational Methods & Reactor Physics (M&C 2009) Saratoga Springs, New York, 2009* (2009).

[74] Schmitt, C., Schmidt, K.-H. & Jurado, B. The GEF model: Assessment of fission-fragment properties over an extended region. *EPJ Web Conf.* **169**, 00022 (2018). URL https://doi.org/10.1051/epjconf/201816900022.

[75] Gef model code website URL www.cenbg.in2p3.fr/-GEF-.

[76] Sibbens, G. *et al.* Morphological and compositional study of ^{238}U thin film targets for nuclear experiments. *AIP Conf. Proc.* **1962**, 030007 (2018). URL https://doi.org/10.1063/1.5035524.

[77] Hahn, O. & Strassmann, F. Nachweis der Entstehung aktiver Bariumisotope aus Uran und Thorium durch Neutronenbestrahlung; Nachweis weiterer aktiver Bruchstücke bei der Uranspaltung. *Naturwissenschaften* **27**, 89–95 (1939). URL https://doi.org/10.1007/BF01488988.

[78] Meitner, L. & Frisch, O. R. Disintegration of Uranium by Neutrons: a New Type of Nuclear Reaction. *Nature* **143**, 239–240 (1939). URL https://doi.org/10.1038/143239a0.

[79] Bohr, N. & Wheeler, J. A. The Mechanism of Nuclear Fission. *Phys. Rev.* **56**, 426–450 (1939). URL https://doi.org/10.1103/PhysRev.56.426.

[80] Wagemans, C. *The nuclear fission process* (CRC Press, Inc, United States, 1991).

[81] Vandenbosch, R. & Huizenga, J. R. *Nuclear fission* (Academic Press New York, 1973).

[82] Turkevich, A. & Niday, J. B. Radiochemical Studies on the Fission of Th^{232} with Pile Neutrons. *Phys. Rev.* **84**, 52–60 (1951). URL `https://doi.org/10.1103/PhysRev.84.52`.

[83] Britt, H. C., Wegner, H. E. & Gursky, J. C. Energetics of Charged Particle-Induced Fission Reactions. *Phys. Rev.* **129**, 2239–2252 (1963). URL `https://doi.org/10.1103/PhysRev.129.2239`.

[84] Konecny, E., Specht, H. J. & Weber, J. Symmetric and asymmetric fission of Ra- and Ac- isotopes. *Physics and Chemistry of Fission* **2**, 3–16 (1974). Proceedings of the Third IAEA Symposium on the Physics and Chemistry of Fission, Rochester, New York.

[85] Weber, J., Britt, H. C., Gavron, A., Konecny, E. & Wilhelmy, J. B. Fission of ^{228}Ra. *Phys. Rev. C* **13**, 2413–2420 (1976). URL `https://doi.org/10.1103/PhysRevC.13.2413`.

[86] Ohtsuki, T., Nakahara, H. & Nagame, Y. Systematic variation of fission barrier heights for symmetric and asymmetric mass divisions. *Phys. Rev. C* **48**, 1667–1676 (1993). URL `https://doi.org/10.1103/PhysRevC.48.1667`.

[87] Polikanov, S. M. *et al.* Spontaneous Fission with an Anomalously Short Period. I. *Soviet Phys.* **JETP 15**, 1016 (1962).

[88] Metag, V., Habs, D. & Specht, H. J. Spectroscopic properties of fission isomers. *Phys. Rep.* **65**, 1–41 (1980). URL `https://doi.org/10.1016/0370-1573(80)90006-X`.

[89] Strutinsky, V. M. Shell effects in nuclear masses and deformation energies. *Nucl. Phys. A* **95**, 420–442 (1967). URL `https://doi.org/10.1016/0375-9474(67)90510-6`.

[90] Strutinsky, V. M. "Shells" in deformed nuclei. *Nucl. Phys. A* **122**, 1–33 (1968). URL `https://doi.org/10.1016/0375-9474(68)90699-4`.

[91] Bjørnholm, S. & Lynn, J. E. The double-humped fission barrier. *Rev. Mod. Phys.* **52**, 725–931 (1980). URL `https://doi.org/10.1103/RevModPhys.52.725`.

[92] Tsinganis, A. *Measurement of the ^{242}Pu(n,f) reaction cross-section at the CERN n_TOF facility*. Ph.D. thesis, National Technical University of Athens (2014).

[93] Möller, P. & Nix, J. R. Calculation of fission barriers. *Physics and Chemistry of Fission* **1**, 103–143 (1974). Proceedings of the Third IAEA Symposium on the Physics and Chemistry of Fission, Rochester, New York.

[94] Sin, M., Capote, R., Ventura, A., Herman, M. & ObložinskÝ, P. Fission of light actinides: ^{232}Th(n,f) and ^{231}Pa(n,f) reactions. *Phys. Rev. C* **74**, 014608 (2006). URL `https://doi.org/10.1103/PhysRevC.74.014608`.

[95] Boldeman, J. W., Gogny, D., de L. Musgrove, A. R. & Walsh, R. L. Fission fragment angular distributions for neutron fission of ^{230}Th. *Phys. Rev. C* **22**, 627–637 (1980). URL https://link.aps.org/doi/10.1103/PhysRevC.22.627.

[96] Mirea, M., Tassan-Got, L., Stephan, C., Bacri, C. O. & Bobulescu, R. C. Fine structure of the 0.7 MeV resonance in the ^{230}Th neutron-induced fission cross-section. *Europhys. Lett. (EPL)* **73**, 705–711 (2006). URL https://doi.org/10.1209/epl/i2005-10454-x.

[97] Blons, J., Mazur, C., Paya, D., Ribrag, M. & Weigmann, H. Rotational Bands in Asymmetrically Deformed ^{231}Th. *Phys. Rev. Lett.* **41**, 1282–1285 (1978). URL https://doi.org/10.1103/PhysRevLett.41.1282.

[98] Sicre, A. *et al.* Fission-fragment angular distributions for ^{230}Th(n,f) in the vicinity of the 715 keV resonance. *Nucl. Phys. A* **445**, 37–56 (1985). URL https://doi.org/10.1016/0375-9474(85)90359-8.

[99] Lynn, J. E. The concept of vibrational resonances associated with the secondary and tertiary wells of a multi-humped fission barrier. *J. Phys. G: Nucl. Phys.* **9**, 665–681 (1983). URL https://doi.org/10.1088/0305-4616/9/6/011.

[100] Möller, P., Madland, D. G., Sierk, A. J. & Iwamoto, A. Nuclear fission modes and fragment mass asymmetries in a five-dimensional deformation space. *Nature* **409**, 785–790 (2001). URL https://doi.org/10.1038/35057204.

[101] Möller, P. *et al.* Heavy-element fission barriers. *Phys. Rev. C* **79**, 064304 (2009). URL https://doi.org/10.1103/PhysRevC.79.064304.

[102] Tassan-Got, L. *et al.* Fission program at n_TOF. *EDJ Web Conf.* **211**, 03006 (2019). URL https://doi.org/10.1051/epjconf/201921103006.

[103] Sin, M., Capote, R., Herman, M. W. & Trkov, A. Extended optical model for fission. *Phys. Rev. C* **93**, 034605 (2016). URL https://doi.org/10.1103/PhysRevC.93.034605.

[104] Capote, R., Chiba, S., Soukhovitskiĭ, E. S., Quesada, J. M. & Bauge, E. A Global Dispersive Coupled-Channel Optical Model Potential for Actinides. *J. Nucl. Sci. Technol.* **45**, 333–340 (2008). URL https://doi.org/10.1080/18811248.2008.9711442.

[105] Koning, A. J., Hilaire, S. & Duijvestijn, M. C. TALYS-1.0. *EDP Sciences* **214**, 211–214 (2008). URL https://doi.org/10.1051/ndata:07767. Proceedings of the International Conference on Nuclear Data for Science and Technology, April 22-27, 2007, Nice, France.

[106] Koning, A. J. & Delaroche, J. P. Local and global nucleon optical models from 1 keV to 200 MeV. *Nucl. Phys. A* **713**, 231–310 (2003). URL https://doi.org/10.1016/S0375-9474(02)01321-0.

[107] Koning, A. J., Hilaire, S. & Goriely, S. *TALYS-1.95* (2019).

[108] Maslov, V. M. Direct and compound interactions for the neutron-induced fission cross section determination. *EPJ Web Conf.* **8**, 02002 (2010). URL https://doi.org/10.1051/epjconf/20100802002.

[109] Maslov, V. M. Pairing effects in ^{232}Th neutron-induced fission cross section. *Nucl. Phys. A* **743**, 236–255 (2004). URL `https://doi.org/10.1016/j.nuclphysa.2004.08.007`.

[110] Maslov, V. M. *et al.* Neutron Data Evaluation of ^{232}Th. *IAEA-INDC(BLR)-016* (2003).

[111] Abfalterer, W. P. *et al.* Measurement of neutron total cross sections up to 560 MeV. *Phys. Rev. C* **63**, 044608 (2001). URL `https://doi.org/10.1103/PhysRevC.63.044608`.